ORGANIC LIGHT-HARVESTING MATERIALS FOR POWER GENERATION

A Dissertation

Presented to

The Academic Faculty

by

Fadi M. Jradi

In Partial Fulfillment

of the Requirements for the Degree

Doctor of Philosophy in the

School of Chemistry and Biochemistry

Georgia Institute of Technology

May 2016

ORGANIC LIGHT-HARVESTING MATERIAL FOR POWER GENERATION

Approved by:

Dr. Seth R. Marder, Advisor
School of Chemistry and Biochemistry
Georgia Institute of Technology

Dr. Bernard Kippelen
School of Electrical Engineering
Georgia Institute of Technology

Dr. Jean-Luc Brédas
School of Physical Science and Engineering
King Abdullah University of Science and Technology

Dr. John R. Reynolds
School of Chemistry and Biochemistry
Georgia Institute of Technology

Dr. David M. Collard
School of Chemistry and Biochemistry
Georgia Institute of Technology

Date Approved: March 9th, 2016

To my family in Lebanon and Syria

ACKNOWLEDGEMENTS

This dissertation, although bearing my name, is hardly the achievement of a single person. In fact, it is the product of ideas and efforts of a group of people who, other than sharing the same scientific curiosity, share the willingness to mentor, to offer knowledge freely, to be patient, to accept occasional failures, and to contribute selflessly to the promotion of science, and other individuals around them, often at the expense of their own time, progress, and comfort.

First and foremost, this dissertation would not have been possible without the mentorship of Prof. Seth Marder, who found himself, on many occasions, having to re-establish sense and order into a frustrated and bewildered mind; "You have to learn to accept that some projects will not work" was his response when I was trying to beat a dead project back to life, "Given an infinite amount of time, it might work, but unfortunately time is irreplaceable; learn from the failures and move on". This is an excerpt from the many conversations we had throughout the years that encompassed several aspects of my journey through Ph.D. life. The many lessons I learned, inside and outside the lab, will linger with me long after I leave Georgia Tech, and I hope to one day be at a position to offer that same level of advice and kindness to a host of future scientists.

Throughout this journey I find myself particularly grateful to Dr. Stephen Barlow and Dr. Timothy Parker for their day-to-day guidance; for their valuable input and discussions on my research; for helping me analyze and make sense of my data; for editing my papers and thesis chapters, and finally for making sure that I am doing the chemistry in an efficient, correct, and safe manner. I would also like to thank the many Marder Lab research scientists and postdoctoral fellows, namely Dr. Denise Bale, Dr. Yadong Zhang, Dr. Raghunath Dasari, Dr. Junxiang Zhang, Dr. Yulia Getmanenko, Dr. Kostantyn Ziabrev and Dr. Iryna Davydenko, for their seemingly endless knowledge in organic chemistry, synthetic methodologies, characterization of organic materials, and their helpful suggestions and discussions especially at times when things seemed gloomy.

I am also extremely thankful and grateful to all my colleagues and friends at the Marder Lab who made this journey enjoyable, showed extreme hospitality, contributed to scientific and rather random conversations, and definitely eased my transition to the United States. In specific I would like to thank Marcel Said, Janos Simon, Karttikay Moudgil, Matthew Cooper, Dr. Anthony Giordano, and Dr. Sergio Paniagua.

I also wish to thank the many collaborators I have had the opportunity to work with over the years: Particularly, I wish to thank Prof. Mostafa El-Sayed and the members of his group, Dr. Xiongwu Kang, Dr. Paul Szymanski and Daniel O'Neil, for their scientific insights and discussions, and for providing us with the tools and expertise to test our dyes in dye-sensitized solar cells; Prof. Harry Anderson, and Jinzse Wong, at the University of Oxford, for their help and discussion relating to the work on the panchromatic sensitizers; Prof. Scott Saavedra and Yilong Zheng, at the University of Arizona, for providing the tools and expertise to characterize monolayers and determine charge transport rates across interfaces; Prof. Andrew Holmes, Dr. David Jones, and Dr. Wallace Wong, and their group members, Dr. Jegadesan Subbiah, James Banal, Nicholas Hui and Paul Geraghty, at the University of Melbourne, for giving me the opportunity to visit Melbourne and engage in exciting research in organic photovoltaics and organic solar concentrators, and for rendering my visit enjoyable and memorable.

I would also like to thank the members of my committee, Prof. Jean-Luc Brédas, Prof. John Reynolds, Prof. Bernard Kippelen, and Prof. David Collard for their invaluable scientific input and insightful discussions, and for helping me grow as a person and as a scientist throughout my five years as a Ph.D. student.

Finally, I am grateful to my parents, Amal and Mostafa, and my brother Dany for their continuous support, encouragement, and love, and for providing the stability and security I needed when things seemed uncertain. I thank all my friends in Lebanon, Atlanta, and across the globe, who have left a remarkable imprint in me and helped define who I am today, and Prof. Bilal Kaafarani who played, and continues to play, a pivotal role in my personal life and career.

TABLE OF CONTENTS

LIST OF TABLES

LIST OF FIGURES

LIST OF ABBREVIATIONS

D	Donor
A	Acceptor
M	Molecule
HOMO	Highest occupied molecular orbital
LUMO	Lowest unoccupied molecular orbital
vis.	Visible
NIR	Near infra-red
UV	Ultra-violet
DSSC	Dye-sensitized solar cell
OPV	Organic photovoltaic
PCE	Power conversion efficiency
IPCE	Incident photon-to-current conversion efficiency
J-V	Current-voltage
NMR	Nuclear magnetic resonance
HRMS	High resolution mass spectrometry
EA	Electron Affinity
IE	Ionization Energy
CV	Cyclic Voltammetry
Calc.	Calculated
HPLC	High-performance liquid chromatography
DCM	Dichloromethane
DMF	N,N-Dimethylformamide
THF	Tetrahydrofuran
DMSO	Dimethyl sulfoxide
CT	Charge transfer
CS	Charge separated
DSC	Differential scanning calorimetry
d	Days
h	Hours
min	Minutes
sec	Seconds
et al.	*Et alia*
kcal	Kilocalorie
mol	Mole
mmol	Millimole
g	Gram
mg	Milligram
PDI	Perylene diimide
Sq	Squaraine
Por	Porphyrin
PL	Photoluminescence
EQE	External quantum efficiency
Abs.	Absorbance
a.u.	Arbitrary units

equiv.	Equivalents
rt	Room temperature
eV	Electronvolts
cm	Centimeters
cm^{-1}	Wavenumber
TiO_2	Titania
ITO	Indium-Tin oxide
ZrO_2	Zirconium oxide
ZnO	Zinc oxide
Al_2O_3	Alumina
CA	Carboxylic acid
PA	Phosphonic acid
nm	nanometer
APCE	Absorbed photon-to-current conversion efficiency
Gen	Generation
FTO	Fluorine-doped Tin oxide
Pt	Platinum
NHE	Normal hydrogen electrode
vs.	versus
LDA	Lithium diisopropylamide
^{i}Pr	isopropyl
tert-	tertiary
CDCA	Chenodeoxycholic acid
M	mol/L
L	Liter
mL	Milliliter
$CHCl_3$	Chloroform
$CDCl_3$	Deuterated chloroform
NBS	N-Bromosuccinimide
BuLi	Butyl lithium
ps	picosecond
FF	Fill factor
Hz	Hertz
ca.	Circa
MLCT	Metal-to-ligand charge transfer
$FeCp_2$	Ferrocene
$FeCp_2^*$	Decamethylferrocene
CBE	Conduction band edge
PM-ATR	Potential modulated-attenuated total reflectance
TLC	Thin layer chromatography
ICT	Intermolecular charge transfer

Other abbreviations are explained in the text.

LIST OF SYMBOLS

P_{in}	Incident power
P_{max}	Maximum power point
V_{OC}	Open-circuit voltage
J_{SC}	Short-circuit current
ε_{max}	Extinction coefficient at maximum absorption
λ	Wavelength
λ_{max}	Wavelength at maximum absorption
λ_{onset}	Wavelength at the onset of absorption
$E_{1/2}$	Half-wave potential
$E_{1/2}^{+/0}$	First half-wave oxidation potential
$E_{1/2}^{0/-}$	First half-wave reduction potential
$E_{0\text{-}0}^{opt}$	Optical gap
$E_{0\text{-}0}^{elec}$	Electrochemical gap
T_m	Melting temperature
$E_{(S^+/S^*)}$	Excited-state oxidation potential
$E_{(S^+/S)}$	Ground-state oxidation potential
^oC	Degrees Celsius
K	Kelvin
k_{ei}	Charge injection rate constant
Å	Angstrom
η_{ing}	Efficiency of charge injection
η_{reg}	Efficiency of regeneration
η_{cc}	Efficiency of charge collection
f	Oscillator strength
$-\Delta G_{ei}^0$	Driving force for electron injection
$-\Delta G_{reg}^0$	Driving force for dye regeneration
V	Volts
A	Amperes
W	Watt
E_F	Fermi level energy
E_{CB}	Conduction band edge
E_{redox}	Redox potential
ΔG_{diss}^0	Driving force for exciton dissociation
q	Elementary charge
e	Electron
ϕ_p	Photon flux
u	ungerade
g	gerade
μ_T	Transition dipole
τ_{obs}	The average lifetime of the excited state
τ	Electron lifetime in TiO_2
δ	Chemical shift

Other abbreviations are explained in the text.

SUMMARY

This dissertation focuses on the design, synthesis, and characterization of a variety of organic dyes, semiconducting materials, and surface redox-active modifiers of potential interest to organic-based emerging photovoltaics. A discussion of the materials' optoelectronic properties, their ability to modify and promote electron transfer through an organic/transparent conducting-oxide interface, and finally their effect on the photovoltaic properties of devices utilizing them as light-harvesters is provided where relevant. In chapters 2 and 3, mono-chromophoric squaraine-based sensitizers and covalently linked, dual-chromophoric, porphyrin-squaraine sensitizers are investigated as light absorbers in dye-sensitized solar cells (DSSCs). Combined, both chapters attempt to address two problems often encountered with squaraine-based DSSCs; The lack of panchromatic absorption and aggregation on the surface. Chapter 4 discusses the design and synthesis of asymmetric perylene diimide phosphonic acid (PDI-PA) redox-active surface modifiers, and reports on the electron-transfer rates and efficiencies across the interface of an ITO electrode modified with these perylene diimides. Finally, in chapter 5, two series of hole-transport materials based on oligothiophenes and benzodithiophenes are reported: optoelectronic properties and preliminary performance of organic photovoltaic (OPV) devices fabricated with them is discussed.

CHAPTER 1 INTRODUCTION

1.1 MEETING THE GLOBAL ENERGY DEMAND AND ADDRESSING ENVIRONMENTAL CHALLENGES – HARVESTING SOLAR ENERGY

According to the "2015 Energy and Climate Outlook", published by the Massachusetts Institute of Technology's Joint Program on the Science and Policy of Global Change, the world's population is projected to increase by 23% to reach 9.6 billion by the year 2050. With this population increase, the world's energy consumption rate and consequently greenhouse gases (GHG) production are projected to increase by 34% and 19% to 25.4 terawatts (TW) and 64 gigatons (Gt), respectively, by the year 2050.[1] *Note:* The GHG emission estimate provided above is given in terms of "carbon dioxide equivalent" (CO_2-eq) which describes the different GHG in a common unit.

Compared to pre-industrial levels (years 1860–1880), this increase in GHG emission is projected to increase the global mean surface temperature (global warming) between 1.9–2.6 °C by mid-century; raise sea levels by 0.15–0.23 meters due to thermal expansion and melting of ice sheets and land glaciers; and increase the acidity of the oceans from an average pH of 8.13 to a pH of 7.82 by the year 2100.[1] CO_2 remains by far the largest contributor to GHG constituting around 73% of the total emissions, with fossil fuel burning being the primary source of its production. According to the latest assessment report by the Intergovernmental Panel on Climate Change,[2] burning fossil fuel for electricity generation and transportation, together, accounted for 50% of the global CO_2 emission in 2010, and is projected to account for a similar percentage at mid-century.[1]

Ways to reduce the GHG emissions, in an attempt to stabilize their concentration in the atmosphere at a level that might prevent adverse effects on the global environment, have been the subject of 21 yearly meetings by the United Nations Framework on Climate Change (UNFCCC), through their annual Conference of Parties (COP) meetings. These meetings began after the Rio Earth Summit in 1992 and continued since then with the last one (COP21) taking place in Paris–France, between November and December

2015.[3] The COP21's aim is to achieve "a legally binding and universal agreement on climate aimed at keeping the global warming below 2 °C"[3] and member countries were asked to present their efforts and plans to reduce GHG.

Prior to the meeting in November, the major GHG emitting countries submitted proposals, referred to as Intended Nationally Determined Contributions (INDCs), which highlight their GHG emission caps in the upcoming 15 years and the policies that are going to be implemented, mainly in the transportation and electricity sectors, to meet these caps.[1] For example, the United States of America, China, the European Union and Japan pledged to decrease their emission by 24–40% over the next 15 years through either preventing the construction of new coal power plants that do not implement carbon capture and storage technology, or phasing coal-based power generation by providing sufficient support to power generation from nuclear and renewable sources, such as wind and solar power, with the aim to triple or quadruple their production by 2030. If these promises are met, the highest percentage increase in power generation between 2015 and 2050 would come from renewable energy sources, which is projected to increase by 608% to constitute around 7.1% of the total energy generated from all sources by mid-century.[1]

These projections are of course subject to change and they are, in-part, dependent on the technological advances achieved in the field of renewable energy production, particularly solar power. Solar power has the greatest potential to satisfy the future need for renewable energy;[4] ca. 90,000 TW of solar power strikes the earth's surface, out of which 600 TW are of practical value, when we account only for energy that hits terrestrial land, and subtract energy lost to processes such as reflection and/or absorption by species in the atmosphere. These numbers are significantly higher than the projected global power consumption in 2050 (25.4 TW), and indicate that harvesting only a fraction of the solar power should be sufficient to meet or provide a significant portion of the ever rising demands. In the following section, the current status of solar cells is reviewed, including the various technologies presently under examination, their solar-to-electric power conversion efficiencies (PCEs), their advantages, disadvantages and future

directions. Subsequently, sections 1.3 and 1.4 review the subfields of dye-sensitized solar cells (DSSCs), and organic photovoltaics (OPVs) in more details.

1.2 CURRENT STATUS OF SOLAR CELLS

The PCE of a solar cell is the most commonly used parameter to compare the performance of one solar cell to another. It is defined as the ratio of energy output from the solar cell (P_{out}), to the incident energy from the sun (P_{in}), Eq. (1):

$$\text{PCE} = \frac{P_{out}}{P_{in}} \qquad \text{Eq. (1)}$$

A complete and up-to-date list that highlights the highest confirmed PCEs for most photovoltaic devices, both on a laboratory scale (submodule) and a module scale (cells with surface area larger than 800 cm^2), is published bi-yearly in the journal "Progress in Photovoltaics", with the latest update (version 47) published in November 2015.[5] Table 1.1, is a representative list of the different technologies (generations) of solar cells and their submodule and module PCEs.

Table 1.1 Representative list of confirmed terrestrial cell PCEs under the global AM1.5 spectrum.[a] Data presented are from the solar cell efficiency tables (version 47).[5]

		PCE (%)	
Type		Submodule	Module
1st Gen.	Silicon	25.6 ± 0.5	22.9 ± 0.6
2nd Gen.	GaAs	28.8 ± 0.9	24.0 ± 1.0
3rd Gen.	OPV	11.0 ± 0.3	8.7 ± 0.3 (OPV)
	DSSC	11.9 ± 0.4	
	Perovskite	15.6 ± 0.6	

[a]AM1.5 corresponds to the relative path length of sunlight through the earth's atmosphere at 48.2º angle from zenith point, with a temperature of 25 ºC.

As demonstrated in Table 1.1, 1st and 2nd generation photovoltaics achieve PCE values that are higher than 20%,[5] and have been commercially available for quite some

time, which indicates that the technological capability to harvest the sunlight already exists. To put this 20% PCE in context, meeting this year's global energy demand with solar energy alone can be theoretically achieved by covering 0.21% of the earth's surface with photovoltaics with 10% PCE. However, despite their commercialization and obvious advantages over traditional energy sources such as burning coal – ca. 1200 g of CO_2-eq/kWh is produced from burning coal compared to ca. 30 g of CO_2-eq/kWh produced in the manufacturing of photovoltaics.[6] the aforementioned photovoltaics, suffer from relatively high production costs with relatively long energy pay-back,[7] are material-expensive and in some cases can rely on potentially toxic materials that have limited abundance on earth.[6,8,9]

In order to ensure sustainable growth in the photovoltaic market, it is necessary to improve the cost-effectiveness (affordability) of photovoltaics compared to other energy sources such as burning coal, and reduce the environmental impact of their production and end-of-life (waste) management, where current photovoltaics can generate up 100 tons of solid waste per a MW, unless they are recycled.[8] This has led to the emergence of new photovoltaic concepts, which have been referred to as 3rd generation in (Table 1.1), which were first introduced in the early 1990s with dye sensitized solar cells (DSSCs)[10,11] and organic photovoltaics (OPVs),[12] and have more recently yielded perovskite (D^+ $PbHal_3$; Pb is Lead, D is an organic cation, and Hal is halogen) photovoltaics (PPVs).[13-15] These new technologies attract significant interest owing to their reduced production cost; they can be solution processed from potentially low-cost and abundant material; are thin, lightweight and may be useful for flexible applications.[16,17]

Compared to 1st and 2nd generation photovoltaics these "emerging photovoltaics" based on OPVs and DSSCs are still less efficient, with certified submodule PCEs ca. 12% and module PCEs that, at best, approach 9% (Table 1.1).[5] PPVs, on the other hand, despite being around for less than 5 years, have already achieved certified submodule PCE ca. 15%.[18] However, unlike PPVs, and earlier generation solar cells which rely on inorganic active materials – such as metals or metal halides, OPVs and many DSSCs utilize organic semiconducting materials,[19,20] and organic sensitizers,[21,22] respectively, as their active materials.

Organic materials and sensitizers rely on abundant elements,[23] they are relatively inexpensive to make and purify, and are highly modular, which is evident by the widespread use of organic compounds in a wide range of industries including the drug industry, the food industry, and the textile industry. As the optical, electrical and physical properties of organic compounds became more understood, they found their way into electronics such as active materials for light-emitting devices,[24-26] field-effect transistors,[27,28] and solar cells. Throughout this thesis, the application of organic materials in solar cells namely in DSSCs and OPVs will be highlighted. The central role of these materials in capturing light and converting it to electricity will be discussed in terms of their design, optical and electronic properties, and solar cell performance. Challenges that face the development of these materials, as well as paths to move forward, will also be presented.

1.3 DYE SENSITIZED SOLAR CELLS (DSSCS)

1.3.1 DSSC device configuration and operational principles

The concept of a DSSC evolved from photo-electrochemistry,[29,30] namely from the photolysis of water in an electrochemical cell,[31] however, instead of converting optical energy into chemical energy, a DSSC converts optical energy to electrical energy.[29] The most common DSSC device configuration is presented in Figure 1.1b.[21] The device is comprised of two transparent conducting oxides (usually Fluorine-Doped Tin Oxide - FTO); one is coated with a ca. 10 μm thick layer of mesoporous TiO_2 particles (containing pores whose diameter is between 10 and 50 nm) to which the organic or metal organic sensitizer is adsorbed, and a TiO_2 light-scattering layer (ca. 4 μm thick and 400–800 nm in diameter),[32-34] while the other (counter FTO electrode) is coated with a thin layer of platinum. After the two electrodes are brought together, an electrolyte solution; an organic solvent containing a redox shuttle and additives,[35] is introduced via a hole in the counter electrode, which is later on sealed.

Earlier designs, Figure 1.1a, employed a thin semiconducting layer; typically titania (TiO_2), although others such as zinc oxide (ZnO), tin oxide (SnO_2) have been

used, to adsorb the light-harvesting sensitizer. The PCE of these devices never exceeded 1%, mainly due to insufficient light absorption by the sensitizer, where ca. 1% of the incident light was absorbed.[36,37] The breakthrough happened when O'Regan and Grätzel replaced the thin TiO_2 layer, with a thick mesoporous TiO_2 layer, Figure 1.1b,[10] whose surface area was 2000 fold higher than that of the thin TiO_2. This modification resulted in higher dye loading, and consequently better light harvesting, where 46% of the incident light hitting the cell was absorbed, giving rise to a PCE ca. 7%, under AM1.5 spectrum.[10]

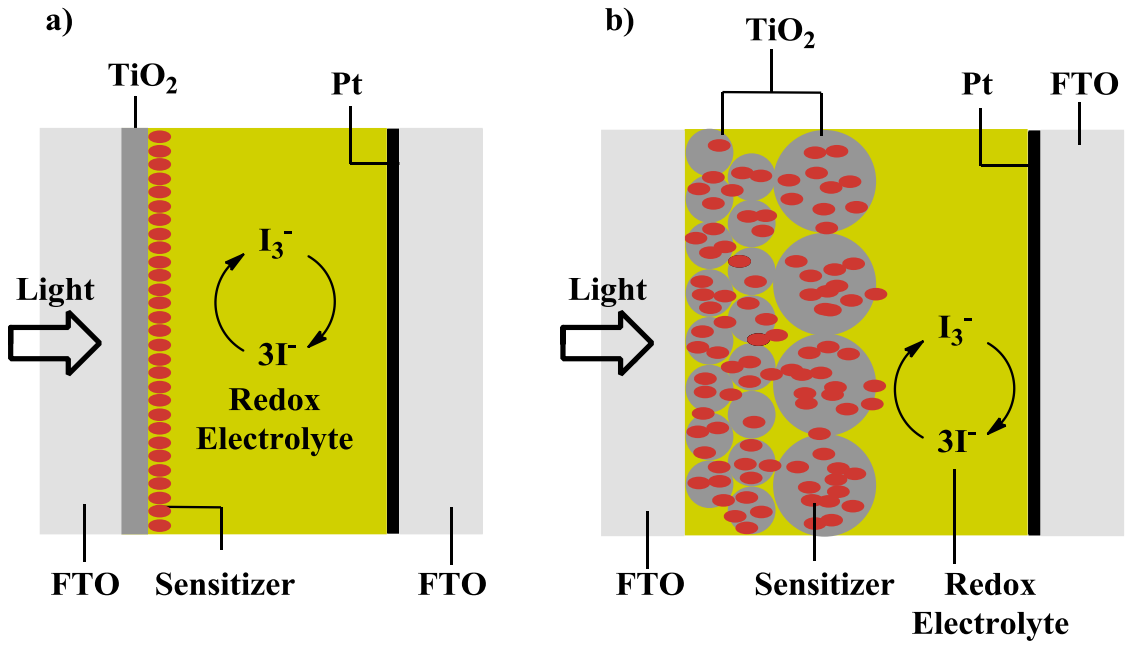

Figure 1.1 A schematic overview of a DSSC employing a thin (left), and mesoporous (right) TiO_2 semiconductor layers. The latter type is currently preferred.

The electron transfer reactions in a DSSC that result in photocurrent are highlighted with green arrows in Figure 1.2. After photo-excitation of the sensitizers by incident light (step 1), the photo-excited electrons are injected into the TiO_2 conduction band (E_{cb}-energy onset of the band consisting of unoccupied orbitals where electron transport can occur), and are then collected at the respective electrode (steps 2 and 4). Meanwhile the oxidized dye is reduced by electron transfer from the electrolyte (step 3), which is, in turn, re-reduced by the platinum-coated counter electrode to complete the regenerative cycle (step 5). To ensure efficient power generation after photon absorption, the excited sensitizers should inject electrons into the conduction band of TiO_2 before

they relax to the ground state. In a typical DSSC, electron injection occurs on the pico- to femto-second time regime and therefore is much faster than relaxation of typical dye excited states (nanosecond or longer) thus overcoming its effect.[21,38] On the other hand, electron transport from the TiO_2 into the electrode occurs on the millisecond time scale,[21,39,40] and as a result, recombination of the injected electron into the oxidized dye and/or the oxidized electrolyte is possible (steps 6 and 7, respectively). Recombination to the oxidized dye is usually minimized by the rapid dye regeneration via the electrolyte,[21] while the recombination to the oxidized electrolyte could be problematic and depends on the nature of the electrolyte; electrolytes that reduce the sensitizer by an outer-sphere electron transfer mechanism (chemical species involved are not in contact), such as cobalt based redox shuttles, tend to have higher recombination rates, [41] than electrolytes which operate via an inner-sphere electron transfer mechanism (proceeds via a covalent linkage),[42] such as triiodide/iodide redox shuttle, Figure 1.2.[41]

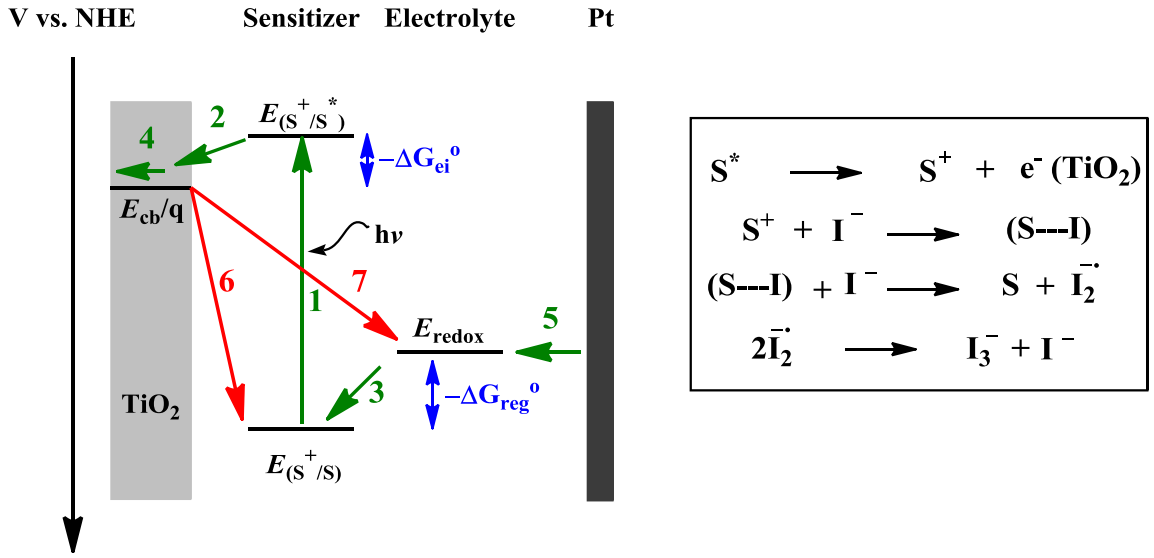

Figure 1.2 (Left) A simple energy level diagram highlighting the basic electron-transfer processes that lead to power generation (green lines), and some recombination processes that competes with the aforementioned processes (red lines). In blue is the driving force for charge injection ($-\Delta G_{ei}^{\circ}$) and dye regeneration ($-\Delta G_{reg}^{\circ}$). (Right) the pathway for the reduction of the oxidized dye (S^+) by iodide; (S---I) indicates a complex between the dye cation and the iodide that is believed to be involved in the reduction of the dye.

For the aforementioned electron transfer processes to proceed efficiently, a driving force for electron injection ($-\Delta G_{ei}^{\circ}$) from the photo-excited dye into TiO_2, and from the electrolyte to the oxidized dye ($-\Delta G_{reg}^{\circ}$) is needed. The former process requires

the presence of ca. 150 mV driving force between the dye's excited-state oxidation potential $E_{(S^+/S^*)}$ and TiO_2's E_{cb},[38] while the latter depends on the redox potential of the electrolyte employed and its reduction mechanism. For instance, DSSCs employing the triiodide/iodide redox shuttle, whose redox potential is ca. +0.35 V vs. NHE, a driving force at least +0.30 V is needed between the redox potential of the electrolyte and $E_{(S^+/S)}$ to allow for dye regeneration.[43]

This description of the operating principles and energetic requirements in a DSSC does not include other chemical complexity of the device that can influence device operation – for example it does not account for the effect of the electrolyte additives,[44,45] pH of the electrolyte,[46] and the dipole of the attached molecules[21] on the driving force for electron injection. Nevertheless, it provides a good starting point, from a material design perspective, as it defines energetic limits that the sensitizers' oxidation potentials have to operate within.

1.3.2 Power conversion in DSSCs

The aforementioned processes contribute to power generation in a DSSC device and can be correlated to device parameters as described in the current density-voltage (*J-V*) curve, blue curve, in Figure 1.3. Under illumination, the aforementioned curve intersects with the vertical and horizontal axes, with the intersection points corresponding to the short-circuit current density (J_{SC}) and the open-circuit voltage (V_{OC}), respectively. These values represent the maximum current and voltage attained by the solar cell, however, at both these values the power generated is equal to zero, because the corresponding voltage and current values, respectively, are equal to zero. The black curve in Figure 1.3 represents the power output from a cell as a function of voltage. The maximum power output (P_{max} on the black curve) is defined as the product of the J_{max} and V_{max} as described in Equation (2), with the power conversion efficiency equal to the ratio of P_{max} to the incident solar power P_{in}.

$$\mathrm{PCE} = \frac{P_{max}}{P_{in}} = \frac{V_{max} \times J_{max}}{P_{in}} = \frac{V_{OC} \times J_{SC} \times \mathrm{FF}}{P_{in}} \qquad \text{Eq. (2)}$$

$$FF = \frac{P_{max}}{J_{SC} \times V_{OC}} = \frac{J_{max} \times V_{max}}{J_{SC} \times V_{OC}} \qquad \text{Eq. (3)}$$

P_{max} can also be expressed in terms of J_{SC} and V_{OC} if a parameter, referred to as the fill factor (FF), is considered. The FF is described in Equation (3) as the ratio of P_{max} to the product of J_{SC} and V_{OC} and can be graphically represented by comparing the area of the green rectangle to the area of the red rectangle in Figure 1.3. The maximum theoretical value of the FF is V_{OC} dependent but in practice it falls short of this number due to factors such as electron transfer from the photo-anode to the electrolyte (shunting), or by series resistances in the cell.[41]

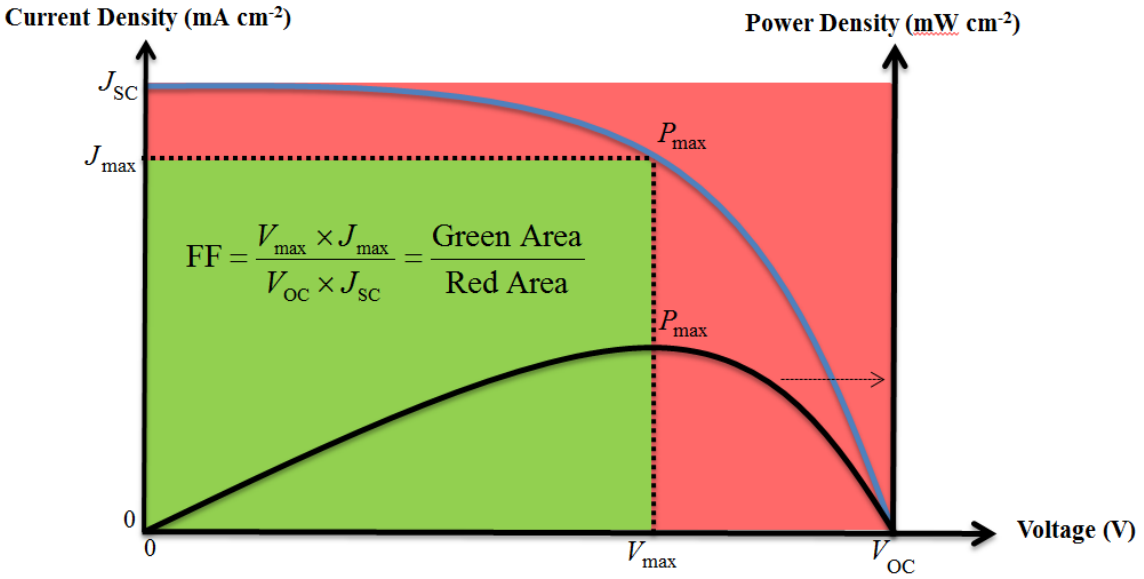

Figure 1.3 Representative *J-V* curve for a solar cell under illumination; the parameters V_{OC}, J_{SC}, FF, and P_{max}, $P_{th,max}$ are also presented.

In DSSCs, V_{OC} is limited by the difference between the absolute redox potential of the electrolyte E_{redox}, for example the values listed in Figure 1.4, and the Fermi level energy, E_f/q (q is the charge of an electron), of the semiconducting TiO_2. In addition, V_{OC} is generally reduced from this limiting value, with an important source of loss being the recombination rate of electrons in TiO_2 with acceptors in the electrolyte.[41] The recombination rate of electrons is usually studied via transient absorption measurements, and is reported in terms of electron lifetime (τ_0) as is going to be highlighted in chapters 2 and 3. Also, by changing the electrolyte from the triiodide/iodide redox shuttle, to other

electrolyte systems, such as those based on cobalt, for example $[Co(dtb)_3]^{3+/2+}$ and $[Co(phen)_3]^{3+/2+}$ in Figure 1.4, V_{OC} can be increased.

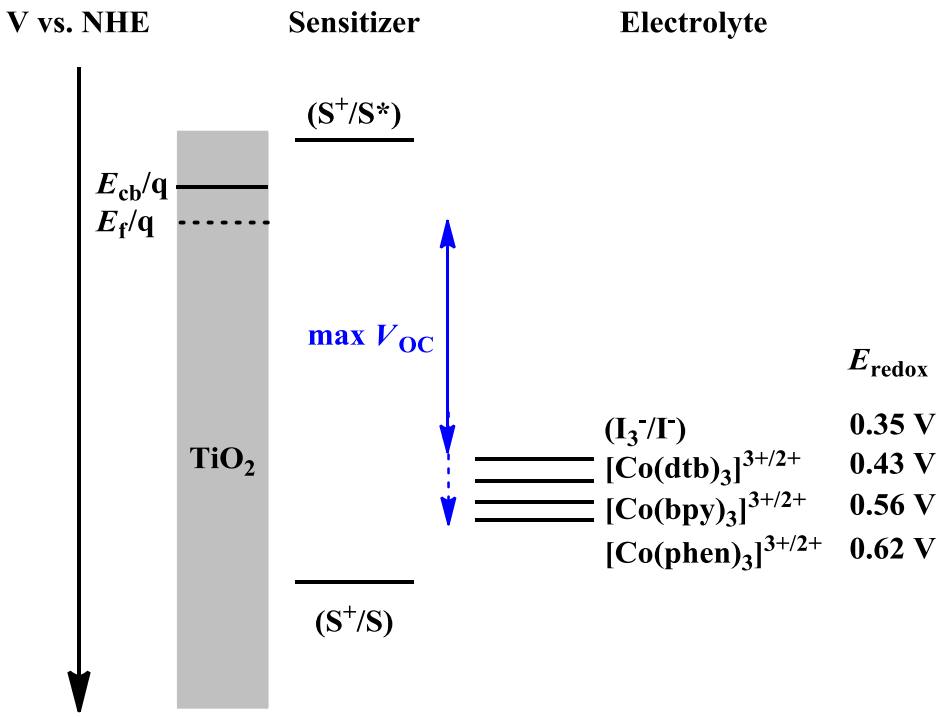

Figure 1.4 Schematic energy diagram of a mesoporous TiO_2 electrode sensitized with a dye. Also showing are the redox potentials of different cobalt based redox shuttles vs. NHE; dtb: 4,4'-di-*tert*-butyl-2,2'-bipyridine; bpy: 2,2'-bipyridine; phen: 1,10-phenanthroline.[47]

Finally, J_{SC} depends on the ability of the dye-coated TiO_2 film to absorb photons at a given wavelength ($\alpha(\lambda)$), the incident photon flux (ϕ_p), the electron injection efficiency (η_{inj}) into the TiO_2 E_{cb}, dye regeneration efficiency by the electrolyte (η_{reg}), and the electron collection efficiency (η_{cc}) at the electrode, as shown in Equation (4)

$$J_{SC} = q\left(\int_{\lambda_{TiO2}}^{\lambda_{dye}} \phi_p \alpha(\lambda)\, d\lambda\right)\eta_{inj}\eta_{reg}\eta_{cc} \qquad \text{Eq. (4)}$$

where q is the charge of an electron, and λ_{TiO2} and λ_{dye} are the absorption onsets of the TiO_2 particles and adsorbed dyes, respectively.[41]

Almost all of the solar irradiance reaching the earth's surface falls between 300 nm and 2500 nm, with more than half the energy in the range of 400 to 950 nm.[48] The

term inside the integral in Equation (4) describes how well the solar cell absorbs light, with the wavelengths of interest limited by the optical gap of the dye, and the bandgap of TiO_2. Since anatase TiO_2 (the crystal form preferred for DSSCs) has a bandgap of 3.2 eV (λ_{onset} = 388 nm),[49] which does not overlap well with the aforementioned solar irradiance, most of the light absorption responsible for the operation of the cell is from the adsorbed sensitizer.

The onset of absorption of the sensitizer (or the intersection of its normalized absorption and emission spectra) is used to estimate its optical energy gap, $E_{0\text{-}0}^{opt}$, and consequently the excited state oxidation potential, $E_{(S^+/S^*)}$, according to $E_{(S^+/S^*)} = E_{(S^+/S)} - E_{0\text{-}0}^{opt}$ ($E_{(S^+/S)}$ is determined from electrochemistry). So the $E_{0\text{-}0}^{opt}$ that can be used will depend on the previously mentioned limitations on $E_{(S^+/S^*)}$ and $E_{(S^+/S)}$ that relate to obtaining acceptable electron injection and dye regeneration efficiency. For example, in a system employing the triiodide/iodide redox shuttle, the minimum $E_{0\text{-}0}^{opt}$ that a sensitizer should have for the system to function is 1.30 eV (corresponds to $\lambda_{onset} \approx 950$ nm), this is calculated as follows: the $E_{(S^+/S^*)}$ should be more reducing than the E_{cb} of TiO_2 which is generally accepted to be at -0.50 V vs. NHE,[21,50-52] by at least 150 mV, as indicated in the previous section, while the $E_{(S^+/S)}$ should more oxidizing than the triiodide/iodide redox potential (+0.35 V vs. NHE) by at least 0.30 V. Adding all the voltages gives the aforementioned number. The term outside the integral in Equation (4) also states that after light absorption, the electrons need to be injected efficiently into TiO_2, collected at the electron-collecting electrode with little electron recombination, and finally the oxidized dye needs to be efficiently regenerated by the electrolyte. When all terms are taken into account a theoretical limit on the photocurrent density with an triiodide/iodide electrolyte is ca. 32 $mAcm^{-2}$ under AM1.5.[53]

The incident photon-to-current conversion efficiency (IPCE) is a percentage value that is proportional to the J_{SC} under monochromatic illumination of the cell, divided by the photon flux striking the cell as described in Equation 5.

$$\text{IPCE}(\lambda) \propto \frac{J_{SC}(\lambda)}{q\phi_b(\lambda)} \qquad \text{Eq. (5)}$$

where q is the electron charge

A representative IPCE spectrum is shown in Figure 1.5. As an example, this IPCE indicates that ca. 85% of the photons that strike the cell with energy of 2.1 eV (λ = 600 nm), result in current generation, and that essentially no 800 nm photons, or those a higher wavelengths, result in current, which is likely due to non-absorbance of light, by the TiO_2 adsorbed dye, at this wavelength. For a DSSC to achieve the aforementioned J_{SC} ca. 32 $mAcm^{-2}$, the IPCE should have a value of 100% between 300 nm and 950 nm.

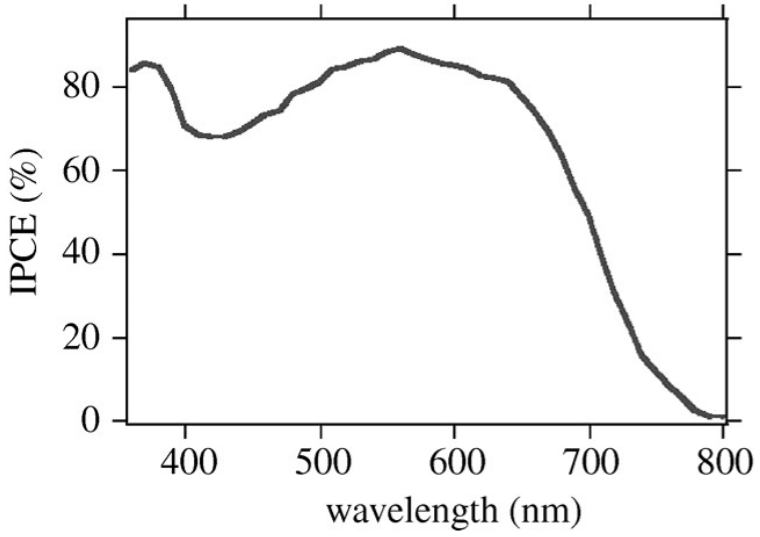

Figure 1.5 A representative IPCE spectrum

1.3.3 Sensitizers in DSSCs

Sensitizers are a central component of DSSCs, and for those to absorb light efficiently (optimize the term inside the integral in Equation 4) and to be energetically compatible with the various components of the DSSC (optimize the terms outside the integral), the sensitizers should have:

1. Panchromatic absorption, i.e. the absorption spectrum of the sensitizer should cover the whole visible region and extend into the near-infrared (NIR);
2. Anchoring groups that bind the dye onto the TiO_2 surface, and preferably conjugated to the sensitized to allow for efficient electron transfer to TiO_2. Anchoring groups such as carboxylic- and phosphonic- acids are often utilized with carboxylic acids resulting in better performance in studies so

far,[54-56] while devices based on phosphonic acids have shown greater stability due to stronger binding to TiO_2;[55,57]

3. $|E_{(S^+/S^*)}| > |E_f/q|$ and $E_{(S^+/S^*)} > E_{redox}$, as already explained.
4. Minimized unfavorable aggregation of the sensitizer; further details on the effect of aggregation in a particular system are discussed in Section 1.3.3.5; and
5. Photo, thermal and electrochemical stability.

1.3.3.1 Ruthenium-based sensitizers

Ruthenium-based sensitizers dominated the early years of DSSCs, a trimeric ruthenium complex was an essential component in the success of the 1991 work,[10] and they continue to be well studied,[21,58] with the best performing dyes being **1.1** and **1.2**,[34,59,60] in Figure 1.6. The onset of the IPCE of **1.2** is at ca. 920 nm, the IPCE then increases to reach 80% at around 750 nm, is maintained until 500 nm, and then it starts to drop gradually. This IPCE resulted in J_{SC} = 21 $mAcm^{-2}$, which with a V_{OC} = 0.74 V, and a FF = 72% gave rise to a PCE of 11.1%. Despite the initial increase in PCE, from the initial reports of O'Regan and Gratzel, ruthenium-based DSSCs have plateaued around 11%.[61] Many reasons have contributed to this halt such as their limited absorption in the NIR and their incompatibility with electrolytes other than triiodide/iodide. The regeneration of ruthenium-based dye with the triiodide/iodide redox couple has been shown to need a 600 mV difference between the redox potential of the electrolyte and $E_{(S^+/S)}$.[43,45,62] This means that ruthenium based DSSCs will have a minimum loss-in-potential; which can be estimated from the difference between the sensitizer's optical gap and the V_{OC} of the cell, of 0.75 V (0.60 V for dye regeneration and 0.15 V for charge injection into TiO_2). With this in mind, a ruthenium dye whose absorption onset is at 950 nm, will then have a maximum obtainable PCE of ca. 14%.[62]

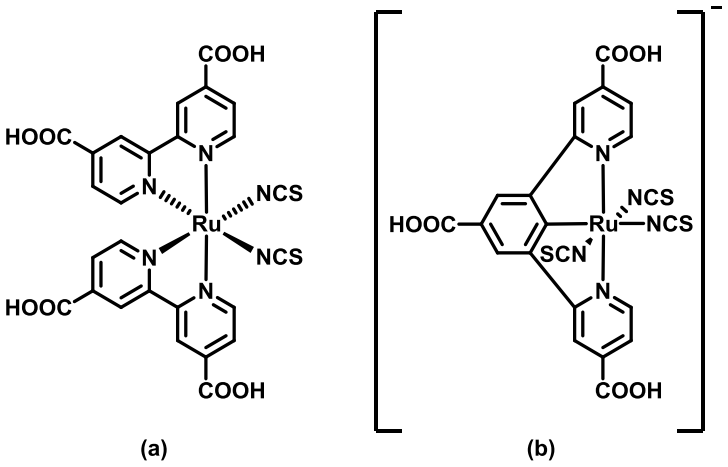

Figure 1.6 Molecular Structure of the best performing ruthenium based sensitizers: (a) **1.1**, and (b) the "black dye", **1.2**.

1.3.3.2 Strongly absorbing "push-pull" ruthenium-free sensitizers

In this thesis, organic sensitizers that follow a "push-pull" geometry will be solely discussed, Figure 1.7. These "push-pull" sensitizers have an electron donating unit (**D**) and an electron accepting unit (**A**) connected by a π-bridge so they will be referred to as "D-π-A" sensitizers. D-π-A sensitizers are highly modular due to the abundance of a wide variety of organic donors that possess different ionization energies (IEs) (minimum energy required to remove an electron from a molecule), and organic acceptors with different electron affinities (EAs); (the maximum energy released on capture of an electron by the molecule, both values are defined as a positive quantity throughout the text)[63] as well as the presence of an extensive array of synthetic tools and techniques that can covalently link these components into an organic sensitizer. This modularity allows for control over the optical properties of organic dyes; absorption onset, and maxima to achieve panchromatic absorption, as well as the electrochemical potentials; i.e. the energy of $E_{(S^+/S^*)}$ and $E_{(S^+/S)}$, to maintain energetic compatibility with the semiconductor and the redox shuttle.

Organic sensitizers generally have molar extinction coefficients, or molar absorptivities, that can be on the order of 10^5 $M^{-1}cm^{-1}$, and are higher than ruthenium based dyes whose molar absorptivities are at best on the order of 10^4 $M^{-1}cm^{-1}$.[56,64-67] This allows for enhanced light absorption and reduces the amount of dye necessary to achieve

absorbance higher than 1 (>90% absorption of the incident light), which in turn reduces the amount of material required for device fabrication either by requiring less sensitizer, or by utilizing thinner mesoporous TiO_2 layers. These factors have encouraged researchers to develop an understanding of the properties of "push-pull" sensitizers in DSSCs: To date hundreds[21,22,68-70] of ruthenium-free dyes have been designed, synthesized, and incorporated into DSSCs; including coumarin dyes, indoline dyes, triarylamine dyes, perylene dyes, hemicyanine dyes, porphyrin dyes, phthalocyanine dyes, and squaraine dyes.

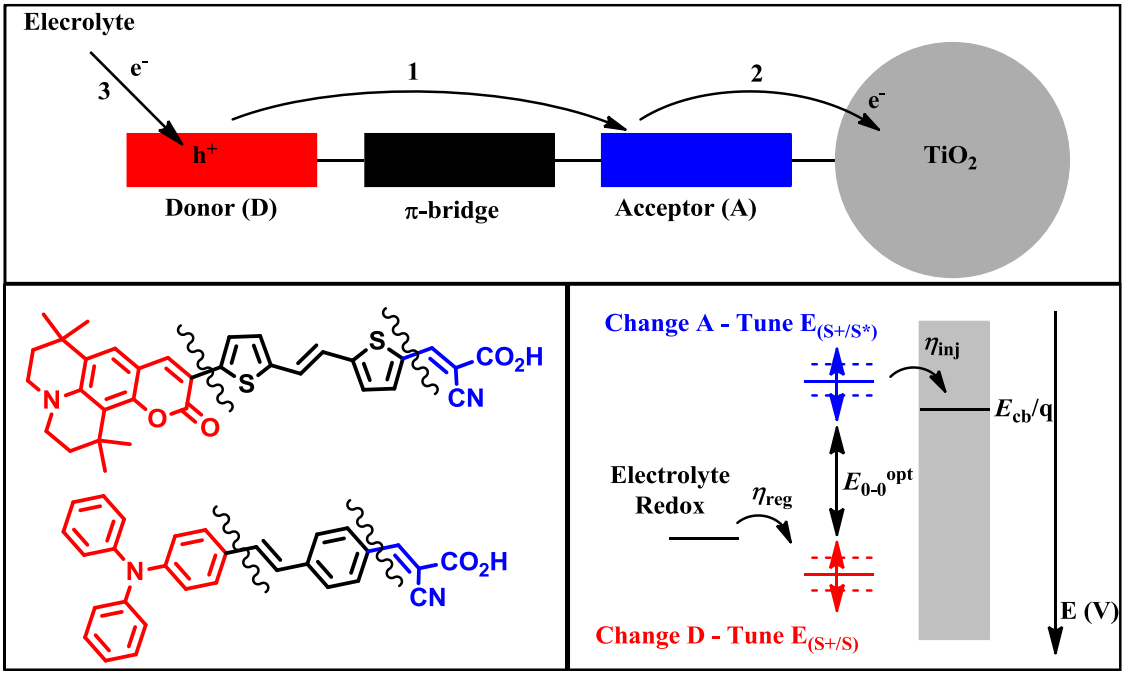

Figure 1.7 (Top) Schematic of a D-π-A sensitizer showing the intramolecular charge transfer upon photoexcitation (1 and 2), and the regeneration by the electrolyte (3). (Bottom left) Representative indolene based (PCE 8.2%),[64] and triarylamine based dyes (PCE 9.1%),[71] that follow the D-π-A geometry. The wavy lines indicate locations where these dyes can be modulated; any of the three components can be changed separately to tune a desired property such as the dye's oxidation potentials (red and blue dotted lines), electron injection efficiency η_{inj} and dye regeneration efficiency η_{reg} (Bottom Right).

In a D-π-A sensitizer, the highest occupied molecular orbital (HOMO) tends to be located predominantly on the donor end of the molecule, while the lowest unoccupied molecular orbital (LUMO) is predominantly on the acceptor. Thus, after photo-excitation a net electron transfer from the donor to the acceptor takes place, and positions the

electron density predominantly on the acceptor, which facilitates its injection into TiO_2. This same process positions the hole predominantly on the donor near the electrolyte, which facilitates both the dye regeneration process and hinders the recombination from TiO_2 into the dye, (Figure 1.7).

In the past two years, several DSSCs employing either a single D-π-A dye,[66,72-76] or multiple D-π-A dyes,[77-79] have achieve PCEs up to 13% and 14%, respectively, which places them ahead of their ruthenium-based counterparts. The single-dye cells mentioned above were based on either a porphyrin or a perylene sensitizer, Figure 1.8. Porphyrins have intrinsically strong light absorption in their Soret (400-450 nm, ε ca. 10^5 $M^{-1}cm^{-1}$) and Q (550-700 nm, ε ca. 10^4 $M^{-1}cm^{-1}$) bands, and have been extensively studied as sensitizers in DSSCs with relative success.[80-82] For example, the porphyrin D-π-A dye, **1.3**, consisting of a donor diaryl-amine on one end, and an acceptor benzothiadiazole ethynylbenzoic acid on the other end has IPCE that onsets around 780 nm and rises to reach values above 80%, which is essentially maintained over the whole visible part of the solar spectrum, Figure 1.9. This IPCE resulted in J_{SC} = 18.1 $mAcm^{-2}$ and power conversion efficiencies of ca. 13%.[75]

Similarly, D-π-A sensitizers, such as **1.4**, with *N*-annulated perylene donors and benzothiadiazole benzoic acid acceptors were more recently reported. Compared to a typical perylene, the extended conjugation, as well as the intramolecular charge transfer character of **1.4**, bathochromically shifted its solution absorption onset to around 650-700 nm.[83] This, added to relatively high molar extinction coefficients (>10^4 $M^{-1}cm^{-1}$), gave IPCE values that reached 90% over the 700-450 nm range before gradually decreasing to 10% at around 350 nm. This resulted in J_{SC} ca. 20 $mAcm^{-2}$ and PCEs as high as 12.5%.[73,74] Similar J_{SC} and even higher PCE values were reported in DSSCs that employed multiple co-sensitized dyes to achieve panchromatic absorption.[77-79]

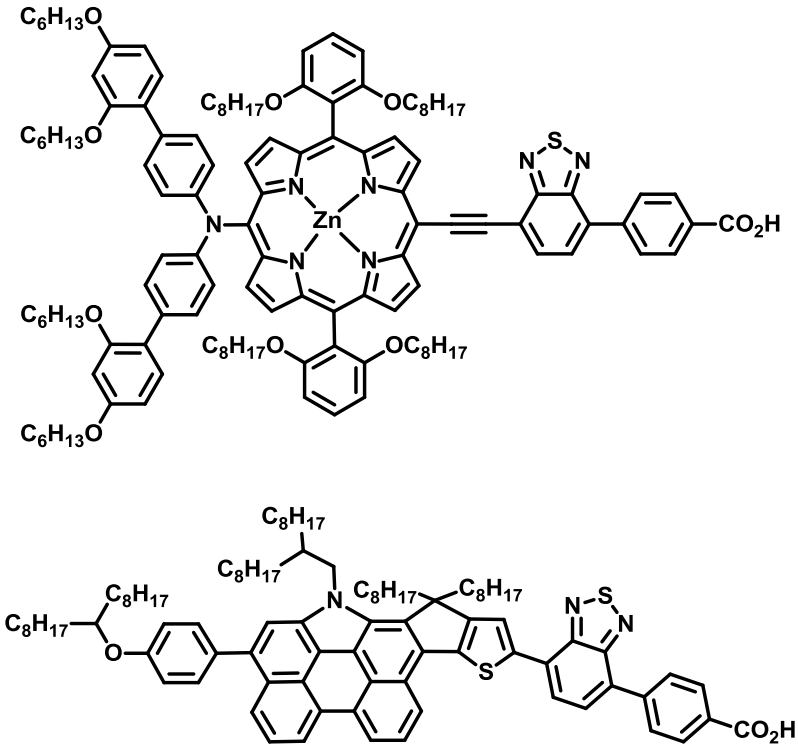

Figure 1.8 Molecular structure of a porphyrin based sensitizer **1.3** and a perylene-based sensitizer **1.4** with PCE of 13% and 12%, respectively.

J_{SC} values approaching 20 mAcm^{-2} are not uncommon with ruthenium-based DSSCs, however the significant advantage these D-π-A dyes have over ruthenium is in their V_{OC} values. While ruthenium-based cells did not achieve V_{OC} values higher than 0.85 V,[61] due to their incompatibility with redox shuttles other than iodide/triiodide, cells fabricated with the two above mentioned D-π-A dyes exhibited V_{OC} values that reached as high as 0.96 V,[74] in single-dye cells and surpassed 1.00 V in co-sensitized cells.[78] This is because of their compatibility with cobalt-based electrolyte $[Co(phen)_3]^{3+/2+}$, whose redox potential is 0.27 V higher than that of triiodide/iodide, as shown in Figure 1.4.

In order to push the PCE of such D-π-A sensitizers beyond 15% more light needs to be harvested. The IPCE of **1.3** is shown in Figure 1.9, and although more photocurrent can be obtained by bringing the IPCE values in the visible region closer to 100%, the increase is not expected to be of very large magnitude as the IPCE values are already at ca. 80%. Harvesting near infra-red light, on the other hand, has the potential of increasing the photocurrent in a more substantial manner. **1.3**, has an $E_{(S^+/S^*)}$ that provides ca. 0.35 mV extra driving force for charge injection into TiO_2 and a $E_{(S^+/S)}$ that provides ca. 0.10

mV extra driving force for dye regeneration over what is considered necessary by $[Co(phen)_3]^{3+/2+}$. This means that a sensitizer whose optical gap is ca. 1.35 eV, i.e an near infra-red absorbing dye, should be able to replace **1.3**, and potentially result in better performing DSSCs, if it also retains the ability of **1.3** to absorb high energy light.

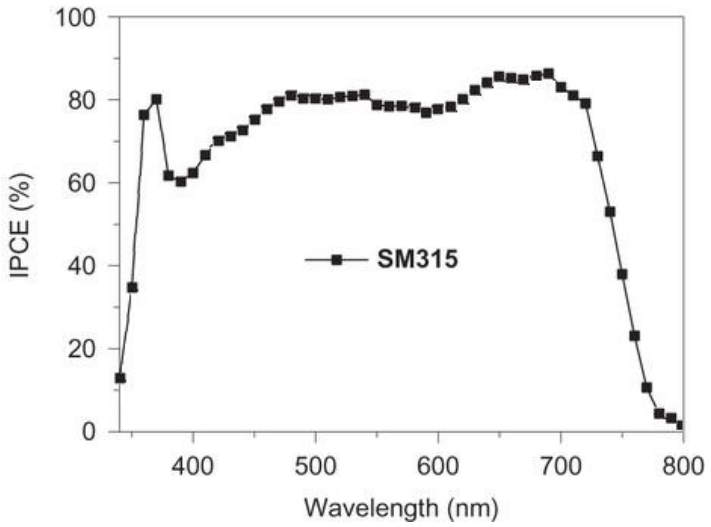

Figure 1.9 The IPCE spectra of porphyrin **1.3**.

1.3.3.3 Near infra-red absorbing sensitizers

Several classes of dyes have been utilized as near infra-red sensitizers due to their inherent near infra-red absorption including cyanines,[84-86] squaraines,[56,67,87] and phthalocyanines.[88-90] All of these dyes have a strong absorption band ($\varepsilon > 10^5$ $M^{-1}cm^{-1}$) at wavelengths longer than 600 nm. These extinction coefficients are an order-of-magnitude higher than those of the Q bands of porphyrins. In addition, these dyes can, with appropriate design, achieve absorption at wavelengths higher than 800 nm via either extending their conjugation, or via introducing and/or enhancing intramolecular charge transfer characteristics.[91,92] Another way to achieve near infra-red absorption is to covalently link multiple chromophores into an extended sensitizer.[93-98] Although this approach did achieve panchromaticity[97,99] and PCEs up to 11%,[93] linking multiple chromophores can be synthetically demanding and low yielding, which can add to the cost of device fabrication and amount of starting material required.

In the next section, one class of near infra-red sensitizers, squaraine dyes, will be discussed in detail as they will be the subject of two research chapters in this thesis. Considerable attention has been given to squaraine dyes as they are conceptually easy to synthesize, modify, and have the optoelectronic properties that render them interesting for a wide variety of applications that range from optical recording, photodynamic therapy, ion sensing, and solar cells.[92]

1.3.3.3.1 Near infra-red squaraine sensitizers

1.3.3.3.1.1 Overview and synthesis of squaraines

First reported in the mid-1960s[100,101] squaraines are the condensation products of squaric acid (**1.5** in Figure 1.10), or some of its derivatives such as squaric esters (**1.7**, R = *n*-butyl in Figure 1.10) or squarylium dichloride,[102] and electron-rich (hetero)arenes such as *N*,*N*-dialkylanilines, pyrroles, thiophenes, phenols and indolinium salts.[86,102,103] This synthetic versatility allows for the fine-tuning of their properties, such as color and solubility, towards a specific application. Squaraines are members of the polymethine family, and unlike cyanines (other members of polymethine family), which are charged, squaraine are zwitterionic and hence formally neutral. They do, however, share some similarities to cyanines, which will be addressed in the next section.

In their most common and basic form, squaraines are symmetric and assume a D-A-D geometry with electron-rich end groups, and an electron-deficient squaraine core, **1.6** in Figure 1.10 is a representative symmetric squaraine.[104] However, D-A-D' structures can be realized if a squaric acid derivative, such as squaric ester is used in the condensation. The later makes it possible to isolate the semi-squaraine **1.8**, which then can be further condensed with a different (hetero)arene, **1.9**, to get **1.10**, a representative asymmetric squaraine in (Figure 1.10).[105] Both **1.6** and **1.10** in Figure 1.10 form with 1,3 regio-chemistry of the donors on the squaraine, with the oxygens in the 2,4 positions.[106]

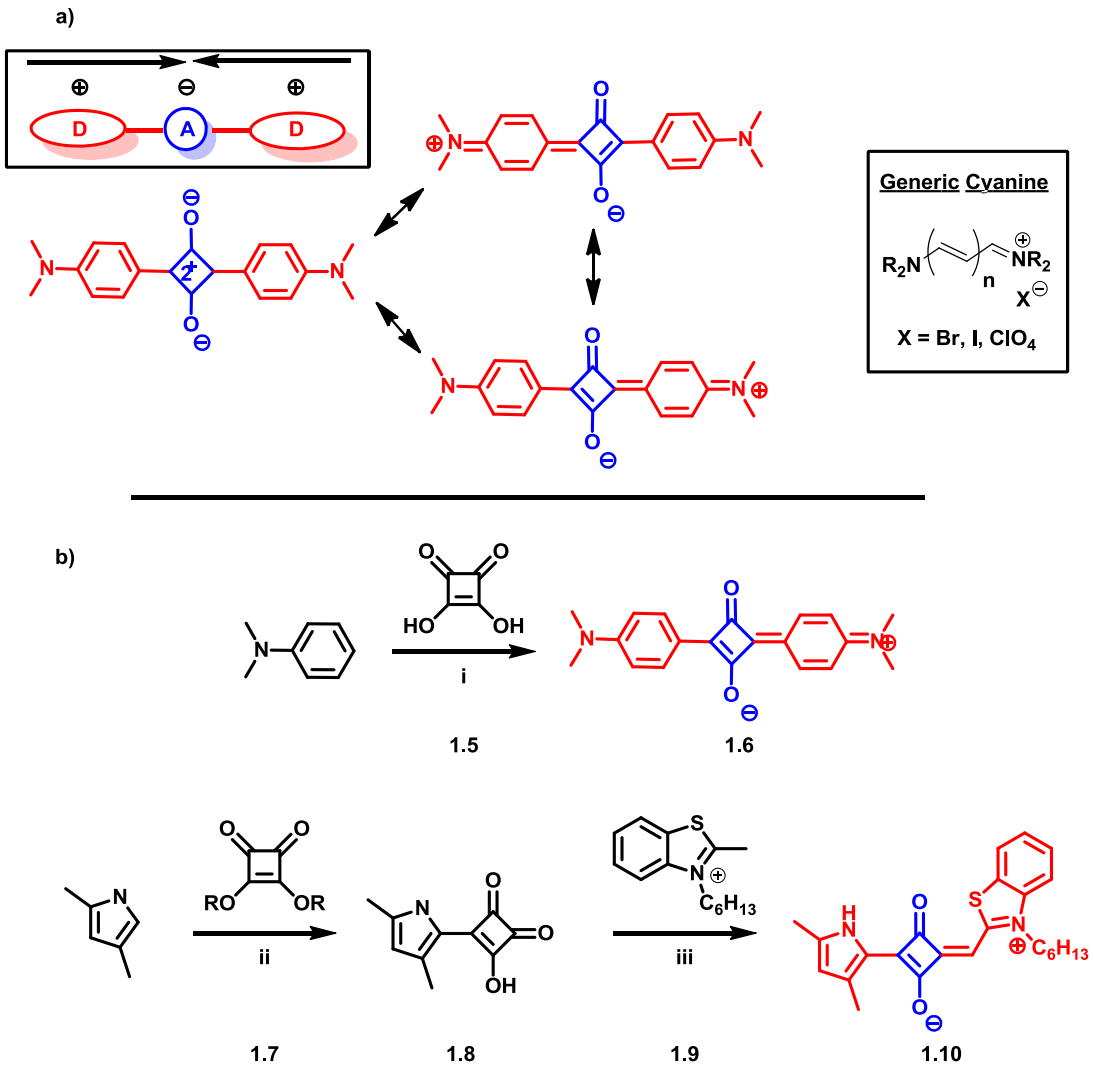

Figure 1.10 (a) A representative squaraine showing its D-A-D nature and its resonance structures, also shown a generic structure of cyanine (b) Structures of a symmetric squaraine **1.6**, and an asymmetric squaraine **1.10**. The synthetic routes shown are representative of what is commonly used to achieve each type of squaraine: (i) dimethylaniline/**1.5** (2:1), toluene/butanol, reflux, 8 h; 50% (ii) a) 2,4-diemthylpyrrole/**1.7** (1:1), ethanol, reflux, overnight; b) THF, LiOH, 3 h then HCl/H_2O; 50% (iii) toluene/butanol, imidazole, reflux, 4h; 59%.

In the synthesis of symmetric squaraines an excess of the (hetero)arene (at least 2 molar equivalents) is used, and the reaction is typically heated at reflux over an extended period of time in a mixture of a polar protic solvent, such as acetic acid or an alcohol, (ethanol, iso-propanol or butanol), and an aromatic hydrocarbon (benzene or toluene).[86,102,103] Water from the condensation is typically removed azeotropically with a Dean-Stark trap. The yields of this reaction vary widely; however, it is observed that

more electron-rich (hetero)arenes are higher yielding.[102,107] Following the first condensation a semi-squaraine intermediate is generated, which rapidly condenses with the second equivalent of the nucleophile to produce the symmetric squaraine. It should be noted that the second condensation may not be highly regio-selective and may in some cases lead to the formation of some amount of the 1,2-regioisomer where the two oxygens are in the 3,4 positions.

The synthesis of the asymmetric squaraines, for example compound **1.10** in Figure 1.10, requires the isolation of the semi-squaraine **1.8**. This can either be done by adding a large molar excess of the squaric acid, **1.5**, compared to the (hetero)arene, or through the use of an equimolar ratio of a squaric acid derivatives such as **1.7** in Figure 1.10.[103] The former approach is undesirable as it requires the removal of the excess squaric acid, which can be tedious, and also wastes starting material. The later approach is more widely used, where the condensation product is easily hydrolyzed to get **1.8**, which is in turn condensed with the second (hetero)arene to get the desirable asymmetric squaraine.[102] As anticipated, the added reaction steps result in lower overall reaction yields for the asymmetric squaraines when compared to their symmetric counterparts. Another method that generates the semi-squaraine as part of the reaction scheme has been developed, however it is not universally used. In their report, Law and coworkers,[108] have sensitized a semi-squaraine using a [2+2] cycloaddition reaction between 4-methoxybenzoyl chloride, and 1,1,2,2-tetraethoxyethene in the presence of a base, followed by hydrolysis to get the semi-squaraine which was condensed with different aniline derivatives to achieve asymmetric squaraines.[108]

1.3.3.3.1.2 Optical properties of squaraines

In solution, squaraines exhibit an intense ($\varepsilon > 10^5$ $M^{-1}cm^{-1}$) absorption band in the red region of the solar spectrum with absorption maxima typically between 550 and 700 nm depending on the nature of the donor end groups.[102,108] However this band is narrow with a spectral bandwidth ($\Delta\lambda$) around 0.1 eV at half-height, and around 0.5 eV at the peak's base, Figure 1.11a. This absorption band can be further red shifted toward 800 nm, and even beyond into the near-IR,[109] through either the introduction of stronger donors, such as in the case of the symmetric squaraines **1.11**,[110] and **1.12**,[111] or through enhancing

the charge transfer characteristic, such as in the asymmetric squaraines **1.13** and **1.14** in Figure 1.11c.[91]

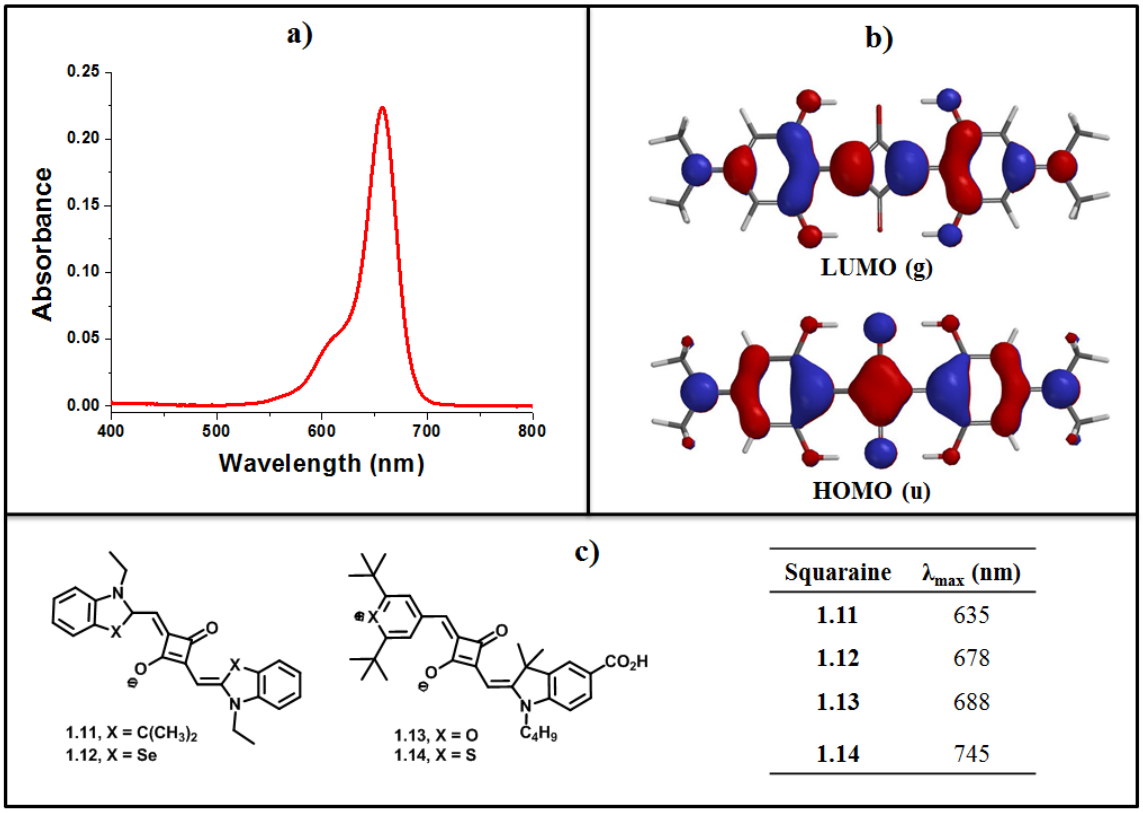

Squaraine	λ_{max} (nm)
1.11	635
1.12	678
1.13	688
1.14	745

Figure 1.11 (a) A typical squaraine absorption profile in dichloromethane. (b) Frontier molecular orbitals (HOMO and LUMO) in a typical symmetrical squaraine, calculated via Density Functional Theory (DFT) using the (Becke, three-parameter, Lee-Yang-Parr hybrid functional-B3LYP) and the 6-31G** basis set (c) Molecular structures of symmetrical squaraines **1.11** and **1.12** and asymmetrical squaraines, **1.13** and **1.14**, as well as their absorption maxima (table).

In the symmetric squaraines, Figure 1.11c, changing X from carbon in the case of indoline **1.11** to selenium in the benzo-selenazole **1.12** bathochromically shifted the absorption maximum by 0.13 eV due to the more donating nature of selenium compared to carbon. The same effect was seen in the asymmetric squaraines were going from the pyrylium asymmetrical dye **1.13** to its thiopyrylium derivative **1.14** bathochromically shifted the absorption maximum by 0.14 eV, due to the increased charge-transfer characteristics of the dye. Although, as seen in Figure 1.11a, squaraines usually do not have significant absorption in the region between the main absorption band and the UV region, high energy absorption can be introduced, via appropriate design, either by

covalently linking groups that have local high-energy absorption to the donor ends of the squaraine,[112] or by substituting one of the oxygens on the central cyclobutene with groups such as diethylbarbiturate.[113]

The transition that gives rise to this strong absorption is an S_0 to S_1 transition where an electron gets excited from the squaraine's highest occupied molecular orbital (HOMO) to the lowest unoccupied molecular orbital (LUMO).[114] The S_1 state has been shown to have some D-A-D charge transfer (CT) character,[85] and the transition from S_0 to S_1 proceeds with a high oscillator strength, typically between 1.3 and 1.7,[99,112] i.e. a large transition dipole from S_0 to S_1. This is due to (1) the delocalization of the electron density over the length of the molecule in each of the HOMO and LUMO wave-functions, (2) the good overlap between the two one-electron wave-functions and (3) the change in phase going from the HOMO to the LUMO, as can be seen in Figure 1.11b.

In the solid state, or on films, the absorption spectrum of squaraines broadens and a second peak usually appears that is blue shifted compared to the main squaraine absorption band, Figure 1.12. This change in the absorption spectrum is usually attributed to the formation of aggregates, commonly H-aggregates (H stands for hypsochromic), and is a consequence of the planarity of squaraines, and their charge transfer properties; intermolecular electrostatic interactions between the electron rich donor ends of one squaraine and the electron deficient C_4O_2 core of another have been observed, and result in an intermolecular distance ca. 3.5 Å, comparable with the π-π interaction distance.[86]

These spectral changes observed in the formation of H-aggregates can be explained by the molecular exciton theory,[115] which discusses these aggregates, and hence the transitions, in terms of coupling of the transition moments of the specific molecules. In H-aggregates, it is established that the aggregating dyes are parallel to each other and are stacked plane-to-plane (face-on), which causes their individual transition dipoles to interact and result in two possible excited states. In one case, the dipoles will point in the same direction, and their interaction would result in non-zero net transition dipole, and hence render the excitation allowed. In the case of the H-aggregate this allowed transition is higher in energy, than the non-allowed transition, due to electrostatic

repulsion between the dipoles pointing in the same direction, Figure 1.12. This will result in a hypsochromically shifted band compared to the monomer absorption band. This is the exact opposite in the case of the J-aggregate which arises when molecules are arranged end-to-end, were the allowed transition is now lower in energy due to electrostatic attractions between the dipoles pointing in the same direction. These transitions as well as the dipoles are sketched in Figure 1.12.[116]

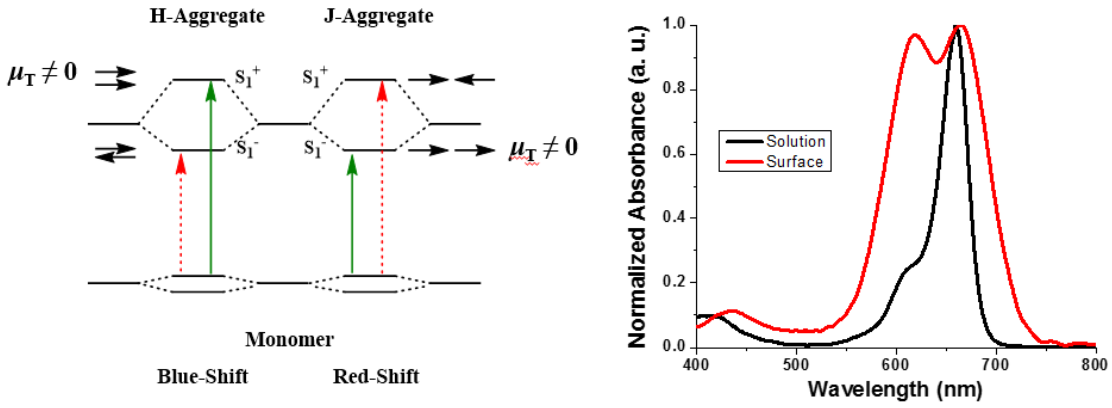

Figure 1.12 (Left) Schematic representation of the relationship between chromophore arrangement and spectral shift based on the molecular exciton theory. The allowed transitions are highlighted in solid green lines, while the forbidden are highlighted in dashed red lines. (Right) Absorption spectra of asymmetric 1.26 in solution and on the surface of TiO_2 clearly showing spectral broadening and the presence of a new feature.

1.3.3.4 Squaraine-based DSSCs

Squaraines as near infra-red sensitizers appeared in 1999 when Zhao *et al*. doped a ruthenium-based DSSC with 1% indoline-based squaraine **1.15**, Figure 1.13, to achieve a 12% increase in the DSSC's PCE to reach 6.6%.[117] Although the squaraine did not perform well on its own (PCE ca. 2.0% compared to ca. 11% in the case of the ruthenium-only device) it demonstrated its potential as near infra-red sensitizer. This potential was further explored by Sayama *et al*.[118] who co-sensitized yellow and red cyanine dyes with a blue indoline-based squaraine, **1.16**, to achieve PCE ca. 3.0%.

In the following years, several reports explored the effect of different squaraine donors, on the photovoltaic properties.[118-120] For the most part these squaraines were symmetric and were tethered to the TiO_2 through alkyl spacers that presumably did not

allow effective electronic coupling from the excited state of the squaraine through the anchoring group. In 2005, Li *et al.*[119] investigated the effect of changing the squaraine – TiO_2 separation on PCEs. They reported a series of *N*,*N*-dialkyl-anilines with carboxylic acid anchoring groups that are separated from the aniline nitrogen by different lengths carbon units, squaraines **1.17**, and **1.18** in Figure 1.13. They suggested that the squaraine **1.17**, which had carboxylic acid closer to the donor, performed better due to the decreasing distance between the sensitizer and the semiconductor which is expected to enhance the electron injection rates. This resulted in a maximum PCE of 3.4% with IPCEs that reached as high as 70% in certain parts of the solar spectrum.

Alex *et al.*[121] explored a wider variety of donors that included, in addition to *N*,*N*-alkyl aniline and indolines, benzo-thiazoles and benzo-selenazoles, and studied their effect on PCEs. More importantly, unlike earlier reports, they explored the effect of having an asymmetric squaraines on PCE, **1.19**. Although, overall, the PCEs were not as high as those previously reported, they did observe that asymmetric squaraines performed better than their symmetric counterparts. This enhanced performance was attributed to the "unidirectional flow of electrons on excitation of the asymmetrical squaraines as opposed to flow of electrons towards the center of the molecule".[121] This observation created interest in asymmetrical squaraines and gave them preference over symmetrical squaraines. Along this process two main issues were recognized; (1) these squaraines aggregated heavily with each other on TiO_2 with detrimental effects on the device performance. In Alex *et al.*'s work, the IPCE of benzo-selenazole, **1.20**, did not exceed 1.0% although its solid state spectra showed a wide absorption. When this benzo-selenazole was replace by indoline, **1.21**, the out-of-plane methyl groups reduced aggregation and increased the IPCE to around 20%.[121] (2) The other issue was electronic; none of these dyes maintain conjugation into the acceptor/anchoring group, and this presumably ultimately limited electron injection efficiency into TiO_2.

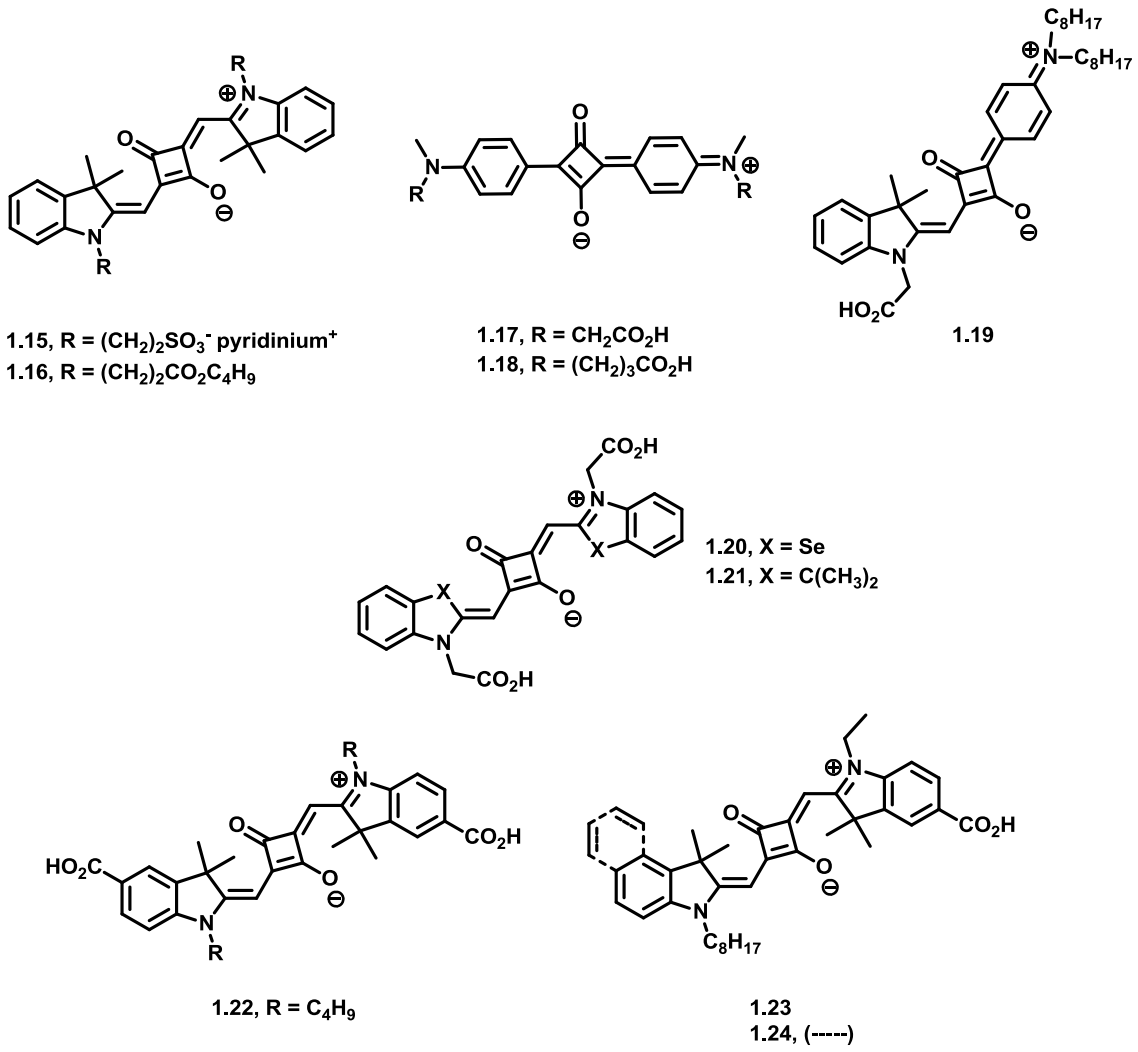

Figure 1.13 Molecular structures of a representative sample of symmetrical and asymmetrical squaraines highlighted in this section.

The importance of extending the conjugation into the acceptor/anchoring group was demonstrated by Chen *et al.*[120] with squaraine **1.22** (Figure 1.13) where the anchoring group is now conjugated to the indoline. This improved the PCE to 4.0% with IPCEs between 30% to 50% over the visible region of the solar spectrum.[120] Later, Yum *et al.*[122] introduced asymmetry into a very similar indoline based squaraine, **1.23**, which caused an increase in the PCE to 4.5% via directing the electron flow towards TiO_2 and hence increasing the electronic coupling. Geiger *et al.* extended the conjugation of **1.23**, and hence bathochromically shifted its main absorption band, in the benzoindoline based squaraine **1.24**. This modification enhanced the near infra-red absorption and increased the molar extinction coefficient which jointly resulted in an enhanced PCE to 5.4%.[123]

In 2011, Paek *et al.* synthesized a dimethylfluoreneaniline/indole based asymmetric squaraine, **1.25**, with a PCE equal to 6.3%.[124] **1.25** showed a broad absorption spectrum characterized by a full-width at half maximum fo ca. 100 nm, much wider than the width of ca. 50 nm that is typically seen in squaraines with an absorption maximum at 669 nm (ε ca. 93000 $M^{-1}cm^{-1}$); however it lacked high energy absorption namely in the 400-570 nm region, which caused a dip in its IPCE (30%) compared to that at low energy (50%). Nevertheless, **1.25** achieved good J_{SC} values of ca. 14 $mAcm^{-2}$, in the presence of a 50:1 CDCA/**1.25** ratio (chenodeoxycholic acid (CDCA, **1.29**), is a bile acid that is almost always added into the sensitizer dipping solution in DSSCs as a co-adsorbent to help de-aggregate the sensitizers)[125,126] in the dipping solution which further demonstrates the importance of reducing aggregation in squaraines.

Later in the same year, Shi *et al.* realized the importance of adding high energy absorption to the squaraine to increase the dye's panchromaticity and thus light harvesting capability.[67] They reported squaraine **1.26** which utilized a thiophene as a bridging unit and as a high energy absorbing group; **1.26** had a low energy (650-700 nm) and high energy (380-450 nm) molar absorptivities on the order of 10^5 $M^{-1}cm^{-1}$ and 10^4 $M^{-1}cm^{-1}$, respectively. This added high-energy absorption increased the IPCE to above 50% in the 400-770 nm region of the solar spectrum and resulted in PCEs equal to 6.7%. However, similar to **1.25**, **1.26** also suffered from aggregation, as evident from the presence of an H-aggregate peak, Figure 1.12, when the dye is adsorbed on TiO_2 even in the presence of 100:1 CDCA/**1.26** ratio.

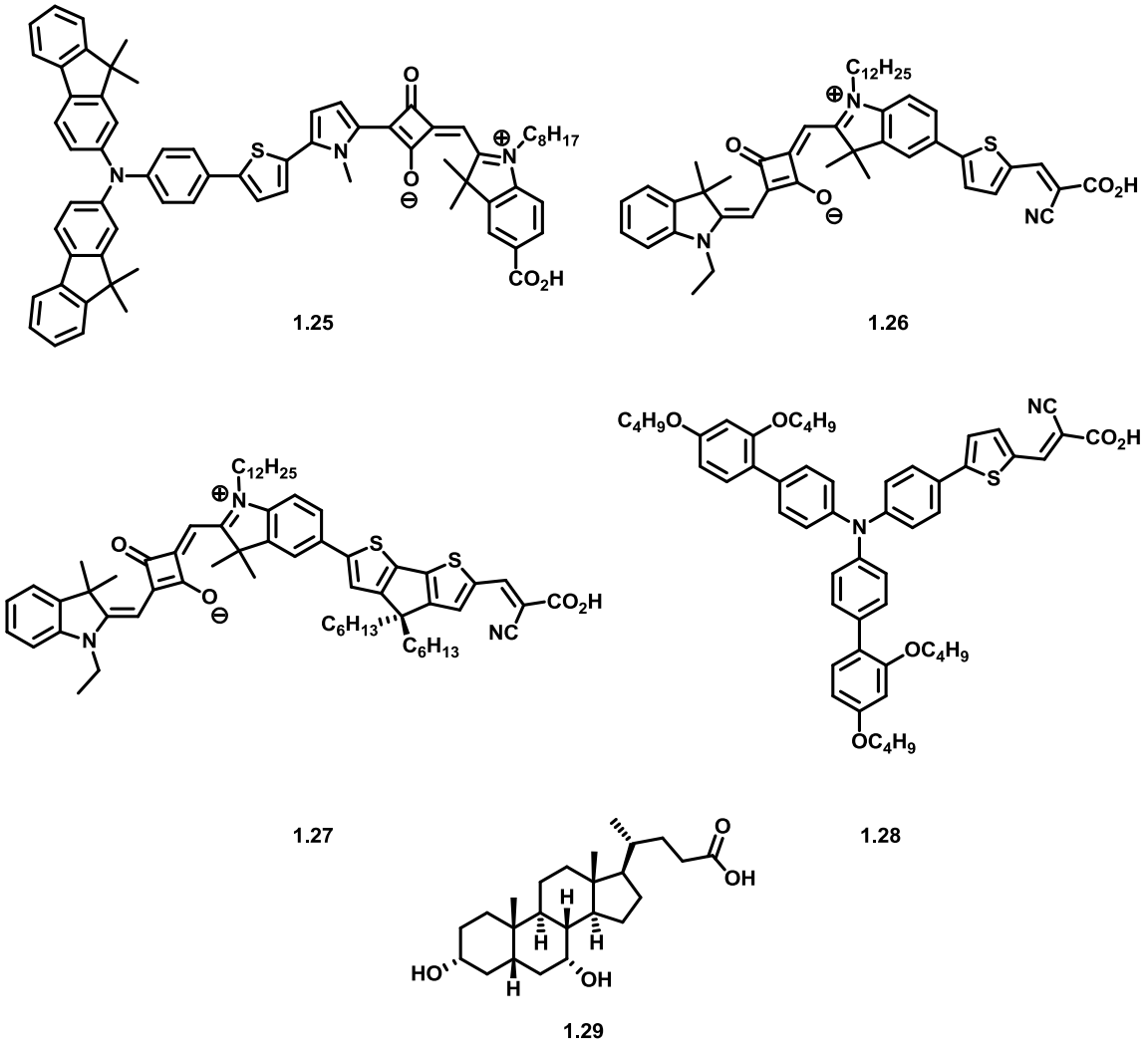

Figure 1.14. Molecular structures of the highest performing unsymmetrical squaraine dyes reported in literature up to the year 2014. Shown also is the molecular structure of CDCA (**1.29**) and the triarylamine based dye, **1.28**.

In 2013, Delcamp *et al.* replaced the thiophene bridging unit with a 4,4-di-*n*-hexyl-cyclopentadithiophene bridge, **1.27**,[112] which also exhibits high energy absorption between 450-550 nm (ε ca. 40000 $M^{-1}cm^{-1}$). More importantly the gem-di-*n*-hexyl substituents extend above and below the plane of the π-conjugated squaraine plane, helping in deaggregating the dyes on TiO_2, and leading to a drop in the intensity of the H-aggregate peak compared to the squaraine main absorption peak, with no obvious drop in the absorbance of the high energy peak (cyclopentadithiophene based). Devices fabricated with **1.27** showed, in the presence of CDCA, an increase both in the IPCE and J_{SC} when compared to **1.26**, with IPCE values higher than 60% throughout the visible

spectrum, and J_{SC} values up to 16.4 $mAcm^{-2}$. This higher J_{SC} value ultimately resulted in a higher PCE of 7.3% in DSSCs based on **1.27**, a value that was further increased to 7.9% upon co-sensitization with another dye **1.28**, a diarylamine based dye with high energy absorption (400-550 nm) that compliments those of **1.27**, Figure 1.13.[127]

1.3.3.5 Aggregation in squaraine-based DSSCs

In almost all squaraine-based DSSCs, CDCA is used to break up aggregation; Yum *et al.* reported a 33% increase in the PCE when CDCA was added as a co-adsorbent with an asymmetrical squaraine.[128] Similarly, in the case of compounds **1.25** and **1.26**, increasing the ratio of CDCA/**1.25** from 20:1 to 50:1 caused a 27% increase in PCE,[124] while increasing the ratio of CDCA/**1.26** from 100:1 to 400:1 increased the PCE by 8%.[112] Pandey *et al.* synthesized a series of six indoline-based symmetrical squaraines that differed from each other by the length of the alkyl chain on their indole nitrogen atoms.[129] In their work increasing the length of the alkyl chain from ethyl (2 carbon atoms) to dodecyl (12 carbon atoms) increased both the V_{OC} and the J_{SC} values by increasing the electron lifetime, through suppressing electron recombination to the electrolyte, and through reducing dye aggregation on the surface, respectively. Although these differences resulted in an increase of the PCE from 1.5% (ethyl) to 2.2% (dodecyl), adding CDCA alone increased the PCE from 2.2% (dodecyl) to 3.5% (dodecyl + CDCA).[129] This effect was also observed with compound **1.27**, where increasing the ratio of CDCA/**1.27** caused a decrease in the absorbance of the H-aggregate peak relative to that of the squaraine absorption band, Figure 1.15a.[112]

The deleterious effects of aggregation on PCE in squaraine-based DSSCs is perhaps counterintuitive; assuming that the aggregates are as strongly absorbing as the monomers, a widened absorption profile resulting from aggregation should cover more of the solar spectrum and hence harvest more light. However, it was found that it is rather the opposite in terms of photo charge generation; in one work, Tatay *et al.* studied the photovoltaic performance of a DSSC based on **1.30**, Figure 1.15, in terms of interfacial electron transfer kinetics.[130] The absorption spectrum of **1.30** showed an absorption maximum at 655 nm and a $\Delta\lambda$ at half height of ca. 50 nm, which upon adsorption on TiO_2

increased to around 150 nm with absorbance > 1 between 550-710 nm, Figure 1.15b. However, when they compared the luminescent properties of **1.30** adsorbed on ZrO_2, (ZrO_2's conduction band energy is higher than the **1.30**'s $E_{(S^+/S^*)}$, thus prevents electron injection from the latter) to that in solution, they found out that only the monomeric squaraine contributed to emission, while the excited aggregates underwent rapid fluorescence quenching. In addition, when they measured the IPCE, Figure 1.15c, of DSSC fabricated with **1.30**, they found out that it looked similar to the absorption spectrum of the monomeric squaraine in solution, which they have shown to be due to electron injection into TiO_2, after excitation, to be restricted only to the monomeric squaraine present on the surface, and not the aggregates.

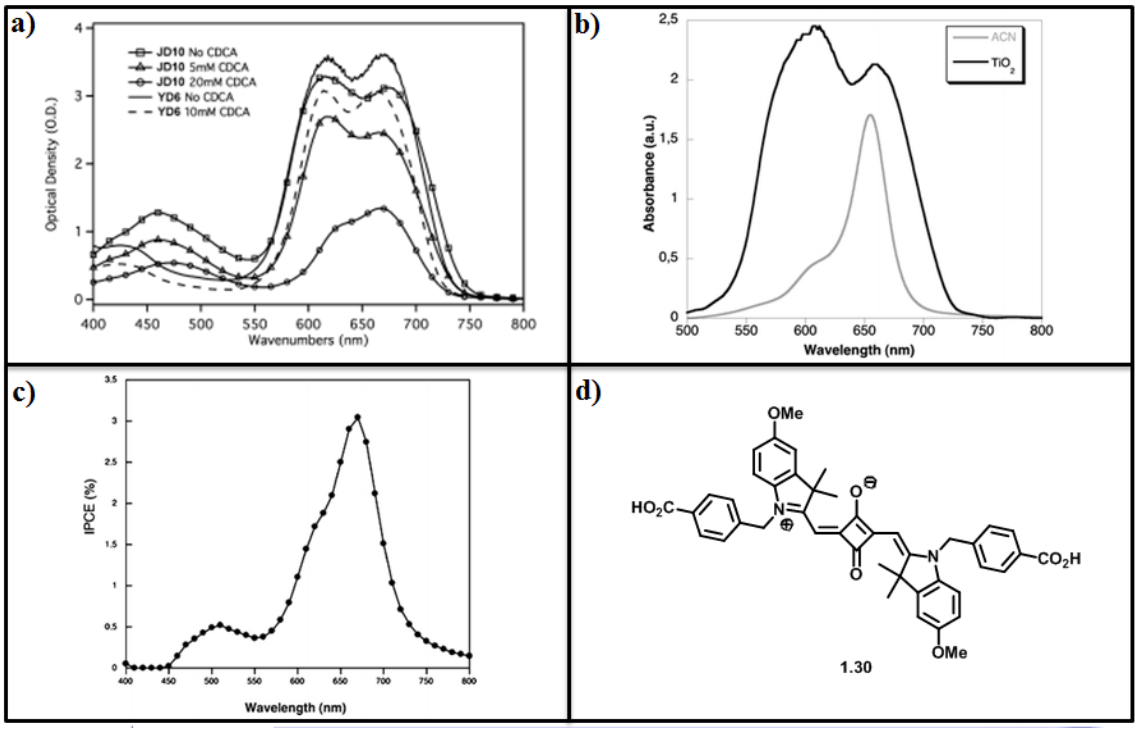

Figure 1.15 (a) Optical density measurements of JD10 (compound **1.27**) and YR6 (compound **1.26**) on TiO_2 as a function of increased CDCA concentration, reproduced from Delcamp *et al.*[112] (b) The absorption spectrum of a 1.30 in solution (Acetonitrile) and TiO_2. (c) The IPCE of a DSSC fabricated from 1.30. Reproduced from Tatay *et al.*[130]

1.3.3.6 Open-circuit voltage in squaraine DSSCs

Throughout the last decade the performance of squaraine based DSSCs increased from 3.9% to 7.3%,

Table 1.2, an increase that is mainly attributed to the 30% increase in J_{SC} values due to broader absorption spectra, and suppression of aggregation as discussed in the previous section. This increase in photocurrent was not reciprocated by an increase in the V_{OC} and FF, which remained on average unchanged, with the former around 0.63 V and the latter consistently around 70%. These low V_{OC} values in squaraines contribute to a minimum of 1.07 V loss-in-potential, Table 1.2. This loss-in-potential was the primary reason that many workers in the field moved away from ruthenium-based dye DSSCs.

In order to increase the V_{OC} values, changing the redox shuttle from iodide/triiodide to others that have higher redox potentials and require less of a driving force for dye regeneration should be thought after. This is seen, to some extent, in solid state DSSCs reported for compounds **1.26** and **1.27** in Table 1.2. In a solid-state DSSC, the liquid electrolyte such as iodide/triiodide couple is replaces with a hole-transport material, such as spiro-MeOTAD. The first oxidation potential of which in solution is +0.72 V vs NHE,[131] 0.37 V higher than the potential of the iodide/triiodide couple, and solid state DSSC fabricated with **1.26** and **1.27** (**1.26**ss, and **1.27**ss in Table 1.2) showed increased V_{OC} values by ca. 70 mV.[67,132] Although spiro-MeOTAD might not be the optimal redox shuttle in this case, it hints into the validity of this approach to increase the V_{OC} values. Cobalt-based electrolytes, Figure 1.4, can be very promising candidates for increasing V_{OC} values in squaraine-based DSSCs; these electrolytes were previously found to be very successful in other classes of dyes that suffered from low V_{OC} values. For example, V_{OC} of the porphyrin based dye YD2-*o*-C8 increased by 0.20 V with cobalt-based electrolyte and the loss in voltage decreased to 0.86 V.[66]

Table 1.2 The photovoltaic performance, electrochemical potentials, optical gaps and losses in potential of the squaraine dyes discussed in Section 1.3.3.4 both in a liquid DSSC, and a solid state DSSC (1.26ss and 1.27ss).

Dye	J_{SC} / mAcm^{-2}	V_{OC} / V	FF / %	PCE / %	$E_{(S^+/S)}$[a] [V]	$E_{(S^+/S^*)}$[a] [V]	$E_{0\text{-}0}^{opt}$ [eV]	V_{loss}[b] [V]
1.22	11.6	0.49	54	3.9	+ 0.96	- 0.96	1.92	1.43
1.23	10.5	0.60	71	4.5	+ 0.98	- 0.94	1.92	1.32
1.24	11.3	0.67	72	5.4	+ 0.81	- 1.00	1.81	1.14
1.25	13.9	0.61	74	6.3	+ 0.92	- 0.76	1.68	1.07
1.26	14.8	0.64	71	6.7	+ 0.80	- 0.94	1.74	1.10
1.27	16.4	0.64	70	7.3	+ 0.73	- 1.01	1.74	1.10
1.26ss	6.61	0.71	58	2.7	+ 0.80	- 0.94	1.74	1.03
1.27ss	7.30	0.71	61	3.2	+ 0.73	- 1.01	1.74	1.03
YD2-*o*-C8[c]	15.0	0.77	71	7.6	+ 0.82	- 1.29	1.86	1.09
YD2-*o*-C8[d]	17.3	0.97	66	11.9	+ 0.82	- 1.29	1.86	0.86

J_{SC}, V_{OC} and PCE values are all reported based on the optimized device in the respective reference. [a)]Electrochemical values are reported vs. NHE (Normal Hydrogen Electrode). [b)]The loss in potential is calculated according to the following equation $V_{loss} = E_{0\text{-}0}^{opt} - V_{OC}$;[c)]Cell prepared using iodide/triiodide redox shuttle.[d)]Cell prepared using the $[Co(bipyridyl)_3]^{3+/2+}$ redox shuttle.

In the next section, an overview of organic photovoltaics, their operational principle, and material design will be discussed in some detail as they will be the highlight of one research chapter in this thesis. Particular attention will be given to the design of donor semiconducting material in OPV, which is the focus of chapter 5 of this thesis.

1.4 ORGANIC PHOTOVOLTAICS (OPVs)

1.4.1 Organic photovoltaic operational principles

A key factor that sets OPVs apart from conventional p-n junction photovoltaics (PV) is the presence of the heterojunction between its two organic semiconductors, which from this point on will be referred to as an electron-donating material (D), and an electron-accepting material (A). Both donors and acceptors can be either an organic polymer or a small molecule, with donors having low ionization energies (IE) (which when considered in the context of Koopmanns' theorem, is equal to the energy of high-lying HOMOs), and acceptors having high electron affinities (EA) (low-lying LUMOs).[133]

Figure 1.16, overviews in a simplistic manner the current understanding of photon-to-electron power conversion process in an OPV. Unlike p-n junctions where photon absorption results in free charges that can be easily transported to the corresponding electrodes, absorption of a photon in an OPV by either the donor, or the acceptor (not shown in Figure 1.16 for simplicity), results in the formation of an exciton that is confined to a small volume (few nm^3) and has a binding energy (0.1 to 1 eV),[134] which is substantially larger than thermal energy at room temperature kT(300 K) = 26 meV.[135] The exciton binding energy for a material M can be defined according to Equations (6) and (7)

$$M + M^* \rightarrow M^+ + M^- \qquad \text{Eq. (6)}$$

$$E_{EBE} = IE_M - EA_M - E_{0,0}{}^{opt}{}_M \qquad \text{Eq. (7)}$$

where E_{EBE} is the exciton binding energy, IE_M is the material's ionization energy, EA_M is the material's electron affinity, and $E_{0\text{-}0}{}^{opt}{}_{,M}$ is the material's optical gap.

The exciton should diffuse to a donor/acceptor heterojunction for it to dissociate. After diffusing to the heterojunction, the exciton (excited singlet state - S_1^D in Figure 1.16B) transfers energy, in an ultrafast process, into an excited charge transfer (CT_n) state based on an oxidized donor (D^+) and a reduced acceptor (A^-), process 2 in Figure 1.16A. Although this transfer process overcomes the intramolecular Coulombic attraction holding the singlet exciton together, the charges in this excited CT_n state are still electrostatically interacting across the heterojunction.[136] This excited CT_n state while undergoing thermal relaxation into lower CT_1 states, or possible electronic relaxation to the ground state, can evolve into a charge separated (CS) state with the electron now localized in the acceptor and the hole in the donor.[134,136] The charges are then transported, process 3, to the respective electrode via the donor or the acceptor and thus generating current in the external circuit.

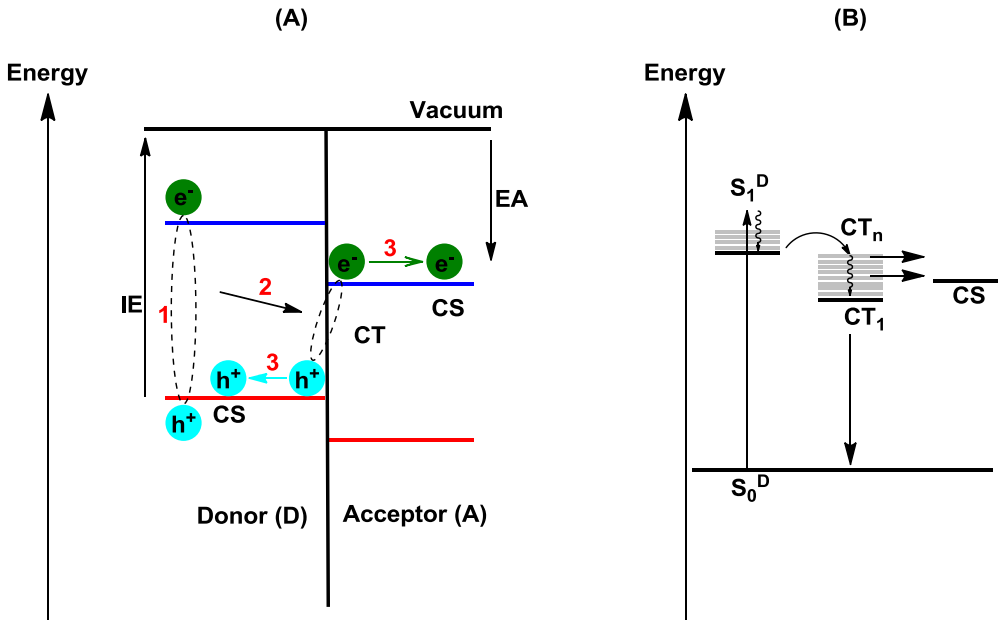

Figure 1.16 (A) An energy level diagram of a typical OPV under illumination. The red lines represent filled charged transport states, and the blue lines represent empty charge transport states. IE and EA denote the ionization energy of the donor molecule, and the electron affinity of the acceptor molecule, respectively. (B) Electronic state diagram. S_0^D donates the singlet ground state of the donor, S_1^D donates the singlet excited state reached after optical excitation. CT_1 is the lowest charge transfer state, and CT_n represent charge transfer states of higher energy.

In 1986, C. W. Tang reported an organic photovoltaic cell that had two organic layers; a copper phthalocyanine (CuPc) hole-transport material and a perylene diimide

(PV) electron-transport material, sandwiched between an indium tin oxide (ITO) coated glass, and a silver electrode. Tang's solar cell demonstrated a PCE ca. 1%, which was unprecedented at the time[137] where efficiencies well below 0.1% were reported earlier.[138] This two-layer configuration (BL in Figure 1.17), was crucial in determining the solar cell's photovoltaic properties, and is different from earlier organic photovoltaics which consisted of a single organic material sandwiched between a low work-function metal and a high work-function metal or a conducting oxide, SM in Figure 1.17.[139] *Note:* Work function is defined as the energy necessary to remove an electron originally at the Fermi level and place it at rest at a point in free space just outside the surface.

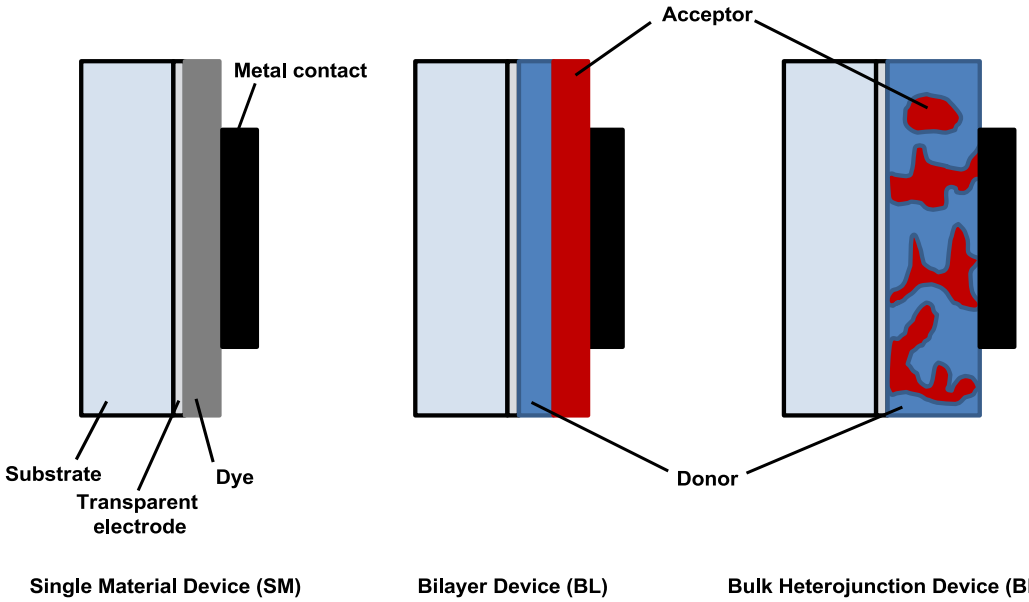

Figure 1.17 Cross section of a single material device (LM), a bilayer device (BL) and a bulk heterojunction device (BH).

Tang's BL device configuration PCE was limited its ability to dissociate the excitons before they decay to the ground state, i.e. the generated excitons need to reach an interface during their lifetime.[133] The exciton diffusion length (L), which is inversely proportional to both the exciton diffusion coefficient and the exciton lifetime, is a crucial parameter to keep in mind when designing organic photovoltaics, as it dictates the maximum thickness of the cell and the fraction of light it can absorb. Typical exciton diffusion length in organic molecules is between 5 and 20 nm,[140] which is around a tenth of the thickness required by the active layer to absorb a high proportion of the incident

light, where it is preferred that the film's absorbance is between 2-3 which corresponds to light absorption efficiency >90%.[133] These small diffusion lengths meant that only excitons that are generated within 10 nm of the interface have a good probability of dissociating. This triggered the design of devices that incorporate mixed organic layers in an attempt to increase the probability of an exciton finding an interface. In 1991, Hiramoto *et al.*[141] reported a three-layer organic photovoltaic that has a 40 nm mixed perylene-phthalocyanine layer in between a 40 nm perylene and a 40 nm phthalocyanine layers. This mixed layer acted as a photo-generation layer where the excitons are split and then transported via the "pure" layers to the electrodes. This three layer OPV paved the way for BH organic photovoltaics, Figure 1.14, which are still one of the more efficient device configurations.

In 1992, Sariciftci *et al.*[142] demonstrated that photoexcitation of a mixture of a poly-phenylene vinylene polymer and fullerene resulted in a pico-second electron transfer from the polymer to the fullerene – a rate that is more than two order of magnitudes faster than competing radiative and non-radiative recombination processes, thus resulting in charge transfer quantum efficiency close to unity, an interesting property that can be exploited in OPVs if a way to increase the probability of the exciton finding an interface is achieved. In 1995, Yu *et al.*[12] reported an organic photovoltaic that utilized a blend of the aforementioned photoconductive polymer and fullerene (or its derivatives) that achieved a PCE ca. 3%, two orders-of-magnitude higher than SM devices made from the polymer alone. In the report, a 1:4 mixture of the polymer/fullerene dissolved in 0.5 weight % xylene solution was spin casted on ITO coated substrate, and capped with a metal contact. This blend created an interpenetrating network of polymer and fullerene materials which resulted in a large interfacial area in the bulk of the blend hence the name "bulk-heterojunction". In this conformation, a generated exciton will be within few nanometers from an interface which enhances the efficiency of charge separation.

1.4.2 Power conversion efficiency in OPVs

As discussed in Section 1.3.2 and Equation 2 the PCE is the product of the short-circuit current (J_{SC}), the open-circuit voltage (V_{OC}) and the FF over the incident solar

power. As with the case of DSSC, this thesis will focus on increasing the PCE of OPVs by increasing their J_{SC} through enhancing the spectral properties of the organic donor material without dramatically affecting the other two parameters.

The maximum J_{SC} in an OPV, as in DSSC, is a function of the photon flux at a particular wavelength $\phi_p(\lambda)$, and the external quantum efficiency $\eta_{EQE}(\lambda)$, referred to as IPCE in the DSSC field, which is defined by how efficiently an incident photon give rise to an electron flowing in the external circuit. The $\eta_{EQE}(\lambda)$ is the product of efficiencies associated with absorption, diffusion and dissociation of the excitons into charges, and then transportation and collection of the charges at the electrodes, Equation 8:[133]

$$J_{SC} = \int e\, \eta_{EQE}(\lambda)\, \phi_p(\lambda)\, d\lambda \qquad \text{Eq. (8)}$$

The fill factor and V_{OC} are not the highlight of this thesis; however for an overview of factors affecting the reader is referred to the works of Kippelen *et al.*[133] Janssen *et al.*[134] and Burke *et al.*[143] This being said, the upper limit of V_{OC} can be estimated from the difference between the IE of the donor and the EA of the acceptor according to Equation 9:

$$V_{OC} = \frac{1}{q}\left(IE_D - EA_A\right) \qquad \text{Eq. (9)}$$

Where, q is the elementary charge and in practice V_{OC} falls short of this limit due to voltage losses that accompany the different processes following photon absorption until charge collection. The shortfall is generally between 0.3 and 0.7 V depending on the system.[133,134,143,144]

Relevant to the operation of an OPV are the frontier orbitals (HOMO and LUMO) of the donor and the acceptor semiconductor materials, as they generally determine their optical and electronic properties. The donor material is often assumed to be the main light absorber because of its superior spectral properties compared to fullerene derivatives (most commonly used class of acceptors as will be discussed in 1.4.3.1) which absorb

light weakly above 400 nm.[145] To compensate for the fullerene's spectral shortcomings, the donor material should have good overlap with the solar spectrum, where an optical gap around 1.32 eV (940 nm) would be ideal, for the same reasons stated in Section 1.3.2. The driving force of exciton dissociation ($-\Delta G_{diss}$) is given by Equation (10);

$$-\Delta G_{diss} = IE_D - EA_A - E_{0-0}^{opt}(D) \quad \text{Eq. (10)}$$

where IE_D is the donor's ionization energy, EA_A is the acceptor's electron affinity, and $E_{0-0}^{opt}(D)$ is the donor's optical gap, and a $-\Delta G_{diss}$ value that is greater than zero should theoretically provide for sufficient driving force for exciton dissociation. In literature, however, the driving force of exciton dissociation has been also expressed in terms of offset of the donor and acceptor's EAs.

The EAs of the universally utilized fullerene acceptors, $PC_{61}BM$ **1.32** in Figure 1.18, and $PC_{71}BM$ are ca. + 3.9 eV,[145,146] and since an EA offset of around 0.1-0.3 eV has been shown to be needed between the donor and the acceptor,[147] (note: some reports claim that a driving force of at least 0.3 eV is needed)[133,144] for efficient exciton dissociation, the EA of the donor should be no higher than +3.8 eV. Since an optical gap of 1.32 eV is targeted, the IE of the donor should be around +5.1 eV, and theoretically, such a system will be able to achieve PCE up to 20%, if EQE values close to unity across the visible and near IR regions of the solar spectrum are achieved, and if voltage losses of 0.3 V, and FF values of 0.7 are assumed.

1.4.3 Organic materials in OPV

1.4.3.1 Acceptors

Typical electron acceptors are fullerenes, and rylene diimides (namely naphthalene diimide, and perylene diimide), however, through structural modification, other organic semiconductors can be engineered to possess electron-transport characteristics by introducing electron withdrawing groups, such as cyano, carbonyl, imide, into their conjugated backbone, which stabilizes the LUMO through mixing of the orbitals. One example is 6,13-bis(triisopropylsilylethynyl) (TIPS)-pentacene which is hole-transport material that was turned into an electron-transport material via the

structural modification, and used as an electron acceptor in OPV employing P3HT donor.[148] Similar effects can be achieved through replacing alkyl groups in π-backbones with perfluoroalkyl groups,[149] or via the replacement of carbon atom with more electronegative atoms such as oxygen or nitrogen, as for example changing thiophene to thiazole or thiadiazole.[150]

Among the various acceptors, fullerenes, C_{60}, **1.31** in Figure 1.18, and its derivatives stand unrivaled in OPVs. Since Heeger *et al.* observed photo-induced electron transfer into them from an organic polymer in 1992,[142] and later on fabricated the first BH organic photovoltaic utilizing them in 1995,[12] fullerene derivatives, Figure 1.18, dominated the field as electron acceptors.[145] To date, the best performing OPV devices fabricated with either a polymer-[151] or a small molecule-[152] donor material achieved their high PCEs (10.5% and 9.80% respectively) with a fullerene derivatives, $PC_{71}BM$, which is a derivative of **1.31** that has better light absorption in the visible region.[153] Their success is owed to many factors that include large electron affinity and strong tendency to accept electrons, [154] adequate electron mobility (on the order of 10^{-3} $cm^2V^{-1}s^{-1}$; mobility is defined as the drift velocity per unit electric field,[155,156] in three dimensions due to the delocalization of the LUMO over the whole surface of the molecules, ability to form favorable morphological networks with donor semiconductors forming both pure and mixed domains,[151] and reversible electrochemical reduction.[154]

Despite their wide success, fullerene derivatives have drawbacks, which give the researchers in the field an incentive to pursue other type of acceptors. They have limited absorption in the visible and near infrared, limited optical gap tunability,[157] and high synthetic cost. In addition, **1.32** and $PC_{71}BM$ were not ideal partners for large band gap polymers where OPVs made from poly-(3-hexylthiophene) (P3HT)/ **1.32** blends (the most studied system in OPV) suffered from low V_{OC} due to the large mismatch between the P3HT and **1.32** LUMO (ca. 1.0 eV) which limited their PCE to a maximum of 5%.[158] Efforts to raise the LUMO of fullerene materials yielded better PCEs with P3HT donors where using an indane-C_{60}-bisadduct ($IC_{60}BA$), Figure 1.14, whose LUMO is 0.17 eV > **1.32**, yielded higher V_{OC}'s and PCE ca. 6.5%.[159]

In recent years, a wide variety of electron-transporting materials have been reported as electron acceptor in OPVs with PCE's reaching as high as 8.4% as of last year.[160-165] The majority of these high performing OPVs rely on a rylene diimide electron acceptor, mainly perylene diimide, **1.34** and **1.35** in Figure 1.18, which are promising small molecule electron acceptors, due to their high electron affinity (+3.9 eV for bay-unmodified perylene diimide), and high electron mobility, which can outperform those of fullerene.[166,167] Other electron acceptors for OPVs have been studied and a more comprehensive list of acceptor materials can be found in literature such as amide/imide functionalized polymer non-fullerene acceptors, benzothiadiazole-based copolymers, diketopyrrolopyrrole based acceptors, electron deficient fused aromatics, and oligothiophene thiophene dioxide acceptors.[157,167,168]

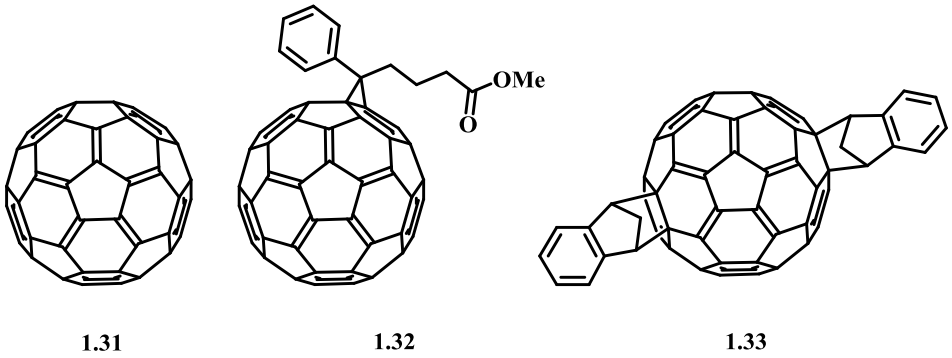

1.31 **1.32** **1.33**

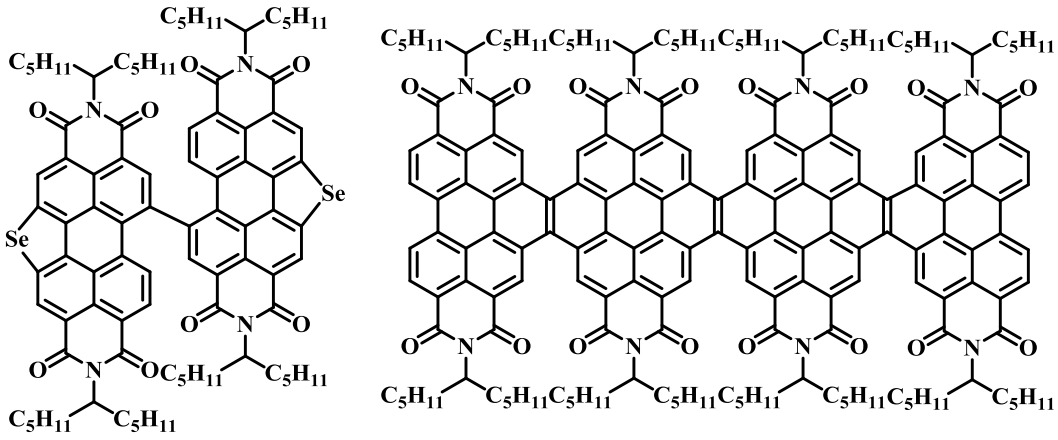

1.34 **1.35**

Figure 1.18 Molecular structure of C_{60} (**1.31**) and its derivatives $PC_{61}BM$ (**1.32**) and $IC_{61}BA$ (**1.33**), non-fullerene acceptors **1.34** (PCE 8.4%),[161] and **1.35** (PCE 8.3%).[162]

1.4.3.2 Donors

1.4.3.2.1 Polymers

The first extensively studied class of donor polymers in OPV was based on poly(phenylenevinylenes) (PPV) derivatives.[12,169-172] Although early devices achieved PCEs below 1% under AM1.5 illumination, these PCEs increased to around 2.5%,[171] and then 3.3% through the use of proper casting solvents (morphology control) and improved electrical contacts, respectively.[172] Some of these PPV polymers were characterized by high V_{OC} values up to 0.82 V as a result of HOMO energy levels around +5.4 eV, however the large band-gap values of ca. 2.1 eV of these PPV materials limited their J_{SC} to a maximum of 6 $mAcm^{-2}$.

Attempts to increase the J_{SC} through the introduction of lower band-gap polymers followed, and relative success was achieved with poly(3-hexylthiophene) (P3HT) donor polymers.[173] P3HT has smaller band-gap (ca. 1.85 eV) than PVV, and hence has the ability to absorb lower energy light previously inaccessible. In addition, it demonstrates good hole mobility, necessary for charge transport to the electrode.[174] Brabec *et al.* in 2002 reported an OPV based on a P3HT:fullerene blend that gave rise to J_{SC} ca. 9 $mAcm^{-2}$ which is unprecedented with PPV:fullerene blends.[175] This resulted in extensive research in OPVs based on this system, especially on understanding and optimizing the processing of the active layer and annealing conditions in an attempt to control the morphology of the bulk heterojunction. These efforts successfully increased the J_{SC} and fill factor of OPVs based on this blend and consequentially the PCE to a maximum of 11.3 $mAcm^{-2}$, 69%, and 5.2% respectively.[158,176] P3HT had inherent shortcomings such as a high lying HOMO (ca. +4.8 eV) which limited the V_{OC} in P3HT devices to around 0.6V with PCBM as an acceptor, which even with 100% EQE over the P3HT absorption window will limit the PCE to ca. 7.8% assuming 70% FF.[173] Other factors affecting P3HT/PCBM blends such as P3HT molecular weight received considerable attention as they affected the morphology of the blend and ultimately the device performance; too low molecular weight tend to form more crystalline morphology while higher molecular weight P3HT tends to stay amorphous.[173,177]

As a logical step forward, research in electron-donating polymers is currently focused on developing low-band-gap polymers, that are capable of harvesting more light, the higher IEs of which has the potential of achieving higher V_{OC} values with PCBM. This new class of polymers is referred to as third generation semiconducting polymers and is composed of alternating copolymers with push-pull motifs.[178-180] In the last five years, high V_{OC} values of over 1.0 V (**1.36**, PCE = 4.5%),[181] J_{SC} values over 20% (**1.38**, PCE = 9.4%),[182] and FF around 75%[183] (**1.37**, PCE = 9.7%) have been achieved separately in BHJ solar cells employing different "push-pull" polymers. These values are very promising and suggest that through careful design, a "push-pull" polymer can combine all of these attributes and push PCEs to ever higher values. As notable examples, Liu *et al.*[151] and Zhao *et al.*[200] have recently reported "push-pull" donor polymers with PCEs exceeding 10% and 11% respectively, where a maximum PCE value of 11.7% was achieved.

In addition to their high PCEs, these materials are compatible with an array of fullerene-based acceptors (unlike **1.39** which is another high performing material that performs well exclusively with $PC_{71}BM$[184]) which frees them from the constraints imposed by the acceptor. Also, their high hole-mobility (order of 10^{-2} $cm^2V^{-1}s^{-1}$) resultant from their high crystallinity and pure polymer domains enables them to maintain these high PCEs in thick films, which is important for good light absorption and industrial production. Figure 1.19, shows the structure of the "push-pull" donor polymers discussed in this section, and for a more general understanding of this class of polymers and design rules reader is referred to the following review articles;[20,178-180]

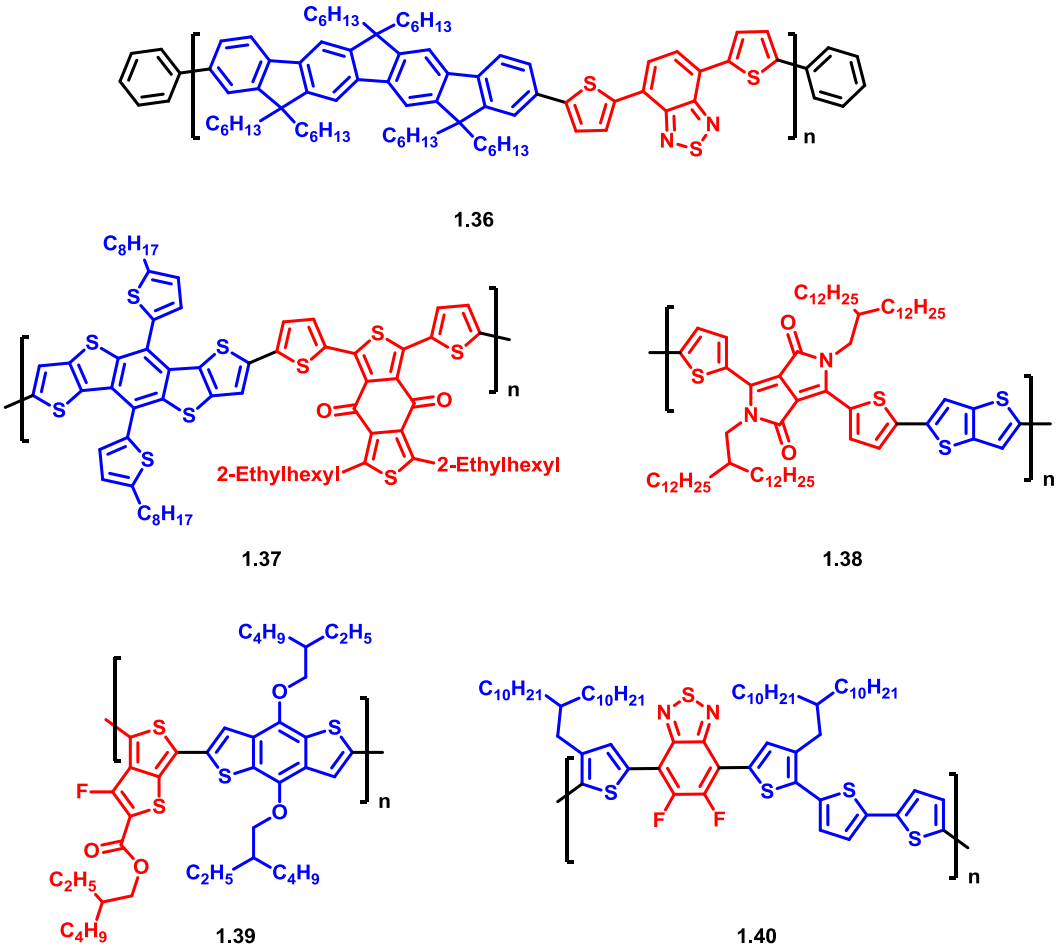

Figure 1.19 Molecular structure of "push-pull" donor polymers for OPVs; donor motifs are highlighted in blue, while acceptors motifs in red

1.4.3.2.2 Small molecules

Alongside polymers, small molecules have been increasingly studied as donors in OPVs. Part of the interest in small molecules arises from their well-defined molecular structures, defined molecular weights, and reproducibility where high purity small molecules can be prepared without batch to batch variations via well-controlled chemical transformations. The same optical and electronic requirements that are expected of polymers are expected of small molecules; (1) small optical gap to allow for the absorption of red and near infra-red photons, (2) wide spectral bandwidth for good overlap with the solar spectrum, (3) good hole transport properties, (4) formation of favorable morphologies with electron acceptors, (5) excited state energies (IE – $E_{0\text{-}0}^{opt}$) that are sufficiently above that of the acceptor, in order to ensure efficient exciton

dissociation and (6) IE sufficiently larger than the EA of the acceptor to obtain adequate voltages.

The first report of an organic solar cell based on small molecule was dated back to 1975 by Tang and Albert,[138] where a chlorophyll-a dye was sandwiched between two electrodes to achieve PCEs around 10^{-3}%. Due to their enhanced optical properties, namely large extinction coefficients in the red region of the solar spectrum, metal phthalocyanine and merocyanine dyes, increased the PCEs of OPVs by few orders-of-magnitude to around 1%, where it is noteworthy to mention that in the case of merocyanine donors, V_{OC} values of ca. 1.2 V where achieved.[139,185,186] When bilayer donor-acceptor devices were introduced, copper phthalocyanines, again, were the donor material of choice and cells based on it resulted in PCEs of ca. 1% and 2.5% in a single junction and multiple junction setting, respectively.[137,187] After the introduction of bulk heterojunction devices, a 1:1 copper phthalocyanines:fullerene blend resulted in OPVs with PCE around 3.5% courtesy of high J_{SC} values of ca. 15 $mAcm^{-2}$.[188] A PCE that was further improved to around 5% in a device that had a three layer geometry where a mixed phthalocyanine:fullerene layer was sandwiched between a pure donor and acceptor layers.[189] This geometry allowed for efficient charge transport in the pristine layers after the exciton dissociates in the mixed layer. In addition to phthalocyanines other organic dyes were also found to be good electron donors in OPVs, squaraines based donors achieved PCEs around 5.5% with $PC_{71}BM$ in a bulk heterojunction device and 5.7% with fullerene in a thermally annealed nanocrystalline heterojunction.[190,191]

Other than organic dyes, fused acenes such as pentacene, and tetracene have attracted considerable interest as donors in organic photovoltaics due to their high hole-mobility over 1 $cm^2V^{-1}s^{-1}$ (beneficial in transporting the hole to the electrode), wide spectral bandwidth (ca. 200 nm) and thermal stability.[192] Kippelen *et al.* first fabricated an efficient OPV device using pentacene as a small molecule donor and fullerene as the acceptor material. Under 1 sun illumination the device demonstrated power conversion efficiency of 2.7%, even with low V_{OC} (0.36 V) and fill factor, due to an impressive J_{SC} values of 15 $mAcm^{-2}$.[193] Substitutions on the acene backbone allow the tuning of the frontier energy levels and hence increase the V_{OC}, where values up to 1.06 V where

reported.[194] The high crystallinity of acenes, although allowing high charge transport, causes phase separation when blended with fullerene based acceptors which decreases device performances. Tuning the crystallinity of this class of material by engineering the side groups is necessary to achieve better device performances.

Similar to polythiophenes, oligothiophenes are heavily researched in the field of organic photovoltaics due to their high charge mobility and ease of modification, especially frontier orbital tuning and physical properties such as solubility and packing. Similar to acenes, unsubstituted oligothiophenes are easy to crystallize and hence tend to phase separate when blended with fullerene acceptors which limited their performance. Only after a 1:5 blend of sexithiophene (6T)/C_{60} was used a PCE of 2.4% was achived.[195] Also similar to P3HT, oligothiophene based materials exhibit large optical gap which limited their light harvesting abilities. As with P3HT, an approach to solve this problem was through the introduction of electron withdrawing group in the backbone of the oligothiophene to form a donor-acceptor "push-pull" small molecule. This strategy extends the absorption spectrum of the "push-pull" small molecule towards longer wavelength via an intramolecular charge transfer process.

Adding dicyanovinyl groups (has strong electron-withdrawing ability) onto the extremities of a **1.41** formed an acceptor-donor-acceptor small molecule **1.42** with a smaller optical gap ($E^{opt}_{0\text{-}0}$ = 1.56 eV, λ_{onset} = 794 nm) when compared to 6T. Bulk heterojunction devices fabricated with a **1.42**/C_{60} blend gave PCEs as high as 5.2%.[196] The above two oligothiophenes were vacuum deposited; adding alkyl chain substituents on the backbone of the oligothiophene increased their solubility and allowed for solution processed organic photovoltaics to be fabricated. **1.43**, which is a hexylthiophene core with rhodanine end groups (acceptor) and six octyl solubilizing chains had high extinction coefficients approaching 10^5 $M^{-1}cm^{-1}$, an optical gap around 1.69 eV, and high crystallinity with hole-transport mobility on the order of 10^{-4} $cm^2V^{-1}s^{-1}$. These characteristics yielded a PCE of around 6.1% with high J_{SC} of 14 $mAcm^{-2}$ and V_{OC} of 0.92 V.[197] Replacing the central thiophene with a more electron-rich planar structure such as dithienosilole connected to two thiadiazolopyridine acceptors, **1.44** resulted in a PCE of 6.7% with $PC_{71}BM$.[198] This "push-pull" donor showed strong absorption especially in

the near IR region of the solar spectrum, and had a remarkably high hole-mobility equal to 0.1 $cm^2V^{-1}s^{-1}$.

More recently efficiencies approaching 10% have been achieved with push-pull small molecules donors.[152,199] One of these champion donors, **1.45**, has a structure which is very similar to **1.43**, with one fewer thiophene and cyano-rhodanine electron accepting end groups instead of rhodanine.[152] This material shows high crystallinity in films evident by the formation of a *J*-aggregate peak in its absorption profile, shows hole-mobility values ca. 7×10^{-4} $cm^2V^{-1}s^{-1}$, and has a small optical gap of 1.60 eV (λ_{onset} = 777 nm). Cells fabricated from a **1.45**:$PC_{71}BM$ blend achieved average PCEs of 9.80% with a highest reported value of 10.1%, courtesy of both high J_{SC} ~ 16 $mAcm^{-2}$ (EQE above 60% across the visible part of the solar spectrum), and V_{OC} = 0.92 V and good fill factor.

The structure of some of the discussed small molecule push-pull donors is present in Figure 1.20. Although, considerable progress has been achieved with donor design in the past decade, plenty of room for progress is still available, especially on the light-harvesting front. Where a material whose optical gap is 1.60 eV should theoretically be able to achieve J_{SC} ca. 26 $mAcm^{-2}$, much higher than what **1.45** is achieving. In addition, as discussed earlier in this chapter, the ideal donor material in OPV should have an optical gap around 1.32 eV to ensure that an adequate portion of the solar flux is being harvested.

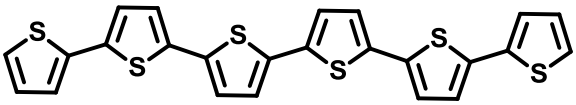

1.41

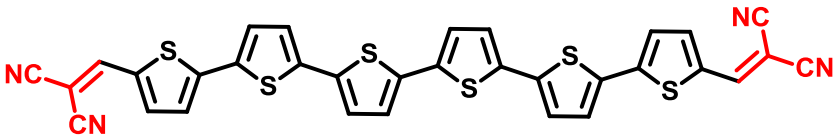

1.42

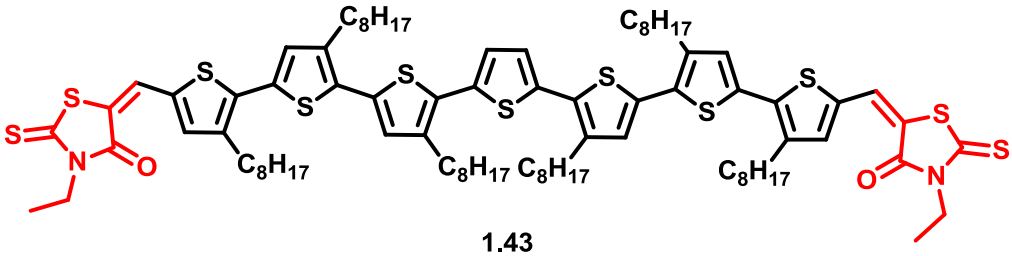

1.43

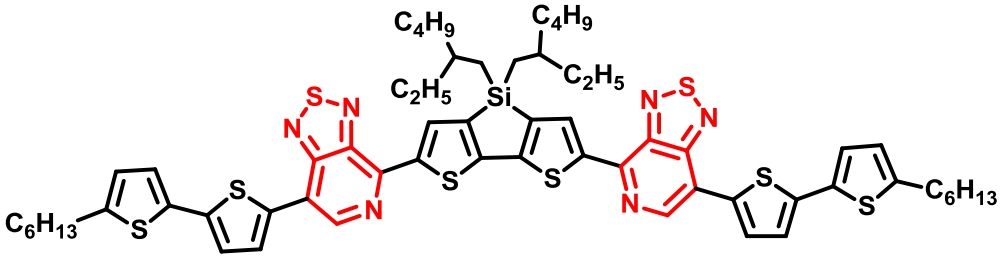

1.44

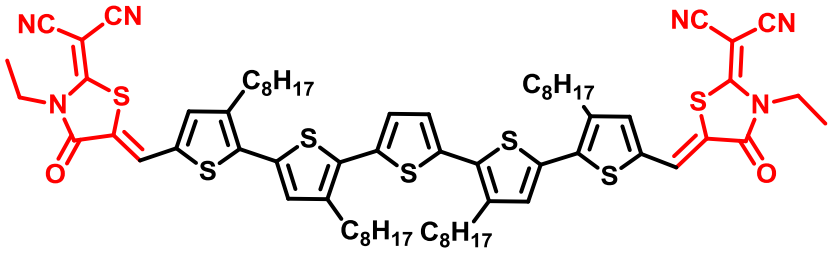

1.45

Figure 1.20 Molecular structure of "push-pull" donor small molecules for OPVs; electron acceptors motifs are highlighted in red.

1.5 ORGANIZATION OF THESIS AND GENERAL OVERVIEW

This general introduction to dye sensitized solar cells and organic photovoltaics serves as the gateway to the later chapters, namely in terms of material design, since the bulk of the thesis describes the design, synthesis and characterization of organic dyes, organic small molecule semiconducting materials, and organic redox active surface modifiers.

Chapter 2 describes the design, synthesis, and opto-electronic characterization of a series of near infra-red asymmetric squaraine sensitizers for dye sensitized solar cells. This chapter builds on previous work published from our group, and attempts to address some of the questions raised in the aforementioned work. The performance of these materials in a dye-sensitized solar cell, as well as kinetics of electron injection into TiO_2 and charge recombination into the electrolyte will be briefly described.

Chapter 3 discusses the design, synthesis and opto-electronic properties of squaraine dyes exhibiting panchromatic light absorption. The adopted approach covalently links a high-energy absorbing chromophore to a low-energy-absorbing chromophore to produce a dual-chromophoric material that has a broad absorption profile. The performance of these materials in a dye-sensitized solar cell setting as well as kinetics of charge injection into titania will be overviewed.

Chapter 4 highlights the design, synthesis and optical characterization of a series of asymmetric perylene bisimides phosphonic acid surface modifiers. Their extent of aggregation on surfaces such as TiO_2 and indium tin oxide (ITO) is monitored optically through absorption and fluorescence spectroscopy, and the rates of electron transfer from PDI deposited on an ITO electrode is measured.

Chapter 5 describes the design, synthesis, opto-electronic and thermal properties of a series of organic small-molecule semiconducting materials to be used as donors in organic photovoltaics. These materials are alterations of small molecules reported in literature, and attempt to address some of their shortcomings via molecular design. The performance of these materials in organic photovoltaic device will be briefly addressed.

Chapter 6 summarizes the findings reported in the thesis, and provides a roadmap towards future directions regarding this research.

1.6 REFERENCES

(1) http://globalchange.mit.edu/files/2015%20Energy%20%26%20Climate%20Outlook.pdf.

(2) http://www.ipcc.ch/pdf/presentations/Kenya%20Tanzania%20outreach%20event.pdf.

(3) http://www.cop21paris.org/about/cop21.

(4) Schiermeier, Q.; Tollefson, J.; Scully, T.; Witze, A.; Morton, O. *Nature* **2008**, *454*, 816.

(5) Green, M. A.; Emery, K.; Hishikawa, Y.; Warta, W.; Dunlop, E. D. *Prog. Photovolt. Res. Appl.* **2016**, *24*, 3.

(6) Fthenakis, V. M.; Kim, H. C. *Solar Energy* **2011**, *85*, 1609.

(7) Mann, S. A.; de Wild-Scholten, M. J.; Fthenakis, V. M.; van Sark, W. G. J. H. M.; Sinke, W. C. *Prog. Photovolt. Res. Appl.* **2014**, *22*, 1180.

(8) Fthenakis, V. *Proc. IEEE* **2015**, *103*, 283.

(9) Fthenakis, V. *Renew. Sust. Energ. Rev.* **2009**, *13*, 2746.

(10) O'Regan, B.; Gratzel, M. *Nature* **1991**, *353*, 737.

(11) Bach, U.; Lupo, D.; Comte, P.; Moser, J. E.; Weissortel, F.; Salbeck, J.; Spreitzer, H.; Gratzel, M. *Nature* **1998**, *395*, 583.

(12) Yu, G.; Gao, J.; Hummelen, J. C.; Wudl, F.; Heeger, A. J. *Science* **1995**, *270*, 1789.

(13) Lee, M. M.; Teuscher, J.; Miyasaka, T.; Murakami, T. N.; Snaith, H. J. *Science* **2012**, *338*, 643.

(14) Liu, M.; Johnston, M. B.; Snaith, H. J. *Nature* **2013**, *501*, 395.

(15) Kojima, A.; Teshima, K.; Shirai, Y.; Miyasaka, T. *J. Am. Chem. Soc.* **2009**, *131*, 6050.

(16) Zhou, Y.; Fuentes-Hernandez, C.; Shim, J.; Meyer, J.; Giordano, A. J.; Li, H.; Winget, P.; Papadopoulos, T.; Cheun, H.; Kim, J.; Fenoll, M.; Dindar, A.; Haske, W.; Najafabadi, E.; Khan, T. M.; Sojoudi, H.; Barlow, S.; Graham, S.; Brédas, J.-L.; Marder, S. R.; Kahn, A.; Kippelen, B. *Science* **2012**, *336*, 327.

(17) Pagliaro, M.; Ciriminna, R.; Palmisano, G. *ChemSusChem* **2008**, *1*, 880.

(18) Green, M. A.; Emery, K.; Hishikawa, Y.; Warta, W.; Dunlop, E. D. *Progress in Photovoltaics: Research and Applications* **2015**, n/a.

(19) Anthony, J. E. *Chem. Mater.* **2011**, *23*, 583.

(20) Zhou, H.; Yang, L.; You, W. *Macromolecules* **2012**, *45*, 607.

(21) Hagfeldt, A.; Boschloo, G.; Sun, L.; Kloo, L.; Pettersson, H. *Chem. Rev.* **2010**, *110*, 6595.

(22) Mishra, A.; Fischer, M. K. R.; Bäuerle, P. *Angew. Chem., Int. Ed.* **2009**, *48*, 2474.

(23) Hans Wedepohl, K. *Geochim. Cosmochim. Acta* **1995**, *59*, 1217.

(24) Tang, C. W.; VanSlyke, S. A. *Appl. Phys. Lett.* **1987**, *51*, 913.

(25) Burroughes, J. H.; Bradley, D. D. C.; Brown, A. R.; Marks, R. N.; Mackay, K.; Friend, R. H.; Burns, P. L.; Holmes, A. B. *Nature* **1990**, *347*, 539.

(26) Zhang, Q.; Li, J.; Shizu, K.; Huang, S.; Hirata, S.; Miyazaki, H.; Adachi, C. *J. Am. Chem. Soc.* **2012**, *134*, 14706.

(27) Bao, Z.; Dodabalapur, A.; Lovinger, A. J. *Appl. Phys. Lett.* **1996**, *69*, 4108.

(28) Tsumura, A.; Koezuka, H.; Ando, T. *Appl. Phys. Lett.* **1986**, *49*, 1210.

(29) Nozik, A. J. *Annu. Rev. Phys. Chem.* **1978**, *29*, 189.

(30) Memming, R. *Electrochim. Acta* **1980**, *25*, 77.

(31) Fujishima, A.; Honda, K. *Nature* **1972**, *238*, 37.

(32) Zhang, Z.; Ito, S.; O'Regan, B.; Kuang, D.; Zakeeruddin Shaik, M.; Liska, P.; Charvet, R.; Comte, P.; Nazeeruddin, M. K.; Péchy, P.; Humphry-Baker, R.; Koyanagi, T.; Mizuno, T.; Grätzel, M. In *J. Phys. Chem.* 2007; Vol. 221, p 319.

(33) Huang, F.; Chen, D.; Zhang, X. L.; Caruso, R. A.; Cheng, Y.-B. *Adv. Funct. Mater.* **2010**, *20*, 1301.

(34) Y. Chiba, A. I., Y. Watanabe, R. Komiya, N. Koide and L. Y. Han *Japanese Journal of Applied Physics*, *45*, L638.

(35) Boschloo, G.; Häggman, L.; Hagfeldt, A. *J. Phys. Chem. B* **2006**, *110*, 13144.

(36) Kamat, P. V.; Fox, M. A.; Fatiadi, A. J. *J. Am. Chem. Soc.* **1984**, *106*, 1191.

(37) Matsumura, M.; Mitsuda, K.; Yoshizawa, N.; Tsubomura, H. *Bull. Chem. Soc. Jpn.* **1981**, *54*, 692.

(38) Koops, S. E.; O'Regan, B. C.; Barnes, P. R. F.; Durrant, J. R. *J. Am. Chem. Soc.* **2009**, *131*, 4808.

(39) Kambe, S.; Nakade, S.; Kitamura, T.; Wada, Y.; Yanagida, S. *J. Phys. Chem. B* **2002**, *106*, 2967.

(40) Solbrand, A.; Lindström, H.; Rensmo, H.; Hagfeldt, A.; Lindquist, S.-E.; Södergren, S. *J. Phys. Chem. B* **1997**, *101*, 2514.

(41) Hamann, T. W.; Ondersma, J. W. *Energy Environ. Sci.* **2011**, *4*, 370.

(42) Tuikka, M.; Hirva, P.; Rissanen, K.; Korppi-Tommola, J.; Haukka, M. *Chem. Commun.* **2011**, *47*, 4499.

(43) Boschloo, G.; Hagfeldt, A. *Acc. Chem. Res.* **2009**, *42*, 1819.

(44) Redmond, G.; Fitzmaurice, D. *J. Phys. Chem.* **1993**, *97*, 1426.

(45) Ardo, S.; Meyer, G. J. *Chem. Soc. Rev.* **2009**, *38*, 115.

(46) Rothenberger, G.; Fitzmaurice, D.; Graetzel, M. *J. Phys. Chem.* **1992**, *96*, 5983.

(47) Feldt, S. M.; Gibson, E. A.; Gabrielsson, E.; Sun, L.; Boschloo, G.; Hagfeldt, A. *J. Am. Chem. Soc.* **2010**, *132*, 16714.

(48) http://rredc.nrel.gov/solar/spectra/am1.5/.

(49) Kalyanasundaram, K.; Grätzel, M. *Coord. Chem. Rev.* **1998**, *177*, 347.

(50) Hagfeldt, A.; Graetzel, M. *Chem. Rev.* **1995**, *95*, 49.

(51) Anderson, N. A.; Lian, T. *Annu. Rev. Phys. Chem.* **2005**, *56*, 491.

(52) Asbury, J. B.; Anderson, N. A.; Hao, E.; Ai, X.; Lian, T. *J. Phys. Chem. B* **2003**, *107*, 7376.

(53) Snaith, H. J. *Adv. Funct. Mater.* **2010**, *20*, 13.

(54) Brennan, B. J.; Llansola Portoles, M. J.; Liddell, P. A.; Moore, T. A.; Moore, A. L.; Gust, D. *Phys. Chem. Chem. Phys.* **2013**, *15*, 16605.

(55) Murakami, T. N.; Yoshida, E.; Koumura, N. *Electrochim. Acta* **2014**, *131*, 174.

(56) Jradi, F. M.; Kang, X.; O'Neil, D.; Pajares, G.; Getmanenko, Y. A.; Szymanski, P.; Parker, T. C.; El-Sayed, M. A.; Marder, S. R. *Chem. Mater.* **2015**, *27*, 2480.

(57) Mulhern, K. R.; Orchard, A.; Watson, D. F.; Detty, M. R. *Langmuir* **2012**, *28*, 7071.

(58) Argazzi, R.; Murakami Iha, N. Y.; Zabri, H.; Odobel, F.; Bignozzi, C. A. *Coord. Chem. Rev.* **2004**, *248*, 1299.

(59) Nazeeruddin, M. K.; Kay, A.; Rodicio, I.; Humphry-Baker, R.; Mueller, E.; Liska, P.; Vlachopoulos, N.; Graetzel, M. *J. Am. Chem. Soc.* **1993**, *115*, 6382.

(60) Nazeeruddin, M. K.; Péchy, P.; Renouard, T.; Zakeeruddin, S. M.; Humphry-Baker, R.; Comte, P.; Liska, P.; Cevey, L.; Costa, E.; Shklover, V.; Spiccia, L.; Deacon, G. B.; Bignozzi, C. A.; Grätzel, M. *J. Am. Chem. Soc.* **2001**, *123*, 1613.

(61) Nazeeruddin, M. K.; De Angelis, F.; Fantacci, S.; Selloni, A.; Viscardi, G.; Liska, P.; Ito, S.; Takeru, B.; Grätzel, M. *J. Am. Chem. Soc.* **2005**, *127*, 16835.

(62) Hardin, B. E.; Snaith, H. J.; McGehee, M. D. *Nat Photon* **2012**, *6*, 162.

(63) Parker, T. C.; Marder, S. R. *Synthetic Methods in Organic Electronic and Photonic Materials: A Practical Guide*; Royal Society of Chemistry, 2015.

(64) Wang, Z.-S.; Cui, Y.; Dan-oh, Y.; Kasada, C.; Shinpo, A.; Hara, K. *J. Phys. Chem. C* **2007**, *111*, 7224.

(65) Ito, S.; Miura, H.; Uchida, S.; Takata, M.; Sumioka, K.; Liska, P.; Comte, P.; Pechy, P.; Gratzel, M. *Chem. Commun.* **2008**, 5194.

(66) Yella, A.; Lee, H.-W.; Tsao, H. N.; Yi, C.; Chandiran, A. K.; Nazeeruddin, M. K.; Diau, E. W.-G.; Yeh, C.-Y.; Zakeeruddin, S. M.; Grätzel, M. *Science* **2011**, *334*, 629.

(67) Shi, Y.; Hill, R. B. M.; Yum, J.-H.; Dualeh, A.; Barlow, S.; Grätzel, M.; Marder, S. R.; Nazeeruddin, M. K. *Angew. Chem.* **2011**, *123*, 6749.

(68) Martinez-Diaz, M. V.; de la Torre, G.; Torres, T. *Chem. Commun.* **2010**, *46*, 7090.

(69) Liang, M.; Chen, J. *Chem. Soc. Rev.* **2013**, *42*, 3453.

(70) Lee, C.-P.; Lin, R. Y.-Y.; Lin, L.-Y.; Li, C.-T.; Chu, T.-C.; Sun, S.-S.; Lin, J. T.; Ho, K.-C. *RSC Advances* **2015**, *5*, 23810.

(71) Hwang, S.; Lee, J. H.; Park, C.; Lee, H.; Kim, C.; Park, C.; Lee, M.-H.; Lee, W.; Park, J.; Kim, K.; Park, N.-G.; Kim, C. *Chem. Commun.* **2007**, 4887.

(72) Yella, A.; Mai, C.-L.; Zakeeruddin, S. M.; Chang, S.-N.; Hsieh, C.-H.; Yeh, C.-Y.; Grätzel, M. *Angew. Chem.* **2014**, *126*, 3017.

(73) Yao, Z.; Zhang, M.; Li, R.; Yang, L.; Qiao, Y.; Wang, P. *Angew. Chem. Int. Ed.* **2015**, *54*, 5994.

(74) Yao, Z.; Zhang, M.; Wu, H.; Yang, L.; Li, R.; Wang, P. *J. Am. Chem. Soc.* **2015**, *137*, 3799.

(75) Mathew, S.; Yella, A.; Gao, P.; Humphry-Baker, R.; CurchodBasile, F. E.; Ashari-Astani, N.; Tavernelli, I.; Rothlisberger, U.; Nazeeruddin, M. K.; Grätzel, M. *Nat Chem* **2014**, *6*, 242.

(76) Wu, H.; Yang, L.; Li, Y.; Zhang, M.; Zhang, J.; Guo, Y.; Wang, P. *J. Mater. Chem. A* **2016**.

(77) Xie, Y.; Tang, Y.; Wu, W.; Wang, Y.; Liu, J.; Li, X.; Tian, H.; Zhu, W.-H. *J. Am. Chem. Soc.* **2015**, *137*, 14055.

(78) Kakiage, K.; Aoyama, Y.; Yano, T.; Oya, K.; Fujisawa, J.-i.; Hanaya, M. *Chem. Commun.* **2015**, *51*, 15894.

(79) Kakiage, K.; Aoyama, Y.; Yano, T.; Oya, K.; Kyomen, T.; Hanaya, M. *Chem. Commun.* **2015**, *51*, 6315.

(80) Griffith, M. J.; Sunahara, K.; Wagner, P.; Wagner, K.; Wallace, G. G.; Officer, D. L.; Furube, A.; Katoh, R.; Mori, S.; Mozer, A. J. *Chem. Commun.* **2012**, *48*, 4145.

(81) Higashino, T.; Imahori, H. *Dalton Trans.* **2015**, *44*, 448.

(82) Li, L.-L.; Diau, E. W.-G. *Chem. Soc. Rev.* **2013**, *42*, 291.

(83) Huang, C.; Barlow, S.; Marder, S. R. *J. Org. Chem.* **2011**, *76*, 2386.

(84) Pydzińska, K.; Ziółek, M. *Dyes Pigm.* **2015**, *122*, 272.

(85) Bigelow, R. W.; Freund, H.-J. *Chem. Phys.* **1986**, *107*, 159.

(86) Law, K. Y. *Chem. Rev.* **1993**, *93*, 449.

(87) Zhang, K.; Qin, C.; Yang, X.; Islam, A.; Zhang, S.; Chen, H.; Han, L. *Adv. Energy M.* **2014**, *4*, n/a.

(88) Ragoussi, M.-E.; Ince, M.; Torres, T. *Eur. J. Org. Chem.* **2013**, *2013*, 6475.

(89) Kimura, M.; Nomoto, H.; Suzuki, H.; Ikeuchi, T.; Matsuzaki, H.; Murakami, T. N.; Furube, A.; Masaki, N.; Griffith, M. J.; Mori, S. *Chem.--Eur. J.* **2013**, *19*, 7496.

(90) Ince, M.; Yum, J.-H.; Kim, Y.; Mathew, S.; Grätzel, M.; Torres, T.; Nazeeruddin, M. K. *J. Phys. Chem. C* **2014**, *118*, 17166.

(91) Maeda, T.; Nitta, S.; Nakao, H.; Yagi, S.; Nakazumi, H. *J. Phys. Chem. C* **2014**, *118*, 16618.

(92) Sreejith, S.; Carol, P.; Chithra, P.; Ajayaghosh, A. *J. Mater. Chem.* **2008**, *18*, 264.

(93) Luo, J.; Xu, M.; Li, R.; Huang, K.-W.; Jiang, C.; Qi, Q.; Zeng, W.; Zhang, J.; Chi, C.; Wang, P.; Wu, J. *J. Am. Chem. Soc.* **2014**, *136*, 265.

(94) Jiao, C.; Zu, N.; Huang, K.-W.; Wang, P.; Wu, J. *Org. Lett.* **2011**, *13*, 3652.

(95) Mai, C.-L.; Huang, W.-K.; Lu, H.-P.; Lee, C.-W.; Chiu, C.-L.; Liang, Y.-R.; Diau, E. W.-G.; Yeh, C.-Y. *Chem. Commun.* **2010**, *46*, 809.

(96) Wu, C.-H.; Chen, M.-C.; Su, P.-C.; Kuo, H.-H.; Wang, C.-L.; Lu, C.-Y.; Tsai, C.-H.; Wu, C.-C.; Lin, C.-Y. *J. Mater. Chem. A* **2014**, *2*, 991.

(97) Shiu, J.-W.; Chang, Y.-C.; Chan, C.-Y.; Wu, H.-P.; Hsu, H.-Y.; Wang, C.-L.; Lin, C.-Y.; Diau, E. W.-G. *J. Mater. Chem. A* **2015**, *3*, 1417.

(98) Wu, H.-P.; Ou, Z.-W.; Pan, T.-Y.; Lan, C.-M.; Huang, W.-K.; Lee, H.-W.; Reddy, N. M.; Chen, C.-T.; Chao, W.-S.; Yeh, C.-Y.; Diau, E. W.-G. *Energy Environ. Sci.* **2012**, *5*, 9843.

(99) Jradi, F. M.; O'Neil, D.; Kang, X.; Wong, J.; Szymanski, P.; Parker, T. C.; Anderson, H. L.; El-Sayed, M. A.; Marder, S. R. *Chem. Mater.* **2015**, *27*, 6305.

(100) Sprenger, H. E.; Ziegenbein, W. *Angew. Chem. Int. Ed. Engl.* **1968**, *7*, 530.

(101) Treibs, A.; Jacob, K. *Angew. Chem. Int. Ed. Engl.* **1965**, *4*, 694.

(102) Keil, D.; Hartmann, H. *Dyes Pigm.* **2001**, *49*, 161.

(103) Beverina, L.; Salice, P. *Eur. J. Org. Chem.* **2010**, *2010*, 1207.

(104) Law, K.-Y.; Bailey, F. C.; Bluett, L. J. *Can. J. Chem.* **1986**, *64*, 1607.

(105) Beverina, L.; Ruffo, R.; Patriarca, G.; De Angelis, F.; Roberto, D.; Righetto, S.; Ugo, R.; Pagani, G. A. *J. Mater. Chem.* **2009**, *19*, 8190.

(106) Xia, G.; Wu, Z.; Yuan, Y.; Wang, H. *RSC Advances* **2013**, *3*, 18055.

(107) Bonnett, R.; Motevalli, M.; Siu, J. *Tetrahedron* **2004**, *60*, 8913.

(108) Law, K. Y.; Bailey, F. C. *J. Org. Chem.* **1992**, *57*, 3278.

(109) Yagi, S.; Hyodo, Y.; Matsumoto, S.; Takahashi, N.; Kono, H.; Nakazumi, H. *J. Chem. Soc., Perkin Trans. 1* **2000**, 599.

(110) Scherer, D.; Dörfler, R.; Feldner, A.; Vogtmann, T.; Schwoerer, M.; Lawrentz, U.; Grahn, W.; Lambert, C. *Chem. Phys.* **2002**, *279*, 179.

(111) Sprenger, H. E.; Ziegenbein, W. *Angew. Chem. Int. Ed. Engl.* **1967**, *6*, 553.

(112) Delcamp, J. H.; Shi, Y.; Yum, J. H.; Sajoto, T.; Dell'Orto, E.; Barlow, S.; Nazeeruddin, M. K.; Marder, S. R.; Grätzel, M. *Chem--Eur. J.* **2013**, *19*, 1819.

(113) Beverina, L.; Ruffo, R.; Mari, C. M.; Pagani, G. A.; Sassi, M.; De Angelis, F.; Fantacci, S.; Yum, J.-H.; Grätzel, M.; Nazeeruddin, M. K. *ChemSusChem* **2009**, *2*, 621.

(114) Fu, J.; Padilha, L. A.; Hagan, D. J.; Van Stryland, E. W.; Przhonska, O. V.; Bondar, M. V.; Slominsky, Y. L.; Kachkovski, A. D. *JOSA B* **2007**, *24*, 67.

(115) Kasha, M.; Rawls, H.; Ashraf El-Bayoumi, M. *Pure Appl. Chem.* **1965**, *11*, 371.

(116) Mishra, A.; Behera, R. K.; Behera, P. K.; Mishra, B. K.; Behera, G. B. *Chem. Rev.* **2000**, *100*, 1973.

(117) Zhao, W.; Jun Hou, Y.; Song Wang, X.; Wen Zhang, B.; Cao, Y.; Yang, R.; Bo Wang, W.; Rui Xiao, X. *Sol. Energy Mater. Sol. Cells* **1999**, *58*, 173.

(118) Sayama, K.; Tsukagoshi, S.; Mori, T.; Hara, K.; Ohga, Y.; Shinpou, A.; Abe, Y.; Suga, S.; Arakawa, H. *Sol. Energy Mater. Sol. Cells* **2003**, *80*, 47.

(119) Li, C.; Wang, W.; Wang, X.; Zhang, B.; Cao, Y. *Chem. Lett.* **2005**, *34*, 554.

(120) Chen, Y.; Zeng, Z.; Li, C.; Wang, W.; Wang, X.; Zhang, B. *New J. Chem.* **2005**, *29*, 773.

(121) Alex, S.; Santhosh, U.; Das, S. *Journal of Photochemistry and Photobiology A: Chemistry* **2005**, *172*, 63.

(122) Yum, J.-H.; Walter, P.; Huber, S.; Rentsch, D.; Geiger, T.; Nüesch, F.; De Angelis, F.; Grätzel, M.; Nazeeruddin, M. K. *J. Am. Chem. Soc.* **2007**, *129*, 10320.

(123) Geiger, T.; Kuster, S.; Yum, J. H.; Moon, S. J.; Nazeeruddin, M. K.; Grätzel, M.; Nüesch, F. *Adv. Funct. Mater.* **2009**, *19*, 2720.

(124) Paek, S.; Choi, H.; Kim, C.; Cho, N.; So, S.; Song, K.; Nazeeruddin, M. K.; Ko, J. *Chem. Commun.* **2011**, *47*, 2874.

(125) Chen, M.; Gratzel, M.; Thomas, J. K. *J. Am. Chem. Soc.* **1975**, *97*, 2052.

(126) Kay, A.; Graetzel, M. *J. Phys. Chem.* **1993**, *97*, 6272.

(127) Hagberg, D. P.; Jiang, X.; Gabrielsson, E.; Linder, M.; Marinado, T.; Brinck, T.; Hagfeldt, A.; Sun, L. *J. Mater. Chem.* **2009**, *19*, 7232.

(128) Yum;, J. H.; Moon;, S. J.; Humphry-Baker;, R.; Walter;, P.; Geiger;, T.; Nüesch;, F.; Grätzel;, M.; Nazeeruddin, M. d. K. *Nanotechnology* **2008**, *19*, 424005.

(129) Pandey, S. S.; Inoue, T.; Fujikawa, N.; Yamaguchi, Y.; Hayase, S. *Journal of Photochemistry and Photobiology A: Chemistry* **2010**, *214*, 269.

(130) Tatay, S.; Haque, S. A.; O'Regan, B.; Durrant, J. R.; Verhees, W. J. H.; Kroon, J. M.; Vidal-Ferran, A.; Gavina, P.; Palomares, E. *J. Mater. Chem.* **2007**, *17*, 3037.

(131) Burschka, J.; Dualeh, A.; Kessler, F.; Baranoff, E.; Cevey-Ha, N.-L.; Yi, C.; Nazeeruddin, M. K.; Grätzel, M. *J. Am. Chem. Soc.* **2011**, *133*, 18042.

(132) Dualeh, A.; Delcamp, J. H.; Nazeeruddin, M. K.; Grätzel, M. *Appl. Phys. Lett.* **2012**, *100*, 173512.

(133) Kippelen, B.; Bredas, J.-L. *Energy Environ. Sci.* **2009**, *2*, 251.

(134) Janssen, R. A. J.; Nelson, J. *Adv. Mater.* **2013**, *25*, 1847.

(135) Brédas, J.-L.; Cornil, J.; Heeger, A. J. *Adv. Mater.* **1996**, *8*, 447.

(136) Bakulin, A. A.; Rao, A.; Pavelyev, V. G.; van Loosdrecht, P. H. M.; Pshenichnikov, M. S.; Niedzialek, D.; Cornil, J.; Beljonne, D.; Friend, R. H. *Science* **2012**, *335*, 1340.

(137) Tang, C. W. *Appl. Phys. Lett.* **1986**, *48*, 183.

(138) Tang, C.; Albrecht, A. *J. Phys. Chem.* **1975**, *62*, 2139.

(139) Chamberlain, G. *Solar cells* **1983**, *8*, 47.

(140) Lunt, R. R.; Giebink, N. C.; Belak, A. A.; Benziger, J. B.; Forrest, S. R. *J. Appl. Phys.* **2009**, *105*, 053711.

(141) Hiramoto, M.; Fujiwara, H.; Yokoyama, M. *Appl. Phys. Lett.* **1991**, *58*, 1062.

(142) Sariciftci, N.; Smilowitz, L.; Heeger, A. J.; Wudl, F. *Science* **1992**, *258*, 1474.

(143) Burke, T. M.; Sweetnam, S.; Vandewal, K.; McGehee, M. D. *Adv. Energy M.* **2015**, *5*, n/a.

(144) Scharber, M. C.; Muhlbacher, D.; Koppe, M.; Denk, P.; Waldauf, C.; Heeger, A. J.; Brabec, C. J. *Adv. Mater.* **2006**, *18*, 789.

(145) He, Y.; Li, Y. *Phys. Chem. Chem. Phys.* **2011**, *13*, 1970.

(146) Ishida, M.; Park, S. W.; Hwang, D.; Koo, Y. B.; Sessler, J. L.; Kim, D. Y.; Kim, D. *J. Phys. Chem. C* **2011**, *115*, 19343.

(147) Veldman, D.; Meskers, S. C. J.; Janssen, R. A. J. *Adv. Funct. Mater.* **2009**, *19*, 1939.

(148) Lim, Y.-F.; Shu, Y.; Parkin, S. R.; Anthony, J. E.; Malliaras, G. G. *J. Mater. Chem.* **2009**, *19*, 3049.

(149) Sakamoto, Y.; Suzuki, T.; Kobayashi, M.; Gao, Y.; Fukai, Y.; Inoue, Y.; Sato, F.; Tokito, S. *J. Am. Chem. Soc.* **2004**, *126*, 8138.

(150) Lin, Y.; Fan, H.; Li, Y.; Zhan, X. *Adv. Mater.* **2012**, *24*, 3087.

(151) Liu, Y.; Zhao, J.; Li, Z.; Mu, C.; Ma, W.; Hu, H.; Jiang, K.; Lin, H.; Ade, H.; Yan, H. *Nat. Commun.* **2014**, *5*.

(152) Kan, B.; Li, M.; Zhang, Q.; Liu, F.; Wan, X.; Wang, Y.; Ni, W.; Long, G.; Yang, X.; Feng, H. *J. Am. Chem. Soc.* **2015**, *137*, 3886.

(153) Wienk, M. M.; Kroon, J. M.; Verhees, W. J.; Knol, J.; Hummelen, J. C.; van Hal, P. A.; Janssen, R. A. *Angew. Chem.* **2003**, *115*, 3493.

(154) Xie, Q.; Perez-Cordero, E.; Echegoyen, L. *J. Am. Chem. Soc.* **1992**, *114*, 3978.

(155) Hummel, R. E. *Electronic properties of materials*; Springer Science & Business Media, 2011.

(156) Mihailetchi, V. D.; van Duren, J. K.; Blom, P. W.; Hummelen, J. C.; Janssen, R. A.; Kroon, J. M.; Rispens, M. T.; Verhees, W. J. H.; Wienk, M. M. *Adv. Funct. Mater.* **2003**, *13*, 43.

(157) Lin, Y.; Zhan, X. *Mater. Horiz* **2014**, *1*, 470.

(158) Ma, W.; Yang, C.; Gong, X.; Lee, K.; Heeger, A. J. *Adv. Funct. Mater.* **2005**, *15*, 1617.

(159) Zhao, G.; He, Y.; Li, Y. *Adv. Mater.* **2010**, *22*, 4355.

(160) Sun, D.; Meng, D.; Cai, Y.; Fan, B.; Li, Y.; Jiang, W.; Huo, L.; Sun, Y.; Wang, Z. *J. Am. Chem. Soc.* **2015**, *137*, 11156.

(161) Meng, D.; Sun, D.; Zhong, C.; Liu, T.; Fan, B.; Huo, L.; Li, Y.; Jiang, W.; Choi, H.; Kim, T.; Kim, J. Y.; Sun, Y.; Wang, Z.; Heeger, A. J. *J. Am. Chem. Soc.* **2016**, *138*, 375.

(162) Zhong, Y.; Trinh, M. T.; Chen, R.; Purdum, G. E.; Khlyabich, P. P.; Sezen, M.; Oh, S.; Zhu, H.; Fowler, B.; Zhang, B.; Wang, W.; Nam, C.-Y.; Sfeir, M. Y.; Black, C. T.; Steigerwald, M. L.; Loo, Y.-L.; Ng, F.; Zhu, X. Y.; Nuckolls, C. *Nat Commun* **2015**, *6*.

(163) Hwang, Y.-J.; Li, H.; Courtright, B. A. E.; Subramaniyan, S.; Jenekhe, S. A. *Adv. Mater.* **2016**, *28*, 124.

(164) Cnops, K.; Zango, G.; Genoe, J.; Heremans, P.; Martinez-Diaz, M. V.; Torres, T.; Cheyns, D. *J. Am. Chem. Soc.* **2015**, *137*, 8991.

(165) Cnops, K.; Rand, B. P.; Cheyns, D.; Verreet, B.; Empl, M. A.; Heremans, P. *Nat Commun* **2014**, *5*.

(166) Li, C.; Wonneberger, H. *Adv. Mater.* **2012**, *24*, 613.

(167) Nielsen, C. B.; Holliday, S.; Chen, H.-Y.; Cryer, S. J.; McCulloch, I. *Acc. Chem. Res.* **2015**, *48*, 2803.

(168) Sonar, P.; Fong Lim, J. P.; Chan, K. L. *Energy Environ. Sci.* **2011**, *4*, 1558.

(169) Halls, J. J. M.; Walsh, C. A.; Greenham, N. C.; Marseglia, E. A.; Friend, R. H.; Moratti, S. C.; Holmes, A. B. *Nature* **1995**, *376*, 498.

(170) Sariciftci, N. S.; Braun, D.; Zhang, C.; Srdanov, V. I.; Heeger, A. J.; Stucky, G.; Wudl, F. *Appl. Phys. Lett.* **1993**, *62*, 585.

(171) Shaheen, S. E.; Brabec, C. J.; Sariciftci, N. S.; Padinger, F.; Fromherz, T.; Hummelen, J. C. *Appl. Phys. Lett.* **2001**, *78*, 841.

(172) Brabec, C. J.; Shaheen, S. E.; Winder, C.; Sariciftci, N. S.; Denk, P. *Appl. Phys. Lett.* **2002**, *80*, 1288.

(173) Dennler, G.; Scharber, M. C.; Brabec, C. J. *Adv. Mater* **2009**, *21*, 1323.

(174) Sirringhaus, H.; Tessler, N.; Friend, R. H. *Science* **1998**, *280*, 1741.

(175) Schilinsky, P.; Waldauf, C.; Brabec, C. J. *Appl. Phys. Lett.* **2002**, *81*, 3885.

(176) Irwin, M. D.; Buchholz, D. B.; Hains, A. W.; Chang, R. P. H.; Marks, T. J. *Proc. Natl. Acad. Sci.* **2008**, *105*, 2783.

(177) Dang, M. T.; Hirsch, L.; Wantz, G. *Adv. Mater.* **2011**, *23*, 3597.

(178) Pandey, L.; Risko, C.; Norton, J. E.; Brédas, J.-L. *Macromolecules* **2012**, *45*, 6405.

(179) Li, Y. *Acc. Chem. Res.* **2012**, *45*, 723.

(180) Liu, C.; Wang, K.; Gong, X.; Heeger, A. J. *Chem. Soc. Rev.* **2016**.

(181) Zheng, Q.; Jung, B. J.; Sun, J.; Katz, H. E. *J. Am. Chem. Soc.* **2010**, *132*, 5394.

(182) Choi, H.; Ko, S.-J.; Kim, T.; Morin, P.-O.; Walker, B.; Lee, B. H.; Leclerc, M.; Kim, J. Y.; Heeger, A. J. *Adv. Mater.* **2015**, *27*, 3318.

(183) Huo, L.; Liu, T.; Sun, X.; Cai, Y.; Heeger, A. J.; Sun, Y. *Adv. Mater.* **2015**, *27*, 2938.

(184) Liang, Y.; Xu, Z.; Xia, J.; Tsai, S. T.; Wu, Y.; Li, G.; Ray, C.; Yu, L. *Adv. Mater.* **2010**, *22*, E135.

(185) Wöhrle, D.; Meissner, D. *Adv. Mater.* **1991**, *3*, 129.

(186) Morel, D. L.; Ghosh, A. K.; Feng, T.; Stogryn, E. L.; Purwin, P. E.; Shaw, R. F.; Fishman, C. *Appl. Phys. Lett.* **1978**, *32*, 495.

(187) Yakimov, A.; Forrest, S. *Appl. Phys. Lett.* **2002**, *80*, 1667.

(188) Uchida, S.; Xue, J.; Rand, B. P.; Forrest, S. R. *Appl. Phys. Lett.* **2004**, *84*, 4218.

(189) Xue, J.; Rand, B. P.; Uchida, S.; Forrest, S. R. *Adv. Mater.* **2005**, *17*, 66.

(190) Wei, G.; Wang, S.; Sun, K.; Thompson, M. E.; Forrest, S. R. *Adv. Energy M.* **2011**, *1*, 184.

(191) Wei, G.; Xiao, X.; Wang, S.; Zimmerman, J. D.; Sun, K.; Diev, V. V.; Thompson, M. E.; Forrest, S. R. *Nano Lett.* **2011**, *11*, 4261.

(192) Anthony, J. E. *Chem. Rev.* **2006**, *106*, 5028.

(193) Yoo, S.; Domercq, B.; Kippelen, B. *Appl. Phys. Lett.* **2004**, *85*, 5427.

(194) Barlier, V. S.; Schlenker, C. W.; Chin, S. W.; Thompson, M. E. *Chem. Commun.* **2011**, *47*, 3754.

(195) Sakai, J.; Taima, T.; Yamanari, T.; Saito, K. *Sol. Energy Mater. Sol. Cells* **2009**, *93*, 1149.

(196) Fitzner, R.; Reinold, E.; Mishra, A.; Mena-Osteritz, E.; Ziehlke, H.; Körner, C.; Leo, K.; Riede, M.; Weil, M.; Tsaryova, O.; Weiß, A.; Uhrich, C.; Pfeiffer, M.; Bäuerle, P. *Adv. Funct. Mater.* **2011**, *21*, 897.

(197) Li, Z.; He, G.; Wan, X.; Liu, Y.; Zhou, J.; Long, G.; Zuo, Y.; Zhang, M.; Chen, Y. *Advanced Energy Materials* **2012**, *2*, 74.

(198) Sun, Y.; Welch, G. C.; Leong, W. L.; Takacs, C. J.; Bazan, G. C.; Heeger, A. J. *Nat. Mater.* **2012**, *11*, 44.

(199) Kan, B.; Zhang, Q.; Li, M.; Wan, X.; Ni, W.; Long, G.; Wang, Y.; Yang, X.; Feng, H.; Chen, Y. *J. Am. Chem. Soc.* **2014**, *136*, 15529.

(200) Zhao, J.; Li, Y.; Yang, G.; Jiang, K.; Lin, H.; Ade, H.; Ma, W; Yan, H. *Nature Energy*, **2016**, *1*, 15027.

CHAPTER 2 NEAR INFRA-RED ASSYMETRIC SQUARAINE SENSITIZERS FOR DSSCS: THE EFFECT OF π-BRIDGES AND ANCHORING GROUPS ON SOLAR CELL PERFORMANCE

2.1 INTRODUCTION

The current state-of-the-art DSSCs are based on two major class materials; zinc porphyrins and perylenes. These large π-aromatic molecules are attractive due to their good photostability, high extinction coefficients and synthetic modularity, were PCEs up to 13% have been achieved.[1,2] Porphyrins are characterized by a strongly absorbing Soret band and a weaker Q band at 400 and 600 nm, respectively; however these aforementioned bands are narrow and not optimal for light harvesting. Elongating the π-conjugation and breaking the symmetry of porphyrins cause spectral broadening and increases the absorptivity of the Q band.[3] This broadened absorption spectrum, among other things, contributed to the record PCEs with porphyrin based sensitizers, where photon-to-current conversion efficiency (IPCE) over 80% was achieved through an appreciable portion of the visible spectrum, Figure 1.9.[2] DSSCs based on perylene sensitizers, on the other hand, have just recently crossed 10% PCEs despite intensive research. An important factor that previously contributed to their weak performance is their weak electron-donating ability, which reduces the efficiency by which photo-excited electrons are injected into the semiconducting titania. Current research directions aims towards increasing the electron donating capabilities of perylenes via molecular design through, as one example, *N*-annulation of the perylene at the bay position which increases their electron donating capabilities.[4] When incorporated into a donor-acceptor "push-pull" dye these *N*-annulated perylene sensitizers, Figure 1.8, achieved PCEs up to 12.5% with IPCE values above 80% between 400 and 600 nm before they gradually decrease towards zero at 800 nm.[1]

Considering that losses of light due to reflection and absorption by the fluorine doped tin oxide (FTO) glass and TiO_2, typically used for fabrication of DSSC, can amount up to 10%,[5] the IPCE of devices based on the aforementioned two classes of materials in the visible region is close to optimal. Moving forward, to make DSSCs competitive using these classes of materials competitive with traditional photovoltaic devices, improved near infrared (NIR) light harvesting, up to 940 nm, is needed.[6] Squaraine dyes[7] are characterized by high molar absorptivities, 10^5 $M^{-1}cm^{-1}$ at 650 nm, and when compared, for example, to porphyrin dyes, which have similar molar absorptivities at their Soret band (λ_{max} ca. 450 nm), it is obvious that squaraine dyes are better situated to harvest NIR light on the condition that additional features capable of absorbing high energy photons can be introduced.[8-10]

Over the years, the performance of squaraine-based DSSCs have been limited by a relatively low open circuit voltage $V_{OC,}$[11] significant dye aggregation that reduced the short circuit current $J_{SC,}$[12,13] and a relatively low high-energy absorption between 400-600 nm, which lead to low IPCE values in this absorption region. Symmetric and asymmetric squaraine sensitizers with PCEs up to 5.6% have been reported in the last decade;[14-17] however, recently, using appropriate structural modifications, these PCE values were first increased to 6.7% with **2.1**,[12] Figure 2.1, which introduced high energy absorption *via* the use of a thiophene (T) bridge, and then to 7.3% with **2.2**,[13] which replaced the thiophene bridge with a cyclopenta-bithiophene (CPDT) bridge equipped with 2 hexyl chains at its central carbon. With CPDT, the J_{SC} increased to 16.4 mA/cm^2 in **2.2** in comparison with 14.8 mA/cm^2 in **2.1**, an effect that was ascribed to a combination of enhanced high-energy absorption by the π-bridge and disruption of aggregation by the hexyl chains on CPDT.[13]

In this chapter, the effect of other π-bridges (blue in Figure 2.1) that have high energy absorption bands complementary to the NIR absorption of the squaraine were further studied in an attempt to increase the squaraines performance in DSSC. In particular, 4-hexyl-4*H*-dithienopyrrole (DTP), dithienothiophene (DTT), and 4,4-bis(2-ethylhexyl)-4*H*-dithienosilole (DTS) have been covalently linked to a squaraine donor yielding asymmetrical push-pull donor-π-acceptor (D-π-A) structures (Figure 2.1).

Furthermore, the two branched out-of-plane 2-ethylhexyl chains of DTS substituted squaraines are expected to further reduce dye aggregation, compared to **2.2**, which, as will be presented later in this chapter, has considerable positive effect on squaraine performance in a DSSC namely by enhancing the J_{SC}, IPCEs, and the overall dye cell performance.

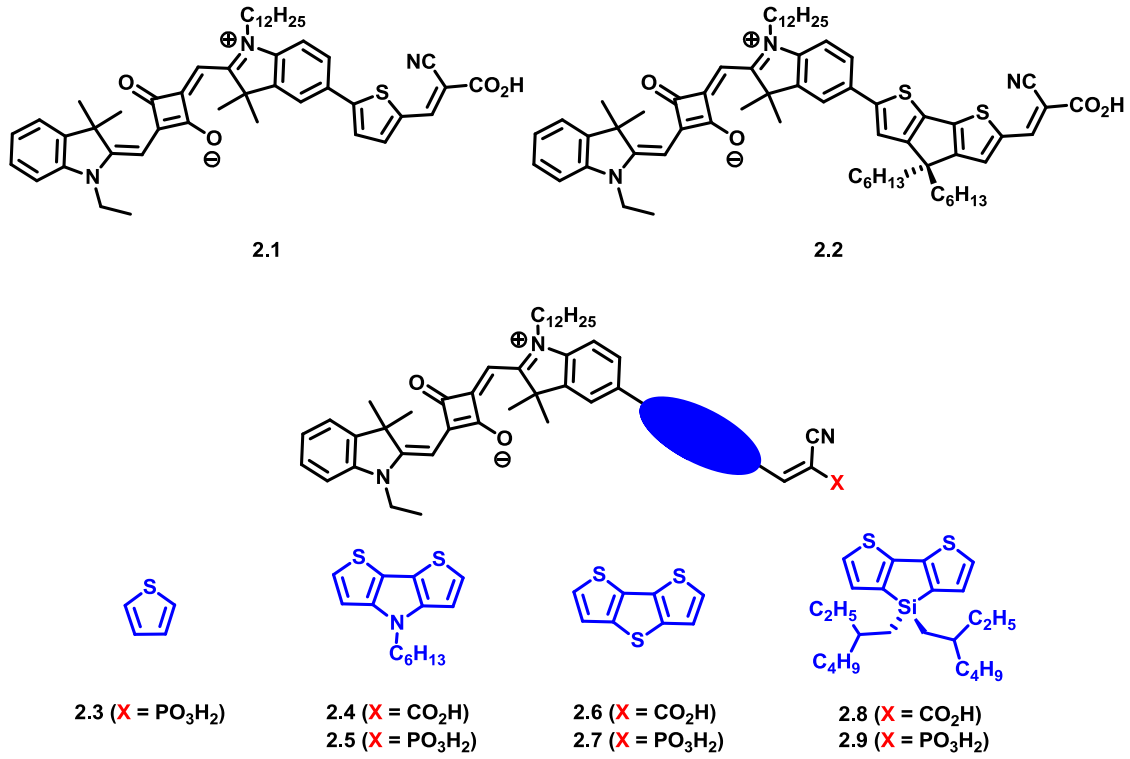

Figure 2.1 Molecular structures of the squaraine dyes discussed in this chapter. **2.1**,[12] **2.2** and **2.4**[13] have been reported previously.

Carboxylic acid, and cyanoacrylic acid (CA) anchoring groups are the anchoring groups in the majority of photosensitizers in literature.[18,19] The former anchoring group was heavily utilized in ruthenium-based sensitizers where the electron transfer is dominated by metal to ligand charge transfer (MLCT), while the latter is used more frequently with organic "push-pull" systems, due to its excellent electron withdrawing ability which aid in "pulling" the electron density of the LUMO closer to the titania surface. In addition, CA anchoring groups can be readily incorporated into the sensitizers towards the end of the synthesis via a Knoevenagel condensation,[20] which minimizes the number of purification steps required in the presence of an acid, and finally, the

carboxylic acids are known to form bonds (monodentate, bidentate, and H-bonds) with surface hydroxyl groups on metal oxides with equilibrium binding constants, *K*, on the order of 10^5 M^{-1}.[21]

Although, DSSCs fabricated with sensitizers utilizing CA binding groups have been shown to outperform analogs with different anchoring groups[22-24] (enhancement is often manifested as higher J_{SC}) the reasons behind this are still under debate and have been attributed to a variety of factors. For example, Brennan *et al.* compared three different porphyrin-based dyes that differ only by their anchoring groups; carboxylic acid vs. silatrane vs. phosphonic acid (PA). Compared to the other two, devices fabricated with sensitizers utilizing CA anchoring group showed 55% higher J_{SC} attributed to higher surface coverages resulting from an upright orientation of the dye on the titania surface,[22] which maximizes the number of dye molecules bound per surface area.[25]

Phosphonic acid (PA) anchoring groups are arguably the most studied anchoring groups after CA groups in DSSCs. They provide excellent stability and an adsorption strength (to metal oxide) that is ca. 80 times higher than that of CA.[26] Sensitizers with PAs experience negligible desorption in the presence of water (a common contaminant in liquid electrolyte DSSCs), with desorption rates up to 1000 times slower than analogues with CAs.[27,28] Mulhern *et al.*[29] and Murakami *et al.*[24] have independently demonstrated that devices fabricated with PA dyes are much more stable under prolonged operating times compared to their CA counterparts and responded better to stress tests. This being said, devices utilizing dyes having multiple CA anchoring groups have also shown prolonged device stability after 1000 hours of light soaking.[16] Given this enhanced device stability, along with promising performance, where PCE = 8.0%[30] and 6.4%[31] were reported with DSSCs utilizing PA based dyes, this chapter also describes the synthesis of the PA analogues of the CA squaraines reported in Figure 2.1, and compares their optical, electronic, and photovoltaic properties to those of their CA counterparts.

2.2 RESULTS AND DISCUSSION

2.2.1 Synthesis of the sensitizers

The syntheses of the target squaraine dyes **2.1** and **2.3**-**2.9** are described in Scheme 2.1 and Scheme 2.2. The desired fused bridges **2.13**, **2.14**, and **2.19**, Scheme 2.1, were synthesized either from the commercially available compound **2.10** or from the advanced intermediates **2.15**, and **2.16**. On the other hand the desired bridge **2.20** was acquired commercially from Frontier Scientific Inc. Compound **2.17** was prepared from commercially available 3-bromothiophene via base-catalyzed oxidative homo-coupling followed by Buchwald–Hartwig ring closure with *n*-hexylamine as described in literature.[32,33] Formylation of **2.17** was achieved by first, reacting it with one molar equivalent of lithium diisopropylamide (LDA) to generate the lithiated intermediate, which was then trapped with *N*,*N*-dimethylformamide (DMF) to give compound **2.12**.[34] Synthesis of **2.14** was achieved in a "one-pot" protection-lithiation-trapping-deprotection protocol as follows; in-situ protection of **2.12** was achieved by using *N*,*O*-dimethylhydroxylamine hydrochloride to form the intermediate **2.21**, which allows the use of a lithiating agent (*n*-butyllithium, or LDA) to deprotonate selectively the 6-position to get intermediate **2.22**; trapping with tributyltin chloride yielded intermediate **2.23**, which was then deprotected via an aqueous workup to provide **2.14**, which was used in the next step without further purification.[35] The desired dithienothiophene bridge, **2.13**, was synthesized in a similar manner; the commercially available dithienothiophene, **2.10**, was formylated by first lithiation with *n*-butyllithium then trapping with DMF to produce dithienothiophene carboxaldehyde, **2.11**, which then underwent the same one pot protection-lithiation-trapping-deprotection protocol similar to **2.12** to get the desired product **2.13**.

To synthesize compound **2.19**, Scheme 2.1, 2-bromothiophene was protected at the 5-position with a trimethylsilyl group, followed by a base-catalyzed halogen-dance reaction, and $CuCl_2$ promoted oxidative coupling to get **2.16**.[36] A halogen-lithium exchange reaction of **2.16** followed by trapping with dichloro[bis(2-ethylhexyl)]silane yielded a 2,6-bis(trimethyl silyl) derivative of **2.18**,[37] which upon reaction with *N*-bromosuccinimide,[37] and reductive de-bromination using zinc dust[38] yielded compound

2.18. Compound **2.18** was then mono-lithiated and trapped with trimethyltin chloride, in a manner similar to what was described before, to afford the desired bridge **2.19**. A shorter reaction pathway to get **2.18** was also attempted were a lithium-halogen exchange reaction was performed directly on compound **2.15**, prior to trapping with dichloro[bis(2-ethylhexyl)]silane to result in **2.18**. This approach, however, is not as clean and results in lower product yields; 50-60%, as opposed to >70% overall reaction yield over three steps. The one-pot aldehyde protection-lithiation-trapping-deprotection procedure described in the previous paragraph was also attempted on a 2-carboxaldehyde derivative of compound **2.18**, which was obtained via a Vilsmeier-Haack reaction in 80% yield,[39] however the reaction resulted in a complex mixture that was difficult to purify, and after several attempts this method wasn't further pursued.

The synthesis of the squaraine sensitizers, Scheme 2.2, goes through the common asymmetrical squaraine intermediate **2.28**, which was synthesized as described previously by Shi *et al*.;[40] Briefly, a phenyl hydrazine was transformed to the respective hydrazone upon reaction with 3-methyl-2-butanone,[41] and then to the indole via an acid catalyzed Fischer indole synthesis.[42] *N*-Alkylation with an iodoalkane followed by deprotonation of the resultant quaternary salt yielded the *N*-alkylated indoline, which upon condensation with a diethyl squarate gave the semi-squaraine ester.[43] Concurrently, the condensation of 4-bromo-*N*-substituted indoline, prepared in a similar manner as described above from 4-bromophenylhydrazene, with the aforementioned semi-squaraine ester gave rise to the asymmetrical squaraine bromide, **2.28**. A Stille coupling of squaraine **2.28** with functionalized π-bridges **2.13** (DTT) and **2.14** (DTP), Scheme 2.1, gave the corresponding aldehydes **2.30** and **2.31** in ca. 50% yields.[44] **2.33** on the other hand was prepared in two steps, first via a Stille coupling between **2.28** and **2.19** (DTS), to give **2.32**, which after a Vilsmeier-Haack reaction gave rise to **2.33** in a 47% yield over the two steps.[39] Finally, a Suzuki coupling reaction between **2.28** and the commercially acquired **2.20**, gave rise to **2.29** in 65% yields.[40]

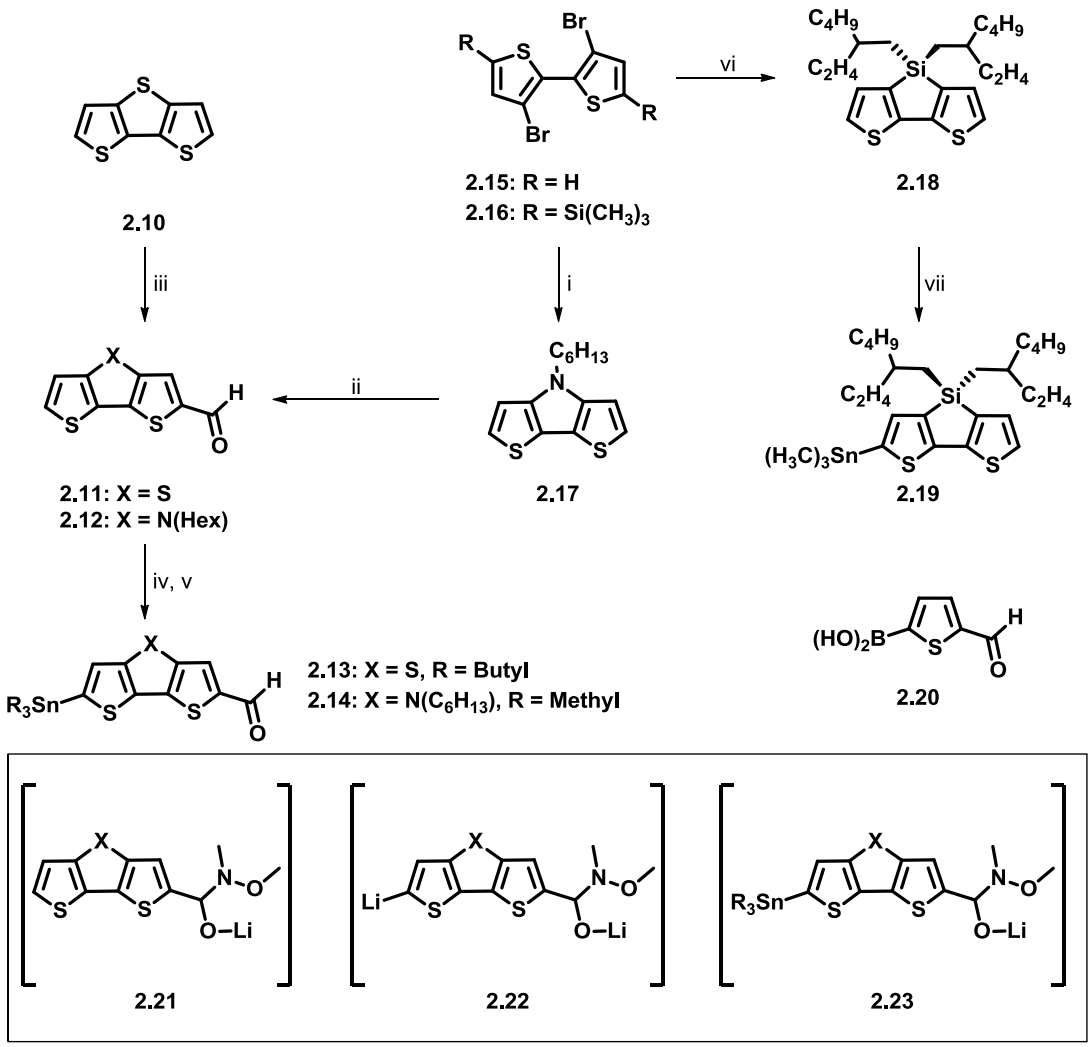

Scheme 2.1 Preparation of the fused π-Bridges; (i) Pd_2dba_3, BINAP, *tert*-BuONa, Toluene, reflux overnight; 54% (ii) a) LDA, THF, -78 ^oC, b) DMF, - 78 ^oC to rt; 72% (iii) a) *n*-butyllithium, THF, -78 ^oC, b) DMF, rt; 67% (iv) a) $CH_3ON(H)CH_3$•HCl, THF, -78 ^oC; b) LDA (2.00 eq.), -78 ^oC, 1h; c) 2.12, -78 ^oC; d) LDA, -78 ^oC; e) Me_3SnCl (1.50 eq.), -78 ^oC for 2h then to rt; f) Water, rt. 79% from ^1H NMR (v) a) $CH_3ON(H)CH_3$•HCl, THF, -78 ^oC; b) *n*-butyllithium (2.00 eq.); c) **2.11**; d) LDA, -78 ^oC; e) Me_3SnCl (1.50 eq.), -78 ^oC for 2h then to rt; f) Bu_3SnCl (1.05 eq.); 87% from ^1H NMR (vi) 1) a) *n*-butyllithium (2.0 eq.), THF, -78 ^oC; b) $(2\text{-Ethylhexyl})_2SiCl_2$, -78 ^oC; >90% 2) NBS (0.1 M in THF), rt, 30 min; yield over two steps 78% 3) zinc dust, propanol, water, acetic acid, reflux, overnight; quantitative (vii) a) *n*-butyllithium (1.0 eq.), THF, -78 ^oC, b) Me_3SnCl, -78 ^oC to rt; 60% from ^1H NMR. Highlighted in the box are the presumed intermediates for the in-situ protection-lithiation-trapping-deprotection step; **2.21**-**2.23**.

Knoevenagel condensation of compounds **2.29**-**2.31** and **2.33** with cyanoacetic acid provided the **CA** based dyes **2.1**, **2.4**, **2.6** and **2.8** in 50%, 34%, 60% and 70% yields, respectively. Along the same lines, Knoevenagel condensations of the same series of

compounds with diethyl cyanomethyl phosphonate yielded the squaraine phosphonates **2.34**-**2.37** in 50-80% yields, Scheme 2.2. Hydrolysis of the phosphonates with bromotrimethyl silane gave the desired **PA** dyes **2.3**, **2.5**, **2.7** and **2.9** in 85%, 93%, 50% and 85% yields, respectively. Compound **2.9**, which was obtained in ca. 85% yield contained ~10% of what we assign as the mono phosphonic acid, monoethyl ester by HPLC analysis, and high resolution mass spectrometry, Figure A.5 and Figure A.6. Compound **2.7** was obtained in lower yield compared to the rest of the series possibly as a result of its lower solubility in the reaction solvent (dichloromethane).

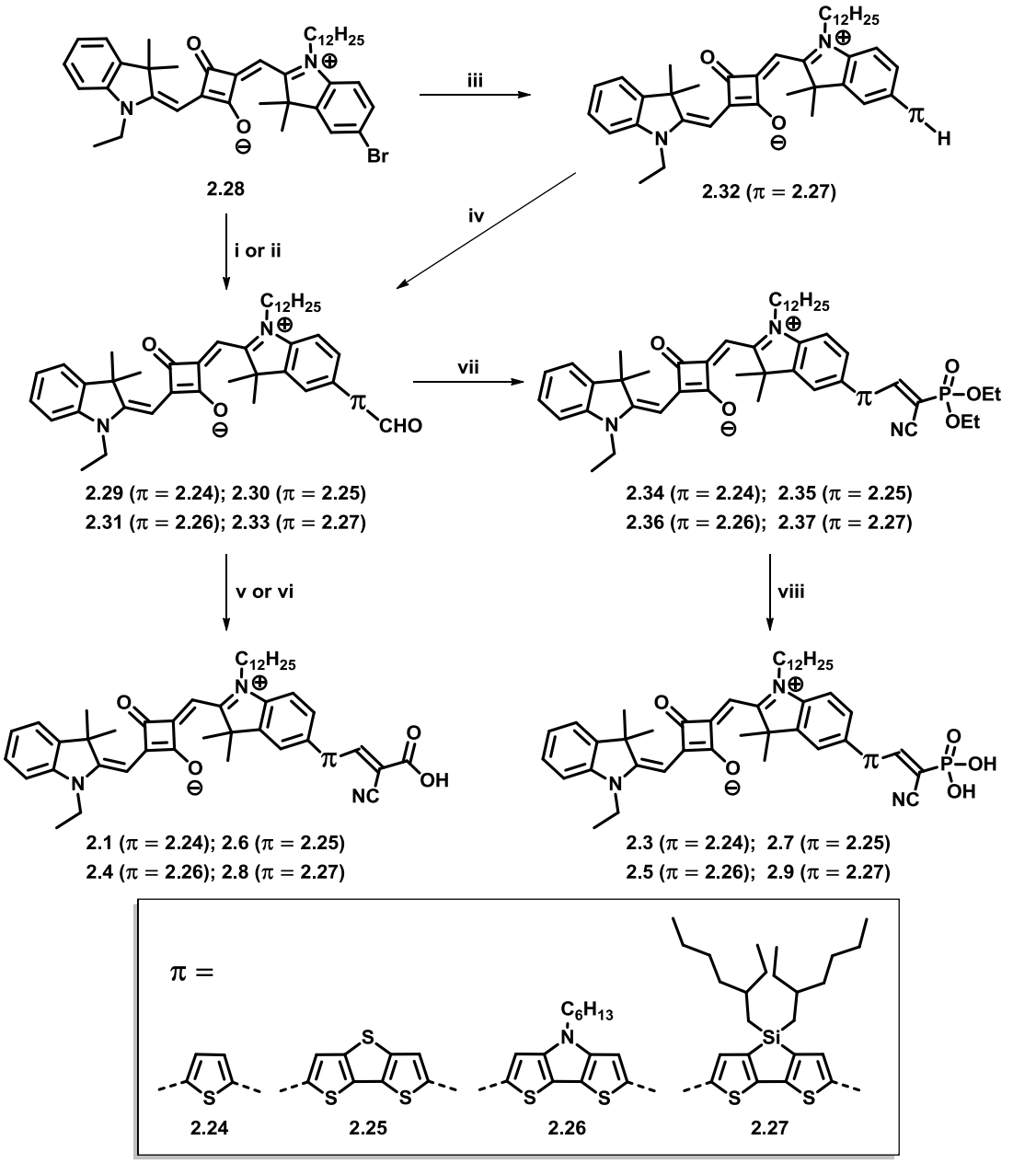

Scheme 2.2 Preparation of the target squaraine CA and PA sensitizers; (i) (for **2.29**) **2.20**, $PdCl_2(dppf)\cdot CH_2Cl_2$, K_2CO_3, toluene, methanol, 70 ^oC, overnight; (ii) (for **2.30** and **2.31**, respectively) **2.13** or **2.14**, $Pd(PPh_3)_2Cl_2$, toluene, 70 ^oC, overnight; (iii) **2.19**, $Pd(PPh_3)_2Cl_2$, toluene, 70 ^oC, overnight; (iv) DMF, $POCl_3$, 0 ^oC to 70 ^oC, 3 h; (v) **2.29** or **2.30** or **2.31**, $CNCH_2CO_2H$, piperidine, toluene, 70 ^oC, 4-6 h; (vi) **2.33**, $CNCH_2CO_2H$, $(NH_4)_2CO_3$, propanoic acid, toluene, 100 ^oC, overnight; (vii) $CNCH_2PO(OCH_2CH_3)_2$, $(NH_4)_2CO_3$, propanoic acid, toluene; (viii) (a) TMSBr, $ClCH_2CH_2Cl$, 70 ^oC; 2-4 h; (b) methanol, water, rt.

2.2.2 Optoelectronic properties and aggregation effects

Upon photo-excitation in push-pull donor-acceptor sensitizers, charge is transferred from the donor to the acceptor meditated through orbitals on the conjugated bridge. Hence, modifying the bridge affects the optical properties of the dyes.[19] Table 2.1, summarizes the optical and electronic properties of the sensitizers **2.1** and **2.3-2.9** presented in Figure 2.1. In each of the two series (for example the dyes with CA anchoring group) replacing the thiophene bridge **2.24** by the more extended DTT (**2.25**), DTP (**2.26**), and DTS (**2.27**) bridges resulted in a bathochromic shift of the low-energy squaraine-based band (λ_{max}). The extent of this shift, though, was minimal with the largest shift being 0.03 eV upon substituting thiophene in compound **2.1**, with DTP in compound **2.4**, Figure 2.2 and Table 2.1. However, as anticipated, these conjugated bridges introduced high-energy bands between 400 and 550 nm, with molar extinction coefficients ranging from 26,000 $M^{-1}cm^{-1}$ for **2.1** with the thiophene bridge up to 42,000 $M^{-1}cm^{-1}$ for **2.4** with dithienopyrrole bridge, Figure 2.2. In both series, the absorption maximum of the bridge-based absorption also varied in, with DTP bridges being the most red-shifted, followed by DTS, then DTT and finally thiophene bridges.

The molar extinction coefficients of the main squaraine band (ε_{max}) decreased with the extension of the conjugation with that of **2.4** 43% greater than that of **2.1**. However, this reduction in the extinction coefficient at the absorption maximum was compensated to some extent by the band broadening possibly attributed to a higher extent of intramolecular charge transfer in the less aromatic pyrrole-containing DTP, which rendered the integrated area under the absorption peaks similar to or even higher than in the case of the dye with the thiophene bridge, as indicated in the oscillator strength values *f* in Table 2.1. The CA and PA groups had little effect on the squaraine absorption band, but their effect on the high-energy bridge-based bands was more pronounced and led to hypsochromic shift by as high as 0.13 eV in the case of the DTP bridge, **2.4** and **2.5**, in Figure 2.2.

Table 2.1 Optical and electrochemical properties of the CA and PA sensitizers presented in Figure 2.1.

Dyes	λ_{max} [nm][a)]	ε [$M^{-1}cm^{-1}$][a)]	f [b)]	$E_{0\text{-}0}^{opt}$[eV][c)]	$E_{(S^+/S)}$ [V][d)]	$E_{(S^+/S^*)}$ [V][e)]
2.1	659	279,000	1.39	1.76	+0.80	−0.96
2.3	655	311,000	1.49	1.85	+0.86	−0.99
2.4	670	160,000	1.34	1.74	+0.74	−1.00
2.5	670	204,000	1.43	1.82	+0.82	−1.00
2.6	662	231,000	1.28	1.76	+0.80	−0.99
2.7	661	259,000	1.43	1.84	+0.85	−0.99
2.8	667	257,000	1.58	1.82	+0.84	−0.98
2.9	666	214,000	1.32	1.83	+0.88	−0.95

[a)]Derived from absorption spectra in ethanol; [b)]Oscillator Strength: $f = 4.31\times10^{-9}\int\varepsilon(\nu)d\nu$;[c)]Determined from the intersection of the normalized absorption and emission spectra, as shown in Figure 2.5. [d)] Half-wave ground state oxidation potentials vs. NHE determined via cyclic voltammetry in THF containing 0.1M *n*-Bu_4NPF_6. [e)] Calculated according to the following equation $E_{(S^+/S^*)} = E_{(S^+/S)} - E_{0\text{-}0}^{opt}$

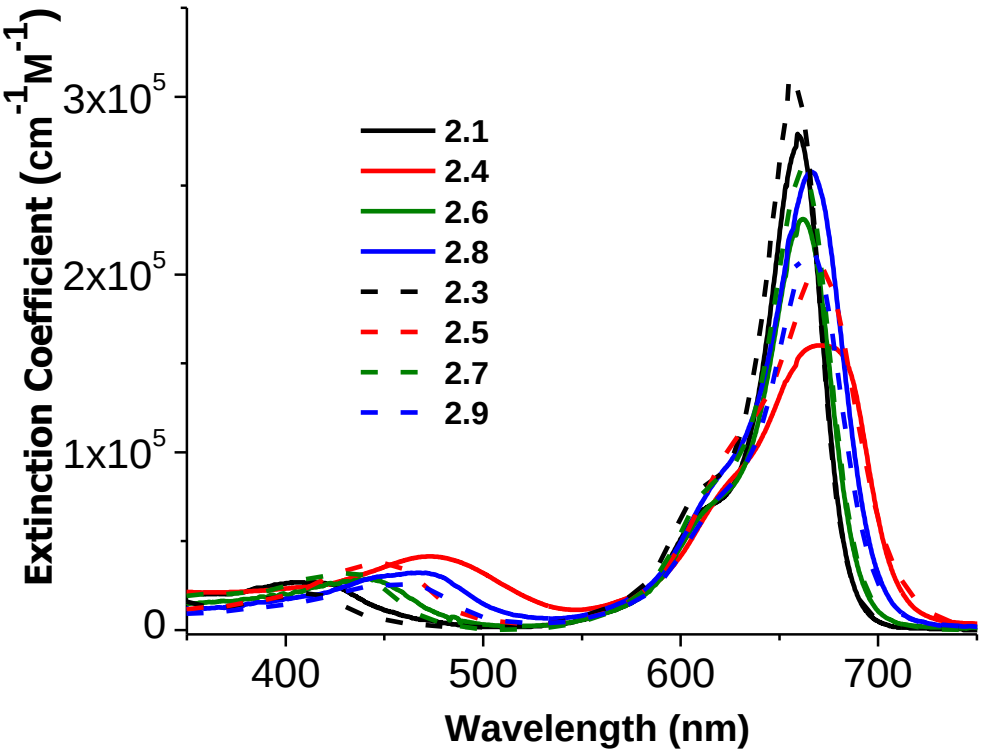

Figure 2.2 UV-vis absorption spectra of the dyes presented in Figure 2.1 recorded in ethanol. The solid lines correspond to the dyes with carboxylic acid anchoring groups, while the dashed lines correspond to dyes with phosphonic acid anchoring groups.

The ground-state oxidation potential $E_{(S^+/S)}$ and the excited-state oxidation potential $E_{(S^+/S^*)}$ of a dye with respect to the electrochemical redox potential of the DSSC electrolyte and the conduction band edge (CBE) of TiO_2, respectively, are critical for solar cell operation. To ensure optimal solar cell performance, sufficient driving force is required for both charge injection from the excited dye into TiO_2 CBE and the dye regeneration by the iodide/triiodide redox couple (I_3^-/I^-). The energy difference between $E_{(S^+/S^*)}$ and the CBE of TiO_2 (−0.5 V vs. NHE)[45,46] dictates this driving force, which for efficient charge injection, is required to be at least 150 meV.[47] To ensure efficient dye regeneration by the triiodide/iodide redox couple (+0.30 V vs. NHE),[48] a value of $E_{(S^+/S)}$ higher than + 0.65 V vs. NHE is recommended.[48] The ground-state oxidation potential of the CA and PA dyes were determined by cyclic voltammetry measurements, Figure 2.3 while the excited state oxidation potentials were calculated according to the following equation $E_{(S^+/S^*)} = E_{(S^+/S)} - E_{0\text{-}0}^{opt}$ where $E_{0\text{-}0}^{opt}$ is the optical gap of the materials determined from the intersection of the normalized absorption and emission spectra, as shown in Figure 2.5. Based on these criteria all of the CA and PA dyes should exhibit

sufficient driving force ($-\Delta G_{ei}^{0}$) for charge injection into TiO_2, Figure 2.4 and Table 2.3 of at least 450 mV, which is significantly higher than what is required. The ground-state potentials $E_{(S^+/S)}$ of all dyes ranged between +0.74 V and +0.88 V vs. NHE, which is higher than the value of +0.65 V required for efficient dye regeneration.

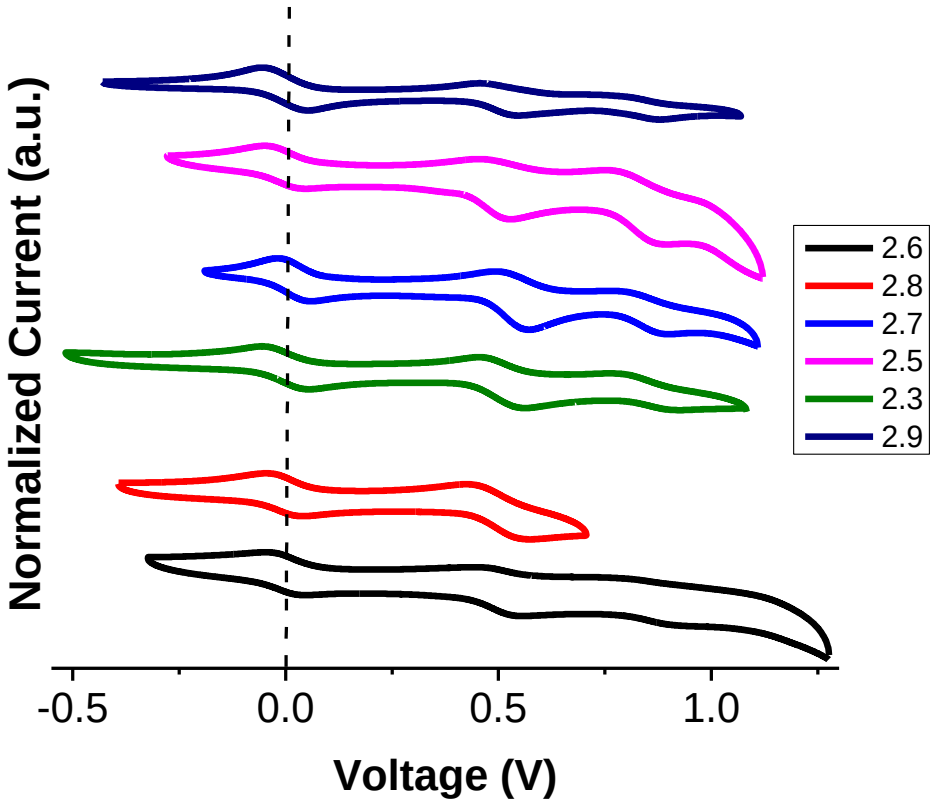

Figure 2.3 Cyclic voltammetry measurements showing the oxidation potentials of the series of dyes synthesized in THF containing 0.1M *n*-Bu_4NPF_6. Potentials were referenced to ($FeCp_2^{*+/0}$) redox couple by using decamethylferrocene (–0.46 V vs. ferrocene) as an internal reference. $E(FeCp_2^{+/0})$ is +0.80 V vs. NHE.[49] All cyclic voltamograms were recorded at a scan rate of 50 mVs^{-1}.The cyclic voltammograms for compounds **2.1** and **2.4** are not shown as they are already reported in literature.[40,50]

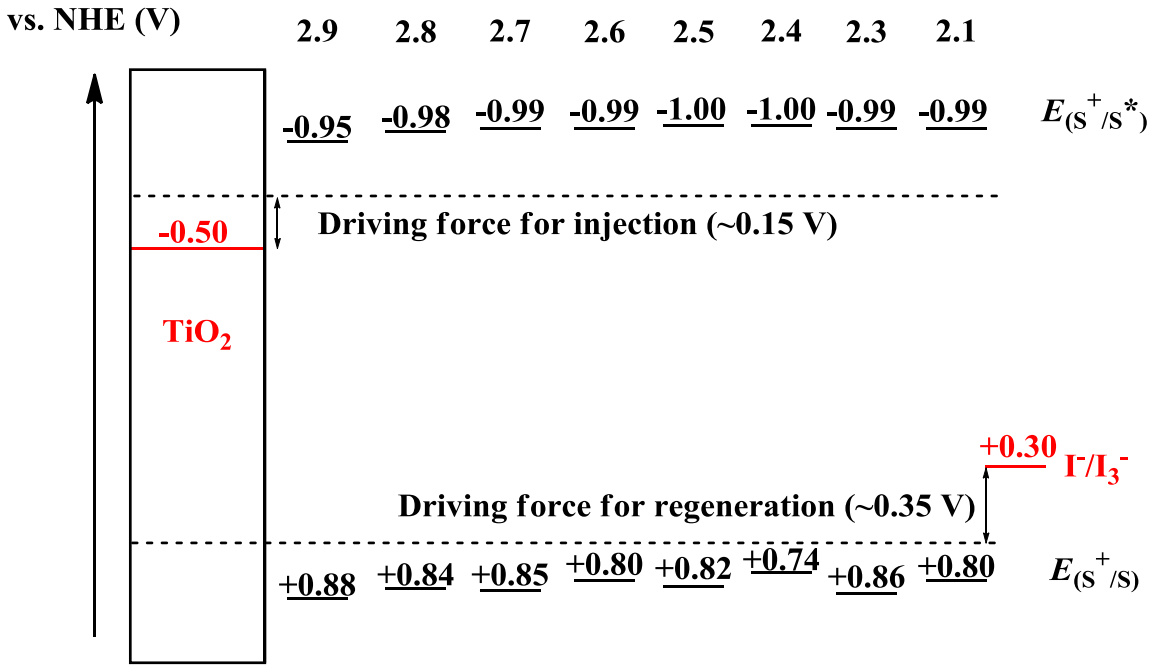

Figure 2.4 A schematic showing the ground-state oxidation potential, $E_{(S^+/S)}$, and the excited-state oxidation potentials, $E_{(S^+/S^*)}$, of the CA and PA dyes. Also shown are the TiO_2 (conduction band edge) CBE, and the redox potential of the triiodide/iodide redox shuttle (I^-/I_3^-). The minimum driving forces for the electron injection into the TiO_2 CBE from the excited dye, and the driving force to regeneration of the oxidized dye by the electrolyte are also presented.

Although all materials showed sufficient driving forces for both electron injection into TiO_2 and dye regeneration by the electrolyte, as evident from Figure 2.4, it is necessary to point out that the position of the $E_{(S^+/S^*)}$, potential is not optimal for these materials as there is around 300 mV of extra driving force that could be theoretically removed without altering the electron injection efficiency into the CBE of TiO_2. If achieved, this will reduce the loss-in-voltage, defined as ($E_{0\text{-}0}^{opt}$ - V_{OC}) in chapter 1, in DSSCs employing these dyes and will allow for harvesting lower energy photons, as the optical gap of these materials will be reduced.

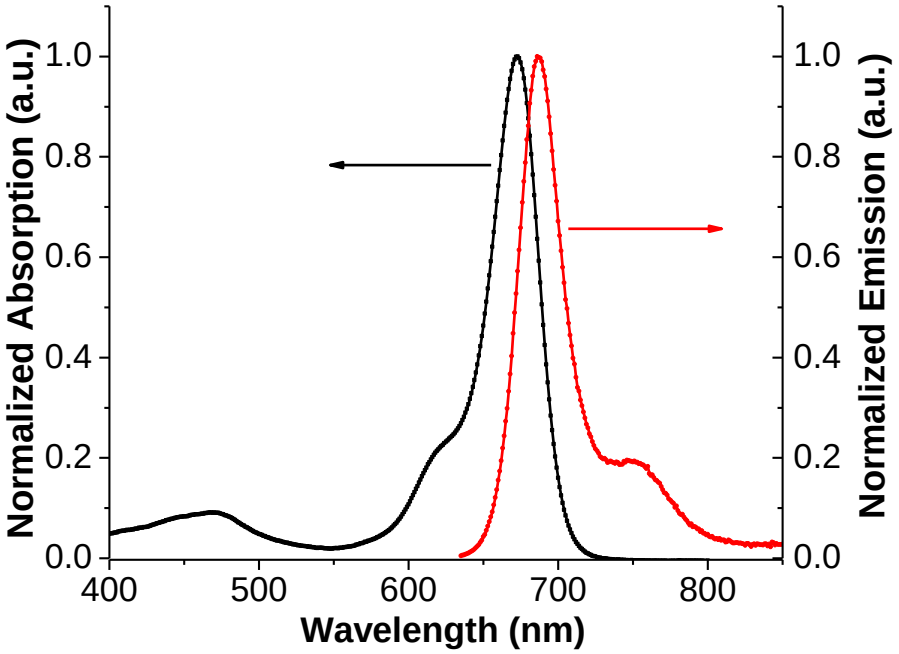

Figure 2.5 A Representative spectrum showing the normalized absorption and emission spectra for compound **2.8**. The optical gap is estimated at the intersection of the two spectra. The corresponding spectra for the rest of the dyes are in the experimental section.

In order to gain additional insight into the optical behavior of dyes in a functioning cell, namely upon aggregation, the absorption spectra of the CA and PA dyes in Figure 2.1 on TiO_2 films were collected, and the spectra are presented in Figure 2.6 TiO_2 films were immersed into a dye solution dissolved in ethanol/$CHCl_3$ (4:1) containing 3α,7α-dihydroxy-5β-cholic acid (chenodeoxycholic acid, CDCA; an amphiphilic molecule that belongs to the bile acid family[51] that has been shown to form elongated micelles in aqueous media,[52,53] and has been extensively used in DSSCs to assist disaggregation of dyes) for 1 hour at room temperature. The films were then washed with ethanol and dried under nitrogen before the UV-Vis absorption spectra were collected.

In addition to the general broadening of the spectra expected for the dyes adsorbed on surfaces, a strong peak close to, but blue-shifted from the main squaraine absorption band was observed. This peak has been observed before for squaraine dyes and is usually attributed to H-aggregation. [54,55] In the dyes containing the DTS bridge, *i.e.*

2.8 and **2.9**, this H-aggregate peak, which is otherwise well resolved at around 630 nm is reduced into a shoulder; this may be due to the 2-ethylhexyl chains on the bridge, which project out of the plane of the squaraine dyes and thus may reduce π-π stacking and dye aggregation, Figure 2.6. It is necessary to point out that a similar effect was observed for the phosphonic acid dye **2.3**, which has a thiophene bridging unit; however the reason of this behavior is not consistent with its carboxylic acid analogue **2.1**, or with the other dyes that have planar bridges, such as **2.6** and **2.7** which have a DTS bridge. One explanation could be that this particular dye is binding to the TiO_2 surface with a different binding mode compared to the rest of the dyes in the series, which might reduce its ability to interact with nearby dyes.[28,56]

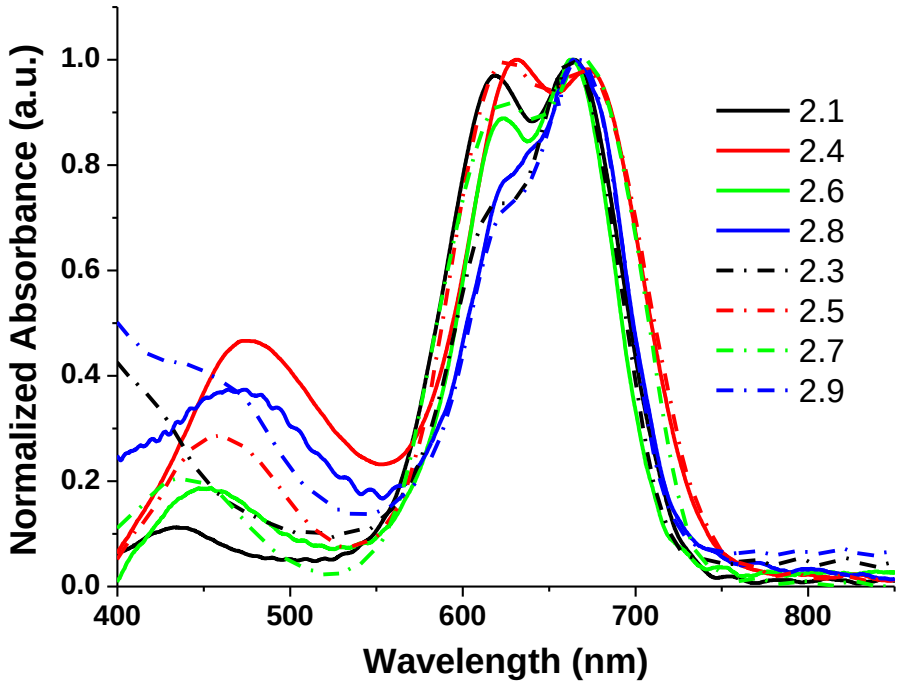

Figure 2.6 Normalized UV-vis absorption spectra of the dyes presented in Figure 2.1 on TiO_2 films. TiO_2 films were dipped in a solution containing 0.05 mM dye and 10 mM CDCA for 1 hour. The solid lines correspond to the dyes with carboxylic acid anchoring groups, while the dashed lines correspond to dyes with phosphonic acid anchoring groups.

2.2.3 Photovoltaic measurements

NOTE: The results discussed in this section are based on experiments that have been conducted by Dr. Xiongwu Kang at the Georgia Institute of Technology. A detailed discussion about device fabrication procedures and characterization will be incorporated

in the collaborative publications. Permission has been obtained to use the data presented in this section.

The photovoltaic characteristics for DSSCs based on each of the following dyes are listed in Table 2.2, and in Figure 2.7. The CA based dyes **2.1**, **2.4** and **2.6** all showed photovoltaic characteristics that are consistent with what was previously reported in literature,[12,13,15] especially with regard to their low V_{OC}, Table 1.2. This consistently low V_{OC} in squaraine based DSSCs have limited their performance despite their relatively high J_{SC}, which previously reached as high as 16.4 mA/cm^2 in the case of **2.2**,[13] putting it slightly lower than that of the champion porphyrin-based dye mentioned in section 1.3.3.2, whose J_{SC} is 18.1 mA/cm^2, and whose PCE of 13% is the highest reported in literature.[2] On the other hand, DSSCs fabricated with **2.8**, saw an increase in V_{OC}, to reach 0.68 V, which is a 50 mV increase over **2.2**. This enhanced V_{OC} combined with a relatively high J_{SC} equal to 19.1 mA/cm^2, DSSCs fabricated with **2.8** exhibited a PCE of 8.9%, an 18% increase over **2.2**. If we consider the absorption spectra of the CA dyes on TiO_2, Figure 2.6, the major difference that set **2.8** apart from the rest of the dyes is the decreased H-aggregation (peak at around 630 nm), thus the increased J_{SC} may due to decreased aggregation due to the out-of-plane 2-ethylhexyl groups, as is shown in the molecular model of compound **2.8**, Figure A.23. On the other hand, dyes in the PA series exhibited much lower PCEs compared to their CA counterparts, which is due in large part to lower J_{SC} values, which dropped by as much as 72% going from **2.6** to **2.7**, as shown in Figure 2.7 and Table 2.2.

Table 2.2 Photovoltaic performance of the optimized dye cells.[a,b]

	Dye Conc. [mM]	CDCA Conc. [mM]	*Voc* [V]	J_{SC} [mA/cm^2]	FF [%]	PCE [%]
2.1	0.1	10	0.65 ± 0.01	14.2 ± 0.3	70 ± 1	6.5 ± 0.1
2.3	0.05	10	0.64 ± 0.01	9.6 ± 0.3	72 ± 1	4.6 ± 0.2
2.4	0.1	10	0.61 ± 0.01	13.5 ± 0.3	68 ± 1	5.6 ± 0.1
2.5	0.05	10	0.64 ± 0.01	5.9 ± 0.4	74 ± 1	2.8 ± 0.3
2.6	0.1	10	0.64 ± 0.01	13.1 ± 0.3	72 ± 1	6.0 ± 0.1
2.7	0.1	50	0.62 ± 0.01	3.7 ± 0.2	76 ± 1	1.8 ± 0.1
2.8	0.05	10	0.68 ± 0.01	19.1 ± 0.2	69 ± 1	8.9 ± 0.2
2.9	0.05	10	0.68 ± 0.01	10.4 ± 0.2	71 ± 1	5.0 ± 0.1

[a]Based on measurements of 3 devices for all dyes with the standard deviation shown. [b]The photovoltaic measurements were conducted in the absence of a mask with a cell active area of 0.36 cm^2, when a mask[57,58] was utilized a decrease of up to 10% in PCE was observed. Dye soaking time is 4 h.

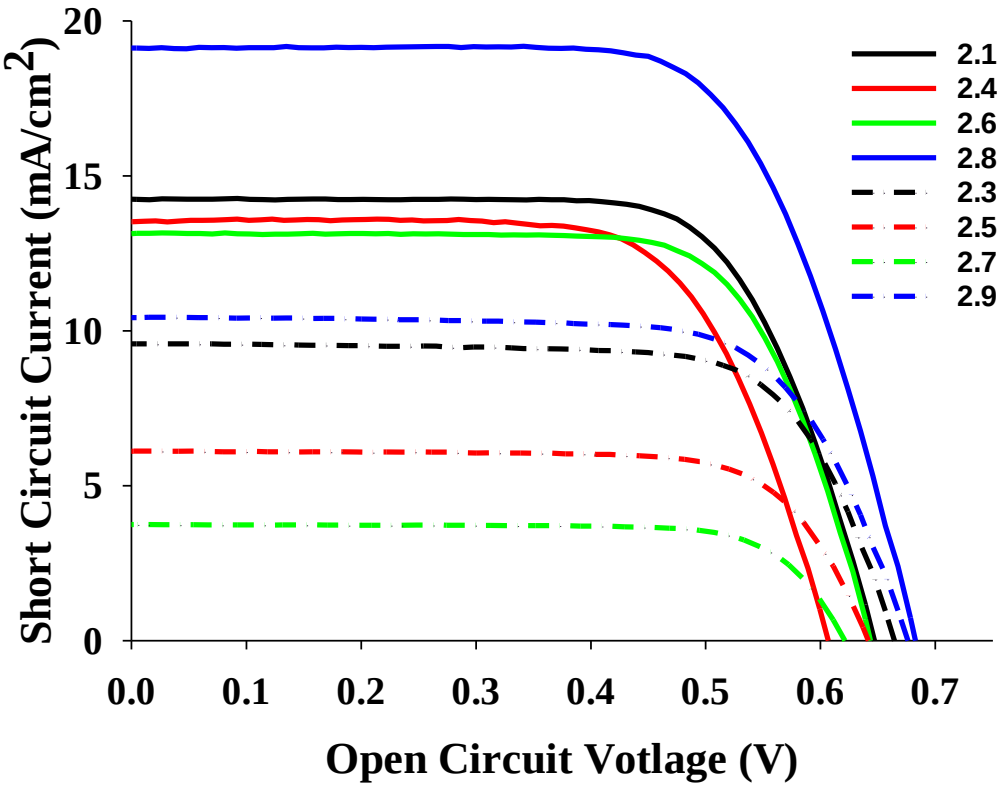

Figure 2.7 Photovoltaic performance of the optimized DSSCs fabricated with the series in Figure 2.1. The solid lines correspond to the dyes with carboxylic acid anchoring groups, while the dashed lines correspond to dyes with phosphonic acid anchoring groups.

To gain insight into the observed trends in J_{SC}, IPCE spectra were recorded for DSSCs made with the respective dyes and the results are shown in Figure 2.8. In general, the IPCE of the dyes in the CA series had an onset around 800 nm, with the exception of **2.8**, blue solid line, the onset of which was around 850 nm. Moreover, **2.8** demonstrated the highest IPCE values among all other dyes in the CA series, reaching as high as 90% at low energies and 82% at higher energies, while all the other dyes plateaued at ca. 70%. The high IPCE values reported for these dyes at lower wavelength, despite their relatively low molar absorptivities in this region, likely results from the presence of the 4 μm light scattering layer formed of anatase particles.[59,60] Dyes in the PA series, on the other hand, showed narrower features and overall lower IPCEs reaching maximum at ~60%, dashed lines in Figure 2.8, where **2.5** and **2.7** achieved an IPCE of only ~30%. The lower IPCE going from CA to PA based molecules relates well to the drop in the J_{SC} and PCEs discussed earlier. This decrease in IPCE in phosphonic acid based dyes is rather common;

this decrease has been attributed to lack of conjugation at the tetrahedral phosphorus center (the P=O bond is generally more usefully presented as P^{+}–O^{-}, where the P–O π-orbitals cannot overlap with aromatic π-orbitals),[61] which disrupts the electron flow from the dye into titania. As an example, Brown, *et al.* synthesized a ruthenium based dye that had PA as well as CA anchoring groups, where the former was utilized to increase binding stability, while the latter was utilized to maintain good electron injection efficiency.[62]

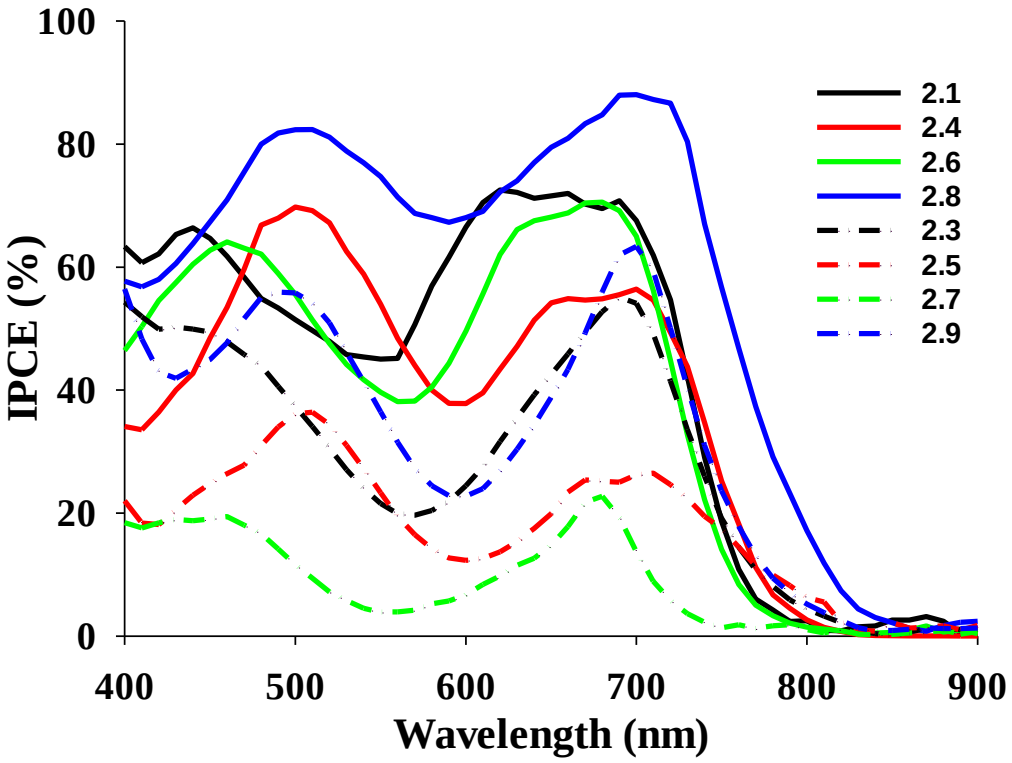

Figure 2.8 IPCE of the optimized DSSCs fabricated with the series in Figure 2.1. The solid lines correspond to the dyes with carboxylic acid anchoring groups, while the dashed lines correspond to dyes with phosphonic acid anchoring groups.

The effects of dye aggregation on the performance of the assembled dye cells with standard I_3^-/I^- electrolyte were explored, and representative results are summarized in Table 2.5 in the experimental section. The presence of CDCA generally increased PCE of the devices, indicating a certain amount of aggregation in all the dyes,[51-53] however, dyes with PA anchoring groups demonstrated a stronger dependence on the CDCA:dye ratio compared to their CA counterparts. Hydrogen bonding of $(RO)_2P(O)OH$,

$ROP(O)(OH)_2$, and PA groups have been reported to be significantly stronger than corresponding carboxylic acids,[63,64] and as a result they might form hydrogen bonded clusters.[65] This increased hydrogen bonding may result in formation of aggregates of PA dyes that are more difficult to disaggregate than their CA counterparts, which could potentially reduce the disaggregating efficiency of CDCA towards PA dyes in comparison with CA dyes.

2.2.4 Charge injection dynamics

NOTE: The results discussed in this section are based on experiments that have been conducted by Daniel O'Neil from Prof. Mostafa El-Sayed's lab at the Georgia Institute of Technology. A detailed discussion about the kinetic measurements will be incorporated in Daniel O'Neil's future thesis. Permission has been obtained to use the data presented in this section.

In an attempt to further understand the observed IPCE, a more detailed study of the charge-injection and recombination dynamics was carried out. IPCE and J_{SC} are mainly determined by light harvesting, charge injection efficiency, charge collection efficiency and dye regeneration efficiency, as highlighted in Equation (4) in section 1.3.2.[19] Unlike traditional ruthenium dyes, squaraines tend to exhibit shorter lived excited states, and relaxation from the excited state to the ground state potentially competes with electron injection to the conduction band of TiO_2. To determine the effect of the excited-state lifetime and charge injection on the dye cell performance, the excited-state lifetimes and decay dynamics of the dyes adsorbed on TiO_2 and Al_2O_3 films in fully assembled cells were measured via femtosecond transient-absorption spectroscopy. It is assumed that the excited state of the dye on Al_2O_3 film decays to the ground state without charge injection, while excited states of dyes on TiO_2 films may quench through electron transfer to the conduction band of TiO_2. The decay dynamics of the excited state on both Al_2O_3 and TiO_2 films were determined by following the excited state absorption peak (typically 475 nm to 550 nm) and summarized in Table 2.3 along with the charge injection and dye regeneration driving force driving forces ($-\Delta G_{ei}^{\circ}$ and $-\Delta G_{reg}^{\circ}$).[47]

Table 2.3 Charge-injection dynamics of compounds **2.1**, **2.4**, and other CA and PA series in Figure 2.1. The fully assembled cells were pumped near the ground state absorption for each dye and probed near their excited state absorption maxima. All data were fit with stretched exponentials. τ_{obs} is the average lifetime of the excited state on either titania (TiO_2) or alumina (Al_2O_3), k_{ei} is the charge injection rate constant, $-\Delta G_{ei}^{\circ}$ is the driving force for electron injection, while $-\Delta G_{reg}^{\circ}$ is the driving force for dye regeneration, and η_{inj} is the charge injection efficiency.

Dye	τ_{obs}**[ps]/TiO_2**	τ_{obs}**[ps]/ Al_2O_3**	k_{ei} **[$10^{-10}s^{-1}$]**	$-\Delta G_{ei}^{\circ}$ **[V]**	$-\Delta G_{reg}^{\circ}$ **[V]**	η_{inj}**[%]**
2.1	1.8	123.9	52.4	0.46	0.50	98.5
2.3	8.3	80.3	10.8	0.49	0.56	89.6
2.4	1.0	14.1	97.6	0.50	0.44	97.6
2.5	16.0	127.3	5.5	0.50	0.52	87.4
2.6	19.8	3942	5.0	0.49	0.50	99.0
2.7	19.1	32.3	2.2	0.49	0.55	41.0
2.8	1.2	22.6	78.9	0.48	0.54	94.6
2.9	4.0	18.5	19.6	0.43	0.58	78.6

Charge-injection efficiencies for the CA containing dyes (≥95%) were higher than those for the PA containing dyes (41-90%). For all the PA containing dyes, k_{ei} (charge injection rate constant) was smaller than that of their CA, which is consistent with the lower IPCE seen for PA dyes, Figure 2.8. This may result from several factors such as (1) excited state deactivation due to increased dye aggregation, as discussed in section 29 (2) decreased electron density near the TiO_2 surface for the PA anchoring group in comparison with the CA counterpart, as a result of broken conjugation and (3) smaller orbital overlap between the PA and the TiO_2 surface compared to the CA anchoring groups, or combinations of these factors. Also, it is important to note that the lifetime of the excited state of the CA dyes with alkyl groups on the π-bridge, e.g. **2.4** (14.1 ps) and **2.8** (22.6 ps), were significantly smaller than those of the non-alkylated π-bridge CA dyes **2.1** (123.9 ps) and **2.6** (3942 ps), possibly due to an increased number of vibrational pathways for deactivation of the excited state in the alkylated π-bridge dyes. Thus, there may be some degree of tradeoff between using alkyl groups to decrease aggregation and increase *Jsc*, although increased deactivation of the excited state from more vibrational pathways may not affect *Jsc* as significantly as aggregation.

After electron injection into the TiO_2 it is important that the injected charge does not recombine with electron acceptors present in the electrolyte. This charge recombination, which can limit both the V_{OC} and J_{SC},[66-68] has been probed by electrochemical impedance spectroscopy and the results are displayed in Table 2.4, and are presented in terms of electron lifetime (τ_0). The most notable observation is that the electron lifetime in cells based on PA dyes are larger than their CA counterparts, as shown in Table 2.4. As an example, the value of τ for the dyes with DTP and DTT bridges more than doubled, going from 5.7 to 14.4 ms in the case of the former and from 6.2 to 14.2 ms in the case of the later, respectively. The same trend was observed for dyes with thiophene and DTS bridges however the extent of the increase was smaller (7.5 and 9.5 ms, and 9.1 to 16.1, respectively).

Within the same series, the electron lifetime demonstrated dependence on the nature of the bridge; Cells fabricated with CA dyes having DTP and DTT bridges

resulted in shorter electron lifetimes (faster recombination) compared to dyes with the thiophene bridge, an effect that is opposite to that observed in the case of PAs. However, dyes with the DTS bridges demonstrated the slowest charge-recombination rates and longest electron lifetime when compared to rest of the dyes in both series. This slower charge recombination rate also manifested itself in the higher V_{OC} values observed with cells fabricated with these dyes, where a V_{OC} of 0.68 V was reported in both cases compared to a 0.63 V average V_{OC} for the rest of the dyes.

Table 2.4 The lifetime of electrons in TiO_2 films determined from impedance measurements on fully fabricated cells

Dyes	**2.1**	**2.3**	**2.4**	**2.5**	**2.6**	**2.7**	**2.8**	**2.9**
τ_0 **(ms)**	7.5	9.5	5.7	14.4	6.2	14.2	9.1	16.1

2.3 CONCLUSION

In summary, in this chapter the effect of four different π-bridges (thiophene, dithienothiophene, dithienopyrrole, and dithienosilole) and two anchoring groups (carboxylic acid, and phosphonic acid) on the optoelectronic properties and DSSC performance of squaraine-based sensitizers were investigated. Dyes with dithienosilole bridges achieved the highest efficiencies in their respective series (8.9% in the case of carboxylic acid anchoring group and 5.0% in the case of phosphonic acid anchoring group), which is attributed to higher J_{SC} and V_{OC} due to lower dye aggregation and slower recombination rates, respectively.

Femtosecond transient absorption spectroscopy showed that going from carboxylic acid to phosphonic acid based dyes resulted in reduction in charge injection efficiency, which coupled with higher affinity towards dye aggregation yielded a lower and narrower IPCE and hence PCEs. On the other hand, electrical impedance measurements showed that phosphonic acid based dyes may exhibit slower charge recombination rates between injected electrons and electron acceptors in the electrolyte than their CA counterpart. The study suggests that aggregation may be alleviated in squaraine-based dyes by including out-of-plane alkyl groups on the π-bridge, as is

evident by the effectiveness of the dithienosilole bridge in increasing the J_{SC}, and ultimately the PCE. Even though these alkyl groups seem to decrease the excited state lifetimes possibly due to increased vibrational deactivation pathways, this study also suggests that the out-of-plane alkyl groups may increase V_{OC} by reducing the interaction of the electrolyte with the TiO_2 surface.

2.4 EXPERIMENTAL SECTION

2.4.1 Synthetic procedures

Commercially available intermediates were purchased and used without further purification. For water-sensitive reactions, commercially acquired anhydrous *N*,*N*-dimethylformamide was used, while, tetrahydrofuran and toluene were dried by the distillation from sodium benzophenone ketyl or used directly from MBRAUN solvent purification system (MBRAUN-SPS). Bases, such as piperidine and diisopropylamine, were distilled over calcium hydride, and stored in Schlenk flasks under nitrogen in the presence of molecular sieves. ^{1}H, $^{13}C\{^{1}H\}$ and ^{31}P NMR spectra were collected on a Bruker 400 MHz spectrometer. Deuterated solvents with tetramethylsilane as an internal standard were used; in the case of ^{31}P NMR, an external reference (tube filled with a solution of phosphoric acid) was utilized and referenced to 0 ppm. Mass spectra were measured on a VG Instruments 70-SE using the electron impact (EI) or fast-atom bombardment (FAB) mode and on an Applied Biosystems 4700 Proteomics Analyzer using MALDI mode. Elemental analyses were carried out by Atlantic Microlab using a LECO 932 CHNS elemental analyzer.

(2.13)

Lithium diisopropylamide (LDA) was prepared as follows. Tetrahydrofuran (2.5 mL) and diisopropylamine (0.76 mL, 5.34 mmol) were introduced into a dry round-bottomed flask and the content was stirred at -78 ^{o}C for 15 min. *n*-Butyllithium (1.70 mL, 4.90 mmol, 2.89 M in hexanes) was then added dropwise at -78 ^{o}C, and the content was stirred for several minutes before allowing it to warm to room temperature. Into a second round-bottomed flask, *N*,*O*-dimethylhydroxylamine hydrochloride (0.24 g, 2.45 mmol) and tetrahydrofuran (2.0 mL) were introduced, and the white suspension was cooled in a

dry ice/acetone bath and stirred for 30 min, after which freshly prepared LDA (4.92 mL, 4.90 mmol) was added dropwise, and the content was stirred for 1 h. Dithieno[3,2-*b*:2',3'-*d*]thiophene-2-carbaldehyde **2.11** (0.50 g, 2.23 mmol) in THF (3.0 mL) was introduced to the flask with deprotonated *N,O*-dimethylhydroxylamine at -78 ^{o}C, and the mixture was stirred for 2 h, after which *n*-butyllithium (2.00 eq., 3.54 mL, 4.68 mmol) was added. The reaction mixture was stirred for an additional 1 h at -78 ^{o}C. Bu_3SnCl (1.20 mL, 2.34 mmol) was then introduced into the reaction mixture, cooling was removed, and the reaction was allowed to warm to room temperature overnight. Water was added to quench the reaction, and the organic layer was extracted with dichloromethane (3 × 50 mL), dried over sodium sulfate, the drying agent was filtered off, and the solvent removed under reduced pressure to obtain the desired product **2.13**, which was used for the next step without further purification (0.99 g, 87%). ^{1}H NMR (400 MHz, $CDCl_3$) δ 9.96 (s, 1H), 7.97 (s, 1H), 7.37 (s, 1H), 2.00 - 0.80 (m , 27H).

(2.14)

LDA was prepared as follows. Tetrahydrofuran (2.7 mL) and diisopropylamine (0.96 mL, 6.82 mmol) were introduced into a dry round-bottomed flask and the content stirred at -78 ^{o}C for 15 min under nitrogen atmosphere. *n*-Butyllithium (2.37 mL, 6.18 mmol, 2.6 M in hexanes) was added dropwise at -78 ^{o}C, and the mixture was stirred for few min before it was allowed to warm to room temperature. Into a second round-bottomed flask, *N,O*-dimethylhydroxylamine hydrochloride (0.20 g, 2.06 mmol) and THF (2.0 mL) were introduced, and the white suspension was stirred at -78 ^{o}C for 30 min after which freshly prepared LDA (4.02 mL, 4.12 mmol) was added dropwise, and the mixture was stirred at -78 ^{o}C for 1 hour. 4-Hexyl-4*H*-dithieno[3,2-*b*:2',3'-*d*]pyrrole-2-carbaldehyde **2.12** (0.50 g, 1.71 mmol) in THF (1.0 mL) was added to the reaction mixture with deprotonated *N,O*-dimethylhydroxylamine at -78 ^{o}C, and the content stirred for 2 h at -78 ^{o}C, followed by the addition of LDA (2.01 mL, 2.06 mmol) and stirring for an additional 1 h. Me_3SnCl (0.50 g, 2.57 mmol) was added, and the reaction mixture was stirred for 2 h while heating up to room temperature. Water was added, and the organic layer was extracted from dichloromethane, dried over sodium sulfate, the drying agent was filtered off, and the solvent was removed under reduced pressure to get a 1:1 mixture of the desired product **2.14**, and **2.12**, which was used as a mixture for the next step

without further purification. ^{1}H NMR (400 MHz, $CDCl_3$) δ 9.88 (s, 1H), 7.66 (s, 1H), 7.05 (s, 1H), 4.25 (t, 2H, J = 6.8 Hz), 1.88 (m, 8H), 0.89 (t, 3H, J = 7.2 Hz), 0.46 (s, 9H).

(2.30)

Compounds **2.28** (0.45 g, 0.67 mmol) and **2.13** (0.34 g, 0.67 mmol) were dissolved in anhydrous toluene (5 mL) and the content was stirred at room temperature under nitrogen atmosphere for 20 min. Bis(triphenylphosphine)palladium(II) dichloride (0.023 g, 0.033 mmol) was introduced to the flask, and the content stirred overnight at 70 ^{o}C. Upon reaction completion, the solvent was removed under reduced pressure, and the crude product was purified via flash chromatography (silica gel, 2:8 ethyl acetate:dichloromethane) to give **2.28** as a green solid (0.27 g, 50%). ^{1}H NMR (300 MHz, $CDCl_3$) δ 9.96 (s, 1H), 7.96 (s, 1H), 7.61-7.57 (m, 2H), 7.55 (s, 1H), 7.38 (d, J = 6 Hz, 1H), 7.33 (t, J = 6 Hz, 1H), 7.18 (t, J = 7.5 Hz, 1H), 7.03 (d, J = 8 Hz, 1H), 6.98 (d, J = 8 Hz, 1H), 6.00 (s, 1H), 5.97 (s, 1H), 4.11 (bs, 2H), 3.96 (bs, 2H), 1.84 (s, 6H), 1.80 (s, 6H), 1.41 (t, J = 7.0 Hz, 3H), 1.35-1.20 (m, 20 H), 0.87 (t, J = 6.9 Hz, 3H); ^{13}C{^{1}H} NMR (100 MHz, $CDCl_3$) δ 182.78, 182.36, 181.15, 178.57, 170.69, 168.43, 149.02, 147.41, 147.00, 143.54, 143.32, 143.18, 142.42, 141.82, 140.63, 138.27, 130.25, 129.28, 129.21, 127.91, 125.95, 124.17, 122.44, 119.86, 116.03, 109.60, 109.45, 87.29, 86.70, 49.62, 48.97, 43.82, 38.63, 31.92, 29.61, 29.55, 29.51, 29.39, 29.34, 27.30, 27.11, 27.06, 26.89, 22.70, 17.51, 14.14, 13.62, 12.12; HRMS (MALDI) *m/z*: $[M]^+$ calcd for $C_{49}H_{54}N_2O_3S_3$, 814.3297; found, 814.3248. Anal. Calcd for $C_{49}H_{54}N_2O_3S_3$: C 72.20, H 6.68, N 3.44, S 11.80; found: C 72.07, H 6.71, N 3.47.

(2.31)

Compounds **2.28** (0.45 g, 0.67 mmol) and **2.14** (0.30 g, 0.67 mmol) were dissolved in anhydrous toluene (5.0 mL), and the content was stirred at room temperature under nitrogen atmosphere for 20 min. Bis(triphenylphosphine)palladium(II) dichloride (0.023 g, 0.023 mmol) was introduced to the flask, and the content stirred overnight at 70 ^{o}C. Upon reaction completion, the solvent was removed under reduced pressure, and the crude product was purified via flash chromatography (silica gel, 0.5:9.5 ethyl acetate:dichloromethane) to give **2.31** as a green solid (0.33 g, 56%).^{1}H NMR (400 MHz, $CDCl_3$) δ 9.89 (s, 1H), 7.66 (s, 1H), 7.62-7.59 (m, 2H), 7.40 (d, J = 7 Hz, 1H), 7.35 (dd,

J_1= 7.6 Hz, J_2 = 0.9 Hz, 1H), 7.24 (s, 1H), 7.20 (t, J = 7.8 Hz, 1H), 7.05 (d, J = 7.8 Hz, 1H), 7.00 (t, J = 8 Hz, 1H), 6.02 (s, 1H), 6.00 (s, 1H), 4.28 (t, J = 6.4 Hz, 2H), 4.13 (bs, 2H), 3.99 (bs, 2H), 1.95 (p, J = 7.4 Hz, 2H), 1.88 (s, 6H), 1.82 (s, 6H), 1.50-1.50 (m, 29H), 0.98-0.87 (m, 6H); $^{13}C\{^1H\}$ NMR (100 MHz, $CDCl_3$) δ 182.80, 182.35, 180.66, 178.68, 170.39, 168.66, 149.59, 147.18, 143.98, 143.21, 142.74, 142.37, 141.87, 140.06, 130.39, 127.89, 125.76, 124.06, 123.60, 122.43, 119.57, 119.14, 119.09, 113.95, 109.59, 109.37, 106.09, 87.20, 86.59, 49.54, 49.06, 47.53, 43.83, 38.57, 31.92, 31.41, 30.32, 29.71, 29.61, 29.55, 29.50, 29.40, 29.34, 27.29, 27.11, 27.08, 26.92, 26.71, 22.70, 22.52, 14.14, 14.03, 12.10. HRMS (MALDI) *m/z*: $[M]^+$ calcd for $C_{55}H_{67}N_3O_3S_2$: 881.4624; found, 881.4649. Anal. Calcd for $C_{55}H_{67}N_3O_3S_2$: C 74.87, H 7.65, N 4.76; found: C 74.94, H 7.73, N 4.61.

(2.32)

Compounds **2.28** (0.17 g, 0.25 mmol) and **2.19** (0.30 g, 0.52 mmol) were dissolved in anhydrous toluene (5.0 mL), and the content was stirred at room temperature under nitrogen atmosphere for 20 min. Bis(triphenylphosphine)palladium(II) dichloride (0.008 g, 0.013 mmol) was introduced to the flask, and the content stirred overnight at 80 ^oC. Upon completion, the solvent was removed under reduced pressure, and the crude product was purified via flash chromatography (silica gel, 1:9 ethyl acetate:chloroform) to give **2.32** as a green solid (0.15 g, 59%). ^1H NMR (400 MHz, $CDCl_3$) δ 7.60-7.52 (m, 2H), 7.39 (d, J = 6.8 Hz, 1H), 7.33 (t, J = 7.8 Hz, 1H), 7.27 (t, J = 2.4 Hz, 1H), 7.23 (d, J = 4.8 Hz, 1H), 7.17 (t, J = 7.2 Hz, 1H), 7.08 (d, J = 4.8 Hz, 1H), 7.02 (d, J = 8.0 Hz, 1H), 6.98 (d, J = 8.0 Hz, 1H), 6.00 (s, 2H), 4.11 (bs, 2H), 4.00 (bs, 2H), 1.89-1.77 (m, 15H), 1.50-1.10 (m, 38H), 1.10-0.95 (m, 4H), 0.90-0.75 (m, 15H). $^{13}C\{^1H\}$ NMR (100 MHz, $CDCl_3$) δ 182.47, 179.57, 178.94, 169.75, 169.25, 148.92, 147.86, 144.43, 144.24, 143.07, 142.32, 142.21, 142.12, 141.98, 141.68, 135.80, 130.73, 129.91, 127.83, 125.53, 125.35, 125.21, 123.78, 122.38, 199.48, 109.67, 109.18, 86.98, 86.39, 49.36, 49.22, 43.87, 38.46, 35.92, 35.65, 35.60, 34.23, 31.92, 30.33, 29.71, 29.61, 29.55, 29.50, 29.39, 29.34, 28.91, 28.88, 28.86, 27.17, 27.12, 27.10, 26.99, 23.01, 22.70, 21.20, 17.73, 17.67, 14.19, 14.15, 12.05, 10.83. HRMS (MALDI) *m/z*: $[M]^+$ calcd for $C_{64}H_{88}N_2O_2S_2Si$: 1008.6022; found, 1008.6057. Anal. Calcd for $C_{64}H_{88}N_2O_2S_2Si$: C 76.14, H 8.79, N 2.77; found: C 75.88, H 8.55, N 2.82.

(2.33).

N,*N*-Dimethylformamide (0.05 mL, 0.59 mmol) was added into a dry flask and cooled down to 0 ^{o}C. Phosphoryl chloride (0.06 mL, 0.59 mmol) was added dropwise to the flask, and content was stirred at room temperature for 1 hour. After the time elapsed, the reaction temperature was lowered again to 0 ^{o}C, and **2.32** (0.12 g, 0.12 mmol) dissolved in *N*,*N*-dimethylformamide (3.5 mL) was added dropwise. After the addition was complete, the reaction temperature was increased to 70 ^{o}C, and the reaction was stirred at that temperature for 3 h. A saturated sodium acetate solution (10.0 mL) was added to quench the reaction, which was stirred for another 2 h at room temperature. The organic layer was extracted with chloroform, dried over sodium sulfate, and the solvent removed under reduced pressure. The crude product was then purified via flash chromatography (silica gel, 0.5:9.5 ethyl acetate:chloroform) to give the desired product **2.33** (0.10 g, 81%).^{1}H NMR (400 MHz, $CDCl_3$) δ 9.89 (s, 1H), 7.72 (s, 1H), 7.60-7.56 (m, 2H), 7.40 (d, J = 7.6 Hz, 1H), 7.35 (dd, J_1= 7.6 Hz, J_2 = 1.08 Hz, 1H), 7.33 (t, J = 1.8 Hz, 1H), 7.19 (t, J_1 = 7.6 Hz, J_2 = 0.5 Hz, 1H), 7.04 (d, J = 8.0 Hz, 1H), 6.99 (d, J = 8.8 Hz, 1H), 6.02 (s, 1H), 6.00 (s, 1H), 4.13 (broad s, 2H), 3.98 (broad s, 2H), 1.90-1.78 (m, 15H), 1.50-1.10 (m, 38H), 1.1-0.90 (m, 4H), 0.92-0.76 (m, 15H); $^{13}C\{^{1}H\}$ NMR (100 MHz, $CDCl_3$) δ 182.57, 180.45, 178.67, 170.31, 168.76, 158.50, 149.16, 148.80, 146.22, 144.39, 143.28, 143.19, 142.92, 142.53, 142.38, 141.88, 139.78, 135.78, 129.66, 127.88, 125.86, 125.70, 125.53, 124.01, 122.41, 119.75, 109.62, 109.34, 87.15, 86.57, 67.98, 49.51, 49.07, 43.83, 38.56, 35.90, 35.88, 35.67, 35.62, 34.23, 31.92, 30.32, 29.61, 29.54, 29.50, 29.39, 29.34, 28.92, 28.89, 28.85, 27.23, 27.09, 26.93, 22.99, 22.96, 22.70, 17.56, 17.49, 14.16, 12.09, 10.81; HRMS (MALDI) *m/z*: $[M]^+$ calcd for $C_{65}H_{88}N_2O_3S_2Si$: 1036.6020; found, 1036.6006.

(2.34)

Compound **2.29** (0.20 g, 0.28 mmol) was dissolved in dry toluene (5.0 mL) and stirred at room temperature under nitrogen atmosphere for 10 min. Diethylcyanomethylphosphonate (0.1 mL, 0.57 mmol), ammonium carbonate (0.11 g, 1.18 mmol) and propanoic acid (0.5 mL) were added, and the reaction mixture was stirred under nitrogen atmosphere at 100 ^{o}C overnight. Upon reaction completion, the solvents were removed under reduced pressure, and the crude product purified via flash

chromatography (silica gel, 2:8 ethylacetate:chloroform) to give **2.34** as a green sticky solid (0.13 g, 53%). ^{1}H NMR (400 MHz, $CDCl_3$) δ 8.05 (d, J = 20 Hz, 1H), 7.66 (d, J = 4.0 Hz, 1H), 7.64 (dd, J_1 = 8.2 Hz, J_2 = 2.0 Hz, 1H), 7.59 (d, J = 1.6 Hz, 1H), 7.40-7.35 (m, 2H), 7.33 (doublet of triplets, J_1 = 7.6 Hz, J_2 = 1.6 Hz, 1H), 7.18 (dt, J_1 = 7.0 Hz, J_2 = 0.6 Hz, 1H), 7.04 (d, J = 8.0 Hz, 1H), 6.87 (d, J = 8.0 Hz, 1H), 6.02 (s, 1H), 5.97 (s, 1H), 4.22 (m, 4H), 4.10 (m, 2H), 3.94 (m, 2H), 1.83 (s, 6H), 1.79 (s, 6H), 1.45-1.15 (m, 29H), 0.86 (t, J = 8.0 Hz, 3H); ^{13}C{^{1}H} NMR (100 MHz, $CDCl_3$) δ 182.27, 181.65, 178.33, 170.96, 168.13, 153.69, 150.46 (d, $J_{C\text{-}P}$ = 8.0 Hz),143.91, 143.22, 142.42, 141.72, 138.53, 135.47, 135.27, 127.94, 126.71, 124.29, 123.47, 122.42, 120.16, 116.10 (d, $J_{C\text{-}P}$ = 10.0 Hz), 109.55, 94.39, 92.38, 87.45, 86.80, 63.45 (d, $J_{C\text{-}P}$ = 5.0 Hz), 49.67, 48.86, 43.74, 38.66, 31.88, 29.57, 29.51, 29.46, 29.35, 29.31, 27.27, 27.06, 27.01, 26.83, 22.67, 16.30, 16.24, 14.12, 12.13; HRMS (MALDI) *m/z*: $[M]^+$ calcd. for $C_{51}H_{64}N_3O_5PS$: 861.4304; found, 861.4281. Anal. Calcd. for $C_{51}H_{64}N_3O_5PS$: C 71.05, H 7.48, N 4.87, found: C 70.77, H 7.40, N 4.76.

(2.35)

Compound **2.30** (0.24 g, 0.29 mmol) was dissolved in dry toluene (5 mL) and stirred at room temperature under nitrogen atmosphere for 10 min. Diethylcyanomethylphosphonate (0.1 mL, 0.58 mmol), ammonium carbonate (0.11 g, 1.18 mmol) and propanoic acid (0.5 mL) were added and the reaction mixture was stirred under nitrogen atmosphere at 100 ^{o}C overnight. Upon the reaction completion solvents were removed under reduced pressure, and the crude product purified via flash chromatography (silica gel, 1:9 ethyl acetate:chloroform) to give **2.35** as a green sticky solid (0.14 g, 50%). ^{1}H NMR (400 MHz, $CDCl_3$) δ 8.14 (d, J = 20 Hz, 1H), 7.93 (s, 1H), 7.63-7.59 (m, 2H), 7.57 (s, 1H), 7.41 (d, J = 8.6 Hz, 1H), 7.36 (dt, J_1 = 8.6 Hz, J_2 = 0.8 Hz, 1H), 7.21 (t, J = 8 Hz, 1H), 7.06 (d, J = 8 Hz, 1H), 7.02 (d, J = 8 Hz, 1H), 6.04 (s, 1H), 6.00 (s, 1H), 4.25 (m, 4H), 4.14 (m, 2H), 3.98 (m, 2H), 1.87 (6H, s), 1.83 (6H, s), 1.50-1.20 (31H, m), 0.89 (t, J = 6.8 Hz, 1H); ^{13}C{^{1}H} NMR (100 MHz, $CDCl_3$) δ 182.34, 181.09, 178.47, 170.67, 168.38, 150.76 (d, $J_{C\text{-}P}$ = 8.0 Hz), 149.37, 147.12, 143.25, 142.40, 141.78, 141.09, 138.07, 137.04, 136.83, 129.83, 129.08 (d, $J_{C\text{-}P}$ = 12.0 Hz), 127.89, 126.02, 124.16, 122.14, 119.81, 116.07, 109.61, 109.45, 94.39, 92.38, 87.33, 86.17, 67.56, 63.54 (d, $J_{C\text{-}P}$ = 5.0 Hz), 49.60, 48.95, 43.80, 38.62, 31.90, 29.59, 29.51,

29.33, 27.29, 27.07, 26.87, 25.60, 22.68, 16.32, 16.26, 14.13, 12.11; HRMS (MALDI) *m/z*: $[M]^+$ calcd. for $C_{55}H_{64}N_3O_5PS_3$: 973.3746; found, 973.3710. Anal. Calcd for $C_{55}H_{64}N_3O_5PS_3$ (%): C, 67.80; H, 6.62; N, 4.31. Found: C, 68.04; H, 6.87; N, 4.15.

(2.36)

Compound **2.31** (0.10 g, 0.11 mmol) was dissolved in anhydrous toluene (5.0 mL) and stirred at room temperature under a nitrogen atmosphere for 10 min. Diethylcyanomethylphosphonate (0.04 mL, 0.23 mmol), ammonium carbonate (0.04 g, 0.45 mmol) and propanoic acid (0.22 mL) were added, and the reaction mixture was stirred under nitrogen atmosphere at 100 ^oC overnight, after which, the solvents were removed under reduced pressure, and the crude product purified via flash chromatography (silica gel, 1:9 ethyl acetate:chloroform) to give **2.36** as a green sticky solid (0.10 g, 85%). ^1H NMR (400 MHz, $CDCl_3$) δ 8.06 (d, J = 20 Hz, 1H), 7.67 (s, 1H), 7.64-7.56 (m, 2H), 7.40 (d, J = 7.0 Hz, 1H), 7.35 (t, J = 7.4 Hz, 1H), 7.23 (s, 1H), 7.19 (t, J = 7.4 Hz, 1H), 7.05 (d, J = 8.0 Hz, 1H), 7.00 (d, J = 8.6 Hz, 1H), 6.03 (s, 1H), 6.00 (s, 1H), 4.33-4.17 (m, 4H), 4.12 (bs, 2H), 3.99 (bs, 2H), 1.93 (p, J = 7.6 Hz, 2H), 1.87 (6H, s), 1.82 (6H, s), 1.50-1.18 (m, 37H), 0.89 (m, 6H); $^{13}C\{^1H\}$ NMR (100 MHz, $CDCl_3$) δ 182.40, 180.59, 178.46, 170.47, 168.60, 151.44, 149.99, 147.94, 144.46, 143.19, 142.85, 142.41, 141.85, 133.83 (d, $J_{C\text{-}P}$= 19.0 Hz), 130.28, 127.89, 125.82, 124.27, 124.09, 122.42, 119.56, 118.12, 117.15, 113.95, 109.51 (d, $J_{C\text{-}P}$ = 21.0 Hz), 106.05, 90.09, 88.06, 87.23, 86.62, 63.30, 63.27, 49.55, 49.04, 47.56, 43.84, 38.59, 31.91, 31.38, 30.21, 29.59, 29.38, , 27.28, 27.09, 26.91, 26.64, 22.69, 22.50, 16.31, 14.13, 14.02, 12.11. HRMS (MALDI) *m/z*: $[M]^+$ calcd. for $C_{61}H_{77}N_4O_5PS_2$: 1040.5073; found, 1040.5019. Anal. Calcd for $C_{61}H_{77}N_4O_5PS_2$: C 70.35, H 7.45, N 5.38. Found: C 69.95, H 7.30, N 5.06.

(2.37)

Compound **2.33** (0.09 g, 0.09 mmol) was dissolved in dry toluene (2.5 mL) and stirred at room temperature and under a nitrogen atmosphere for 10 min. Diethylcyanomethylphosphonate (0.03 mL, 0.17 mmol), ammonium carbonate (0.03 g, 0.35 mmol) and propanoic acid (0.15 mL) were added and the reaction mixture was stirred under nitrogen atmosphere and 80 ^oC overnight. Upon reaction completion solvents were removed under reduced pressure, and the crude product purified via flash

chromatography (silica gel, 1:9 ethylacetate:chloroform) to give **2.37** as a green sticky solid (0.06 g, 61%). ^{1}H NMR (300 MHz, $CDCl_3$) δ 8.06 (d, J = 20 Hz, 1H), 7.61 (t, J = 2.5 Hz, 1H), 7.57-7.50 (m, 2H), 7.37 (d, J = 7.2 Hz, 1H), 7.32 (dt, J_1 = 7.4 Hz, J_2 = 1.1 Hz, 1H), 7.30 (t, J = 1.4 Hz, 1H), 7.16 (t, J = 7.4 Hz, 1H), 7.02 (d, J = 7.8 Hz, 1H), 6.97 (d, J = 8.7 Hz, 1H), 5.99 (s, 1H), 5.96 (s, 1H), 4.30-4.15 (m, 4H), 4.10 (bs, 2H), 3.96 (bs, 2H), 1.90-1.70 (m, 14H), 1.50-1.10 (m, 44H), 0.99 (m, 5H), 0.90-0.70 (m, 15H); ^{13}C{^{1}H} NMR (75 MHz, $CDCl_3$) δ 182.51, 180.68, 178.79, 170.50, 168.86, 158.90, 150.89, 149.54, 146.21, 143.28, 142.76, 142.53, 142.02, 140.70, 138.10 (d, $J_{C\text{-}P}$ = 16.0 Hz), 129.73, 128.03, 126.11, 125.90, 124.18, 122.56, 119.85, 116.83, 109.80, 109.51, 91.58, 89.95, 87.36, 86.74, 63.47, 49.67, 49.14, 43.99, 38.70, 36.03, 35.80, 32.06, 29.74, 29.49, 29.02, 27.38, 27.24, 27.07, 23.13, 22.84, 17.72, 17.61, 16.44, 14.30, 12.24, 10.95. HRMS (MALDI) *m/z*: $[M]^+$ calcd. for $C_{68}H_{89}N_3O_4S_2Si$: 1195.6455; found, 1195.6349.

(2.4)

Compound **2.31** (0.10 g, 0.11 mmol) and cyanoacetic acid (0.02 g, 0.23 mmol) were introduced into a dry flask. Anhydrous toluene (5.0 mL) and anhydrous piperidine (0.05 mL) were added and the reaction was stirred at 70 ^{o}C for 4.5 hours. Upon completion, the solvent was removed under reduced pressure, and the crude product purified by flash chromatography (silica gel, 50:49:1 dichloromethane:ethyl acetate:acetic acid), and then dissolved in methanol and precipitated from acetonitrile to give **2.4** (60 mg, 60%). ^{1}H NMR (400 MHz, $CDCl_3$) δ 8.30 (s, 1H); 7.74 (s, 1H), 7.61 (s, 2H), 7.41 (d, J = 7.2 Hz, 1H), 7.36 (t, J = 7.8 Hz, 1H), 7.21 (t, J = 7.2 Hz, 2H), 7.07 (d, J = 8.0 Hz, 1H), 7.02 (d, J = 6.00 Hz, 1H), 6.08 (s, 1H), 6.02 (s, 1H), 4.27 (broad s, 2H), 4.17 (bs, 2H), 4.05 (bs, 2H), 1.96 (bs, 2H), 1.88 (s, 6H), 1.83 (s, 6H), 1.50-1.20 (m, 31H), 0.95-0.85 (m, 7H); ^{13}C {^{1}H} NMR (100 MHz, $CDCl_3$) δ 182.90, 178.67, 176.54,170.87, 169.13, 150.42, 148.41, 147.73, 144.94, 143.16, 142.92, 142.49, 141.82, 132.92, 130.29, 127.94, 125.84, 125.35, 124.23, 122.23, 122.43, 119.47, 118.80, 117.67, 114.03, 109.88, 109.56, 106.00, 94.01, 87.30, 86.85, 49.61, 49.13, 47.60, 43.98, 38.77, 31.92, 31.41, 30.25, 29.64, 29.62, 29.58, 29.53, 29.43, 29.38, 27.25, 27.11, 26.84, 26.70, 22.70, 22.53, 14.14, 14.04, 12.15; HRMS (MALDI) *m/z*: $[M]^+$ calcd for $C_{58}H_{68}N_4O_4S_2$: 948.4654; found, 948.4682 Anal. Calcd for $C_{58}H_{68}N_4O_4S_2$: C 73.38, H 7.22, N 5.90, S 6.76. Found: C 73.09, H 7.12, N 5.85, S 6.49.

(2.6)

Compound **2.30** (0.08 g, 0.10 mmol) and cyanoacetic acid (0.02 g, 0.20 mmol) were introduced into an oven-dried flask which was evacuated then filled with nitrogen three times. Anhydrous toluene (5.0 mL) and anhydrous piperidine (0.10 mL) were added, and the reaction was stirred at 70 ^{o}C for 6 h. Upon the reaction completion the solvent was removed under reduced pressure, and the crude product purified by flash chromatography (silica gel, 50:49:1 dichloromethane:ethyl acetate:acetic acid), and then precipitated from a mixture of methanol and acetonitrile to give **2.6** (30 mg, 34%). ^{1}H NMR (400 MHz, $CDCl_3$ + CD_3OD (9:1)) δ 8.29 (s, 1H), 7.90 (s, 1H), 7.56 (s, 2H), 7.49(s, 1H), 7.35 (m, 2H), 7.17 (t, J = 7.2 Hz, 1H), 7.04 (t, J = 7.2 Hz, 1H), 6.99 (m, 1H), 5.99 (s, 1H), 5.95 (s, 1H), 4.10 (m, 2H), 3.97 (m, 2H), 1.79 (s, 6H), 1.75 (s, 6H), 1.50-1.10 (m, 24H), 0.83 (m, 3H); ^{13}C{^{1}H} NMR (100 MHz, $CDCl_3$) δ 183.06, 178.47, 176.11, 171.01, 168.90, 148.21, 146.14, 144.55, 142.88, 142.31, 141.66, 141.08, 136.85, 129.54, 129.14, 127.93, 127.70, 125.85, 124.31, 122.34, 119.64, 118.74, 116.02, 109.76, 109.62, 86.98, 86.50, 43.78, 38.67, 31.82, 30.52, 29.60, 29.52, 29.33, 29.24, 27.03, 26.94, 26.63, 24.26, 22.59, 13.97, 11.93 (some peaks are missing due to low solubility of the dye). HRMS (MALDI) *m/z*: $[M]^+$ calcd for $C_{52}H_{55}N_3O_4S_3$: 881.3355; found, 881.3252. Anal. Calcd for $C_{52}H_{55}N_3O_4S_3.H_2O$: C 69.38, H 6.38, N 4.67; found: C 69.17, H 6.19, N 4.44.

(2.8)

Compound **2.33** (0.034 g, 0.032 mmol) was dissolved in dry toluene (2.5 mL) and stirred at room temperature and under a nitrogen atmosphere for 10 min. Cyanoacetic acid (0.006 g, 0.065 mmol), ammonium carbonate (0.013 g, 0.131 mmol) and propanoic acid (0.06 mL) were added and the reaction mixture was stirred under nitrogen atmosphere at 100 ^{o}C overnight. Upon completion, the organic layer was extracted from dichloromethane, dried over sodium sulfate, and evaporated to get the crude product which was dissolved in dichloromethane and precipitated from to give **2.8** as a dark green solid (0.025 g, 70%).^{1}H NMR (400 MHz, $CDCl_3$) δ 8.40 (s, 1H);, 7.77 (s, 1H), 7.59 (m, 2H), 7.41(d, J = 7.4 Hz, 1H), 7.39-7.33 (m, 2H), 7.21 (t, J = 7.8 Hz, 1H), 7.06 (d, J = 8.0 Hz, 1H), 7.02 (d, J = 8.8 Hz, 1H), 6.09 (s, 1H), 6.03 (s, 1H), 4.17 (m, 2H), 4.04 (m, 2H), 1.87 (s, 6H), 1.83 (s, 6H), 1.50-1.00 (m, 46H), 0.90-0.75 (m, 15H); ^{13}C{^{1}H} NMR (100

MHz, $CDCl_3$ + CD_3OD (9:1)) δ 182.91, 178.55, 176.71, 170.69, 169.05, 165.26, 159.55, 149.64, 149.52, 146.74, 146.15, 143.48, 143.04, 142.56, 142.32, 141.76, 141.36, 137.07, 129.67, 127.91, 126.03, 125.82, 124.17, 122.36, 119.65, 117.20, 109.83, 109.50, 87.02, 86.47, 43.85, 38.63, 35.85, 35.81, 35.62, 33.57, 31.86, 29.56, 29.50, 29.45, 29.36, 29.29, 29.28, 28.85, 28.83, 28.80, 28.78, 27.07, 26.99, 26.73, 22.92, 22.91, 22.90, 22.63, 17.51, 17.40, 14.07, 11.98, 10.72; HRMS (MALDI) *m/z*: $[M]^+$ calcd. for $C_{68}H_{89}N_3O_4S_2Si$: 1103.6064; found, 1103.6073. Anal. Calcd for $C_{68}H_{89}N_3O_4S_2Si.H_2O$: C 72.75; H 8.17; N 3.74. Found: C 73.18; H 8.08; N 3.90.

(2.3)

Compound **2.34** (0.09 g, 0.10 mmol) was introduced into a flask, which was pump-filled with nitrogen gas three times. Dichloroethane (3.0 mL) was added and the solution was stirred for 10 min at room temperature; bromotrimethylsilane (0.13 mL, 1.02 mmol) was added and the reaction was stirred at 75 ^oC overnight. Methanol (4.0 mL) and water (6.0 mL) were added to quench the reaction, and after stirring for 1 h while cooling down to room temperature, the organic layer was extracted from dichloromethane, dried over sodium sulfate, and solvent evaporated under reduced pressure to get the crude product which was precipitated from a mixture of dichloromethane and hexanes, filtered and washed with hexanes (150 mL) and acetonitrile (30 mL) to give **2.3** as a dark green solid (0.07 g, 85%).^{1}H NMR (400 MHz, $CDCl_3$ + CD_3OD (9:1)) δ 7.91 (s, 1H), 7.52 (m, 3H), 7.37 (d, J = 7.6 Hz, 1H), 7.32 (t, J = 8.0 Hz, 1H), 7.20 (m, 1H), 7.17 (t, J = 7.2 Hz, 1H), 7.03 (d, J = 8.2 Hz, 1H), 6.91 (d, J = 7.2 Hz, 1H), 6.00 (s, 1H), 5.96 (s, 1H), 4.10 (m, 2H), 3.94 (m, 2H), 1.85-1.70 (bs, 14H);, 1.45-1.10 (m, 23H), 0.85 (t, J = 7.2 Hz, 3H); $^{13}C\{^1H\}$ NMR (100 MHz, $CDCl_3$) δ 182.80, 179.27, 176.87, 170.88, 168.82, 150.09, 144.87, 143.11, 142.99, 142.36, 141.72, 136.89 (d, $J_{C\text{-}P}$ = 16.0 Hz), 136.14, 136.97, 136.81, 136.14, 128.83, 127.91, 126.29, 124.24, 123.13, 122.37, 119.95, 118.95 (d, $J_{C\text{-}P}$ = 7.0 Hz), 109.55, 87.10, 86.60, 49.54, 43.80, 38.67, 34.90, 31.85, 29.56, 29.55, 29.50, 29.47, 29.37, 29.27, 27.08, 27.05, 27.00, 26.72, 22.62, 14.04, 12.00; $^{31}P\{^1H\}$ NMR (161.91 MHz, $CDCl_3$): δ 6.96 (s); HRMS (MALDI) *m/z*: $[M]^+$ calcd. for $C_{47}H_{56}N_3O_5PS$: 805.3664; found, 805.3678.

(2.5)

Compound **2.36** (0.06 g, 0.06 mmol), was introduced into a flask, which was pump-filled with nitrogen gas three times. Dichloroethane (5.0 mL) was added, the solution was stirred for 10 min at room temperature, after which bromotrimethylsilane (0.07 mL, 0.56 mmol) was added, and the reaction was stirred at 80 ^{o}C for 2 h. Methanol (4.0 mL) and water (6.0 mL) were added to quench the reaction, and after stirring for an hour while cooling down to room temperature, the organic layer was extracted from dichloromethane, dried over sodium sulfate, and solvent evaporated under reduced pressure to get the crude product which was precipitated from a mixture of dichloromethane and hexanes, filtered and washed with hexanes (150 mL) and acetonitrile (30 mL) to give **2.5** as a dark green solid (0.05 g, 93%).^{1}H NMR (400 MHz, $CDCl_3$ + CD_3OD (9:1)) δ 7.94 (s, 1H), 7.55-7.44 (m, 3H), 7.38-7.29 (m, 2H), 7.16 (t, J = 7.6 Hz, 1H), 7.22 (s, 1H), 7.03 (d, J = 8.0 Hz, 1H), 6.91 (d, J = 7.8 Hz, 1H)), 6.00 (s, 1H), 5.96 (s, 1H), 4.12 (m, 2H), 3.98 (m, 2H), 1.85 (m, 2H), 1.78 (s, 6H), 1.75 (s, 6H), 1.46-1.16 (m, 33H), 0.85 (t, J = 6.6 Hz, 6H); $^{13}C\{^{1}H\}$ NMR (100 MHz, $CDCl_3$ + CD_3OD (9:1)) δ 182.85, 177.41, 175.54, 170.81, 169.12, 149.12, 148.59, 146.56, 144.06, 143.01, 142.37 (d, $J_{C\text{-}P}$ = 8.0 Hz), 141.71, 134.47, 134.29, 130.66, 127.93, 125.54, 124.24, 122.57, 122.35, 119.28, 118.05, 113.72, 109.66 (d, $J_{C\text{-}P}$ = 17.0 Hz), 106.09, 87.02, 86.52, 47,40, 43.85, 38.71, 31.85, 31.34, 30.19, 29.57, 29.55, 29.54, 29.51, 29.46, 29.38, 29.29, 29.28, 27.10, 27.04, 26.97, 26.68, 26.60, 22.62, 22.46, 14.03, 13.93, 11.99; $^{31}P\{^{1}H\}$ NMR (161.91 MHz, $CDCl_3$) δ 10.58 (s). HRMS (MALDI) *m/z*: $[M]^+$ calcd. for $C_{57}H_{69}N_4O_5PS_2$: 984.4414; found, 984.4447.

(2.7)

Compound **2.35** (0.07 g, 0.07 mmol) was introduced into a flask, which was pump-filled with nitrogen gas three times. Dichloroethane (7.0 mL) was added, the solution was stirred for 10 min at room temperature; a bromotrimethylsilane (0.28 mL, 2.20 mmol) was added, and the reaction was stirred at 75 ^{o}C for 4 h. Methanol (6.0 mL) and water (9.0 mL) were added to quench the reaction, and after stirring for 1 h while cooling down to room temperature, the organic layer was extracted from dichloromethane, dried over sodium sulfate, and solvent evaporated under reduced pressure to get the crude product which was precipitated from a mixture of

dichloromethane and hexanes to give **2.7** as a dark green solid (30 mg, 50%).^{1}H NMR (400 MHz, $CDCl_3$ + CD_3OD (9:1)) δ 7.98 (bs, 1H), 7.78 (bs, 1H), 7.46-7.30 (m, 5H), 7.18 (bs, 1H), 7.06 (bs, 1H), 6.90 (bs, 1H), 5.99 (bs, 2H), 4.12 (bs, 2H), 3.97 (bs, 2H), 1.75 (s, 12H), 1.45-1.10 (23H, m), 0.83 (t, J = 7.0 Hz, 3H); $^{13}C\{^{1}H\}$ NMR (100 MHz, $CDCl_3$ + CD_3OD (9:1), δ): 182.49, 171.34, 169.38, 148.12, 147.31, 146.16, 148.12, 147.31, 146.16, 143.02, 142.63, 142.42, 141.62, 140.81, 137.51, 136.47, 129.57, 128.99, 128.83, 128.00, 125.67, 124.51, 122.38, 119.30, 117.24, 115.92, 109.82, 86.87, 43.90, 38.91, 31.86, 29.57, 29.54, 29.48, 29.39, 29.30, 27.13, 26.96, 26.59, 22.63, 14.06, 12.08; $^{31}P\{^{1}H\}$ NMR (161.91 MHz, $CDCl_3$) δ 8.97 (s). HRMS (MALDI) *m/z*: $[M]^+$ calcd for $C_{51}H_{56}N_3O_5PS_3$: 917.3120; found, 917.3078. Anal. Calcd for $C_{51}H_{56}N_3O_5PS_3.H_2O$; C 65.43, H 6.24, N 4.49; found: C 65.20, H 6.13, N 4.53.

(2.9)

Compound **2.37** (0.05 g, 0.04 mmol) was introduced into a flask and pump-filled with nitrogen gas three times. Dichloroethane (5.0 mL) was added and the solution was stirred for 10 min at room temperature, after which bromotrimethylsilane (0.06 mL, 0.42 mmol) was added and the reaction was stirred at 80 ^{o}C for 2 h. Methanol (4.2 mL) and water (6.4 mL) were added to quench the reaction, and after stirring for an hour while cooling down to room temperature, the organic layer was extracted from dichloromethane, dried over sodium sulfate, and solvent evaporated under reduced pressure to get the crude product which was precipitated from a mixture of dichloromethane and hexanes, filtered and washed with hexanes (150 mL) and acetonitrile (30 mL) to give **2.9** as a dark green solid (0.04 g, 85%).^{1}H NMR (400 MHz, $CDCl_3$ + CD_3OD (9:1)) δ 7.92 (d, J = 20 Hz, 1H), 7.57-7.51 (m, 3H), 7.36 (d, J = 8.0 Hz, 1H), 7.34-7.30 (m, 2H), 7.17 (t, J = 7.0 Hz, 1H), 7.05 (d, J = 8.0 Hz, 1H), 6.70 (d, J = 8.0 Hz, 1H), 6.06 (s, 1H), 5.98 (s, 1H), 4.12 (bs, 2H), 4.01 (bs, 2H), 1.81-1.72 (m, 2H), 1.79 (s, 6H), 1.73 (s, 6H), 1.45-1.05 (m, 40 H), 1.03-0.97 (m, 4H), 0.89-0.74 (m, 16H); $^{13}C\{^{1}H\}$ NMR (100 MHz, $CDCl_3$ + CD_3OD (9:1)): δ 181.95, 171.34, 169.88, 157.23, 148.70, 148.41, 147.81, 146.42, 143.09, 142.95, 142.80, 142.40, 142.17, 141.60, 139.60, 138.45 (d, $J_{C\text{-}P}$ = 19 Hz) , 138.25, 130.27, 128.03, 125.96, 125.90, 124.54, 122.36, 119.58, 117.35, 110.14, 109.83, 86.92, 44.07, 38.98, 35.86, 35.80, 35.60, 35.57, 31.86, 29.56, 29.50, 29.44, 29.36, 29.28, 28.81, 28.79, 27.16, 26.95, 26.93, 26.88, 26.55, 22.92,

22.91, 22.89, 22.63, 17.54, 17.41, 14.06, 14.04, 12.11, 10.70, 10.69; $^{31}P\{^{1}H\}$ NMR (161.91 MHz, $CDCl_3$, δ): 10.64 (s). HRMS (MALDI) *m/z*: $[M]^+$ calcd. for $C_{67}H_{90}N_3O_5PS_2Si$: 1139.5829; found, 1139.5804.

2.4.2 Optical and electrochemical measurements

Electronic spectroscopic data were collected in ethanol on a UV-Vis-NIR spectra in 1 cm quartz cuvette using a Agilent Cary 5000 spectrophotometer, and emission spectra were collected using a Horiba Jobin Yvon Fluorolog-3 equipped with an iHR320 monochrometer, and a CCD detector. Electrochemical measurements were carried out under an inert atmosphere in dry deoxygenated tetrahydrofuran solution containing 0.1 M tetrabutylammonium hexafluorophosphate as electrolyte. A CH-Instrument 620D potentiostat equipped with a conventional three-electrode cell utilizing a glassy carbon working electrode, platinum wire counter electrode, and a silver wire coated with silver chloride as the pseudo-reference electrode, was used for the measurements. Potentials were referenced to the ferrocenium/ferrocene ($FeCp_2^{+/0}$) using decamethyferrocenium/ decamethylferrocene ($FeCp_2^{*+/0}$ was determined to be -0.46 V vs. $FeCp_2^{+/0}$in THF) then to NHE scale ($FeCp_2^{+/0}$ +0.80 V vs. NHE).[49] Cyclic voltamograms were recorded at a scan rate of 50 mV s^{-1}.

2.4.3 High performance liquid chromatography

High performance liquid chromatography (HPLC) traces of the dyes were collected on a Shimadzu Class-VP series HPLC system equipped with a SCL-10A system controller, a SPD-10AV UV-Vis detector, a SPD-M10A diode array detector, and a Chromegabond WR C18 5µ, 120Å, 150 × 4.6 mm column. The mobile phase adapted for the measurements was a 5mM piperidine in methanol solution with a varying percentage of water (10 to 20 %) depending on the nature of the dye. The spectra are shown in the appendix.

2.4.4 Effect of CDCA addition on solar cell performance

Table 2.5 Photovoltaic parameters of photovoltaic devices with **2.8** and **2.9** with different CDCA:dye ratio.

Dye	CDCA:dye ratio	V_{OC} (V)	J_{SC} (mA/cm^2)	FF(%)	PCE (%)
2.8	200	0.68 ± 0.01	19.1 ± 0.2	68 ± 1	8.9 ± 0.2
	100	0.67 ± 0.01	18.6 ± 0.5	69 ± 1	8.6 ± 0.2
	0	0.67 ± 0.01	14.1 ± 0.1	72 ± 1	6.8 ± 0.0
2.9	200	0.68 ± 0.02	10.4 ± 0.2	71 ± 1	5.0 ± 0.1
	100	0.65 ± 0.02	5.1 ± 0.6	72 ± 2	2.6 ± 0.2
	0	0.66 ± 0.01	4.5 ± 0.1	73 ± 1	2.2 ± 0.1

2.5 REFERENCES

(1) Yao, Z.; Zhang, M.; Wu, H.; Yang, L.; Li, R.; Wang, P. *J. Am. Chem. Soc.* **2015**, *137*, 3799.

(2) Mathew, S.; Yella, A.; Gao, P.; Humphry-Baker, R.; CurchodBasile, F. E.; Ashari-Astani, N.; Tavernelli, I.; Rothlisberger, U.; Nazeeruddin Md, K.; Grätzel, M. *Nat Chem* **2014**, *6*, 242.

(3) Tanaka, M.; Hayashi, S.; Eu, S.; Umeyama, T.; Matano, Y.; Imahori, H. *Chem. Commun.* **2007**, 2069.

(4) Jiang, W.; Qian, H.; Li, Y.; Wang, Z. *J. Org. Chem.* **2008**, *73*, 7369.

(5) Hara, K.; Wang, Z. S.; Sato, T.; Furube, A.; Katoh, R.; Sugihara, H.; Dan-Oh, Y.; Kasada, C.; Shinpo, A.; Suga, S. *J. Phys. Chem. B* **2005**, *109*, 15476.

(6) Green, M. A.; Emery, K.; Hishikawa, Y.; Warta, W.; Dunlop, E. D. *Prog. Photovolt. Res. Appl.* **2016**, *24*, 3.

(7) Beverina, L.; Salice, P. *Eur. J. Org. Chem.* **2010**, 1207.

(8) Tatay, S.; Haque, S. A.; O'Regan, B.; Durrant, J. R.; Verhees, W. J. H.; Kroon, J. M.; Vidal-Ferran, A.; Gavina, P.; Palomares, E. *J. Mater. Chem.* **2007**, *17*, 3037.

(9) Paek, S.; Choi, H.; Kim, C.; Cho, N.; So, S.; Song, K.; Nazeeruddin, M. K.; Ko, J. *Chem. Commun. (Cambridge, U. K.)* **2011**, *47*, 2874.

(10) Li, J. Y.; Chen, C. Y.; Lee, C. P.; Chen, S. C.; Lin, T. H.; Tsai, H. H.; Ho, K. C.; Wu, C. G. *Org. Lett.* **2010**, *12*, 5454.

(11) Yen, Y.-S.; Chou, H.-H.; Chen, Y.-C.; Hsu, C.-Y.; Lin, J. T. *J. Mater. Chem.* **2012**, *22*, 8734.

(12) Shi, Y.; Hill, R. B. M.; Yum, J.-H.; Dualeh, A.; Barlow, S.; Grätzel, M.; Marder, S. R.; Nazeeruddin, M. K. *Angew. Chem., Int. Ed.* **2011**, *50*, 6619.

(13) Delcamp, J. H.; Shi, Y.; Yum, J.-H.; Sajoto, T.; Dell'Orto, E.; Barlow, S.; Nazeeruddin, M. K.; Marder, S. R.; Grätzel, M. *Chem.--Eur. J.* **2013**, *19*, 1819.

(14) Yum, J.-H.; Walter, P.; Huber, S.; Rentsch, D.; Geiger, T.; Nüesch, F.; De Angelis, F.; Grätzel, M.; Nazeeruddin, M. K. *J. Am. Chem. Soc.* **2007**, *129*, 10320.

(15) Geiger, T.; Kuster, S.; Yum, J.-H.; Moon, S.-J.; Nazeeruddin, M. K.; Grätzel, M.; Nüesch, F. *Adv. Funct. Mater.* **2009**, *19*, 2720.

(16) Qin, C.; Numata, Y.; Zhang, S.; Yang, X.; Islam, A.; Zhang, K.; Chen, H.; Han, L. *Adv. Funct. Mater.* **2014**, *24*, 3059.

(17) Qin, C.; Numata, Y.; Zhang, S.; Islam, A.; Yang, X.; Sodeyama, K.; Tateyama, Y.; Han, L. *Adv. Funct. Mater.* **2013**, *23*, 3782.

(18) Mishra, A.; Fischer, M. K. R.; Bäuerle, P. *Angew. Chem., Int. Ed.* **2009**, *48*, 2474.

(19) Hagfeldt, A.; Boschloo, G.; Sun, L.; Kloo, L.; Pettersson, H. *Chem. Rev.* **2010**, *110*, 6595.

(20) Jones, G. In *Organic Reactions*; John Wiley & Sons, Inc.: 2004.

(21) Galoppini, E. *Coord. Chem. Rev.* **2004**, *248*, 1283.

(22) Brennan, B. J.; Llansola Portoles, M. J.; Liddell, P. A.; Moore, T. A.; Moore, A. L.; Gust, D. *Phys. Chem. Chem. Phys.* **2013**, *15*, 16605.

(23) Wiberg, J.; Marinado, T.; Hagberg, D. P.; Sun, L.; Hagfeldt, A.; Albinsson, B. *J. Phys. Chem. C* **2009**, *113*, 3881.

(24) Murakami, T. N.; Yoshida, E.; Koumura, N. *Electrochim. Acta* **2014**, *131*, 174.

(25) Gundlach, L.; Szarko, J.; Socaciu-Siebert, L. D.; Neubauer, A.; Ernstorfer, R.; Willig, F. *Phys. Rev. B: Condens. Matter Mater. Phys.* **2007**, *75*, 125320.

(26) Pechy, P.; Rotzinger, F. P.; Nazeeruddin, M. K.; Kohle, O.; Zakeeruddin, S. M.; Humphry-Baker, R.; Gratzel, M. *J. Chem. Soc., Chem. Commun.* **1995**, 65.

(27) Hanson, K.; Brennaman, M. K.; Luo, H.; Glasson, C. R.; Concepcion, J. J.; Song, W.; Meyer, T. J. *ACS Appl. Mater. Interfaces* **2012**, *4*, 1462.

(28) Guerrero, G.; Alauzun, J. G.; Granier, M.; Laurencin, D.; Mutin, P. H. *Dalton Trans.* **2013**, *42*, 12569.

(29) Mulhern, K. R.; Orchard, A.; Watson, D. F.; Detty, M. R. *Langmuir* **2012**, *28*, 7071.

(30) Wang, P.; Klein, C.; Moser, J.-E.; Humphry-Baker, R.; Cevey-Ha, N.-L.; Charvet, R.; Comte, P.; Zakeeruddin, S. M.; Grätzel, M. *J. Phys. Chem. B* **2004**, *108*, 17553.

(31) Stalder, R.; Xie, D.; Islam, A.; Han, L.; Reynolds, J. R.; Schanze, K. S. *ACS Appl. Mater. Interfaces* **2014**, *6*, 8715.

(32) Evenson, S. J.; Rasmussen, S. C. *Org. Lett.* **2010**, *12*, 4054.

(33) Koeckelberghs, G.; De Cremer, L.; Vanormelingen, W.; Dehaen, W.; Verbiest, T.; Persoons, A.; Samyn, C. *Tetrahedron* **2005**, *61*, 687.

(34) Polander, L. E.; Yella, A.; Teuscher, J.; Humphry-Baker, R.; Curchod, B. F. E.; Ashari Astani, N.; Gao, P.; Moser, J.-E.; Tavernelli, I.; Rothlisberger, U.; Grätzel, M.; Nazeeruddin, M. K.; Frey, J. *Chem. Mater.* **2013**, *25*, 2642.

(35) Roschangar, F.; Brown, J. C.; Cooley Jr, B. E.; Sharp, M. J.; Matsuoka, R. T. *Tetrahedron* **2002**, *58*, 1657.

(36) Getmanenko, Y. A.; Tongwa, P.; Timofeeva, T. V.; Marder, S. R. *Org. Lett.* **2010**, *12*, 2136.

(37) Huo, L.; Chen, H.-Y.; Hou, J.; Chen, T. L.; Yang, Y. *Chem. Commun. (Cambridge, U. K.)* **2009**, 5570.

(38) Peng, W.; Wangdong, Z.; Mingfei, X.; Yu, B.; Jing, Z.; Changchun Institute of Applied Chemistry, C. A. o. S., Ed. China, **2009**.

(39) Subramaniyan, S.; Xin, H.; Kim, F. S.; Jenekhe, S. A. *Macromolecules* **2011**, *44*, 6245.

(40) Shi, Y.; Hill, R. B. M.; Yum, J.-H.; Dualeh, A.; Barlow, S.; Grätzel, M.; Marder, S. R.; Nazeeruddin, M. K. *Angew. Chem.* **2011**, *123*, 6749.

(41) Lindsey, J. S.; Brown, P. A.; Siesel, D. A. *Tetrahedron* **1989**, *45*, 4845.

(42) Fischer, E.; Jourdan, F. *Ber. Dtsch. Chem. Ges.* **1883**, *16*, 2241.

(43) Scherer, D.; Dörfler, R.; Feldner, A.; Vogtmann, T.; Schwoerer, M.; Lawrentz, U.; Grahn, W.; Lambert, C. *Chem. Phys.* **2002**, *279*, 179.

(44) Polander, L. E.; Pandey, L.; Barlow, S.; Tiwari, S. P.; Risko, C.; Kippelen, B.; Brédas, J.-L.; Marder, S. R. *J. Phys. Chem. C* **2011**, *115*, 23149.

(45) Hagfeldt, A.; Gratzel, M. *Chem. Rev.* **1995**, *95*, 49.

(46) Kalyanasundaram, K.; Gratzel, M. *Coord. Chem. Rev.* **1998**, *177*, 347.

(47) de Miguel, G.; Marchena, M.; Cohen, B.; Pandey, S.; Hayase, S.; Douhal, A. *J. Phys. Chem. C* **2012**, *116*, 22157.

(48) Boschloo, G.; Hagfeldt, A. *Acc. Chem. Res.* **2009**, *42*, 1819.

(49) Connelly, N. G.; Geiger, W. E. *Chem. Rev. (Washington, DC, U. S.)* **1996**, *96*, 877.

(50) Delcamp, J. H.; Shi, Y.; Yum, J. H.; Sajoto, T.; Dell'Orto, E.; Barlow, S.; Nazeeruddin, M. K.; Marder, S. R.; Grätzel, M. *Chem--Eur. J.* **2013**, *19*, 1819.

(51) Herndon, W. C. *J. Chem. Educ.* **1967**, *44*, 724.

(52) Chen, M.; Gratzel, M.; Thomas, J. K. *J. Am. Chem. Soc.* **1975**, *97*, 2052.

(53) Kay, A.; Graetzel, M. *J. Phys. Chem.* **1993**, *97*, 6272.

(54) de Miguel, G.; Marchena, M.; Ziolek, M.; Pandey, S. S.; Hayase, S.; Douhal, A. *J. Phys. Chem. C* **2012**, *116*, 12137.

(55) de Miguel, G.; Ziolek, M.; Zitnan, M.; Organero, J. A.; Pandey, S. S.; Hayase, S.; Douhal, A. *J. Phys. Chem. C* **2012**, *116*, 9379.

(56) Zhang, L.; Cole, J. M. *ACS Appl. Mater. Interfaces* **2015**, *7*, 3427.

(57) Snaith, H. J. *Energy Environ. Sci.* **2012**, *5*, 6513.

(58) Yang, X.; Yanagida, M.; Han, L. *Energy Environ. Sci.* **2013**, *6*, 54.

(59) Vargas, W. E. *J. Appl. Phys.* **2000**, *88*, 4079.

(60) Koo, H.-J.; Park, J.; Yoo, B.; Yoo, K.; Kim, K.; Park, N.-G. *Inorg. Chim. Acta* **2008**, *361*, 677.

(61) Gilheany, D. G. *Chem. Rev.* **1994**, *94*, 1339.

(62) Brown, D. G.; Schauer, P. A.; Borau-Garcia, J.; Fancy, B. R.; Berlinguette, C. P. *J. Am. Chem. Soc.* **2013**, *135*, 1692.

(63) DeFord, J.; Chu, F.; Anslyn, E. V. *Tetrahedron Lett.* **1996**, *37*, 1925.

(64) Faucon, A.; Lenk, R.; Hemez, J.; Gautron, E.; Jacquemin, D.; Le Questel, J.-Y.; Graton, J.; Brosseau, A.; Ishow, E. *Phys. Chem. Chem. Phys.* **2013**, *15*, 12748.

(65) Peppard, D. F.; Ferraro, J. R.; Mason, G. W. *J. Inorg. Nucl. Chem.* **1958**, *7*, 231.

(66) Koide, N.; Islam, A.; Chiba, Y.; Han, L. Y. *J. Photochem. Photobiol., A* **2006**, *182*, 296.

(67) Fabregat-Santiago, F.; Garcia-Belmonte, G.; Mora-Sero, I.; Bisquert, J. *Phys. Chem. Chem. Phys.* **2011**, *13*, 9083.

(68) Pei, K.; Wu, Y. Z.; Islam, A.; Zhang, Q.; Han, L. Y.; Tian, H.; Zhu, W. H. *ACS Appl. Mater. Interfaces* **2013**, *5*, 4986.

CHAPTER 3 MULTI-CHROMOHPORIC SENSITIZERS FOR PANCHROMATIC ABSORPTION FOR DYE SENSITIZED SOLAR CELLS

3.1 INTRODUCTION

Early panchromatic (by definition panchromatic means: sensitive to light of all colors in the visible spectrum,[1] but in the context of this chapter it will also refer to the ability to absorb near infra-red light up to 940 nm) sensitizers were ruthenium-based,[2] and achieved J_{SC} on the order of 20 $mAcm^{-2}$, with an absorption onset at around 900 nm and an incident photon-to-current conversion efficiency (IPCE) with a maximum of ~80%. However due to the low molar absorptivities of these classes of dyes, the toxicity and scarceness of ruthenium, organic chromophores have been pursued as an alternative.

Organic chromophores may have molar absorptivities (50,000-500,000 $M^{-1}cm^{-1}$) one to two orders-of-magnitude higher than typical ruthenium complexes used in DSSCs because of the large transition dipole moments assigned largely as π-π* transitions that describe the excitation between the ground and typically lowest lying excited state. However, these strong transitions are also often narrow, which is not compatible with achieving panchromaticity. Several approaches to increase the panchromaticity of organic dyes has been investigated including: (1) co-sensitization with chromophores having complementary absorption profiles;[3,4] (2) the use of energy relay dyes that transfer energy from unattached highly photoluminescent chromophores in the electrolytes (that absorb high energy photons) to tethered sensitizers (that absorb low energy photons);[5] (3) the use of light harvesting antennae linked to chromophores, mimicking biomolecules;[6,7] and (4) the use of covalently linked bichromophoric,[8,9] and even trichromophoric, sensitizers,[10] with complementary absorption profiles to achieve increased J_{SC}. Among the above mentioned examples, the very first approach, co-sensitization with complementary chromophores, has proven to be the most successful, and PCEs above 11% have been reported for multiple systems.[11-13]

In one recent example, Kakiage *et al.*[13] reported PCEs higher than 12%, for a DSSC utilizing a carbazole/oligothiophene sensitizer (**3.1**) and a coumarin sensitizer (**3.2**) as co-absorbers, Figure 3.1. The success of this system lies in its impressive IPCE, which has an onset at around 800 nm and reaches the higher than 80% at around 650 nm and which is maintained until around 450 nm, giving rise to a J_{SC} ca. 16 mAcm^{-2}. Even though an impressive PCE is achieved, the reported J_{SC} was still considerably lower than the 33 mAcm^{-2} theoretically achievable in a DSSC, which could be ascribed to the lack of efficient absorption beyond 650 nm in this system. Pursuing higher photocurrents necessitates that red to near infra-red light be absorbed efficiently, something that can be attained with the use of near infra-red absorbing sensitizers either as co-absorbers, in a manner which is similar to the example given, or on their own if they can be engineered to also absorb high energy photons, an ability that they often lack.

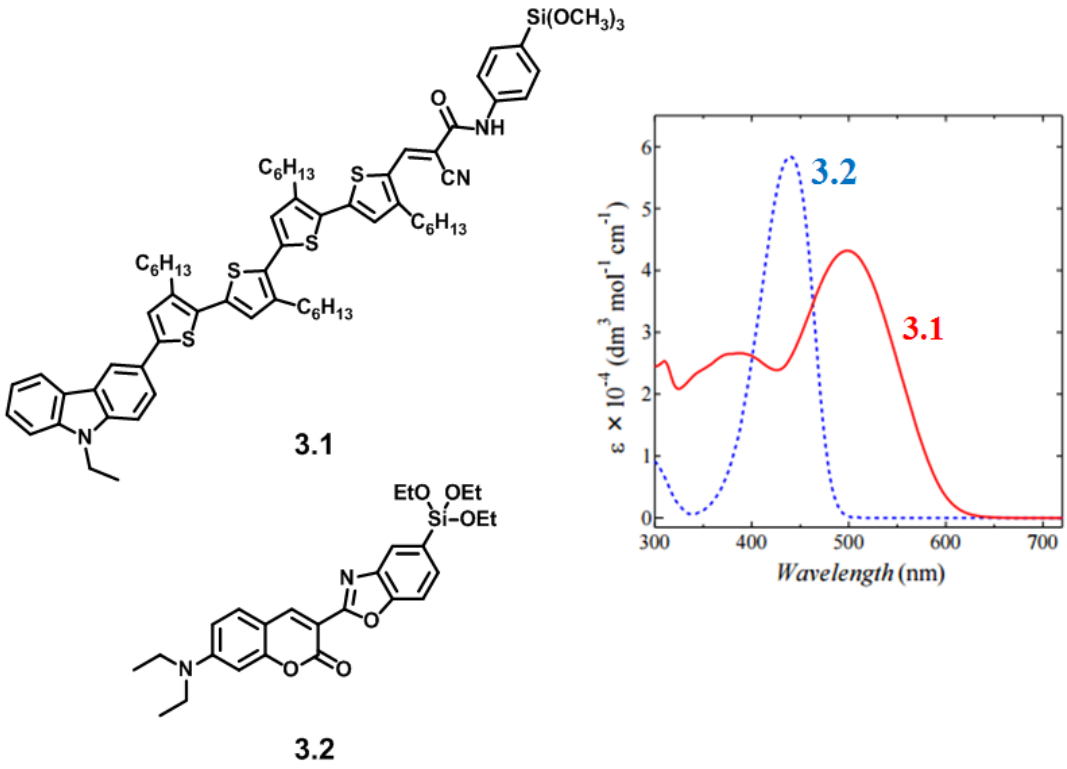

Figure 3.1 Molecular structure of the sensitizers **3.1** and **3.2** along with their respective absorption profiles in solution.

Squaraines,[14,15] and related classes of dyes such as cyanines[16] and phthalocyanines,[17] have been the subject of considerable research in the DSSC

community as they have the ability to absorb photons that are inaccessible to many other classes of sensitizers. Squaraines have high molar extinction coefficients on the order of 10^5 $M^{-1}cm^{-1}$ between 600 to 650 nm, and have the potential to act as promising building blocks toward panchromatic absorption if (1) absorption at higher energy can be achieved, and (2) if their main absorption band can be further red-shifted. Advancements on both fronts have been reported for squaraine-based dyes;[18] high-energy absorption bands have been introduced via the incorporation of bridges between the squaraine and anchoring group,[4,14] donors on the opposite end of the squaraine relative to the anchoring group,[19] or in multichromophoric systems.[8,10] On the other hand, red-shifting the main squaraine absorption band has been achieved through enhancing their charge transfer characteristics as shown in Figure 1.11and reported by Yagi *et al.*, where absorption onsets in the near infra-red (ca. 900 nm) were attained.[20]

In this chapter, an attempt towards increasing both the panchromaticity and near infra-red absorption of squaraine dyes is presented, in which an asymmetric bichromophoric (Por)-(Sq) sensitizer that links a porphyrin chromophore to a squaraine chromophore via an acetylene bridge is designed, synthesized and tested. Porphyrins are well situated to provide increased panchromaticity in squaraine-based dyes due to their absorption profile, which complements that of squaraines; porphyrins typically possess a sharp Soret band (ε ca. 10^5 $M^{-1}cm^{-1}$) between 400 and 450 nm and up to four Q bands (ε ca. 10^4 M^{-1} cm^{-1}) between 500 to 700 nm.[21] In addition, the extended conjugation that results from the covalent linkage of the two π-systems has the potential to red-shift the squaraine-based absorption by around 100 nm into the near infra-red as has been demonstrated with similar a (Por)-(Sq)-(Por) two-photon absorbing chromophore.[10] All of this can potentially be achieved without compromising the unidirectional electron flow (after photoexcitation) from the porphyrin to the squaraine,[21] which in the case of DSSCs, presumably results in charge injection into TiO_2 via proper positioning of a cyanoacrylic (CA) anchoring group on the squaraine moiety of a bichromophoric (Por)-(Sq) system.

The structures of the four (Por)-(Sq) dyes discussed in the chapter are shown in Figure 3.2. The porphyrin and the squaraine are conjugated through an acetylene, and the squaraine and CA anchoring groups are π-bridged by either thiophene (T) (**3.3**, **3.4** and

3.5) or 4,4-bis(2-ethylhexyl)-4*H*-silolo[3,2-*b*:4,5-*b′*]dithiophene (DTS) (**3.6**) units. Alkyl chains of varying length (ethyl and dodecyl) have been introduced on the indoline portion of the squaraine units along with *tert*-butyl and trihexylsilyl groups on the *meta* positions of the *meso* phenyl rings of the porphyrin to decrease aggregation in squaraines and porphyrins, respectively, both of which groups are known to heavily aggregate when deposited on TiO_2 surfaces.[4,22,23] Additionally, 2-ethylhexyl (EtHex) groups are present in the DTS π-bridge; these were shown in Chapter 2 (compound **3.41** in Figure 3.2) both to decrease aggregation and to decrease charge recombination between the electrolyte and TiO_2 in DSSCs,[14] thus increasing both J_{SC} and V_{OC}. As π-bridges, T and DTS are mainly utilized because of their relatively low degree of aromaticity, compared to benzene for example, which is expected to facilitate intramolecular charge transfer to the anchoring group/acceptor and then on to TiO_2.[4]

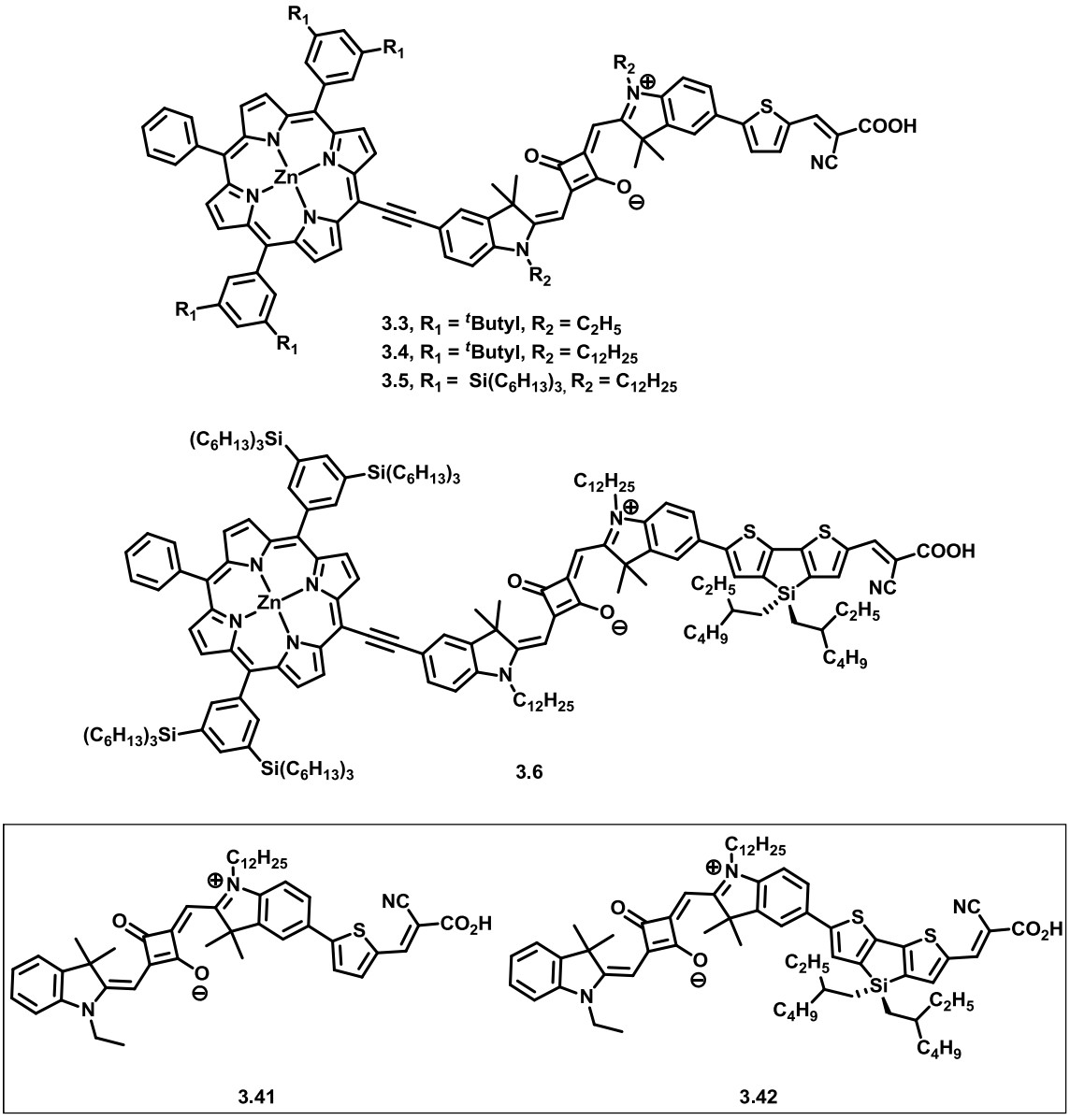

Figure 3.2 Molecular structures of the porphyrin-squaraine (Por)-(Sq) dyes (**3.3**–**3.6**). The molecular structure of squaraine dyes **3.41** and **3.42** are presented as the properties of the Por-Sq dyes are going to be compared to them throughout this chapter.

3.2 RESULTS AND DISCUSSION

3.2.1 Synthesis of the sensitizers

Due to their multicomponent nature, a convergent route was adopted to synthesize compounds **3.3** to **3.6** as highlighted by the retrosynthetic analysis in Figure 3.3. This approach combines all the major pieces towards the end of the synthesis and renders each component easier to handle and the approach as a whole more modular.

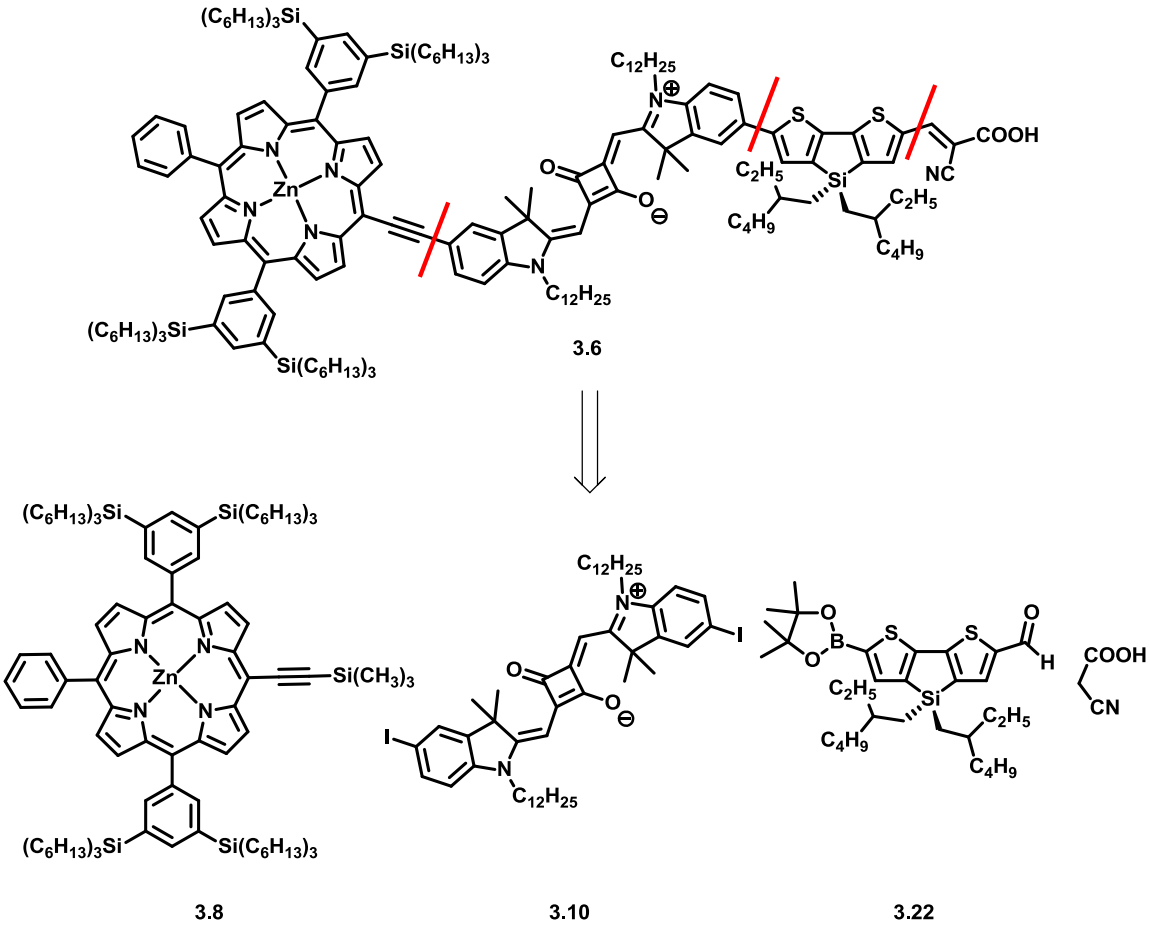

Figure 3.3 Retrosynthetic analysis of compound **3.6**, the rest of the target compounds were synthesized in a similar manner using T instead of DTS. The red wiggly lines indicate sites of covalent attachment of the various components.

The synthesis of asymmetrical porphyrins **3.7** and **3.8**, reported in Scheme 3.1, was performed in collaboration with Ms. Jinsze Wong in Prof. Harry Anderson's lab at the University of Oxford and followed the stepwise approach that was developed by

Senge and others.[24,25] Dipyrromethane (**3.11**), which was prepared via an acid-catalyzed condensation of pyrrole and formaldehyde, was further condensed with benzaldehyde derivatives **3.12** and **3.13** to give the free-base porphyrins **3.14** and **3.15** respectively in low yields. **3.12** was prepared by first brominating di-*tert*-butyl benzene (**3.12A**) to get the bromomethyl derivative (**3.12B**) which was then oxidized by 1,3,5,7-tetraazatricyclo[3.3.1.1^{3,7}]decane (HMTA) to get **3.12** in a Sommelet-type reaction.[26] On the other hand, **2.13** was prepared from 1,3,5-tribromo benzene **3.13A** which was subjected to two consecutive lithiation and trapping reactions the first with trihexylchlorosilane and the second with dimethylformamide (DMF) to give **3.13**.

The reaction of the free-base porphyrins, **3.14** and **3.15** with phenyllithium proceeded via an addition-oxidation mechanism, where an initial attack of the phenyl lithium at the *meso*-position formed a "Phlorin" intermediate which then gave rise to the *meso*-functionalized asymmetrical free-base porphyrins **3.16** and **3.17** upon protonation and oxidation with 2,3-dichloro-5,6-dicyano-1,4-benxoquinone (DDQ). The asymmetrical free-base porphyrins then underwent facile metallation with zinc acetate to give **3.18** and **3.19**, Scheme 3.1, which were then brominated using *N*-bromosuccinimide (NBS) to afford porphyrins **3.20** and **3.21** in high yields. Finally, Sonagashira coupling with trimethylsilyl acetylene gives the desired porphyrins **3.7** and **3.8** in good yields.

The symmetric squaraine building blocks, **3.9** and **3.10**, Scheme 3.2, were synthesized according to a literature procedure,[27] in which squaric acid was condensed with two equivalents of 1-alkyl-5-iodo-3,3-dimethyl-2-methyleneindoline (**3.9A**: alkyl = ethyl and **3.10A**: alkyl = dodecyl) to yield the symmetrical squaraines. The indolines **3.9A** and **3.10A** were synthesized from 4-iodo-phenyl hydrazine in a similar manner to what is described in section 2.2.1 in chapter 2. The synthesis of compound **3.6** required the synthesis of the DTS bridge **3.22** separately and including it towards the end of the synthesis to ensure minimal loss of the precious squaraine porphyrin precursor, as shown in Scheme 3.1. **3.22**, whose synthesis is described in Scheme 3.2, was prepared from the advanced intermediate **3.23** (prepared according to published literature[28-31]) which was brominated with NBS to give **3.24**, which, after protection with 2,2-dimethyl-1,3-

propanediol, yielded **3.25**,[32] which then was subjected to a halogen-lithium exchange reaction and trapping with 2-isopropoxy-dioxaborolane to get the desired bridge **3.22.**[32]

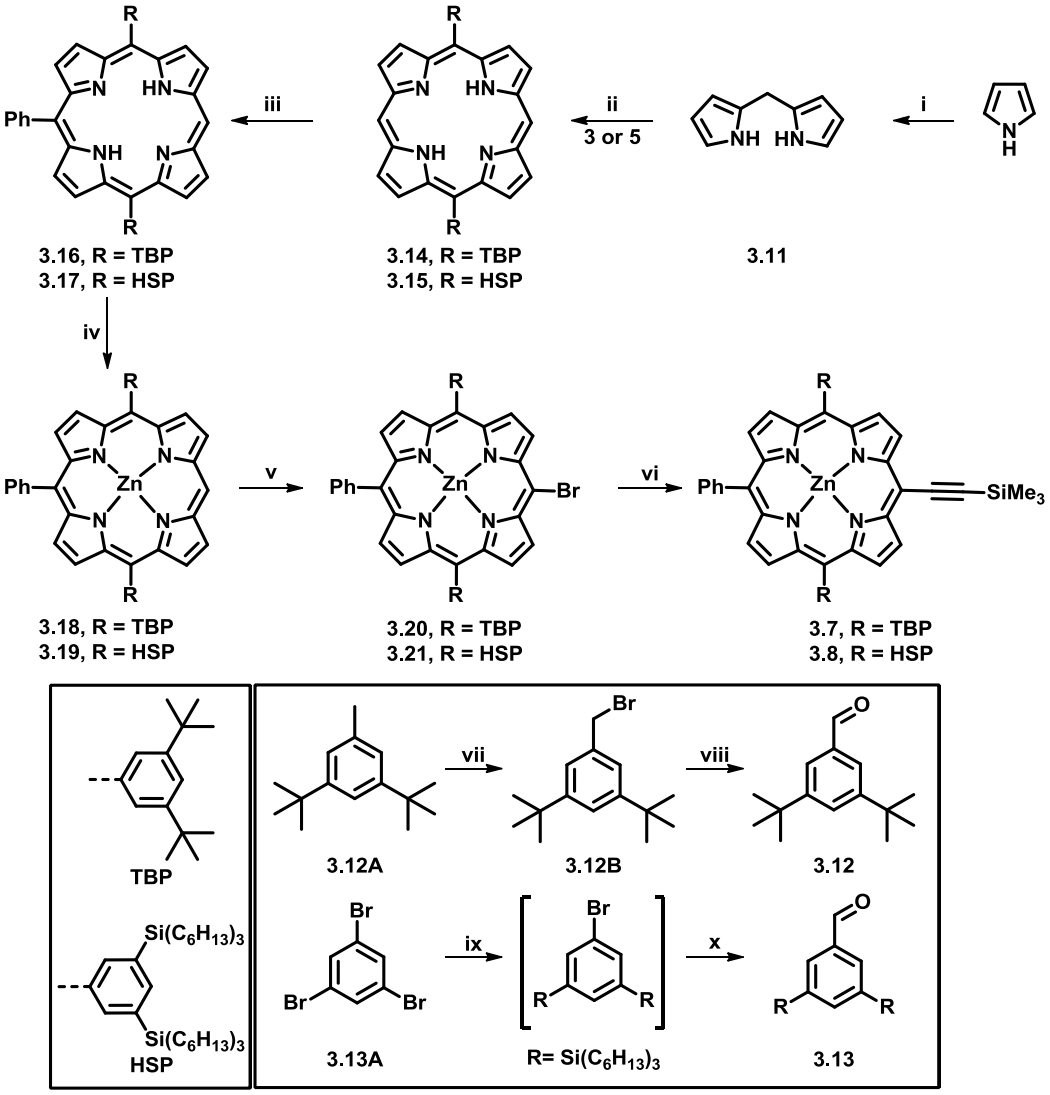

Scheme 3.1 Synthesis of the asymmetrical porphyrins;Formaldehyde, trifluoroacetic acid (TFA), DCM, Na_2CO_3; 44% (ii) a) **3.12** or **3.13**, DCM, TFA; b) DDQ; c) TEA; 26–29% (iii) a) PhLi, THF, b) H_2O, c) DCM, DDQ; 99–69% (iv) $Zn(OAc)_2$, CH_3OH, $CHCl_3$; 74–99% (v) NBS, CH_3Cl, pyridine; 93–95% (vi) trimethylsilyl acetylene, $Pd(OAc)_2$, $(C_6H_5)_3P$, CuI, toluene, trimethylamine; 78–83% (vii) NBS, CH_3Cl, azobisisobutyronitrile AIBN); 98% (viii) HMTA, CH_3Cl; 39% (ix) a) *n*-BuLi, ethylether, b) Trihexylchlorosilane (x) a) *n*-BuLi, ethylether, b) DMF; 29% (2 steps).

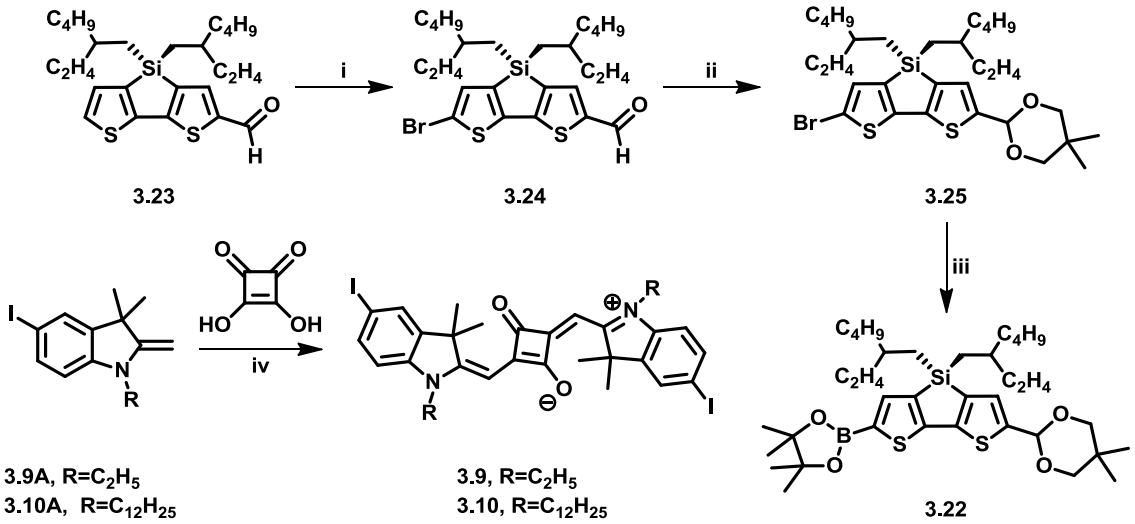

Scheme 3.2 Synthesis of the symmetrical squaraines **3.9** and **3.10**, and the dithienosilole bridge **3.22** i) NBS, DMF, 0 ^{o}C; 95% (ii) 2,2-Dimethyl-1,3-propanediol, p-toluenesulfonic acid, benzene, reflux; 70% (iii) a) *n*-BuLi, THF b) 2-Isopropoxy-4,4,5,5-tetramethyl-1,3,2-dioxaborolane, 44% iv) toluene/butanol, 100 ^{o}C, overnight; 88%.

After all the individual pieces were synthesized, the porphyrin acetylenes **3.7** and **3.8** were coupled to the diiodo squaraines, **3.9** and **3.10**, via a Sonogoshira coupling reaction that included an *in situ* deprotection step with tetrabutylammonium fluoride (TBAF), to yield compounds **3.26** to **3.28**. A large excess (6 molar equivalents) of the diiodo-squaraines was needed to favor the mono-condensation products **3.26**-**3.28** over the bis-condensation products, which were the primary side product isolated from the reaction mixtures, Scheme 3.3. A Suzuki-Miyaura cross-coupling reaction of the resultant compounds with the commercially acquired thiophene boronic acid carboxaldehyde resulted in compounds **3.29** to **3.31** in moderate to good yields. After Knoevenagel condensation of compounds **3.29**-**3.31** with cyanoacetic acids yielded the (Por)-(Sq) dyes **3.3** to **3.5** in, Figure 3.2, in good yields. Along the same lines, the Suzuki-Miyaura coupling of compound **3.28** and the DTS bridge, **3.22**, resulted in the protected dye **3.32**, which was then de-protected using TFA to get **3.33** in almost quantitative yields. The anchoring group, cyanoacrylic acid, was introduced via a Knovenagel condensation with cyanoacetic acid to get **3.6** in a good yield.

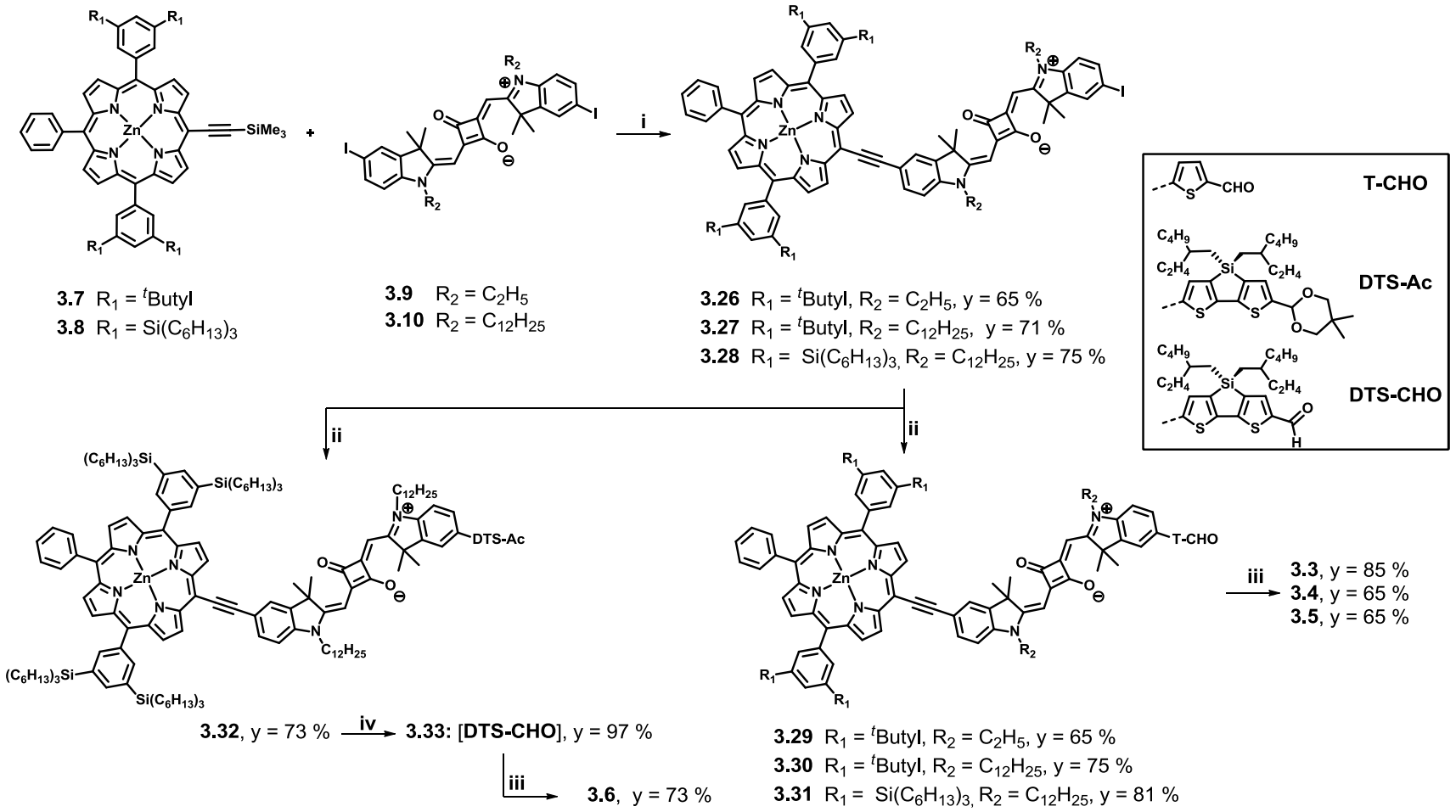

Scheme 3.3 Synthesis of (Por)-(Sq) dyes; [a] (i) Pd_2dba_3, PPh_3, TBAF, CuI, *iso*-Pr_2NH, THF, 45 ^oC, 1 h; 65-75% (ii) (5-formylthiophen-2-yl)boronic acid or **3.22**, Pd(dppf)Cl_2•CH_2Cl_2, K_2CO_3, CH_3OH, toluene; 65–81% (iii) Cyanoacetic acid, piperidine, $CHCl_3$, CH_3CN; 65–85% (iv) TFA, room temperature, overnight; 97%.

During the process of synthesizing the (Por)-(Sq) dyes presented in Figure 3.2, alternative routes were tested, in order to minimize the chance of reaching synthetic dead ends, and to decrease material costs, Scheme 3.4, highlights two alternative routes that thought the synthesis of asymmetrical squaraines with the π-bridges incorporated into them, prior to the addition of the porphyrin; the most precious component in this synthesis. In Route 1, a Suzuki-Miyaura cross coupling reaction of **3.9** with 5-formyl-2-thiopheneboronic acid, **3.34**, was attempted with the goal of producing the asymmetrical squaraine **3.35**. Differential reactivity over the two reactive iodine centers proved to be difficult under the Suzuki-Miyaura reaction conditions and instead the symmetrical squaraine, compound **3.36**, was isolated even when excess of **3.9** was used.

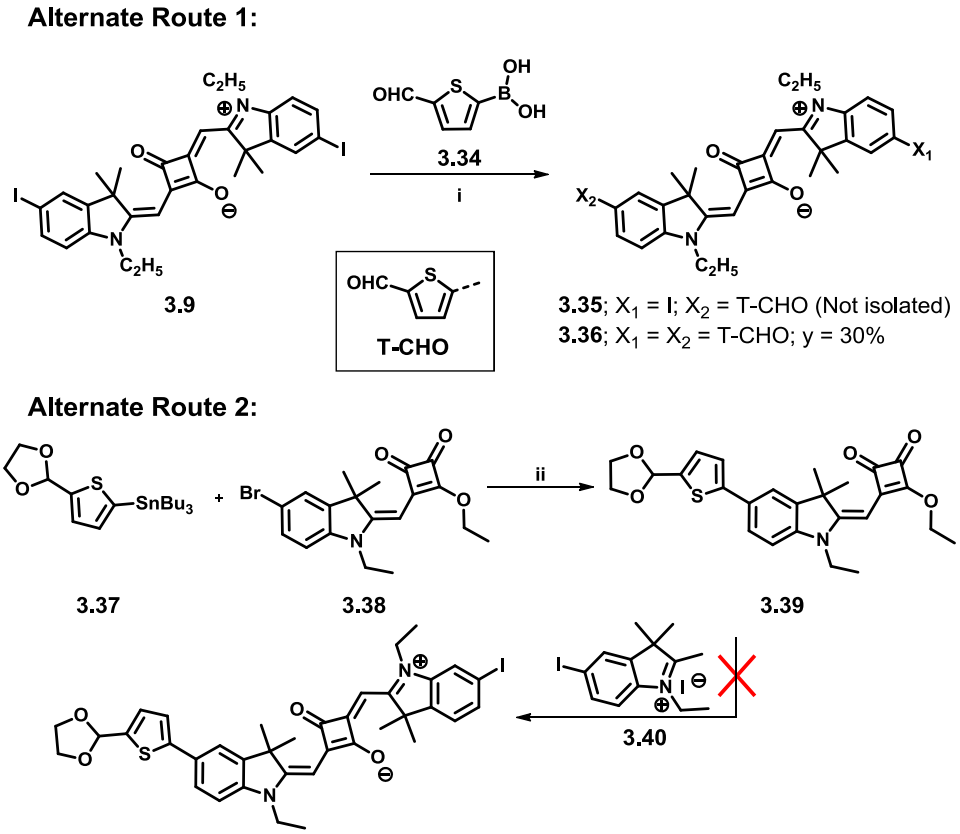

Scheme 3.4 Alternative routes to synthesize the dyes in Figure 3.2 (i) $Pd(dppf)Cl_2 \bullet CH_2Cl_2$, K_2CO_3, CH_3OH, toluene; 30% (ii) $Pd(PPh_3)Cl_2$, toluene, reflux; 60%

After the failure of Route 1, an attempt was made to introduce the bridge at the semi-squaraine stage prior to building the asymmetrical squaraine. For that approach, a protected thiophene tributyltin compound, **3.37** (prepared via first protecting a thiophene-

2-carboxaldehyde, then lithiation and trapping with tributyltin chloride) was coupled to the semi-squaraine **3.38** via a Stille coupling reaction at the 5-bromo position on the indole. This reaction proceeded to give compound **3.39** in a moderate yield, however the condensation of compound **3.39** with compound **3.40** proved problematic and caused a deprotection of the aldehyde and subsequent condensation at that site instead of the squaric ester. Due to the above reasons and the success of the synthetic route presented in Scheme 3.3, these two routes were not explored further.

3.2.2 Optical and electronic properties

The solution absorption spectra of the synthesized (Por)-(Sq) dyes are presented in Figure 3.4, and as expected they can be understood as the sum of the absorption of the two individual pieces with some relative minor perturbations as follows; compared to the parent squaraine **3.41**and **3.42**, the (Por)-(Sq) dyes **3.3**-**3.6** had a ~0.14 eV red-shifted low energy absorption with an onset ca. 770 nm, and an order-of-magnitude increase of the absorptivity in the range from 400 to 500 nm due to the porphyrin's Soret band. Upon increasing the length of the alkyl chain on the squaraine indole groups from ethyl in **3.3** to dodecyl in **3.4**, a slight bathochromic shift was observed. Changing the side chains on the porphyrin had little effect on the (Por)-(Sq) solution absorption; the *tert*-butyl substituted **3.5** and trihexylsilyl substituted **3.6** demonstrated similar spectra. Variation of the π-bridge from T in **3.5** to DTS in **3.6** further red-shifted the squaraine and porphyrin bands by 0.01 eV, due to the extended conjugation. In addition, it caused an increase in the absorptivity in the region around 450-500 nm, which most likely results from the absorption of the DTS π-bridge; this is more evident in the film absorption (Figure 3.5). Another important feature of the absorption spectra of these (Por)-(Sq) dyes, courtesy of their design, is that covalently linking the two chromophores in such a fashion did not result in a strong donor-acceptor coupling which might be expected to cause the disappearance of the recognizably squaraine and porphyrin localized transitions and give rise to only a charge-transfer band at low energy.

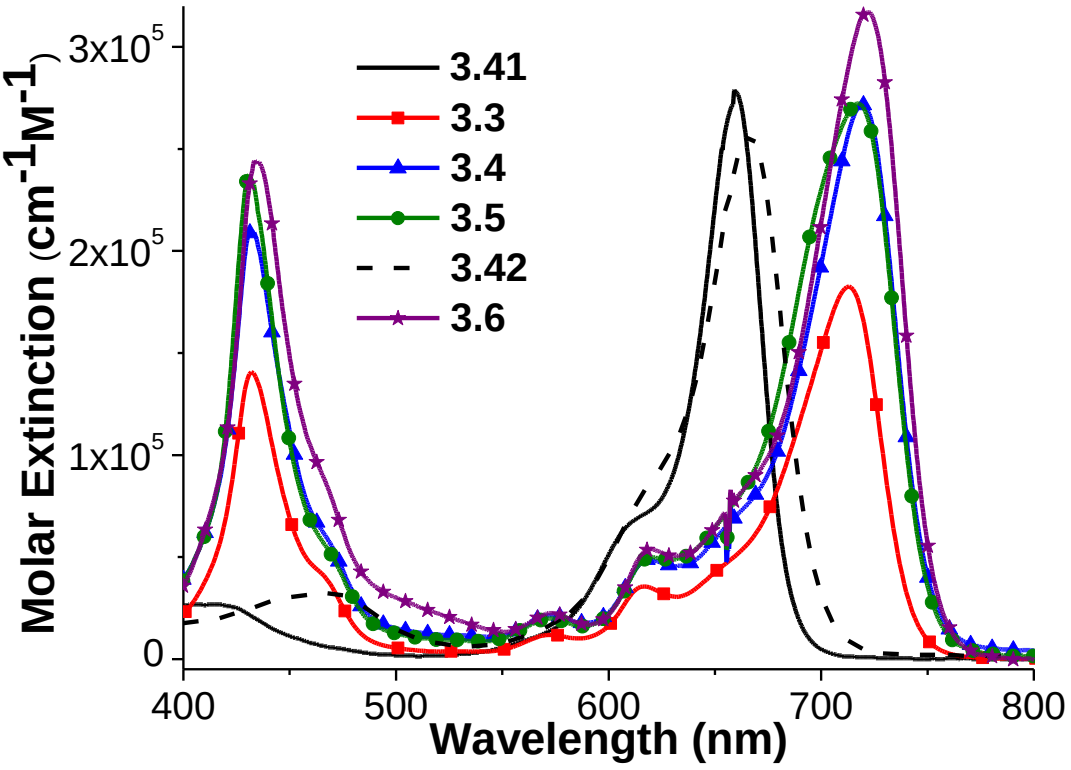

Figure 3.4 UV-vis absorption spectra of the dyes **3.3** to **3.6** in THF. The absorption spectra of **3.41** and **3.42** are also shown for comparison.

The optical density of the dyes adsorbed on TiO_2 was determined and is presented in Figure 3.5 to gain an understanding of the aggregation effects in the surface-bound dyes. General broadening of the absorption profiles for all four dyes, along with red shifting of the squaraine-based absorption band was observed, consistent with what has been previously reported in literature.[4,22] **3.3**, having the shorter alkyl chain on the squaraine moiety, showed a shoulder around 670 nm, which is usually assigned to the H-aggregate.[4,22] The shoulder at ca. 670 nm was reduced with increased alkyl chain length on the squaraine from ethyl (**3.3**) to dodecyl (**3.4**), presumably due to decreased aggregation. The absorption between ca. 480-550 nm in DTS dyes (**3.42** and **3.6**) compared to the other dyes adsorbed on TiO_2 is likely due to the DTS π-bridge. The absorption onset of the (Por)-(Sq) on TiO_2 was red-shifted by 0.1 eV compared to **3.41** and **3.42** which renders these dyes capable of absorbing across the whole visible spectrum, necessary for panchromatic absorption.

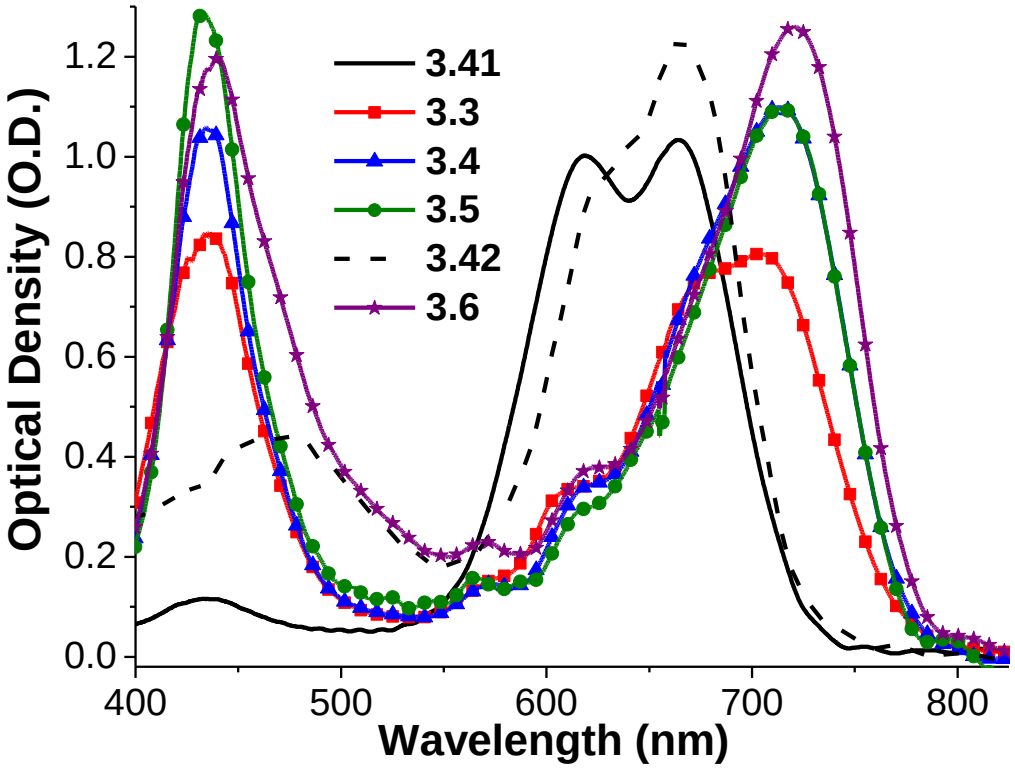

Figure 3.5 UV-vis absorption spectra of dyes **3.3** to **3.6** adsorbed on TiO_2. The films were soaked in a dye solution of 0.05 mM dye with 10 mM (CDCA) for 1 h. The spectra of **3.41** and **3.42** are shown for comparison.

The ground-state oxidation potential of the dye $E_{(S^+/S)}$ compared to the electrochemical potential of the electrolyte and the excited-state oxidation potential of the dyes $E_{(S^+/S^*)}$ compared to the conduction band edge (CBE) of TiO_2 are of major importance in solar cell operation. The CBE of TiO_2 is usually placed at –0.5 V vs. NHE,[33,34] however, it has been shown that this potential can be tuned by factors such as the surface charge, dipoles of the adsorbed molecules,[33] pH of the electrolyte solution,[35] and the presence of cations in the electrolyte.[36] When accounting for such factors, a CBE closer to –0.7 V vs. NHE (200 mV more negative) has been suggested more recently.[37,38] Also, since the density of the semiconductor acceptor states have been shown to increase exponentially,[37] a higher $E_{(S^+/S^*)}$ with respect to the CBE can result in higher electron injection rates (k_{ei}), and hence J_{SC} and PCE.

Table 3.1 summarizes the optical and electrochemical properties of the (Por)-(Sq) dyes **3.3** – **3.6** and compares them to those of squaraines described in chapter 2, **3.41** and

3.42. $E_{S^+/S}$ was determined from cyclic voltammetry measurements as described in the experimental section and demonstrated in the appendix Figure A.19 to Figure A.22, while the E_{S^+/S^*} was determined from the following equation $E_{(S^+/S^*)} = E_{(S^+/S)} - E_{0\text{-}0}^{opt}$ where $E_{0\text{-}0}^{opt}$, the optical gap, was determined from the intersection of the normalized absorption and emission spectra as shown in the appendix Figure A.14 to Figure A.17. Compared to the squaraine dyes, the (Por)-(Sq) dyes have E_{S^+/S^*} that are, on average, 140 mV less negative, which is expected to translate to lower injection rates, even though there is still estimated to be a driving force of 120–320 mV for efficient injection into the CBE of TiO_2. In a similar manner, to provide ample room for dye regeneration by the triiodide/iodide redox couple (0.30 V vs. NHE) an $E_{S^+/S}$ more oxidizing than +0.65 V vs. NHE[39] is recommended. The $E_{S^+/S}$ of the (Por)-(Sq) dyes were ca. 0.90 V vs. NHE while those of the squaraine dyes were ca. +0.82 V vs. NHE, providing driving forces for dye regeneration of ca. 600 mV and ca. 520 mV, respectively. Thus, to a first approximation, both porphyrin containing and squaraine dyes should have sufficient driving force for dye regeneration.

Table 3.1 Optical and electrochemical properties of the dyes mentioned in Figure 3.2.

Dyes	λ_{max} **[nm]**[a)]	**ε [$M^{-1}cm^{-}$]**	$E_{0\text{-}0}^{opt}$ **[eV]**	$E_{(S^+/S)}$ **[V]**	$E_{(S^+/S^*)}$ **[V]**
3.41	659	279,000	1.76	+0.80	–0.96
3.3	718	182,000	1.72	+0.90	–0.82
3.4	713	246,000	1.72	+0.88	–0.84
3.5	717	272,000	1.72	+0.89	–0.83
3.42	657	257,000	1.82	+0.84	–0.98
3.6	722	317,000	1.72	+0.89	–0.83

[a)]Derived from absorption spectra in THF, with the exception of **3.41**, and **3.42**, where spectra in ethanol were used.

3.2.3 Photovoltaic characterization

NOTE: The results discussed in this section are based on experiments that have been conducted by Dr. Xiongwu Kang from Prof. Mostafa El-Sayed's laboratory at the Georgia Institute of Technology. A detailed discussion of device fabrication procedures and characterization will be incorporated in the collaborative publications. Permission has been obtained to use the data presented in this section.

The IPCE spectra of dye cells based on the sensitizers in Figure 3.2 with the respective dye/CDCA ratios given in Table 3.2 are shown in Figure 3.7. The IPCE curve of each dye generally follows the spectral features seen in the optical spectra of the dyes bound to TiO_2 surface shown in Figure 3.5. The (Por)-(Sq) dyes all have nearly equivalent or somewhat greater IPCE values in their high-energy absorption regions (ca. 500 nm) compared to their low energy absorption regions (ca. 750 nm), whereas both squaraine dyes (**3.7** and **3.8)** have greater peak currents in their low energy absorption areas (ca. 700 nm), due to their considerably higher low energy absorption. These slightly more balanced IPCE spectra are, however, not necessarily translated into overall higher PCEs as summarized in Table 3.2, and seen in the *J-V* pot in Figure 3.7.

Within this series of dyes, thiophene π-bridged **3.41** may be compared to thiophene π-bridged **3.3**, **3.4**, and **3.5** to assess the effect of the synthetic addition of porphyrins on the overall DSSC performance. Amongst the (Por)-(Sq) dyes, and as illustrated by space filling models, the steric profile increases from **3.3** to **3.4** to most sterically encumbered **3.5**. Compared to squaraine **3.41**, the reduced J_{SC} in **3.3** could be due, in part, to dye aggregation which manifests itself in the optical density spectra of TiO_2-adsorbed **3.3** as a shoulder at 670 nm. However, since **3.41** also displays aggregation, another contributing factor to the reduced J_{SC} of **3.3** may be from lower charge injection efficiency η_{inj} as discussed in the next section. On the other hand, both **3.4** and **3.5**, two (Por)-(Sq) dyes that are more sterically demanding than **3.3** and **3.41**, show greater J_{SC} which could be attributed to decreased aggregation, as they only differ in the size of their substituents.

When comparing the effect of the substituents on the porphyrin ring, in the two cases where the bulkier [3,5-bis(trihexylsilyl)phenyl]-substituted porphyrins where used, lower J_{SC} was observed compared to the 3,5-bis(*tert*-butyl)phenyl analogue; such as when comparing **3.5** and **3.4** and to a lesser extent when comparing the (Por)-(Sq) **3.6** with its squaraine only analogue **3.42**. Although not studied in-depth herein, this lower J_{SC} in **3.5** vs. **3.4** may be due to the bulkier 3,5-bis(trihexylsilyl)phenyl groups shielding the hole of the oxidized dye from the electrolyte in **3.5** compared to the less sterically shielding 3,5-bis(*tert*-butyl)phenyl in **3.4**. Such shielding could reasonably be expected to reduce dye regeneration and hence reduce J_{SC}. This effect may be larger when comparing **3.6** to its squaraine analogue **3.8**, since **3.42** contain no shielding porphyrin moiety.

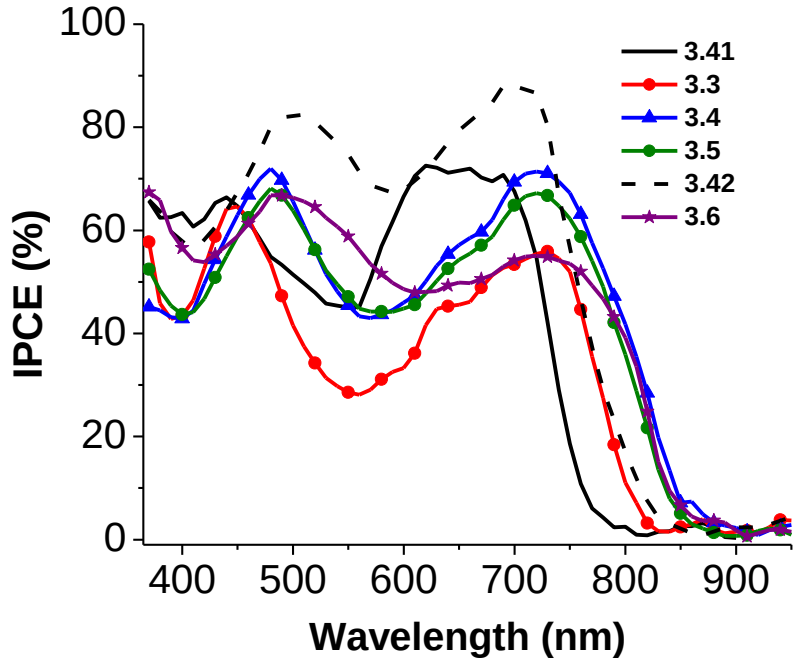

Figure 3.6 IPCE scans for optimized dye cells. TiO_2 films were soaked in dye solutions whose compositions are stated in Table 3.2 for 4 h.

One feature of the IPCE curve of **3.6**, that is different from the other dyes, is that the high-energy region (ca. 400-600 nm) has a higher IPCE peak than the low-energy region (ca. 600-850), which does not line up with its optical absorption profile on TiO_2 in Figure 3.5; The other (Por)-(Sq) dyes show IPCE curves that more closely resemble their optical spectra when adsorbed on TiO_2. The high-energy IPCE observation of **3.6** may be

from a combination of: (1) the porphyrin-based absorption of a photon that internally converts to the low energy excited state that injects with the efficiency of the lower excited state, as can be inferred from Figure 3.8 and Figure 3.9 discussed later, and (2) a DTS-based absorption to a higher excited state that hot injects with somewhat greater efficiency due to proximity of the DTS-based orbital to the TiO_2, this is suggested by the shape of the IPCE curve of **3.6** in the range ca. 500-550, which somewhat follows that of **3.42**. In terms of the V_{OC}, values up to 40 mV higher were observed with **3.6**, when compared to **3.4** and **3.5**, which we speculate are due to the additional 2-ethylhexyl groups on the DTS π-bridge in **3.6**. This is consistent with what has been seen in **3.42**, which, in the previous chapter, has been attributed in part to reduced electron/injected charge recombination due to steric shielding of the 2-ethylhexyl groups.[14]

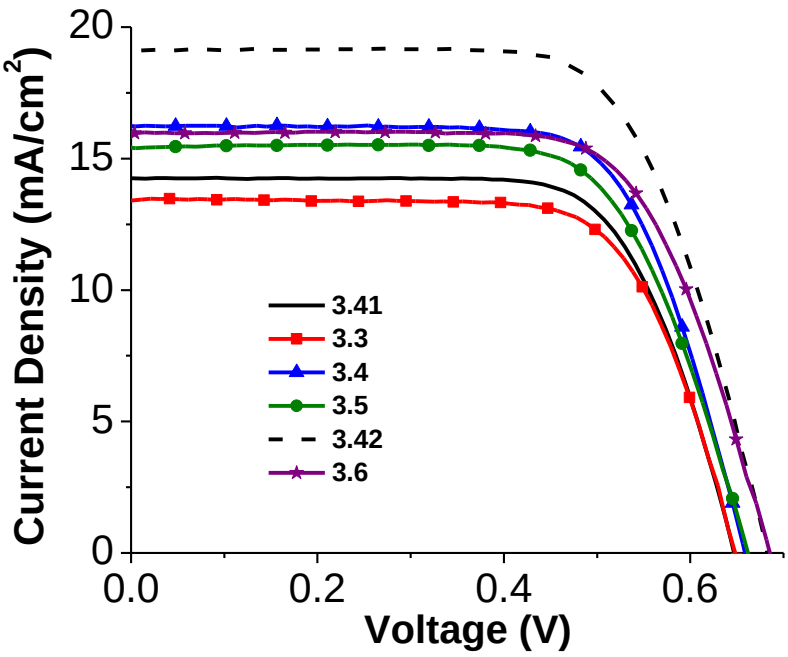

Figure 3.7 Photovoltaic characteristics of optimized cells with TiO_2 films soaked in dye solutions whose compositions are stated in Table 3.2 for 4 h.

Table 3.2 Photovoltaic performance of the optimized dye cells.[a]

	Dye Conc. [mM]	CDCA Conc. [mM]	*V*oc [V]	J_{SC} [mAcm^{-2}]	FF [%]	PCE [%]
3.41	0.1	10	0.65 ± 0.01	14.2 ± 0.3	70.4 ± 0.2	6.5 ± 0.1
3.3	0.1	10	0.65 ± 0.01	13.4 ± 0.1	70.4 ± 0.8	6.1 ± 0.1
3.4	0.05	10	0.66 ± 0.01	16.3 ± 0.4	70.1 ± 0.6	7.5 ± 0.1
3.5	0.05	10	0.65 ± 0.01	15.2 ± 0.1	71.2 ± 0.3	7.1 ± 0.1
3.42	0.05	10	0.68 ± 0.01	19.1 ± 0.2	68.3 ± 0.7	8.9 ± 0.2
3.6	0.1	10	0.69 ± 0.01	16.0 ± 0.2	69.6 ± 0.7	7.6 ± 0.1

[a)] Based on measurements of 3 devices for all dyes with upper/lower measured values shown. The photovoltaic measurements were conducted in the absence of a mask and with a cell active area of 0.36 cm^2.

3.2.4 Electron injection kinetics

NOTE: The results discussed in this section are based on experiments that have been conducted by Daniel O'Neil from Prof. Mostafa El-Sayed's laboratory at the Georgia Institute of Technology. A detailed discussion about the kinetic measurements will be incorporated in Daniel O'Neil's future thesis, and in the collaborative publications. Permission has been obtained to use the data presented in this section.

The IPCE and subsequently the J_{SC} of these dyes depend not only upon their ability to absorb photons but also upon charge injection yield and charge collection efficiency. The injection process was studied using transient-absorption spectroscopy as discussed in Chapter 2 for squaraine dyes. The values of η_{inj} as well as injection rate constants (k_{ei}) together with the charge injection and dye-regeneration driving forces ($-\Delta G_{ei}^{\circ}$ and $-\Delta G_{reg}^{\circ}$) are summarized in Table 3.3.

As shown in Table 3.3, the (Por)-(Sq) containing dyes have lower η_{inj} compared to the squaraine dyes **3.41** and **3.42**. These lower η_{inj} values are consistent with the lower $E_{(S^+/S^*)}$ and ΔG_{ei}° seen in the (Por)-(Sq) dyes, which can slow down the rate of injection as discussed in section 5[37] To reiterate, the squaraine dyes **3.41**and **3.42** provide a charge injection driving force which is ca. 130 mV higher than that the (Por)-(Sq) dyes, which in the latter's case translates into a slower k_{ei}, which is likely the factor that is limiting the injection rate of the (Por)-(Sq) dyes compared to the squaraine dyes. Along the same lines, the lower η_{inj} of ca. 80% for **3.6** is possibly a reason why the low-energy IPCE is lower in **3.6** compared to **3.5** and **3.4**.

Table 3.3 Charge injection dynamics of the synthesized chromophores.[a]

Dye	τ_{obs} [ps]/TiO_2	τ_{obs} [ps]/Al_2O_3	k_{ei} [10^{-10} s^{-1}]	$-\Delta G_{ei}^{\circ}$ [V]	$-\Delta G_{reg}^{\circ}$ [V]	η_{inj} [%]
3.41	1.8	123.9	52.4	0.46	0.50	98.5
3.3	9.0	76.0	9.8	0.32	0.60	84.0
3.4	4.0	29.0	21.6	0.34	0.58	86.0
3.5	7.0	70.3	12.7	0.33	0.59	90.0
3.42	1.2	22.6	78.9	0.48	0.54	94.6
3.6	6.1	32.5	13.3	0.33	0.59	81.3

[a)]The assembled dye cells were pumped near the ground-state absorption for each dye and probed near their excited-state absorption maxima. All data were fit with stretched exponentials.

Since the porphyrin-squaraine dyes have two separate chromophores, the effect of varying the excitation wavelength on the injection rate was examined. **3.4** on TiO_2 was pumped at 470, 575, 630, and 705 nm and Figure 3.8 shows the normalized decay of the dye excited state monitored at 520 nm. The dye exhibits the same dynamics and the same injection rate. Although the higher energy photons of 470 nm do initially excite the dye to a higher energy state than the photons of 705 nm, the injection rate was not accelerated due to increased injection driving force from the higher excited state.

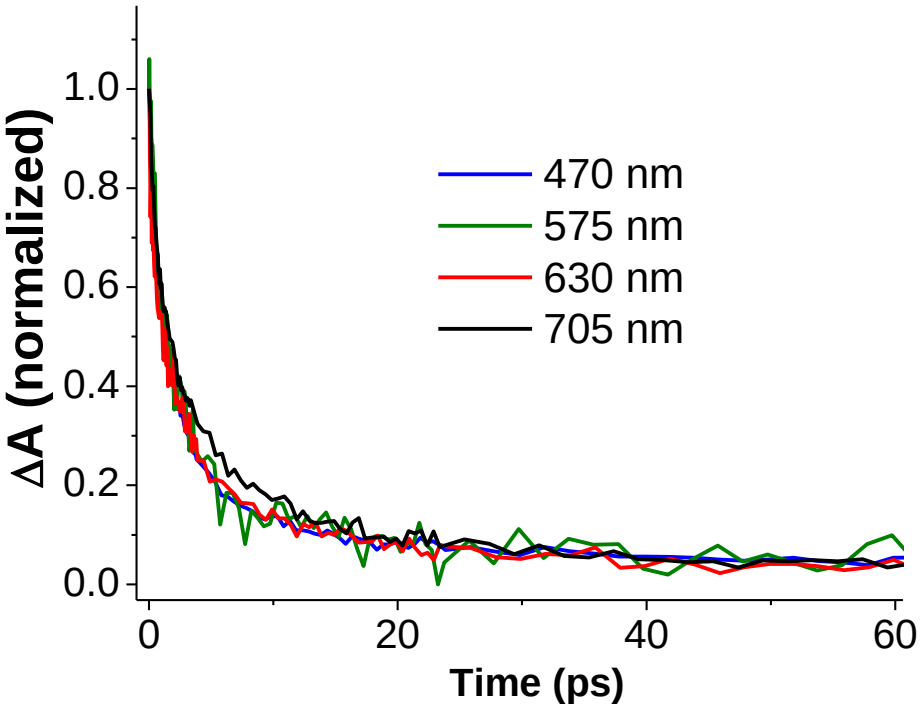

Figure 3.8 Transient absorption traces of **3.4** on TiO_2 pumped at a variety of wavelengths and probed at 520 nm.

The most likely explanation is that the initially formed higher excited state (S_n) internally converts to the lowest excited state, S_1, sufficiently fast that direct injection from S_n is minimal (and porphyrin-based orbitals presumably have much less overlap with the TiO_2). According to Kasha's rule,[40] fluorescence and by extension, other photo-physical processes, occur only from S_1 of a chromophore, so any excitation to higher excited states should result in fluorescence from S_1. The fluorescence excitation spectrum of **3.4**, Figure 3.9, confirms that, at least in solution, excitation across the spectrum of **3.4** populates the S_1 fluorescent state. The fluorescence excitation and multiple-wavelength

excited state decay data indicate that excitation due to the porphyrin likely results in population of S_1 of the dye and thereby contributes to observed photocurrent, at least in **3.4**.

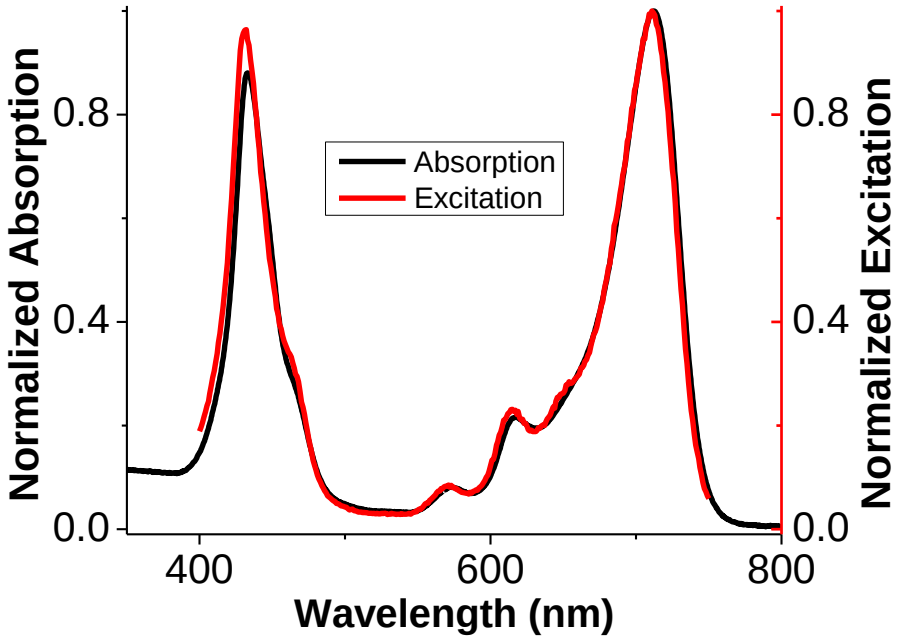

Figure 3.9 Normalized absorption and fluorescence excitation spectra; excitation wavelength from 400 to 750 nm, emission detected at 765 nm.

3.3 CONCLUSION

In this chapter, four multichromophoric porphyrin (Por)-squaraine (Sq) dyes were synthesized by a convergent synthetic approach, and the optoelectronic properties as well as the photovoltaic performances were compared with their squaraine-only analogues. These dual chromophoric systems exhibited large molar extinction coefficients of ca.10^5 $M^{-1}cm^{-1}$ at their porphyrin-based high-energy absorption bands and approximately equally strong squaraine-based low energy absorption bands red-shifted by 0.14 eV when compared to their squaraine only counterparts **3.41** and **3.42**. (Por)-(Sq) dyes **3.4** and **3.5** demonstrated slightly better photovoltaic characteristics (0.6-1.0% higher PCEs) compared to **3.41** due to higher J_{SC} which is largely due to greater IPCE values at wavelengths above ca.750 nm in the (Por)-(Sq) dyes. However, given the lower charge injection efficiency of these dyes compared to **3.41** and **3.42**, the higher J_{SC} in the dyes

3.4–**3.6** in part validates the approach of increasing panchromaticity of the squaraine dyes, even though this increase results more from the red-shift of the squaraine based band rather than increased higher energy porphyrin based absorption. This lower charge injection efficiency (η_{inj}) is likely the result of a lower driving force for electron injection into the TiO2 CBE. Moving forward, quantifying the effect of dye regeneration is required to gather a full understating of the factors causing the discrepancy between the absorption profile of these (Por)-(Sq) and their J_{SC}. If found problematic, one way to improve dye regeneration would be adding an electron donating group to the porphyrin that would localize the hole on that group as opposed to the bulky porphyrin; this could facilitate the regeneration process

3.4 EXPERIMENTAL SECTION

3.4.1 Synthetic procedures

Commercially available intermediates were purchased and used without further purification. For water sensitive reactions, commercially acquired anhydrous *N*,*N*-dimethylformamide (DMF) was used, tetrahydrofuran (THF) and toluene were dried by the distillation from sodium benzophenone ketyl or used directly from an MBRAUN solvent purification system (MBRAUN-SPS). Bases such as piperidine and diisopropylamine, were distilled over calcium hydride, and stored in Schlenk flasks under nitrogen in the presence of molecular sieves. ^{1}H, and ^{13}C{^{1}H} NMR spectra were collected on a Bruker 400 MHz spectrometer. Deuterated solvents with TMS as an internal standard were used. Mass spectra were measured on a VG Instruments 70-SE using the electron impact (EI) or fast-atom bombardment (FAB) mode and on an Applied Biosystems 4700 Proteomics Analyzer using MALDI mode. Elemental analyses were carried out by Atlantic Microlab using a LECO 932 CHNS elemental analyzer.

(3.24)

3.23 (1.76 g, 3.94 mmol) was dissolved in DMF (30 mL) and the mixture was stirred at 0 ^{o}C for 30 minutes. *N*-Bromosuccinimide (0.78 g, 4.41 mmol) was then added at 0 ^{o}C and the reaction mixture was stirred at room temperature for 4 h. The reaction

mixture was then poured over water (50 mL) and extracted with chloroform (2 × 50 mL); the extracts were dried over anhydrous sodium sulfate, and the solvent removed under reduced pressure to give a yellow liquid which was purified via silica gel column chromatography using hexane/chloroform (1:1) as the eluent to obtain the pure product **3.24** (1.52 g, 73% yield). ^{1}H NMR (400 MHz, $CDCl_3$) δ 9.86 (s, 1H); 7.68 (s, 1H); 7.07 (s, 1H); 1.39 (septet, J = 5.5 Hz, 2H); 1.30-1.10 (m, 17H); 0.96 (d, J = 6.3 Hz, 4H); 0.85-0.70 (m, 11H). ^{13}C{^{1}H} NMR (100 MHz, $CDCl_3$) δ 182.64, 157.28, 148.10, 147.59, 144.74, 142.49, 139.49, 132.86, 115.52, 35.82, 35.62, 28.86, 28.81, 22.93, 17.38, 14.11, 10.76; HRMS (ESI): m/z $[M]^+$ Calcd. for $C_{25}H_{38}OBrS_2Si$: 525.1296; found: 525.1311. Anal. Calcd. for $C_{25}H_{37}BrOS_2Si$ (%): C, 57.12; H, 7.09. Found: C, 56.83; H, 6.86.

(3.25)

3.24 (0.91 g, 1.73 mmol), neopentylglycol (0.22 g, 2.02 mmol), p-toluenesulfonic acid monohydrate (0.033g, 0.173 mmol) were refluxed in benzene (10 mL) for 3 hours. The reaction was cooled to room temperature, and sodium bicarbonate solution (50 mL of a 2% w/w solution in water) was added, after which the reaction was stirred for 15 min at room temperature. The organic layer was separated, dried over sodium sulfate, and solvent was removed under reduced pressure to give a red oil which was purified with silica gel column chromatography using a dichloromethane/hexane (1:9) as an eluent to afford the product **3.25** (0.74 g, 70%).^{1}H NMR (400 MHz, $CDCl_3$) δ 7.07 (s, 1H); 6.99 (s, 1H); 5.65 (s, 1H); 3.78 (d, J = 11.0 Hz, 2H); 3.67 (d, J = 11.0 Hz, 2H); 1.41 (septet, J = 5.5 Hz, 2H); 1.31 (s, 3H); 1.28-1.16 (m, 16H); 0.93-0.90 (m, 4H); 0.86 (t, J = 7.0 Hz, 6H); 0.82 (3H, s); 0.79 (dt, J_d = 1.6 Hz, J_t = 7.0 Hz, 6H). ^{13}C{^{1}H} NMR (100 MHz, $CDCl_3$) δ 149.23, 148.53, 142.85, 141.90, 140.99, 132.39, 127.72, 111.07, 98.32, 35.84, 35.76, 35.62, 35.53, 30.20, 28.84, 28.78, 22.98, 21.85, 17.52, 14.15, 10.75; HRMS (ESI): m/z $[M]^+$ Calcd. for $C_{30}H_{47}BrO_2S_2Si$: 611.2043; Found 611.2033.

(3.22)

3.25 (0.40 g, 0.16 mmol) was dissolved in THF (5 mL) and the reaction temperature was reduced to -78 ^{o}C in an acetone/dry ice bath. *n*-Butyllithium (0.34 mL, 0.79 mmol) was added at -78 ^{o}C and the reaction mixture was stirred for 1 h at that temperature. 2-Isopropoxy-4,4,5,5-tetramethyl-1,3,2-dioxaborolane (0.15 mL, 0.72

mmol) was added at -78 ^{o}C, the reaction mixture was stirred at that temperature for 20 min before heating to room temperature and stirring overnight. The reaction was stopped, solvent removed, and crude product **3.22** (0.19 g, 44%) was used for next step without further purification.

(3.17)

3.15 (0.80 g, 0.50 mmol) was placed in a two-necked round-bottomed flask under nitrogen atmosphere and dissolved in dry THF (280 mL). The solution mixture was subjected to three freeze-pump-thaw degas cycles. The porphyrin was cooled to -40°C using a dry ice/acetonitrile mixture. Phenyllithium solution (1.8 M in dibutyl ether, 3.6 mL, 5.53 mmol) was added drop-wise by syringe. The cold bath was removed and the reaction mixture was stirred at room temperature for an additional hour (monitored by TLC). The color of the solution changed from purple to brown. A mixture of THF:water (1:1, 40 mL) was added for the hydrolysis. The reaction mixture was stirred for an additional 20 minutes. 2,3-Dichloro-5,6-dicyano-1,4-benzoquinone (1.37 g, 6.02 mmol) dissolved in dichloromethane (100 mL, 0.06M) was then added and the reaction mixture stirred for one hour. The reaction mixture was concentrated and passed through a short silica plug eluting with a mixture of petroleum ether: CH_2Cl_2 (4:1, 100 mL). The solvent was removed under reduced pressure and the crude mixture was carried forward immediately to make **3.17** without further purification. ^{1}H NMR (200 MHz, $CDCl_3$) δ 10.23 (1H, s); 9.33 (d, J = 4.0 Hz, 2H); 9.02 (d, J = 6.0 Hz, 2H); 8.87 (q, J = 4.0 Hz, 4H); 8.32 (4H, s); 8.22 (dd, J_1= 2.0 Hz, J_2 = 6.0 Hz, 2H); 7.99 (s , 2H); 7.53 (m, 3H), 1.48-0.82 (m, 156 H).

(3.19)

Zinc(II) acetate dehydrate (0.38 g, 1.74 mmol) was dissolved in methanol (4.8 mL) and added to a stirring solution of 3.17 (0.58 g, 0.35 mmol) in chloroform (60 mL). The reaction mixture was stirred for 1 h and checked for completion using UV/vis. The reaction mixture was concentrated and passed through a short plug of silica eluting with dichloromethane, to give purple oil. The residue was purified using a size-exclusion column eluting with a chloroform: pyridine mixture (100:1). The first fraction containing porphyrin dimer was discarded and the second fraction was collected and solvent

removed under reduced pressure to give **3.19** as a purple oil (0.45g, 74 %). ^{1}H NMR (400 MHz, $CDCl_3$ + 1% pyridine-d_5) δ 10.23 (s, 1H), 9.33 (d, J = 4.7 Hz, 2H), 9.02 (d, J = 4.7 Hz, 2H), 8.90 (d, J = 4.9 Hz, 2H), 8.84 (d, J = 4.9 Hz, 2H), 8.32 (d, J = 0.8 Hz, 4H), 8.21 (dd, J_1 = 7.4 Hz, J_2 =1.7 Hz, 2H), 7.99 (t, J = 0.8 Hz, 2H), 7.79-7.66 (m, 3H), 0.74–1.58 (m, 156H). ^{13}C{^{1}H} NMR (100 MHz, $CDCl_3$ + 1% pyridine-*d*5) δ 149.88 148.57, 143.34, 141.16, 140.88, 135.74, 135.40, 135.11, 134.39, 133.49, 132.09, 131.56, 128.71, 127.10, 126.51, 126.34, 123.76, 121.21, 120.74, 33.53, 31.63, 24.08, 22.64, 14.20, 12.68. (MALDI TOF MS) *m/z*: $[M]^+$ Calcd. For $C_{110}H_{176}N_4Si_4Zn$: 1730.23; found 1730.46.

(3.21)

N-Bromosuccinimide (43.9 mg, 0.25 mmol) was dissolved in chloroform (4 mL). This was added to a stirring solution of the porphyrin **3.19** (420 mg, 0.25 mmol) in chloroform (12 mL) and pyridine (0.17 mL). After 10 min, the solution was quenched with acetone (0.25 mL), the solution was concentrated and passed through a short plug eluting with a mixture of petroleum ether:CH_2Cl_2 (4:1). The solvent was removed under reduced pressure to give **3.21** as a dark green oil (0.42 g, 95 %). ^{1}H NMR (400 MHz, $CDCl_3$ + 1% pyridine-*d*5) δ 9.71 (d, J = 4.6 Hz, 2H), 8.93 (d, J = 4.6 Hz, 2H), 8.84 (d, J = 4.7 Hz, 2H), 8.82 (d, J = 4.7 Hz, 2H), 8.26 (d, J = 0.8 Hz, 4H), 8.18 (dd, J_1 = 7.9 Hz, J_2 =1.8 Hz, 2H), 7.98 (t, J = 0.8 Hz, 2H), 7.76-7.67 (m, 3H), 0.74–1.58 (m, 156H). ^{13}C{^{1}H} NMR (100 MHz, $CDCl_3$ + 1% pyridine-*d*5) δ 150.96, 150.80, 150.58, 149.71, 143.56, 141.47, 140.93, 139.07, 134.70, 134.53, 133.21, 132.48, 132.33, 132.02, 127.36, 126.44, 122.62, 121.46, 103.98, 33.73, 31.82, 24.25, 22.84, 14.30, 12.89. (MALDI TOF MS) *m/z*: $[M]^+$ Calcd. for $C_{110}H_{175}BrN_4Si_4Zn$: 1810.65; found: 1810.14.

(3.8)

3.21 (0.10 g, 0.055 mmol), palladium acetate (1.2 mg, 0.006 mmol); copper (I) iodide (2.2 mg, 0.012 mmol), and triphenylphosphine (3.0 mg, 0.012 mmol) were introduced into a Schlenk tube and pump-filled with nitrogen three times. Toluene (3.50 mL), diisopropyl amine (1.88 mL), and pyridine (0.10 mL) were added under nitrogen and the reaction stirred at room temperature for 15 minutes. Trimethylsilylacetylene (0.01 mL, 0.061 mmol) was added and the reaction stirred at 45 ^{o}C for 1 h. The reaction was stopped, solvent removed under reduced pressure, and the crude product was purified via

column chromatography (silica gel, dichloromethane:hexane as (1:9) as an eluent) to obtain **3.8** as a purple solid (70 mg, 70%).^{1}H NMR (400 MHz, $CDCl_3$) δ 9.87 (d, J = 4.6 Hz, 2H); 9.08 (d, J = 4.6 Hz, 2H); 8.97 (m, 4H); 8.38 (d, J = 0.96 Hz, 4H); 8.28 (m, 2H); 8.09 (s, 2H); 7.83 (m, 3H); 1.64-1.53 (m, 24H); 1.51-1.33 (m, 72H); 1.05-1.00 (m, 24H); 0.96 (m, 36H); 0.70 (s, 9H). $^{13}C\{^{1}H\}$ NMR (100 MHz, $CDCl_3$) δ 152.65, 150.88, 150.32, 149.90, 142.74, 140.62, 140.61, 139.16, 134.93, 134.25, 133.17, 132.18, 132.06, 131.00, 127.61, 126.59, 123.26, 122.87, 107.78, 101.09, 99.66, 33.63, 31.73, 24.14, 22.75, 14.25, 12.74. HRMS (MALDI): m/z $[M]^+$ Calcd. for $C_{115}H_{184}N_4Si_5Zn$: 1825.2659; found: 1825.2570. Anal. Calcd. for $C_{115}H_{184}N_4Si_5Zn$: C, 75.54; H, 10.14; N, 3.06. Found: C, 75.80; H, 10.16; N, 3.12.

(3.26)

3.7 (50 mg, 0.054 mmol), **3.9** (230 mg, 0.33 mmol), Pd_2dba_3 (5.0 mg, 0.0054 mmol), triphenylphosphine (5.7 mg, 0.022 mmol), and copper(I) iodide (5.7 mg, 0.030 mmol) were placed in a dry two-necked round-bottomed flask. Under nitrogen, anhydrous THF (1.5 mL) and di-isopropyl amine (1 mL, dried over 4 Å molecular sieves) were added and the reaction mixture was subjected to three freeze/pump/thaw cycles after which the reaction flask was refilled with nitrogen. Tetrabutylammonium fluoride (1 M solution in THF, 0.27 mL, 0.27 mmol) was added and the solution heated to 45 °C under nitrogen and monitored carefully by TLC (5% ethyl acetate in chloroform). After approximately one hour the solvents were removed under reduced pressure and passed through a column of silica eluting with 5% ethyl acetate in chloroform followed by a size exclusion column in THF. After concentration, the product was recrystallized from dichloromethane/hexane yielding **3.26** as a purple solid (50 mg, 65%). ^{1}H NMR (400 MHz, $CDCl_3$ + 1% pyridine-*d*5) δ 9.79 (s, 1 H), 8.99 (d, J = 4.6 Hz, 2 H), 8.99 (d, J = 4.6 Hz, 2 H), 8.83 (d, J = 4.6 Hz, 2 H), 8.78 (d, J = 4.6 Hz, 2 H), 8.17 (dd, J_1 = 7.8 Hz, J_2 = 1.3 Hz, 2 H), 8.04 (d, J = 1.7 Hz, 4 H), 8.00 (d, J = 1.4 Hz, 1 H), 7.98 (s, 1 H), 7.78 (t, J = 1.7 Hz, 2 H), 7.73 – 7.60 (m, 5 H), 7.17 (d, J = 8.2 Hz, 1 H), 6.75 (d, J = 8.2 Hz, 1 H), 6.06 (s, 1 H), 6.03 (s, 1H), 4.17 (br. s, 2 H), 4.02 (br. s, 2 H), 1.95 (s, 6 H), 1.80 (s, 6 H), 1.54 (s, 36 H), 1.49 (t, J = 7.2 Hz, 3 H), 1.38 (t, J = 7.2 Hz, 3 H). $^{13}C\{^{1}H\}$ NMR (100 MHz, $CDCl_3$ + 1% pyridine-*d*5) δ 182.25, 180.57, 179.92, 169.61, 168.42, 152.05,

150.71, 149.93, 149.71, 149.23, 148.35, 144.64, 143.35, 142.81, 142.02, 141.77, 141.59, 136.64, 134.27, 132.93, 131.82, 131.65, 131.56, 131.40, 130.15, 129.90, 127.20, 126.26, 125.33, 123.19, 122.37, 120.61, 120.16, 110.88, 109.52, 98.66, 95.65, 94.49, 87.19, 86.73, 86.50, 49.43, 49.20, 38.71 , 38.39, 35.00, 31.75, 27.13, 27.04, 12.16, 11.88. (MALDI TOF MS): m/z $[M]^+$ Calcd. for $C_{88}H_{85}N_6O_2IZn$: 1427.52; found: 1427.44.

(3.27)

3.7 (50 mg, 0.054 mmol), **3.10** (330 mg, 0.33 mmol), Pd_2dba_3 (5.0 mg, 0.0054 mmol), triphenylphosphine (5.7 mg, 0.022 mmol), and copper(I) iodide (5.7 mg, 0.030 mmol) were placed in a dry two-neck round bottom flask. Under nitrogen, anhydrous THF (1.5 mL) and diisopropylamine (1 mL, dried over 4 Å molecular sieves) were added and the reaction mixture was subjected to three freeze/pump/thaw cycles after which the reaction flask was refilled with nitrogen. Tetrabutylammonium fluoride (1 M solution in THF, 0.27 mL, 0.27 mmol) was added and the solution heated to 45°C under nitrogen and monitored carefully by TLC (5% ethyl acetate in chloroform). After ca. 1 h the solvents were removed under reduced pressure and passed through a column of silica eluting with 5% ethyl acetate in chloroform followed by a size exclusion column in THF. After concentration, the product was recrystallized from dichloromethane/hexane yielding **3.27** as a dark purple solid (65 mg, 71%). ^{1}H NMR (400 MHz, $CDCl_3$) δ 9.86 (d, J = 4.6 Hz, 2H); 9.11 (d, J = 46 Hz, 2H); 8.95 (d, J = 4.8 Hz, 2H); 8.90 (d, J = 4.80 Hz, 2H); 8.25 (dd, J_1 = 6.2 Hz, J_2 = 2.0 Hz, 2H); 8.14 (d, J = 1.5 Hz, 4H); 8.00-7.90 (m, 2H); 7.86 (t, J = 1.7 Hz, 2H); 7.82-7.73 (m, 3H); 7.66-7.56 (m, 2H); 7.16 (d, J = 8.8 Hz, 1H); 6.72 (d, J = 8.2 Hz, 1H), 5.14 (bs, 2H); 4.00 (m, 2H); 3.84 (m, 2H), 1.94 (s, 6H); 1.71 (s, 6H); 1.60 (m, 38H), 1.40-1.20 (m, 38H); 0.91 (m, 6H). ^{13}C{^{1}H} NMR (100 MHz, $CDCl_3$) δ 152.03, 150.85, 150.13,149.97, 148.62, 143.03, 142.33, 141.68, 136.59, 135.79, 134.40, 133.09, 132.18, 131.97, 131.60, 131.34, 130.40, 130.01, 128.28, 127.46, 126.52, 125.55, 125.16, 123.55, 122.47, 120.85, 119.67, 111.23, 109.83, 107.55, 99.73, 96.31, 93.93, 87.38, 86.48, 67.23, 66.47, 49.35, 49.06, 44.01, 43.65, 35.09, 31.95, 31.82, 30.35, 29.63, 29.58, 29.55, 29.47, 29.44, 29.37, 28.92, 27.19, 27.12, 27.08, 27.01, 26.97, 26.89, 24.45, 23.69, 22.73, 14.18. HRMS (MALDI): m/z [M+] Calcd. for $C_{106}H_{125}IN_6O_2Zn$:

1704.8200; found: 1704.8168. Anal. Calcd. for $C_{106}H_{125}IN_6O_2Zn$: C, 74.56; H, 7.38; N, 4.92. Found: C, 74.38; H, 7.55; N, 4.67.

(3.28)

3.8 (81 mg, 0.046 mmol), **3.10** (278 mg, 0.28 mmol), Pd_2dba_3 (4.2 mg, 0.0046 mmol), triphenylphosphine (4.8 mg, 0.019 mmol), and copper(I) iodide (4.8 mg, 0.025 mmol) were placed in a dry two-neck round bottom flask. Under nitrogen, anhydrous THF (2.0 mL) and di-isopropyl amine (0.85 mL, dried over 4 Å molecular sieves) were added and the reaction mixture was subjected to three freeze/pump/thaw cycles after which the reaction flask was refilled with nitrogen. Tetra-*n*-butylammonium fluoride (1 M solution in THF, 0.23 mL, 0.27 mmol) was added and the solution heated to 45 °C under nitrogen and monitored carefully by TLC (5% ethyl acetate in chloroform). After approximately one hour the solvents were removed under reduced pressure and passed through a column of silica eluting with 5% ethyl acetate in chloroform followed by a size exclusion column in THF. After concentration, the product was recrystallized from dichloromethane/hexane yielding **3.28** as a dark purple solid (90 mg, 75%).^{1}H NMR (400 MHz, $CDCl_3$) δ 9.89 (d, J = 4.6 Hz, 2H); 9.06 (d, J = 4.6 Hz, 2H); 8.90 (m, 4H); 8.33 (s, 4H); 8.23 (dd, J_1= 6.2 Hz, J_2= 2.4 Hz, 4H); 8.04-7.98 (m, 4H); 7.82-7.72 (m, 3H); 7.68-7.62 (m, 2H); 7.20-7.73 (d, J = 8.2 Hz, 1H); 6.78 (d, J = 8.2 Hz, 1H); 6.05 (s, 1H); 5.98 (s, 1H), 4.12 (m, 2H); 3.97 (m, 2H), 1.99 (s, 6H); 1.83 (s, 6H); 1.57-1.25 (m, 132H); 1.00-0.93 (m, 28); 0.93-0.87 (m, 42H). $^{13}C\{^1H\}$ NMR (100 MHz, $CDCl_3$) δ 182.29, 180.28, 180.08, 169.83, 169.00, 152.17, 150.83, 150.14, 150.06, 144.65, 142.85, 142.64, 142.52, 142.36, 140.56, 140.52, 139.14, 136.77, 136.64, 134.93, 134.22, 133.09, 132.13, 132.03, 131.82, 131.42, 130.65, 127.57, 126.57, 125.54, 125.34, 123.42, 122.68, 119.58, 111.24, 109.75, 100.29, 99.99, 96.49, 93.20, 87.58, 87.04, 86.60, 49.38, 49.25, 44.05, 43.84, 33.57, 31.95, 31.67, 30.33, 29.65, 29.63, 29.59, 29.55, 29.50, 29.44, 29.39, 29.38, 29.37, 27.24, 27.17, 27.13, 27.09, 27.01, 24.08, 22.72, 22.69, 14.21, 14.16, 12.68. HRMS (MALDI): *m/z* $[M]^+$ Calcd. for $C_{162}H_{245}IN_6O_2Si_4Zn$: 2609.6667; found: 2609.6818. Anal. Calcd. for $C_{162}H_{245I}N_6O_2Si_4Zn$: C, 74.45; H, 9.45; N, 3.22. Found: C, 74.69; H, 9.63; N, 3.24.

(3.29)

3.26 (50 mg, 0.035 mmol), (5-formylthiophen-2-yl)boronic acid (16.4 mg, 0.11 mmol), Pd(dppf)•CH_2Cl_2 (2.90 mg, 0.0035 mmol) and potassium carbonate (24.2 mg, 0.18 mmol) were placed in a dry two-necked round-bottomed flask. Under nitrogen, methanol (0.6 mL) and anhydrous toluene (0.6 mL) were added and the reaction mixture was subjected to three freeze/pump/thaw cycles after which the reaction flask was refilled with nitrogen. The solution was heated to 72 °C; after 1 h of heating the solvents were removed under reduced pressure and passed through a column of silica eluting with ethyl acetate/dichloromethane (1:19) followed by a size exclusion column in THF. After concentration, the product was recrystallized from dichloromethane/hexane yielding **3.29** as a dark purple solid (32 mg, 65%). ^{1}H NMR (400 MHz, $CDCl_3$ + 1% pyridine-d_5) δ 9.88 (s, 1H), 9.79 (d, J = 4.6 Hz, 2H), 8.99 (d, J = 4.6 Hz, 2H), 8.83 (d, J = 4.6 Hz, 2H), 8.78 (d, J = 4.6 Hz, 2H), 8.16 (dd, J_1 = 7.7 Hz, J_2 = 1.3 Hz, 2H), 8.03 (d, J = 1.6 Hz, 4H), 8.01 (d, J = 1.4 Hz, 1H), 7.99 (s, 1 H), 7.78 (t, J = 1.6 Hz, 2H), 7.73 (d, J = 3.8 Hz, 1H), 7.71 – 7.66 (m, 3H), 7.62 (s, 1 H), 7.60 (d, J = 1.6 Hz, 1H), 7.38 (d, J = 3.8 Hz, 1H), 7.19 (d, J = 8.3 Hz, 1H), 6.99 (d, J = 8.3 Hz, 1H), 6.09 (s, 1H), 6.03 (s, 1H), 4.20 (br. s, 2H), 4.06 (br. s, 2H), 1.96 (s, 6H), 1.86 (s, 6H), 1.54 (s, 36H), 1.50 (t, J = 7.2 Hz, 3H), 1.42 (t, J = 7.2 Hz, 3H). ^{13}C{^{1}H} NMR (100 MHz, $CDCl_3$ + 1% pyridine-*d5*) δ 182.57, 181.10, 169.90, 168.47, 154.07, 152.05, 150.70, 149.92, 149.71, 149.61, 148.33, 143.37, 143.15, 142.06, 141.92, 141.53, 137.56, 135.71, 134.30, 132.94, 131.81, 131.65, 131.58, 130.12, 129.89, 128.57, 127.19, 126.64, 126.26, 125.32, 123.69, 123.56, 123.42, 123.19, 122.38, 120.61, 120.38, 120.29, 109.66, 109.40, 98.55, 95.59, 94.62, 87.36, 87.33, 70.62, 49.54, 49.07, 38.81, 38.52, 34.99, 31.84, 27.18, 27.09, 12.23, 12.03. (MALDI TOF) *m/z* $[M]^+$Calcd. for $C_{91}H_{88}N_6O_3SZn$: 1411.60; found: 1411.03.

(3.30)

3.27 (60 mg, 0.035 mmol), (5-formylthiophen-2-yl)boronic acid (16.4 mg, 0.11 mmol), Pd(dppf)•CH_2Cl_2 (3.0 mg, 0.0035 mmol) and potassium carbonate (24 mg, 0.18 mmol) were placed in a dry two-necked round-bottomed flask. Under nitrogen, methanol (0.6 mL) and anhydrous toluene (0.6 mL) were added and the reaction mixture was subjected to three freeze/pump/thaw cycles after which the reaction flask was refilled

with nitrogen. The solution was heated to 72 °C, after 1 h of heating the solvents were removed under reduced pressure and passed through a column of silica eluting with ethyl acetate/dichloromethane (1:19) followed by a size exclusion column in THF. After concentration, the product was recrystallized from dichloromethane/hexane to yield **3.30** as a dark purple solid (45 mg, 75%).^{1}H NMR (400 MHz, $CDCl_3$) δ 9.86 (d, J = 4.2 Hz, 2H); 9.76 (s, 1H); 9.10 (d, J = 4.6 Hz, 2H); 8.95 (d, J = 4.4 Hz, 2H); 8.89 (d, J = 4.8 Hz, 2H); 8.25 (d, J = 6.0 Hz, 2H); 8.14 (d, 1.3 Hz, 4H); 7.96 (m, 2H); 7.86 (t, J = 1.7 Hz, 2H); 7.80-7.73 (m, 3H); 7.65 (d, J = 4.0 Hz, 2H); 7.57 (s, 1H); 7.55 (dd, J_1 = 8.2 Hz, J_2= 2.6 Hz, 2H); 7.31 (d, J = 4.0 Hz, 1H); 7.18 (d, J = 8.4 Hz, 1H); 6.94 (d, J = 8.2 Hz, 1H); 5.60 (bs, 2H); 4.04 (m, 2H); 3.89 (m, 2H); 1.94 (s, 6H); 1.71 (s, 6H); 1.60 (m, 40H), 1.40-1.20 (m, 38H); 0.91 (m, 6H). $^{13}C\{^{1}H\}$ NMR (100 MHz, $CDCl_3$) δ 182.51, 170.15, 168.73, 154.07, 152.03, 151.54, 150.85, 150.11, 149.95, 148.61, 143.68, 143.19, 143.05, 142.82, 142.24, 141.77, 141.71, 137.02, 135.79, 134.40, 133.08, 132.15, 131.96, 131.62, 130.37, 130.01, 128.44, 128.27, 127.45, 126.52, 125.55, 125.18, 123.53, 123.45, 122.49, 120.84, 120.16, 119.90, 109.94, 109.70, 107.57, 99.57, 96.20, 94.09, 84.52, 87.35, 67.32, 66.55, 49.48, 48.93, 44.08, 43.77, 35.09, 34.25, 31.95, 31.82, 30.35, 29.63, 29.58, 29.56, 29.47, 29.38, 28.92, 27.21, 27.19, 27.03, 24.51, 23.69, 22.73, 14.18. HRMS (MALDI): m/z 1688.8861 [M+] (calcd. for $C_{111}H_{128}N_6O_3SZn$: 1688.9060). Anal. Calcd. for $C_{111}H_{128}N_6O_3SZn•H_2O$ (%): C, 77.98; H, 7.66; N, 4.92. Found: C, 78.29; H, 7.66; N, 4.89.

(3.31)

3.28 (82 mg, 0.031 mmol), (5-formylthiophen-2-yl)boronic acid (15 mg, 0.094 mmol), Pd(dppf)•CH_2Cl_2 (3.0 mg, 0.003 mmol) and potassium carbonate (22 mg, 0.16 mmol) were placed in a dry two-neck round bottom flask. Under nitrogen, methanol (1.0 mL) and anhydrous toluene (1.0 mL) were added and the reaction mixture was subjected to three freeze/pump/thaw cycles after which the reaction flask was refilled with nitrogen. The solution was heated to 70 °C overnight. The solvents were removed under reduced pressure and passed through a column of silica eluting with ethyl acetate/dichloromethane (2.5:97.5) followed by a size exclusion column in THF. After concentration, the product was recrystallized from dichloromethane/hexane yielding **3.31**

as a dark purple solid (66 mg, 81%).^{1}H NMR (400 MHz, $CDCl_3$) δ 9.90 (s, 1H); 9.83 (d, J = 4.4 Hz, 2H); 8.99 (d, J = 4.6 Hz, 2H); 8.83 (m, 4H); 8.30 (d, J = 0.82 Hz, 4H); 8.21 (m, 2H); 8.04-7.98 (m, 4H); 7.80-7.70 (m, 4H); 7.66 (m, 2H); 7.42 (d, J = 4.0 Hz, 1H); 7.21 (d, J = 8.0 Hz, 1H); 7.03 (d, J = 8.8 Hz, 1H); 6.12 (s, 1H); 6.07 (s, 1H); 4.14 (m, 2H); 4.02 (m, 2H); 1.99 (s, 6H); 1.89 (s, 6H); 1.56-1.22 (m, 132H); 1.00-0.93 (m, 28H); 0.93-0.87 (m, 42H). ^{13}C{1H} NMR (100 MHz, $CDCl_3$) δ 182.57, 182.29, 180.98, 179.60, 170.28, 169.93, 154.11, 152.09, 150.70, 149.96, 149.84, 143.71, 143.33, 143.07, 142.89, 142.21, 141.93, 140.94, 140.61, 138.95, 137.57, 134.67, 134.27, 132.87, 131.83, 161.68, 130.30, 128.57, 127.35, 126.62, 126.38, 125.52, 125.28, 123.57, 123.07, 122.49, 120.26, 120.13, 109.88, 109.73, 99.22, 95.86, 94.04, 87.72, 49.51, 49.09, 44.14, 43.92, 33.56, 31.94, 31.65, 30.32, 29.64, 29.62, 29.58, 29.55, 29.51, 29.43, 29.40, 29.37, 29.35, 27.28, 27.18, 27.12, 24.07, 22.71, 22.67, 14.18, 14.14, 12.69. HRMS (MALDI): m/z $[M]^+$ Calcd. for $C_{167}H_{248}N_6O_3SSi_4Zn$: 2593.7527; found: 2593.7642. Anal. Calcd. for $C_{167}H_{248}N_6O_3SSi_4Zn$ (%): C, 77.22; H, 9.62; N, 3.24. Found: C, 77.36; H, 9.58; N, 3.33.

(3.32)

3.28 (42 mg, 0.016 mmol), **3.22** (21 mg, 0.032 mmol), Pd(dppf)•CH_2Cl_2 (2.0 mg, 0.002 mmol) and potassium carbonate (10 mg, 0.08 mmol) were placed in a dry two-neck round bottom flask. Under nitrogen, methanol (1.0 mL) and anhydrous toluene (1.5 mL) were added and the reaction mixture was subjected to three freeze/pump/thaw cycles after which the reaction flask was refilled with nitrogen. The solution was heated to 60 °C overnight. The solvents were removed under reduced pressure and passed through a column of silica eluting with ethyl acetate/hexane (3:17) to get **3.32** as a dark purple solid (35 mg, 73%).^{1}H NMR (400 MHz, $CDCl_3$) δ 9.86 (d, J = 4.6 Hz, 2H); 9.03 (d, J = 4.6 Hz, 2H); 8.88 (d, J = 4.8 Hz, 2H); 8.86 (d, J = 4.8 Hz, 2H); 8.30 (d, J = 0.85 Hz, 4H); 8.20 (dd, J_1 = 1.6 Hz, J_2 = 7.8 Hz); 8.02-7.94 (m, 4H); 7.80-7.68 (m, 3H); 7.58-7.50 (m, 2H), 7.26 (m, 1H); 7.15 (d, J = 8.0 Hz, 1H); 7.08 (s, 1H); 7.00 (d, J = 8.4 Hz, 2H); 6.03 (bs, 2H); 5.66 (s, 1H); 4.05 (bs, 4H); 3.79 (d, J = 11.0 Hz, 2H); 3.66 (d, J = 10.8 Hz, 2H); 1.96 (s, 6H); 1.87 (s, 6H); 1.80-1.91 (m, 4H); 1.60-1.10 (m, 178H); 1.00-0.70 (m, 60H). ^{13}C{1H} NMR (100 MHz, $CDCl_3$) δ 182.34, 180.25, 178.79, 170.05, 168.91, 152.19, 150.81, 150.13, 150.06, 149.28, 148.01, 144.67, 144.34, 143.97, 143.20, 142.82, 142.69,

141.73, 141.57, 140.56, 139.13, 134.92, 134.22, 133.41, 133.07, 132.10, 131.79, 131.11, 130.68, 127.95, 127.55, 126.55, 125.73, 125.49, 125.32, 123.37, 122.60, 122.41, 119.57, 119.17, 109.94, 109.71, 109.47, 100.42, 98.45, 96.65, 95.80, 95.03, 93.02, 87.38, 49.50, 49.16, 35.95, 35.87, 35.66, 35.61, 33.56, 31.95, 31.94, 31.66, 30.24, 29.72, 29.65, 29.63, 29.60, 29.57, 29.52, 29.46, 29.41, 29.38, 29.36, 29.90, 29.87, 29.86, 27.33, 27.22, 27.18, 27.13, 24.07, 23.08, 23.03, 23.00, 22.72, 22.69, 21.88, 14.20, 14.15, 12.69. LRMS (MALDI-MS): *m/z* $[M]^+$ Calcd. for $C_{192}H_{292}N_6O_4S_2Si_5Zn$: 3018; found: 3017.

(3.33)

3.32 (35 mg, 0.011 mmol) was dissolved in tetrahydrofuran (2.0 mL) and stirred at room temperature for 5 min. Water (0.5 mL) was added and reaction was stirred for another 5 min. Trifluoroacetic acid (44 µL, 0.58 mmol) was added and the reaction was stirred at room temperature for two days under nitrogen atmosphere. Saturated sodium bicarbonate solution (3 mL) was added and reaction mixture stirred for 1 h at room temperature. The organic layer was extracted with dichloromethane (10 × 3 mL), dried over anhydrous sodium sulfate and solvent removed to get the crude product which was passed through a column of silica eluting with ethyl acetate/hexane (3:17) to get **3.33** as a dark purple solid (33 mg, 97%). ^{1}H NMR (400 MHz, $CDCl_3$) δ 9.90 (d, J = 4.6 Hz, 2H); 9.87 (s, 1H); 9.07 (d, J = 4.6 Hz, 2H); 8.91 (m, 4H); 8.34 (s, 4H); 8.23 (dd, J_1 = 1.4 Hz, J_2 =8.0 Hz, 2H); 8.02 (m, 4H); 7.85-7.72 (m, 4H); 7.63-7.60 (m, 2H); 7.37 (t, J = 1.6 Hz, 1H); 7.20 (d, J = 8.4 Hz, 1H); 7.05 (d, J = 8.8 Hz, 1H); 6.06 (bs, 2H); 4.12 (bs, 2H); 4.07 (bs, 2H); 2.00 (s, 6H); 1.20-1.90 (m, 6H); 1.91 (s, 6H); 1.55-1.15 (m, 176H); 1.00-0.78 (m, 54H). ^{13}C{^{1}H} NMR (100 MHz, $CDCl_3$) δ 182.55, 182.40, 179.94, 179.71, 169.53, 158.47 (t), 152.18, 150.83, 150.14, 150.07, 149.17 (t), 148.68, 146.39, 144.45, 143.31, 142.99, 142.87, 142.58, 142.41, 140.55, 139.74, 139.14, 134.93, 134.21, 133.08, 132.12, 131.18, 130.65, 130.05, 127.56, 126.56, 125.93, 125.84, 125.34, 123.40, 122.66, 119.80, 119.49, 109.90, 109.67, 100.32, 98.45, 96.53, 93.17, 87.52, 49.32, 44.02, 35.94, 35.91, 35.70, 35.65, 33.56, 31.95, 31.49, 29.72, 29.65, 29.63, 29.59, 29.56, 29.52, 29.45, 29.41, 29.37, 29.19, 28.94, 28.92, 28.88, 27.27, 27.21, 27.13, 24.08, 23.08, 22.99, 22.69, 17.60, 17.52, 14.20, 14.15, 12.69. LRMS (MALDI-MS): *m/z* $[M]^+$ Calcd. for $C_{187}H_{282}N_6O_3S_2Si_5Zn$: 2932; found: 2932.

(3.3)

2.29 (25 mg, 0.018 mmol), and cyanoacetic acid (120 mg, 1.40 mmol) were placed in a dry two-necked round-bottomed flask with reflux condenser attached. Under nitrogen, anhydrous chloroform (2.7 mL), anhydrous acetonitrile (2.7 mL) and piperidine (80 μL, 0.70 mmol) were added and the solution heated to reflux at 62 °C for 4 h. The extent of completion of the reaction was monitored by TLC (ethyl acetate/ methanol, 7:1) and MALDI MS. The solvent was removed under reduced pressure and the crude mixture was firstly precipitated from dichloromethane/acetonitrile, and then dichloromethane/hexane to give **3.3** as a black powder (22 mg, 85%). ^{1}H NMR (500 MHz, $CDCl_3$ with 1% pyridine-*d*5), δ 9.79 (d, J = 4.6 Hz, 2H), 8.99 (d, J = 4.6 Hz, 2H), 8.83 (d, J = 4.6 Hz, 2H), 8.78 (d, J = 4.6 Hz, 2H), 8.27 (s, 1H), 8.17 (dd, J_1 = 7.5 Hz, J_2 = 1.5 Hz, 2H), 8.03 (d, J= 1.7 Hz, 4H), 8.01 (d, J = 1.4 Hz, 1H), 7.99 (s, 1H), 7.78 (t, J = 1.7 Hz, 2H), 7.73 (d overlap with other peaks, 1H), 7.72 – 7.61 (m, 5H), 7.36 (d, J = 3.9 Hz, 1H), 7.18 (d, J = 8.3 Hz, 1H), 6.99 (d, J = 8.3 Hz, 1H), 6.09 (s, 1H), 6.03 (s, 1H), 4.19 (br. s, 2H), 4.08 (br. s, 2H), 1.96 (s, 6 H), 1.87 (s, 6H), 1.54 (s, 36H), 1.50 (t, J = 7.2 Hz, 3H), 1.43 (t, J = 7.2 Hz, 3H). ^{13}C{^{1}H} NMR (126 MHz, $CDCl_3$ with 1% pyridine-*d5*) δ 182.62, 182.20, 180.70, 169.67, 168.71, 152.07, 151.48, 150.68, 149.91, 149.74, 149.70, 149.65, 148.33, 143.36, 143.02, 142.88, 142.01, 141.56, 137.00, 135.96, 135.70, 134.26, 132.92, 131.78, 131.63, 131.57, 130.12, 129.89, 128.90, 127.18, 126.52, 126.25, 125.33, 123.70, 123.51, 122.34, 120.59, 120.21, 120.16, 118.73, 116.98, 109.57, 109.44, 98.61, 95.65, 94.53, 87.31, 87.27, 49.46, 49.21, 44.27, 38.74, 38.60, 34.99, 31.75, 27.13, 27.04, 12.18, 12.06. (MALDI TOF MS) *m/z* $[M]^+$ Calcd. for $C_{92}H_{89}N_7O_4SZn$: 1478.61; found: 1478.60. UV/vis (THF + 1% pyridine): λ_{max} (log ε) = 435 (5.16), 576 (4.20), 623 (4.63), 719 nm (5.28).

(3.4)

3.30 (22 mg, 0.015 mmol), and cyanoacetic acid (97 mg, 1.14 mmol) were placed in a dry two-necked round-bottomed flask. Under nitrogen, anhydrous chloroform (2.7 mL), anhydrous acetonitrile (2.7 mL) and piperidine (60 μL, 0.56 mmol) were added and the solution heated at 65 °C for 3 h. The extent of completion of the reaction was monitored by TLC (ethyl acetate/ methanol, 7:1). The solvent was removed under

reduced pressure and the crude mixture was firstly precipitated from dichloromethane/acetonitrile, and then from dichloromethane/hexane to give **3.4** as a black powder (15mg, 65%). ^{1}H NMR (400 MHz, $CDCl_3$ with 1% pyridine-*d*5) δ 9.79 (d, *J* = 4.6 Hz, 2H); 8.98 (d, *J* = 4.6 Hz, 2H); 8.83 (d, *J* = 4.4 Hz, 2H); 8.78 (d, *J* = 4.8 Hz, 2H); 8.28 (s, 1H); 8.16 (d, *J* = 8.8 Hz, 2H); 8.04 (s, 4H); 8.00 (s, 1H); 7.96 (s, 1H); 7.78 (t, *J* = 1.9 Hz, 2H); 7.73-7.60 (m, 6H); 7.37 (d, *J* = 4.0 Hz, 1H); 7.17 (d, *J* = 8.0 Hz, 1H); 6.97 (d, *J* = 8.2 Hz, 1H); 6.09 (s, 1H); 6.04 (s, 1H); 4.09 (bs, 2H); 3.99 (bs, 2H); 1.96 (s, 6H); 1.86 (s, 6H); 1.53 (m, 36H), 1.40-1.20 (m, 41H); 0.91 (m, 6H). ^{13}C{^{1}H} NMR (126 MHz, $CDCl_3$ with 1% MeOH-*d*4): δ 182.79, 178.96, 177.87, 170.40, 169.34, 166.07, 152.82, 152.02, 150.70, 149.80, 149.39, 148.53, 145.02, 143.50, 143.14, 142.85, 142.18, 141.83, 141.51, 138.15, 135.08, 134.30, 132.98, 131.91, 131.81, 131.67, 130.25, 129.35, 128.70, 127.33, 126.65, 126.39, 125.27, 123.70, 123.24, 122.42, 120.72, 120.13, 117.60, 116.44, 110.01, 109.92, 101.11, 98.99, 95.89, 94.19, 87.66, 44.28, 44.12, 43.95, 35.03, 31.90, 31.74, 31.65, 31.57, 29.60, 29.59, 29.56, 29.54, 29.51, 29.49, 29.42, 29.39, 29.33, 27.26, 27.12, 27.07, 27.02, 22.71, 22.68, 22.63, 22.34, 14.10. HRMS (MALDI-MS): *m/z* $[M]^+$ Calcd. for $C_{114}H_{129}N_7O_4SZn$: 1755.9118; found: 1755.9163.

(3.5)

3.31 (66 mg, 0.025 mmol), and cyanoacetic acid (166 mg, 1.14 mmol) were placed in a dry two-necked round-bottomed flask. Under nitrogen, anhydrous chloroform (4.50 mL), anhydrous acetonitrile (4.50 mL) and piperidine (90 μL, 0.97 mmol) were added and the solution heated at 65 °C for 5 hours. The extent of completion of the reaction was monitored by TLC (ethyl acetate/ methanol, 7:1). The solvent was removed under reduced pressure and the crude mixture was purified via column chromatography using deactivated silica gel (1% triethylamine in ethyl acetate was passed through the column which was then repeatedly washed with ethyl acetate to remove the triethylamine) and eluting with methanol/ethyl acetate (3:17) to give **3.5** as a black powder (30 mg, 45%).^{1}H NMR (400 MHz, $CDCl_3$ with 1% pyridine-d5) δ 9.77 (d, *J* = 4.4 Hz, 2H); 8.94 (d, *J* = 4.5 Hz, 2H); 8.78 (d, *J* = 4.6 Hz, 2H); 8.77 (d, *J* = 4.4 Hz, 2H); 8.30 (s, 1H); 8.25 (s, 4H); 8.16 (d, *J* = 6.8 Hz, 2H); 8.00-7.92 (m, 2H); 7.74-7.60 (m, 6H); 7.37 (s, 1H); 7.16 (d, *J* = 8.4 Hz, 1H); 6.99 (d, *J* = 8.4 Hz, 1H); 6.10 (s, 1H); 6.05 (s,

1H); 4.09 (bs, 2H); 4.00 (bs, 2H); 1.95 (s, 6H); 1.87 (s, 6H); 1.55-1.20 (m, 176H); 0.95-0.75 (m, 87H). $^{13}C\{1H\}$ NMR (126 MHz, $CDCl_3$ with 1% MeOH-*d*4) δ 182.94, 178.30, 177.34, 170.42, 169.49, 166.37, 166.23, 152.61, 151.99, 150.65, 149.86, 149.77, 144.90, 143.42, 143.17, 143.08, 142.76, 142.12, 140.95, 140.61, 138.84, 138.05, 135.11, 134.60, 134.23, 132.74, 132.23, 131.70, 130.14, 128.79, 127.23, 126.64, 126.29, 125.10, 123.71, 122.95, 122.47, 122.28, 120.18, 120.09, 117.63, 110.01, 109.75, 101.47, 98.86, 95.68, 94.14, 87.53, 45.84, 44.08, 43.93, 33.47, 31.84, 31.54, 26.91, 29.59, 29.54, 29.50, 29.45, 29.43, 29.37, 29.34, 29.27, 29.26, 27.22, 27.11, 26.99, 26.98, 23.99, 22.58, 14.05, 13.99, 12.60. LRMS (MALDI): *m/z* $[M]^+$ Calcd. for $C_{170}H_{249}N_7O_4SSi_4Zn$: 2664; found: 2664.

(3.6)

3.33 (32 mg, 0.011 mmol), and cyanoacetic acid (71 mg, 0.84 mmol) were placed in a dry two-neck round bottom flask. Under nitrogen, anhydrous chloroform (3.50 mL), anhydrous acetonitrile (3.50 mL) and piperidine (40 μL, 0.42 mmol) were added and the solution heated at 60 °C for overnight. Partial completion was observed via TLC, piperidine (40 μL, 0.42 mmol) was added and reaction stirred overnight at 70 ^oC. The extent of completion of the reaction was monitored by TLC (ethyl acetate/ methanol, 7:1). The solvent was removed under reduced pressure and the crude mixture was purified via column chromatography using deactivated silica gel (1% triethylamine in ethyl acetate was passed through the column which was then repeatedly washed with ethyl acetate to remove the triethylamine) and eluting with methanol/ethyl acetate (10:90) to give **3.6** as a black powder (20 mg, 64%). ^1H NMR (500 MHz, $CDCl_3$ with 1% pyridine-*d*5) δ 9.84 (d, J = 4.5 Hz, 2H); 9.01 (d, J = 4.5 Hz, 2H); 8.84 (dd, J_1 = 5.0 Hz; J_2 = 1.4 Hz, 4H); 8.31 (s, 4H); 8.21 (d, J = 7.0 Hz, 2H); 8.00 (m, 4H); 7.75 (m, 4H); 7.60 (m, 4H); 7.35 (s, 1H); 7.18 (d, J = 8.0 Hz, 1H); 7.03 (d, J = 8.2 Hz, 1H); 6.11 (s, 1H); 6.08 (s, 1H); 4.11 (bs, 2H); 4.06 (bs, 2H); 1.98 (s, 6H); 1.89 (s, 6H); 2.00-1.85 (m, 6H); 1.55-1.15 (m, 178H); 1.00-0.78 (m, 54H). $^{13}C\{^1H\}$ NMR (126 MHz, $CDCl_3$ with 10% pyridine-*d*5) δ 182.35, 179.71, 179.34, 169.50, 169.34, 167.50, 156.22, 152.06, 150.64, 150.14, 149.87, 149.74, 147.85, 146.87, 143.48, 143.25, 142.95, 142.27, 142.15, 141.14, 140.62, 138.80, 138.60, 138.19, 134.50, 134.25, 132.75, 131.68, 131.53, 130.20, 130.18, 127.18, 126.23, 125.88, 125.78, 125.14, 122.41, 119.79, 119.58, 119.05, 109.91, 109.60,

98.88, 95.76, 994.20, 87.42, 49.29, 49.23, 45.69, 43.96, 35.87, 35.82, 35.65, 35.59, 33.51, 31.89, 31.60, 29.67, 29.60, 29.58, 29.55, 29.54, 29.51, 29.47, 29.40, 29.37, 29.32, 29.31, 28.86, 28.84, 28.83, 27.21, 27.14, 27.10, 27.08, 24.05, 22.97, 22.94, 22.67, 22.65, 22.62, 17.60, 17.49, 14.14, 14.10, 12.65, 10.78, 8.57. LRMS (MALDI-MS): *m/z* $[M]^+$ 2999 Calcd. for $C_{190}H_{283}N_7O_4S_2Si_5Zn$: 2999; Found: 2999.

3.4.2 Optical and electrochemical measurements

Electronic spectroscopic data were collected in ethanol on a UV-Vis-NIR spectra were recorded in 1 cm quartz cuvette using a Agilent Cary 5000 spectrophotometer, and emission spectra were collected using a Horiba Jobin Yvon Fluorolog-3 equipped with an iHR320 monochrometer, and a CCD detector. Electrochemical measurements were carried out under an inert atmosphere in dry deoxygenated tetrahydrofuran solution containing 0.1 M tetrabutylammonium hexafluorophosphate as an electrolyte. A CH-Instrument 620D potentiostat equipped with a conventional three-electrode cell utilizing a glassy carbon working electrode, platinum wire counter electrode, and a silver wire coated with silver chloride as the pseudo-reference electrode, was used for the measurements. Potentials were referenced to decamethylferrocene/decamethferrocenium ($FeCp_2^{*+/0}$) by using decamethylferrocene as an internal reference. ($E(FeCp_2^{*+/0})$ was determined to be -0.46 V vs. $FeCp_2^{+/0}$ in THF). Potentials where then transferred to the NHE scale ($FeCp_2^{+/0}$ +0.80 V vs. NHE).[41] Cyclic voltammograms were recorded at a scan rate of 50 mV s^{-1}.

3.5 REFERENCES

(1) http://www.merriam-webster.com/dictionary/panchromatic.

(2) Péchy, P.; Renouard, T.; Zakeeruddin, S. M.; Humphry-Baker, R.; Comte, P.; Liska, P.; Cevey, L.; Costa, E.; Shklover, V.; Spiccia, L.; Deacon, G. B.; Bignozzi, C. A.; Grätzel, M. *J. Am. Chem. Soc.* **2001**, *123*, 1613.

(3) Kuang, D.; Walter, P.; Nüesch, F.; Kim, S.; Ko, J.; Comte, P.; Zakeeruddin, S. M.; Nazeeruddin, M. K.; Grätzel, M. *Langmuir* **2007**, *23*, 10906.

(4) Delcamp, J. H.; Shi, Y.; Yum, J.-H.; Sajoto, T.; Dell'Orto, E.; Barlow, S.; Nazeeruddin, M. K.; Marder, S. R.; Grätzel, M. *Chem. - Eur. J.* **2013**, *19*, 1819.

(5) Hardin, B. E.; Hoke, E. T.; Armstrong, P. B.; Jun-Ho, Y.; Comte, P.; Torres, T.; Fréchet, J. M. J.; Nazeeruddin, K.; Grätzel, M.; McGehee, M. D. *Nat. Photonics* **2009**, *3*, 406.

(6) Warnan, J.; Pellegrin, Y.; Blart, E.; Odobel, F. *Chem. Commun.* **2012**, *48*, 675.

(7) Louahem M'Sabah, B.; Boucharef, M.; Warnan, J.; Pellegrin, Y.; Blart, E.; Lucas, B.; Odobel, F.; Boucle, J. *Phys. Chem. Chem. Phys.* **2015**, *17*, 9910.

(8) Warnan, J.; Gardner, J.; Le Pleux, L.; Petersson, J.; Pellegrin, Y.; Blart, E.; Hammarström, L.; Odobel, F. *J. Phys. Chem. C* **2013**, *118*, 103.

(9) Panda, D. K.; Goodson, F. S.; Ray, S.; Saha, S. *Chem. Commun.* **2014**, *50*, 5358.

(10) Warnan, J.; Buchet, F.; Pellegrin, Y.; Blart, E.; Odobel, F. *Org. Lett.* **2011**, *13*, 3944.

(11) Xie, Y.; Tang, Y.; Wu, W.; Wang, Y.; Liu, J.; Li, X.; Tian, H.; Zhu, W.-H. *J. Am. Chem. Soc.* **2015**, *137*, 14055.

(12) Kakiage, K.; Aoyama, Y.; Yano, T.; Oya, K.; Fujisawa, J.-i.; Hanaya, M. *Chem. Commun.* **2015**, *51*, 15894.

(13) Kakiage, K.; Aoyama, Y.; Yano, T.; Oya, K.; Kyomen, T.; Hanaya, M. *Chem. Commun.* **2015**, *51*, 6315.

(14) Jradi, F. M.; Kang, X.; O'Neil, D.; Pajares, G.; Getmanenko, Y. A.; Szymanski, P.; Parker, T. C.; El-Sayed, M. A.; Marder, S. R. *Chem. Mater.* **2015**, *27*, 2480.

(15) Beverina, L.; Salice, P. *Eur. J. Org. Chem.* **2010**, *2010*, 1207.

(16) Pydzińska, K.; Ziółek, M. *Dyes Pigm.* **2015**, *122*, 272.

(17) Ragoussi, M.-E.; Yum, J.-H.; Chandiran, A. K.; Ince, M.; de la Torre, G.; Grätzel, M.; Nazeeruddin, M. K.; Torres, T. *ChemPhysChem* **2014**, *15*, 1033.

(18) Qin, C.; Wong, W.-Y.; Han, L. *Chem. - Asian J.* **2013**, *8*, 1706.

(19) Choi, H.; Kim, J.-J.; Song, K.; Ko, J.; Nazeeruddin, M. K.; Gratzel, M. *J. Mater. Chem.* **2010**, *20*, 3280.

(20) Yagi, S.; Hyodo, Y.; Matsumoto, S.; Takahashi, N.; Kono, H.; Nakazumi, H. *J. Chem. Soc., Perkin Trans. 1* **2000**, 599.

(21) Webster, S.; Odom, S. A.; Padilha, L. A.; Przhonska, O. V.; Peceli, D.; Hu, H.; Nootz, G.; Kachkovski, A. D.; Matichak, J.; Barlow, S.; Anderson, H. L.; Marder, S. R.; Hagan, D. J.; Van Stryland, E. W. *J. Phys. Chem. B* **2009**, *113*, 14854.

(22) Shi, Y.; Hill, R. B. M.; Yum, J.-H.; Dualeh, A.; Barlow, S.; Grätzel, M.; Marder, S. R.; Nazeeruddin, M. K. *Angew. Chem.* **2011**, *123*, 6749.

(23) Lo, C.-F.; Luo, L.; Diau, E. W.-G.; Chang, I. J.; Lin, C.-Y. *Chem. Commun.* **2006**, 1430.

(24) Senge, M. O. *Acc. Chem. Res.* **2005**, *38*, 733.

(25) Ryan, A.; Gehrold, A.; Perusitti, R.; Pintea, M.; Fazekas, M.; Locos, O. B.; Blaikie, F.; Senge, M. O. *Eur. J. Org. Chem.* **2011**, *2011*, 5817.

(26) Angyal, S. *Organic Reactions* **1954**.

(27) Odom, S. A.; Webster, S.; Padilha, L. A.; Peceli, D.; Hu, H.; Nootz, G.; Chung, S.-J.; Ohira, S.; Matichak, J. D.; Przhonska, O. V.; Kachkovski, A. D.; Barlow, S.; Brédas, J.-L.; Anderson, H. L.; Hagan, D. J.; Van Stryland, E. W.; Marder, S. R. *J. Am. Chem. Soc.* **2009**, *131*, 7510.

(28) Getmanenko, Y. A.; Tongwa, P.; Timofeeva, T. V.; Marder, S. R. *Org. Lett.* **2010**, *12*, 2136.

(29) Huo, L.; Chen, H.-Y.; Hou, J.; Chen, T. L.; Yang, Y. *Chem. Commun.* **2009**, 5570.

(30) Wang, P. Z., Wangdong; Xu, Mingfei; Bai, Yu; Zhang, Jing In *Faming Zhuanli Shenqing*; Shenqing, F. Z., Ed. China, 2009; Vol. CN 101544845.

(31) Subramaniyan, S.; Xin, H.; Kim, F. S.; Jenekhe, S. A. *Macromolecules* **2011**, *44*, 6245.

(32) Jung, M.-H.; Song, K. H.; Ko, K. C.; Lee, J. Y.; Lee, H. *J. Mater. Chem.* **2010**, *20*, 8016.

(33) Hagfeldt, A.; Boschloo, G.; Sun, L.; Kloo, L.; Pettersson, H. *Chem. Rev.* **2010**, *110*, 6595.

(34) Kalyanasundaram, K.; Grätzel, M. *Coord. Chem. Rev.* **1998**, *177*, 347.

(35) Rothenberger, G.; Fitzmaurice, D.; Graetzel, M. *J. Phys. Chem.* **1992**, *96*, 5983.

(36) Redmond, G.; Fitzmaurice, D. *J. Phys. Chem.* **1993**, *97*, 1426.

(37) Listorti, A.; O'Regan, B.; Durrant, J. R. *Chem. Mater.* **2011**, *23*, 3381.

(38) O'Regan, B. C.; Durrant, J. R.; Sommeling, P. M.; Bakker, N. J. *J. Phys. Chem. C* **2007**, *111*, 14001.

(39) Boschloo, G.; Hagfeldt, A. *Acc. Chem. Res.* **2009**, *42*, 1819.

(40) Kasha, M. *Discuss. Faraday Soc.* **1950**, *9*, 14.

(41) Connelly, N. G.; Geiger, W. E. *Chem. Rev.* **1996**, *96*, 877.

CHAPTER 4 ASYMMETRIC PERYLENE DIIMIDE PHOSPHONIC ACID REDOX-ACTIVE SURFACE MODIFIERS; DESIGN, SYNTHESIS, AGGREGATION AND ELECTRON TRANSFER STUDIES AT THE ACCEPTOR-CONDUCTING OXIDE INTERFACE

4.1 INTRODUCTION

Transparent metal oxides (TCOs) are essential electrode materials for applications in organic electronics such as organic light-emitting diodes,[1] and emerging photovoltaics.[2-5] Indium tin oxide (ITO), is the most commonly used TCO, due to its good electrical conductivity and high optical transparency.[6] However, untreated, ITO has shortcomings such as; a polar/hydrophilic surface, that might lead to poor compatibility with organic semiconductors, especially when the latter is solution processed,[7] electrical heterogeneity - presence of electrical hotspots,[8] and a work function that is generally in the range of 4.5 to 4.7 eV, which does not provide for efficient hole injection into many hole-transport materials.[9]

The electronic and chemical properties of ITO can be, however, altered through surface modification, and to this end a variety of methods have been reported such as; acid treatments,[10] oxidative treatments,[11] modification with amine functionalized polymeric materials, such as polyethylenimine ethoxylated,[12] and modification with small molecules.[13] Small molecule modifiers, which are of interest in this chapter, have been widely used in literature to modify oxides and can be used to achieve one or more of the following: (i) lower the surface energy of a particular oxide which allows for better physical contact with the overlaying layer, (ii) tune the oxide's work function, (iii) stabilize the oxide's surface against hydrolysis, (iv) form selective charge carrier at the electrode, and enhance rates of electron transfer across the oxide's interface.[6,14,15]

Small molecule modifiers can be linked to the oxide's surface through either physisorption; a weak binding interaction where the binding energy is approximately

0.01-0.1 eV, or chemisorption, which is a stronger binding interaction with binding energies up to 10 eV.[16] The latter form of interaction involves the formation of strong covalent or ionic bonds between the modifier and the substrate, and is preferred over physisorption in many organic electronic applications as it has the ability to provide more robust monolayers that are resilient to solvent and/or heat exposure. In the literature, many classes of compounds have been shown to modify surfaces, such as (i) organosulfur compounds (thiols, disulfides, and sulfides), which are particularly suitable for the modification of gold surfaces via chemisorption,[17] (ii) organosilicon compounds (chlorosilanes and silyl ethers), which can form stable oxygen-silicon bonds on hydroxyl terminated substrates such as silicon or glass,[18] (iii) carboxylic acids which bind to surfaces via an acid-base reaction between the binding group and the substrate (such as alumina, and ITO),[19,20] and finally (iv) phosphonic acids, which form stronger bonds to surfaces than carboxylic acids, and can bind to surfaces such as titania, alumina, and ITO.[21]

As an example on the modification of the properties of ITO; Panaigua *et al.* studied the effects of tuning the surface energy of ITO with phosphonic acid surface modifiers and observed a decrease of the overall surface energy from ca. 70 mJ/m^2 to ca. 30 mJ/m^2 in detergent-cleaned and plasma-cleaned ITO.[7] On the other hand, fluorine-substituted benzyl phosphonic acids, with varying degrees of fluorinations and position of fluorine atoms on the aromatic ring, were reported to vary the work function of ITO over a range of 1.2 eV, through varying the magnitude and direction of the molecule's dipole moment on the surface.[22]

Surface-modified ITO was shown, in some occasions, to enhance the efficiency or stability of organic electronic device; for example, by reducing the surface energy of ITO with a monolayer of *N*-propyltriethoxysilane adsorbed to its surface, Kim *et al.* demonstrated that the P3HT/$PC_{61}BM$ overlying layer in an OPV could be thermally annealed without experiencing phase separation, as opposed to when unmodified ITO was used, and reported an increase in the OPV's PCE from 0.75% to 3.20%.[23] Also, McGehee *et al.* examined the effects of modifying the surface of TiO_2 with a series of *para*-substituted benzoic acids, with varying dipole moments, on the photovoltaic

performance of a hybrid TiO_2/P_3HT bilayer photovoltaic device.[24] Depending on the direction of the dipole (with respect to TiO_2), the authors were able to tune V_{OC} of the bilayer device by ca. 0.25 V in the dark, Figure 4.1, by altering the work function. In addition, an up to two fold increase in J_{SC} was observed upon modification, which could be due to the increased electron withdrawing ability of some of these modifiers (nitro substituted benzoic acid's LUMO is reported to be ca. 4.0 eV, ca. 1.0 eV higher than the LUMO of benzoic acid),[25,26] as observed by their efficient quenching of the photo-luminescence of the excited P3HT.

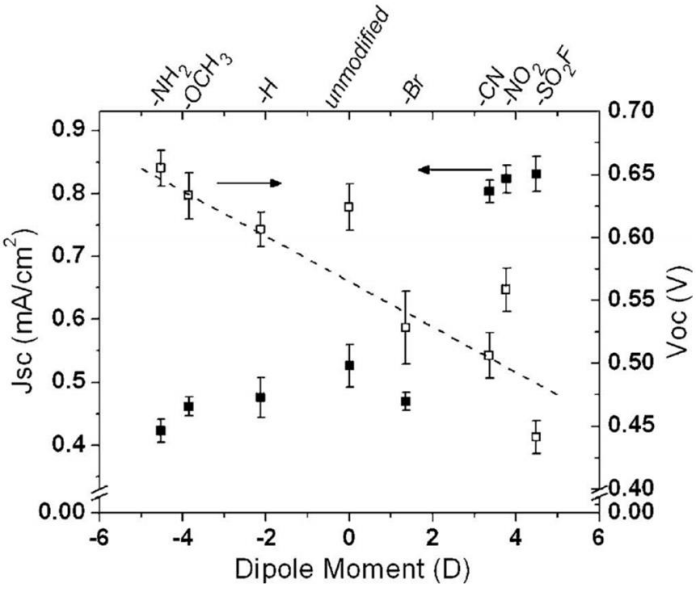

Figure 4.1 The V_{OC} and J_{SC} of bilayer devices fabricated with benzoic acid surface modifiers of varying para-substitutions; Note the direction of the dipole is defined from -ve sign to +ve sign. Reproduced from McGehee *et al.*[24]

Other than tuning the work function and surface energy of ITO, charge collection at the ITO/organic interface is another parameter that can be probed and altered via the adsorption of small molecules. As mentioned earlier, the surface of ITO is electrically heterogeneous, which could be due to the chemical and structural heterogeneity of its surface.[6] Donley *et al.* deposited redox-active ferrocene dicarboxylic acid ($Fe(C_5H_4CO_2H)_2$) onto the ITO surface, through chemisorption to surface hydroxide groups, and measured the electron-transfer to ITO via cyclic voltammetry.[27] The goal was to determine the fraction of electrochemically active sites on ITO surfaces subjected to various solution pretreatment and cleaning procedures.[28] By comparing the hydroxide

surface coverages on piranha-cleaned or amorphous ITO surfaces determined from x-ray photoelectron spectroscopy (XPS) to the electroactive surface coverage determined from electrochemistry, the authors noticed that, although the hydroxide surface coverage was similar in both cases (ca. 50%), the electroactive monolayer coverage varied from 5% in the case of piranha-treated ITO to 31% in amorphous ITO. The authors suggested that although a similar concentration of $Fe(C_5H_4CO_2H)_2$ can be present on the surface, due to the similar hydroxide coverage, electrochemically they might not be detected if they are present on electrochemically "dead regions" on ITO, thus hinting to low apparent surface bound $Fe(C_5H_4CO_2H)_2$. Other studies suggested that only after aggressive cleaning and pretreatment steps can 50 – 80% of the geometric area be rendered electroactive, and this lasts for only few minutes under ambient atmospheric conditions.[29]

Determining the electrochemically active sites on ITO necessitates that these surface-bound redox active modifiers serve as mediators for outer-sphere electron transfer from a solution donor into the ITO. Through assessing the rate of electron transfer (k_S) across the ITO interface from a solution donor ($FeCp_2^{+/0}$), it was found that ITO modified with $Fe(C_5H_4CO_2H)_2$ and 3-thiophene acetic acid (3-TAA) had higher k_S when compared to bare ITO, Table 4.1.[30] However, the electron transfer rate was still lower than that of ITO modified with ca. 50 nm layer of PEDOT:PSS, which could be due to the non optimal electroactive surface coverage as explained earlier.

Table 4.1 Effective electron transport rate coefficient, *k*s, obtained at unmodified ITO, and ITO modified with $Fe(C_5H_4CO_2H)_2$ and 3-TAA, and PEDOT:PSS.[30]

Modification	**k_S from $FeCp_2^{+/0}$ ($\times 10^{-3}$ cm s^{-1})**
Unmodified ITO	0.6
$Fc(CO_2H)_2$	3.9
3-TAA	3.3
PEDOT:PSS	16.0

Building upon these findings, Marrikar *et al.*[29] chemisorbed an alkyl carboxylic derivative of 3,4-ethylenedioxythiophene (EDOT) on acid (HI) treated ITO, and then electrochemically grew copolymer films of PEDOT on the surface. As before, using

solution probe molecules such as $FeCp_2$ and $FeCp_2^*$ ($Cp_2^* = C_5Me_5$), they measured the electron transfer rate from the probe into ITO and found that it is ca. 0.4 cm s^{-1}, four orders-of-magnitude higher than on unmodified ITO, and around one order-of-magnitude higher than ITO modified with PEDOT:PSS.[29] A possible explanation of the observed increase in electron transfer rate is highlighted in Figure 4.2. On the left is a schematic of a solvent cleaned ITO that shows electrochemically active sites "hot-spots" (red regions), and electrochemically inactive sites (grey region). After HI etching, more of the active sites are exposed which can be later on modified with 3,4-ethylenedioxythiophene carboxylic acid (EDOT-CA). Chemisorbed EDOT-CA can then be polymerized electrochemically to result in surface bound PEDOT. The resultant PEDOT individual chains become overlapped forming a continuous redox-active surface from the perspective of the solution probe. After electron transfer into this redox-active PEDOT, the electron transfers through the continuous layer until it reaches an electrochemically active site and injects into ITO.

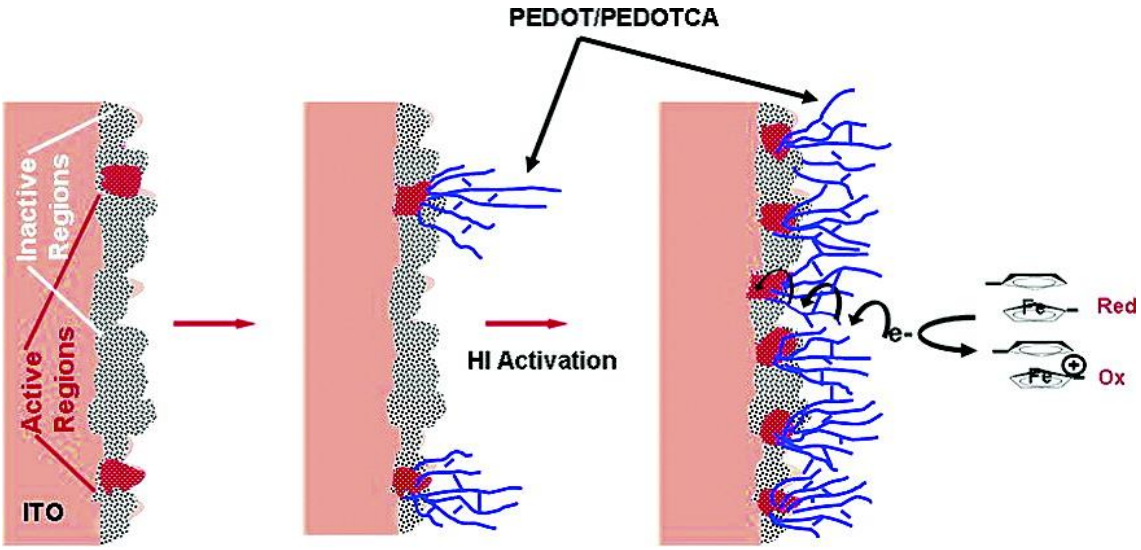

Figure 4.2 (Left) Schematic view of solvent cleaned ITO showing few-well separated electrically active sites. (Right) Copolymer growth from these active sites increases the electrochemical activity towards $FeCp_2$ by creating a nearly continuous electroactive surface. Adopted from Marrikar F. S. *et al.*[29]

In addition to electroactive surface coverage, other factors have been found to contribute to the electron transfer rate across the interface, such as the nature of the anchoring group,[31-33] and molecular orientation and packing. In one work, Hau S. K. *et*

al. deposited fullerene based redox-active modifiers with different anchoring groups on zinc oxide in an inverted heterojunction OPV with a P3HT/PCBM active material, and showed improvements in PCEs due to enhanced photo-induced electron transfer from the active material to the fullerene modified zinc oxide.[33] In another work, Saveedra *et al.* studied the effect of orientation and aggregation of zinc phthalocyanines (ZnPc) on the electron transfer rate at a ZnPc/ITO interface.[34,35] In particular, two ZnPc molecules where synthesized that differed mainly by the number of anchoring group they possessed; one phosphonic acid (PA) in the case of **4.1** and four PAs in the case of **4.2**, Figure 4.3.

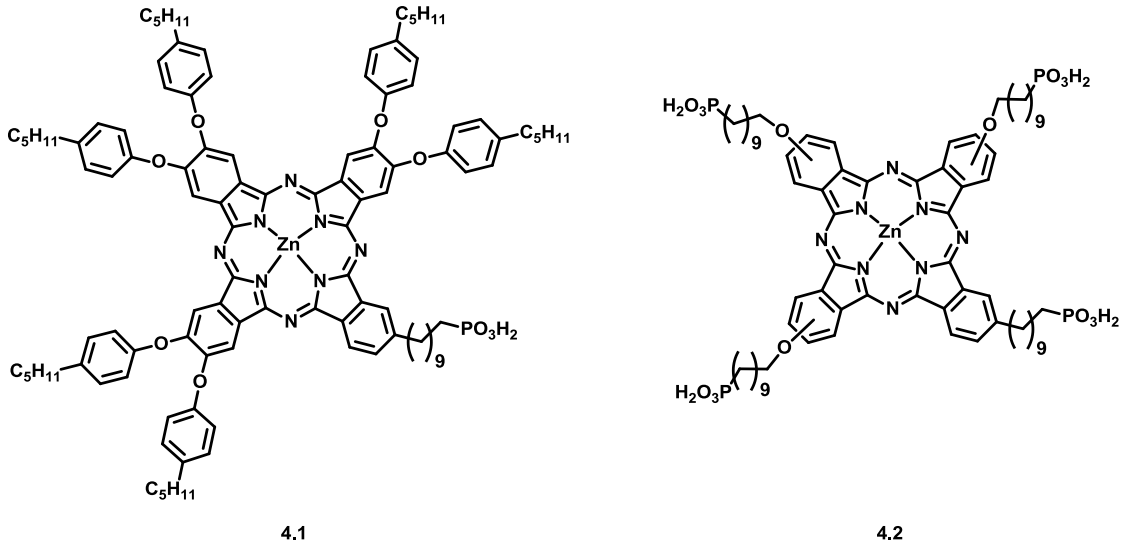

Figure 4.3 Chemical structures of ZnPcPA (**4.1**) and ZnPc$(PA)_4$ (**4.2**).

4.1 was shown to adsorb on the surface as both monomeric and aggregate form, and in a variety of molecular orientations, while **4.2** adsorbs to the ITO surface in a face-on manner, Figure 4.4. Using potential modulated UV-visible attenuated total reflectance measurement (PM-ATR; described in more detail in the caption of Figure 4.4),[35-37] it was shown that in the case of **4.1** the aggregated species had faster charge transfer rates than the monomeric species. Also, different aggregate orientations were identified, and the ones that were largely oriented parallel (in-plane) to the ITO surface exhibited the fastest rate constants, Figure 4.4. The observed effects could be attributed to better charge transfer between the aggregated ZnPc molecules followed by injection into ITO "hot-spots", smaller reorganization energies of the aggregated species,[38] and to shorter tunneling distances in the case of the in-plane orientation vs. upright orientation. When

adsorbed on ITO, **4.2** assumed an in-plane geometry and demonstrated electron transfer rates that are an order-of-magnitude higher than what is observed with **4.1**, which can be attributed to an orientation that can facilitate electron transfer, with tunneling distances calculated to be around 2.8 Å.[34]

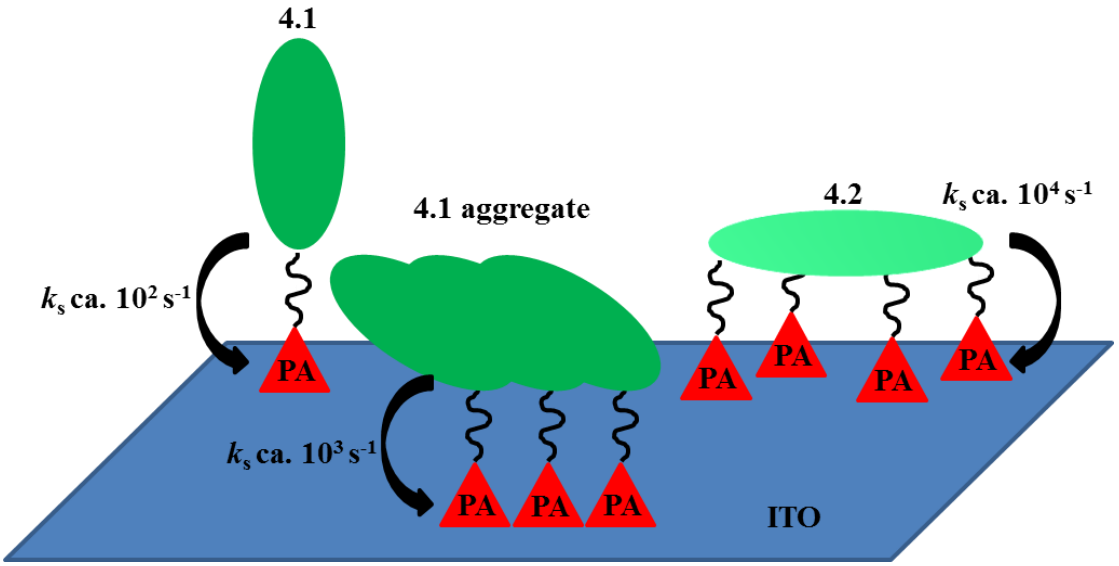

Figure 4.4 A schematic drawing of **4.1** and **4.2** adsorbed on ITO in different orientations and aggregation states. Also shown are the electron transfer rates determined through PM-ATR spectroscopy. *Note:* PM-ATR provides the capability to measure the rate constant of different species on the surface, such as monomers and aggregates, if they have distinct absorption features. It can also enable measurements of the rate constant of molecules with different orientations on the surface using differently polarized light. Rate values that are reported by this method are significantly larger than those estimated from voltammetry (For example: electron-transfer rates determined from voltammetry were estimated to be ca. 1.7 s^{-1} for the **4.1** monomers ca. 2.4 s^{-1} for the **4.1** aggregates and ca. 3.1 s^{-1} for **4.2**; rates that are reported for PM-ATR are shown in Figure 4.4),[34] which is likely attributable to the differences in the fraction of electroactive molecules probed in the two methods. In PM-ATR subpopulations of molecules can be probed separately and are expected to equilibrate more rapidly, while in voltammetric measurements the entire ensemble of electroactive molecules is oxidized or reduced. More importantly both techniques show similar trends for electron-transfer rates, and similar conclusions can be drawn from them.

The impact of increased electron-transfer rate on the performance of CuPc/C_{60} planar heterojunction OPV devices utilizing either a **4.1**/ITO or **4.2**/ITO electrode showed lower series resistance, and an enhanced PCE (0.60% vs. 1.47%) namely from enhanced fill factors and J_{SC}.[34]

More recently,[39] Zheng *et al.* started exploring a series of perylene diimide (PDI) redox active modifiers which, unlike ZnPc, can be used to modify the metal oxide/acceptor interface due to their high electron affinity (estimated at ca. + 3.9 eV for PDIs without core substituents),[40] which are comparable with commonly used acceptor molecules, such as fullerenes in the case of organic photovoltaics. Substituting the PDIs at the ortho- and bay-positions (highlighted by the black arrows in Figure 4.5), can alter their frontier energy levels,[41] and hence their electron affinities, which affords tunability.

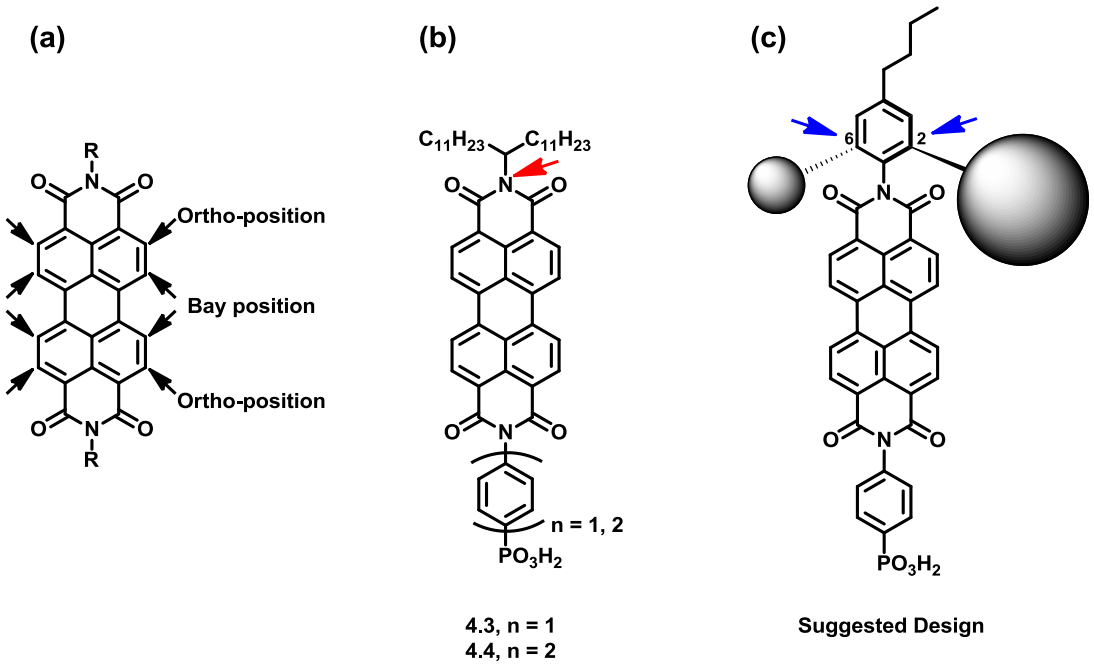

Figure 4.5 (a) A generic perylene diimide with the ortho-and bay positions specified (b) The molecular structure of the PDI-PAs[39] (Note: throughout this chapter the imide position will refer to the position not substituted with the phenyl phosphonic acid, highlighted with a red arrow) (c) The molecular design for PDI modifiers described in this chapter with substitutions at the 2 and 6 positions of the "phenyl-imide" highlighted in blue.

In their work, asymmetric perylene phosphonic acids (PDI-PA), **4.3** and **4.4** in Figure 4.5, with branched 2-undecyldodecyl alkyl chain on their imide position and either a phenyl- or biphenyl-phosphonic acid anchoring groups were synthesized and deposited on ITO. A relationship between orientation, linker length, modification technique (spin-coated vs. self-assembled) and the electron-transfer kinetics across the PDI/ITO interface was established; PM-ATR measurements showed that spin coated **4.3** on ITO had an electron transfer rate (ca. 5×10^5 s^{-1}) that is higher than that of self-assembled **4.3** on ITO (ca. 1.4×10^5 s^{-1}) due to the more out-of-plane orientation of the latter (33º for self-assembled vs. 34º for spin-coated). Also, **4.4** due to its longer linker group (bi-phenyl vs. phenyl) it showed the smallest electron transfer rate (ca. 0.5×10^5 s^{-1}). Nevertheless the effect of aggregation on the aforementioned kinetics could not be probed as both **4.3** and **4.4** aggregated heavily on the ITO surface, irrespective of the modification technique. In this chapter, and in order to gain insight on the effect of aggregation on electron transfer kinetics, a series of asymmetric PDI-PA modifiers equipped with substituents of varying sizes on the 2 and 6 position of the phenyl-imide unit, as shown in Figure 4.6, were designed, synthesized and assessed their extent of aggregation on ITO and its effect on electron-transfer rate.

4.2 RESULTS AND DISCUSSION

4.2.1 Material design

Figure 4.6, shows the molecular structure of the PDI-PA **4.5**-**4.8** studied in this chapter. While **4.3** and **4.4** have branched alkyl chains that point away from the perylene π-cloud, the position of the phenyl (Ph)- and terphenyl (TerPh)-substituents on the 2 and 6 carbons of the aniline groups in **4.5**-**4.8**, renders them facing "inwards" towards the π-cloud, while situated above and below the perylene plane. Also, this arrangement increases the barrier for rotation of these substituents around the phenyl imide C-N compared to **4.3** and **4.4**, whose 2-undecyldodecyl alkyl chain have a lower barrier for rotation around that aforementioned bond. The arrangement of side groups in this manner is necessary to break up aggregation in PDI films or PDI molecules deposited on

surfaces, as perylene diimides have a high tendency to self-associate due to their extended π-network and flat structure.[42]

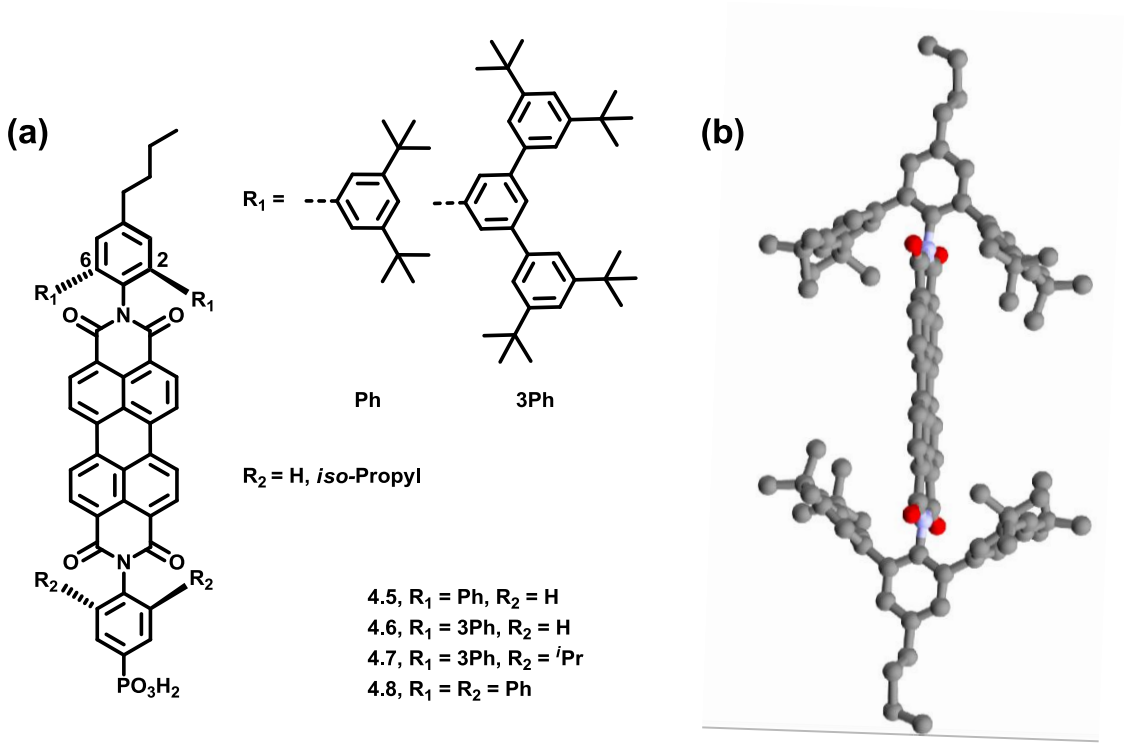

Figure 4.6 (a) The molecular structures of the asymmetrical PDI-PA, **4.5**-**4.8,** synthesized in this chapter (b) The crystal structure of **4.8**, a symmetric analogue of compound **4.5**, that illustrates the orientation of the aryl substituents inwards and above and below the perylene π-system.

Among the PDI-PAs reported in this chapter, PDI **4.5** is expected to reduce aggregation the least as its terminal aryl substituents are the smallest in size. The ability to reduce aggregation is expected to increases sequentially with from **4.5** to **4.6** to **4.7** due to the increasingly large aryl groups, and the presence of two isopropyl groups on the phenyl phosphonic acid in the case of **4.7**. A similar design approach to the one presented in this chapter has been reported in literature where Lin *et al.* functionalized the 1,7 bay position of a PDI with 2,6-diphenylphenoxy groups, which reduced π-interaction between neighboring PDI units and high solid state fluorescence quantum yields; however, this bay substitution did result in a 0.14 eV shift in the absorption maximum as expected for π-donor substituents.[43] Finally, as with the previous work, phosphonic acids were employed as anchoring groups due to their strong binding properties to metal oxides, and ease of modification conditions.

4.2.2 Synthesis of perylene phosphonic acids

Figure 4.7, highlights the retrosynthetic analysis of the PDI-PA **4.5** reported in this chapter; the other two PDI-PA follow this general scheme. Based on the retrosynthetic disconnections highlighted by the red lines, the PDI **4.5** can be divided into three segments, an asymmetrical *N*-(dihaloaryl) perylene imide diester core (**4.9** or **4.10**), aryl boronic ester substituent (**4.11**), and an aniline phosphonic acid anchoring group (**4.12**). The *N*-(dihaloaryl) perylene imide diester core can also be further divided into a perylene dianhydride (**4.13**) and an aniline unit functionalized at the 2 and 6 carbons with halogens (**4.14** of **4.15**). This convergent approach allows for increased modularity and simplifies the synthesis of the other derivatives, **4.6** and **4.7**, where their different substituents can be added towards the end of the synthesis to the already synthesized perylene cores **4.9** or **4.10**.

To synthesize the asymmetric perylene core, a pathway similar to that reported by Xue *et al.* was adopted, Figure 4.8.[44] Base hydrolysis of the commercially available perylene dianhydride **4.13** with potassium hydroxide forms the tetra-carboxylic acid derivative which upon reaction with 1-bromodecane in the presence of potassium iodide and a phase transfer catalyst yields the perylene tetraester **4.16**. Acid-catalyzed hydrolysis of **4.16** yielded the monoanhydride **4.17** in good yields. Compound **4.17** is intrinsically asymmetric since the reactivity difference between its anhydride and ester moieties is sufficiently large to allow a nucleophile attack to selectively take place at the anhydride. Although the solubility difference between **4.17** and **4.16** allows for the isolation of **4.17** through simple filtration and washing of the reaction mixture, the two remaining decyl groups on **4.17** renders it fairly solubility in organic solvents.

The following imidization step, (step iii in Figure 4.8), proved to be difficult and proceeded with low yields, despite attempting several reaction conditions. Initially, 4-butyl-2,6-diiodoaniline, **4.14**, was chosen to condense with **4.17** due to the reactivity of the iodine groups towards subsequent coupling reactions. This reaction, however, was low yielding as it suffered from the dehalogenation of its desired product, **4.9**.

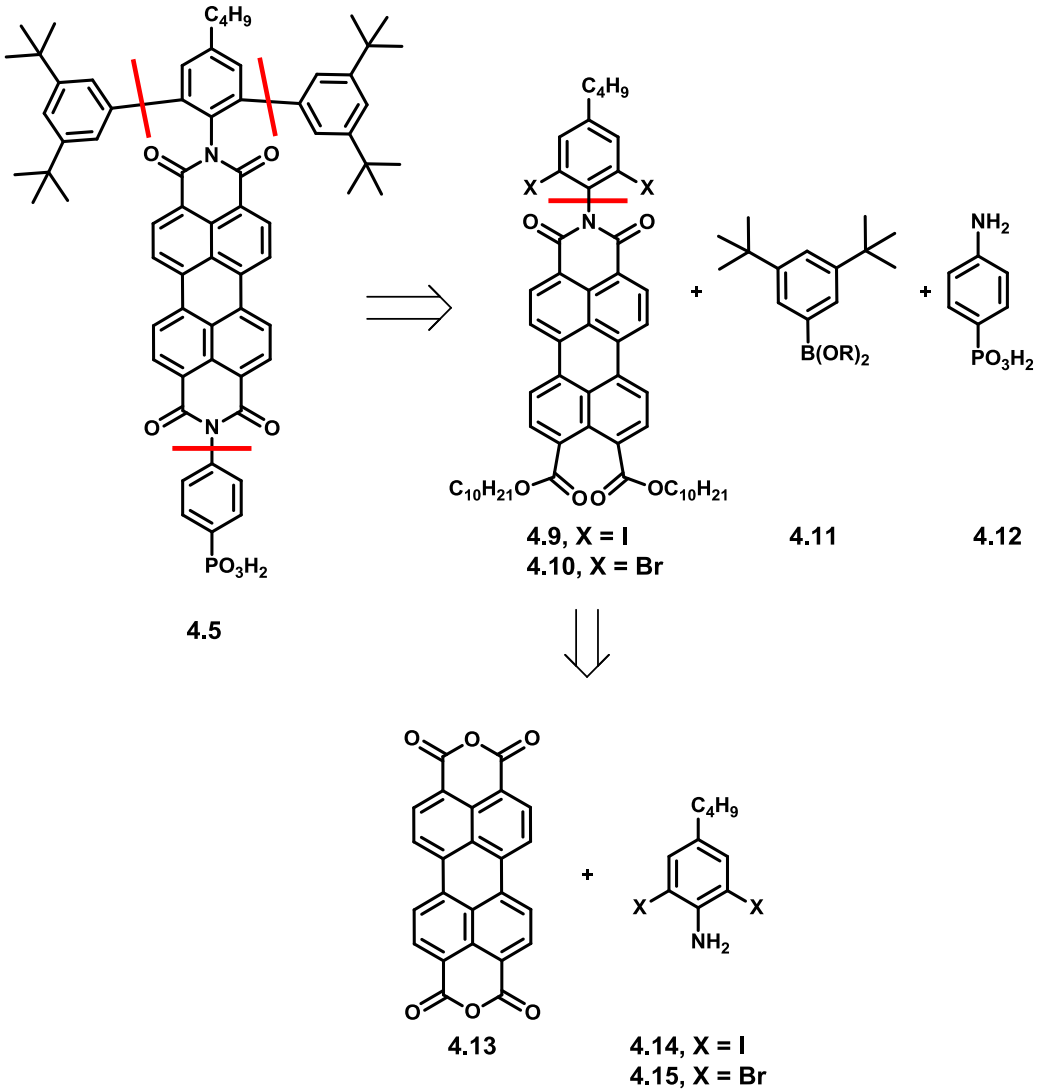

Figure 4.7 Retrosynthetic analysis of compound **4.5**, the rest of the target compounds were synthesized in a similar manner. The red lines indicate sites of covalent attachment of the various components.

Monitoring the reaction by thin layer chromatography (TLC) showed that at any given time only a small fraction of the starting materials reacted, and two major products, **4.9** and its dehalogenated derivative **4.9**-I, could be identified and isolated in a 1:2 ratio. Typical condensation reactions in similar systems require high temperatures (>180 ^{o}C) and prolonged reaction times (up to 24 h) where, for example, condensing 2,6-diisopropyl aniline with **4.13** yields the condensation product in above 60% yields.[45]

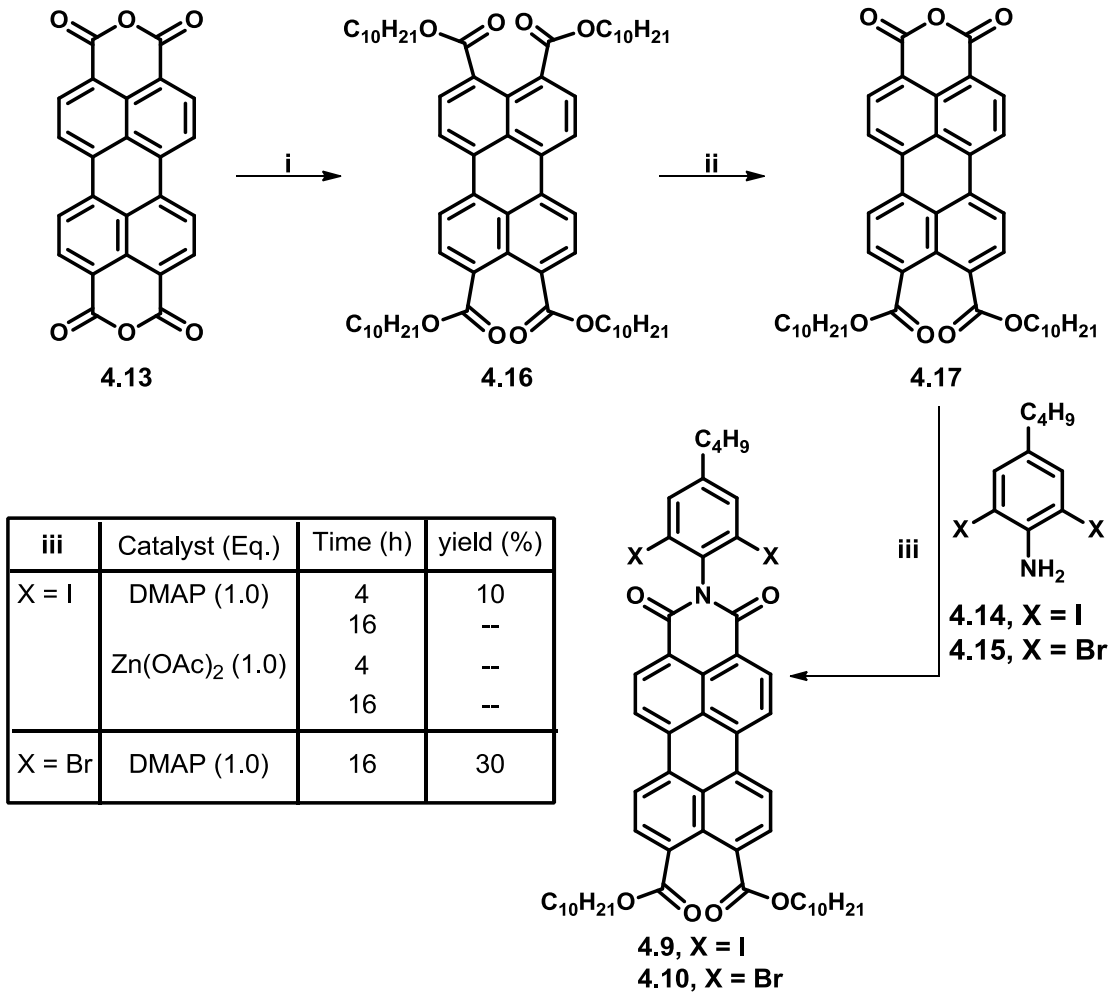

iii	Catalyst (Eq.)	Time (h)	yield (%)
X = I	DMAP (1.0)	4	10
		16	--
	$Zn(OAc)_2$ (1.0)	4	--
		16	--
X = Br	DMAP (1.0)	16	30

Figure 4.8 Synthesis of the asymmetric *N*-(dihaloaryl) perylene imide diester core **4.9** and **4.10** (i) a) KOH, H_2O, 70 ^oC, 0.5 h; b) ALIQUAT 336, KI, 10 min, c) 1-Bromodecane, reflux, 2 h; 92% (ii) a) Dodecane/toluene (1:5), 95 ^oC; b) *p*-Toluenesulfonic acid monohydrate ($TsOH•H_2O$); 75% (iii) **4.14** or **4.15**, DMAP, imidazole/toluene (9:1), 135-140 ^oC, 4-16 h.

In the case of **4.14** and **4.17** the optimal reaction conditions were found to be 4 hours at 135 ^oC in a mixture of imidazole/toluene (9:1) to increase solubility. Extending the reaction time any longer caused further dehalogenation of the remaining **4.9**. In an attempt to increase the yield of the reaction, 4-butyl-2,6-dibromoaniline (**4.15**), was used to benefit from the stronger C–Br bond (ca. 66 $kcalmol^{-1}$ vs. ca. 53 $kcalmol^{-1}$ for C–I bond).[46] Although, heating to 140 ^oC for an extended period (overnight) gave increased yields of ca. 30%, the problem persisted as dehalogenated products were isolated. Even with a 30% yield, the relative availability of the inexpensive starting material and the

high yield of the previous steps, allowed the synthesis of compound **4.10** at a multi-gram scale, which was sufficient to move forward.

Figure 4.9 describes the synthesis of the remaining components described in the retrosynthetic analysis; the phenyl boronic substituents and the two different aniline substituents. The phenyl boronic acid, **4.11**, was prepared by a Miyaura borylation reaction from 1-bromo-3,5-di-tert-butylbenzene and in the presence of bis(pinacolato)diboron in very good yields.[47] The terphenyl, **4.18**, was synthesized via a Suzuki-Miyaura coupling reaction that utilized reaction conditions reported by Finke *et al*; palladium diacetate catalyst, and a 2-dicyclohexylphosphino-2′,6′-dimethoxybiphenyl (S-Phos) phosphine ligand.[48] An iridium catalyzed C-H activation reaction of **4.18** yields **4.19** with a reactive pinacolboron ester functionality. 2,6-Dihalogenated anilines, **4.14** and **4.15**,[49,50] as well as the aniline phosphonates, **4.21** and **4.22**,[51] were synthesized according to the literature procedures as highlighted in Figure 4.9.

A Suzuki-Miyaura coupling reaction between **4.10** and the (ter)phenyl boronates **4.11** and **4.19**, gave perylenes **4.23** and **4.24**, which after acid-catalyzed hydrolysis resulted in the monoanhydrides **4.25** and **4.26**, Figure 4.10. A second imidization reaction involving the latter compounds and aniline phosphonates **4.21** and **4.22** gave rise to the perylene phosphonates **4.27-4.29** which upon ester hydrolysis with bromotrimethyl silane yielded the desired PDI-PAs **4.5-4.7**. As discussed for **4.9** and **4.10**, the imidization step proceeded with difficulty (yields ranging from 20-55% in the best case), and dephosphorylation of **4.27-4.28** was observed when high reaction temperatures and prolonged reaction times were employed. In the case of **4.29**, propanoic acid was used both as a solvent and a catalyst;[52] however, although the reaction worked well when preparing **4.20**, Figure 4.9, the reaction proceeded with low yields in the case of **4.29**, which may be attributed to the deactivation of the aniline, **4.22**, by both steric hindrance from the isopropyl groups and the electron withdrawing phosphonate.

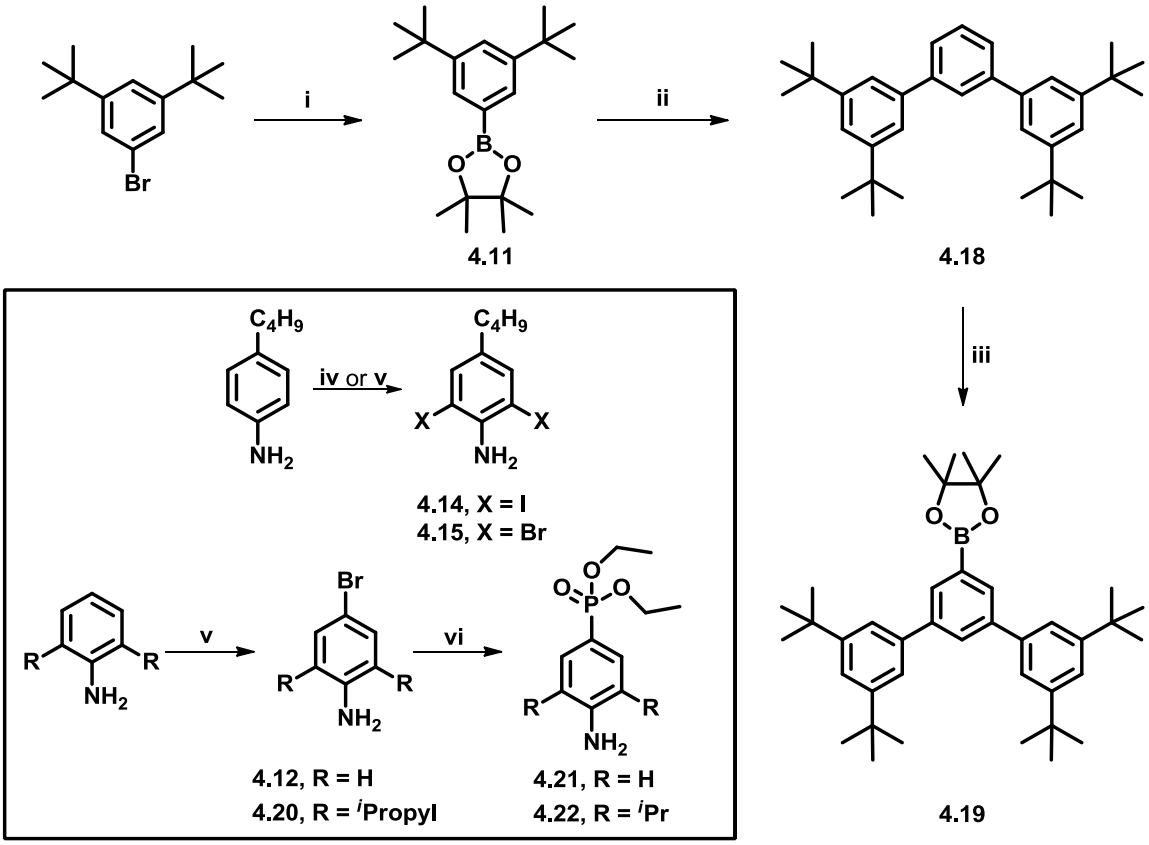

Figure 4.9 Synthesis of the phenyl and terphenyl boronic esters **4.11** and **4.19**, as well as synthesis of the halogenated anilines and the aniline phosphonate anchoring groups; (i) $Pd(dppf)Cl_2$, bis(pinacolato)diboron, KOAc, DMSO, 80 ^oC, 16 h; 80% (ii) 1,3-Dibromobenzene, $Pd(OAc)_2$, S-Phos, NaOH, THF, 60 ^oC, 2h; 60% (iii) Bis(pinacolato)diboron, (1,5-cyclooctadiene)(Methoxy)iridium(I) dimer, 4, 4'-di-*tert*-butyl-2.2'-dipyridil ligand, hexane, 80 ^oC, 4h, 92% (iv) For **4.14**; I_2, Ag_2SO_4, ethanol, RT, 1h; 97% (v) For **4.15**; Br_2, MeOH/DCM 1:1, RT, 2h; 80%; For **4.20**, 77% (vi) **4.12** or **4.20** diethyl phosphonate, $Pd(OAc)_2$, PPh_3, Et_3N, ethanol; 40%

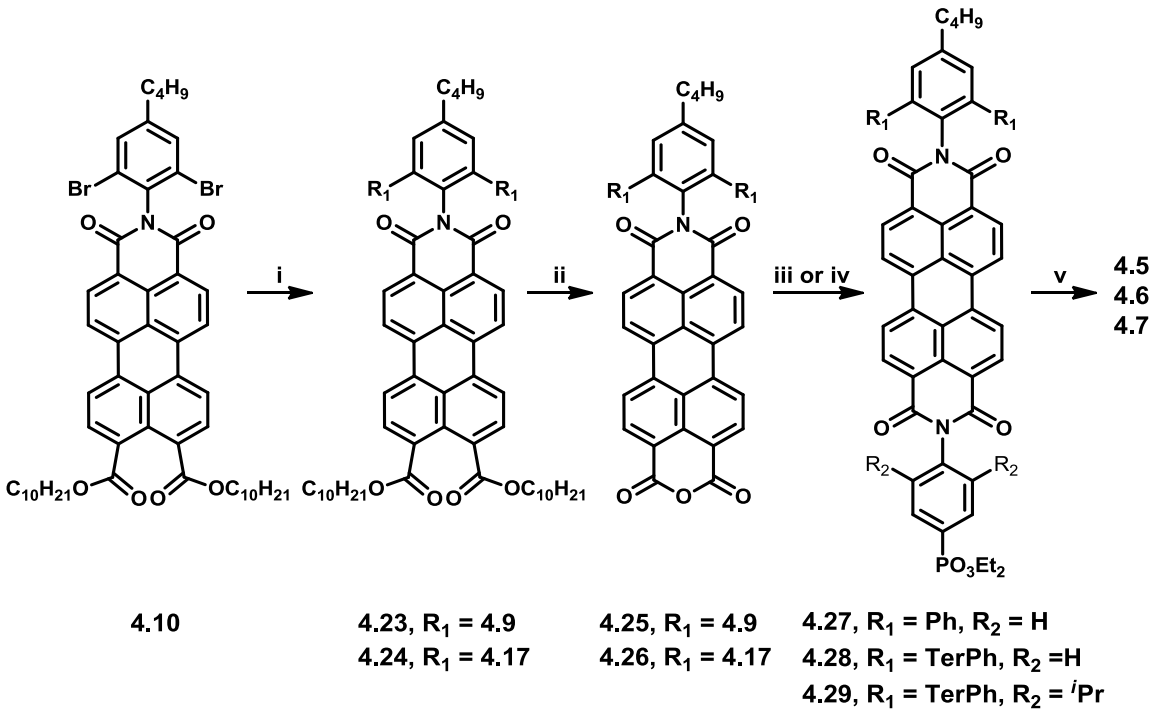

Figure 4.10 Synthesis of the PDI-PAs **4.5**-**4.7** (i) **4.11** or **4.19**, $PdCl_2(dppf).CH_2Cl_2$, toluene, methanol, 70 ^oC, overnight ; 66-76% (ii) *p*-Toluenesulfonic acid, 95 ^oC, 5 h; 70-72% (iii) For **4.27** and **4.28**; **4.21**, $Zn(OAc)_2$, imidazole/toluene, 140 ^oC, 3h; 20-55% (iv) For **4.29**; **4.26**, **4.22**, propanoic acid, 160 ^oC overnight; 27% (v) a) Bromotrimethyl silane, DCM, RT, overnight; b) H_2O/THF with few drops of HCl; 60%.

As mentioned previously, the initial synthetic pathway targeted the synthesis of the iodine substituted PDI, **4.9**, as a gateway towards the synthesis of the bulky PDI-PAs. The reactive iodine atoms were attractive as they could readily react with *tert*-butyl acetylene, **4.30**, or trimethylsilyl acetylene, **4.31** under Sonogashira reaction conditions to give diesters **4.32** and **4.33** in Figure 4.11, which have the same out-of-plane arrangement of substituents that would prevent aggregation in a similar manner to the PDI-PAs highlighted in Figure 4.6. Furthermore, the trimethylsilyl-protected PDI **4.33** can be further reacted with aryl iodide such as **4.35** to produce an acetylene analogue of compound **4.5**, which theoretically should be better in reducing intermolecular interaction between adjacent PDI molecules as the extended structure, courtesy of the acetylene's extra C–C bonds, would cover more of the PDI's backbone.

The reaction of **4.9** with the respective acetylenes proceeded with good yields that ranged between 70 – 80% to give the diesters **4.32** and **4.33**, the latter was further

coupled with 1,3-di-*tert*-butyl-5-iodobenzene, **4.35**, to yield the diester **4.36** in ca. 90% yields. Hydrolyzing the diester to the anhydride led to unidentified purple product that was immobile on silica gel TLC plate unless eluted with polar eluent mixture (MeOH:DCM 5:95). No further work was attempted to unravel the nature of the product mainly due to the success of the approach described earlier, and the low yield of forming **4.19**.

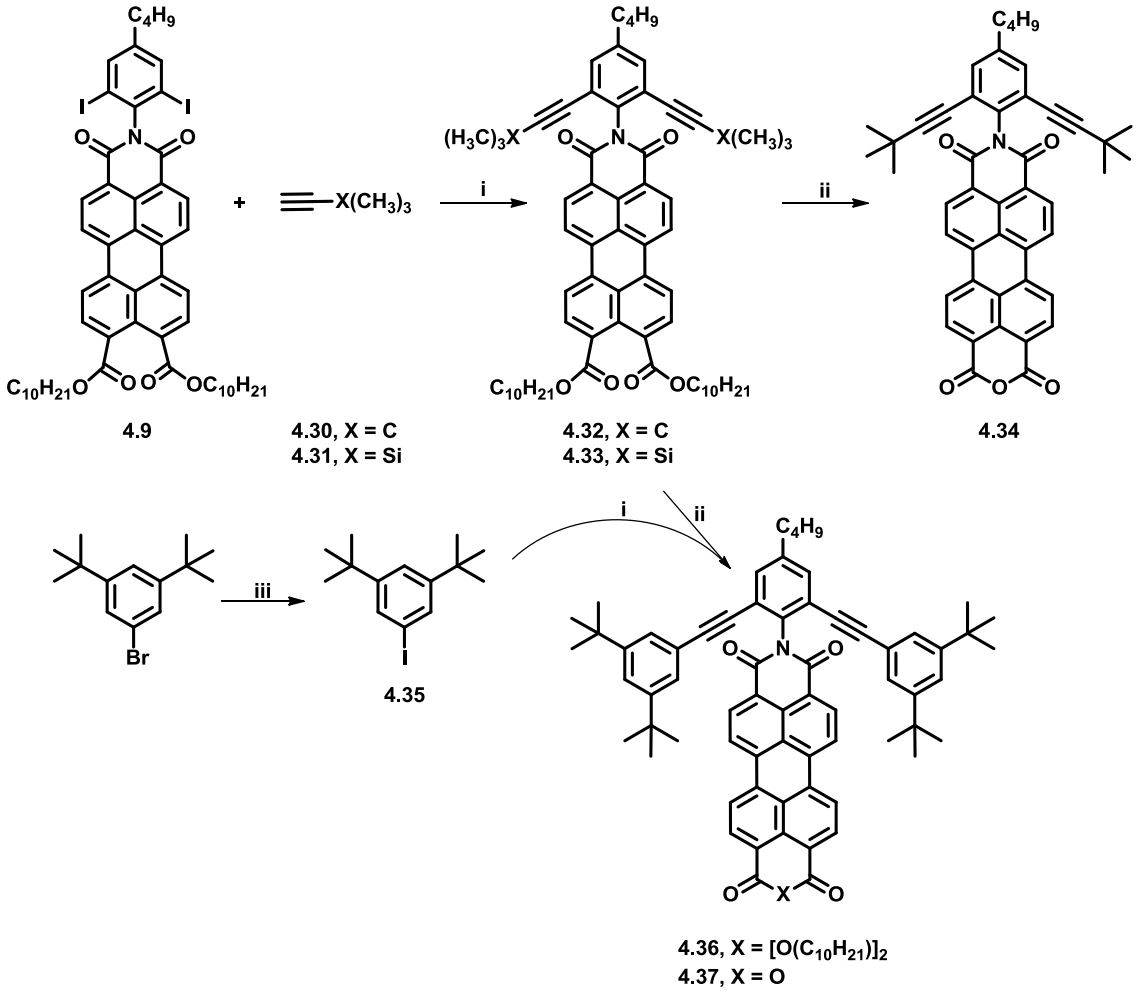

Figure 4.11 Initial route that was abandoned due to decomposition of compounds **4.34** and **4.37** (i) $Pd(PPh_3)_2$, CuI, $(^iPr)_2NH$, THF, 60 ^oC (ii) *p*-Toluenesulfonic acid, 95 ^oC, 5 h.

4.2.3 Determining the extent of aggregation of PDI-PA on TiO_2

Non-aggregated PDIs with only *N*-substituents display an absorption maximum at 527 nm with a strongly pronounced vibronic structure associated with the (0,0) vibronic band in the S_0–S_1 transition.[42] Upon aggregation, the PDI absorption profile broadens and loses its fine vibronic structure as demonstrated in Figure 4.12. Depending on the type of aggregation, J-type or H-type, the PDI absorption profile will be dominated by a peak that is either bathochromically or hypsochromically shifted compared to the (0,0) vibronic band in the non-aggregated PDI. As an example, Würthner *et al* performed concentration dependent UV/Vis absorption measurements on the perylene in Figure 4.12, and showed that upon increasing the concentration from 10^{-7} M to 10^{-5} M, the absorption spectra became dominated by a band the is hypsochromically shifted to the (0,0) band, which suggests the presence of an H-aggregate at high concentration.[53] In the absorption spectra of non-aggregated *N*-substituted PDI, the ratio of the absorptivity of the (0,0) vibronic band at ca. 527 nm to that of the (0,1) vibronic band at ca. 490 nm is equal or greater to 1.6. Upon aggregation, this ratio is significantly decreased with values dropping below 1 if the PDI is substantially aggregated, Figure 4.12.[54]

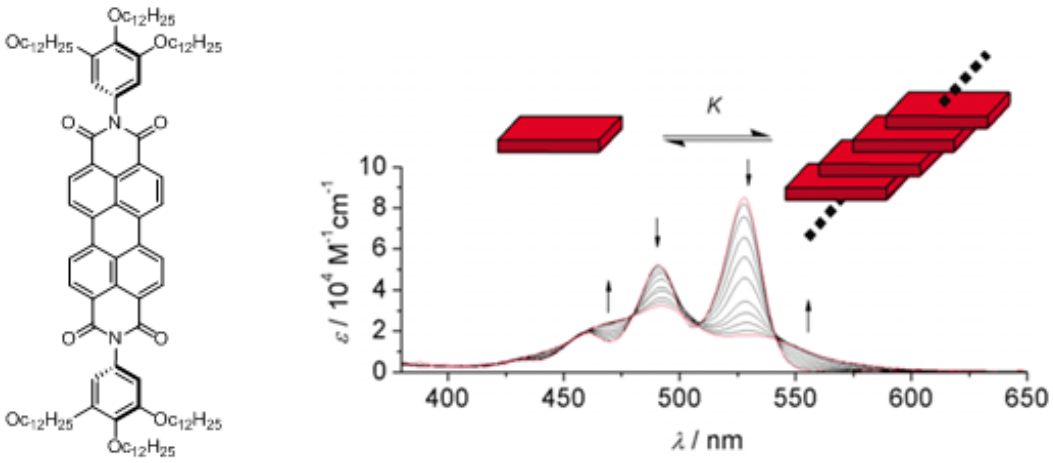

Figure 4.12 Change in the absorption spectrum of a PDI as function of perylene concentration (10^{-7} to10^{-5} M in methylcyclohexane).[53]

Figure 4.13 shows the normalized absorption spectra of compound **4.3** whose structure is presented in Figure 4.5and was part of the previous study. The solution

absorption profile is similar to the *N*-substituted PDIs described above with a (0,0)/(0,1) ratio equal to 1.65 indicating that **4.3** is monomeric in solution. Upon adsorption on TiO_2 this ratio decreases to 0.65 indicating substantial aggregation. In addition, the absorption spectra broadens on TiO_2 surface with an absorption onset, and absorption maximum that are ca. 0.27 eV red-shifted and ca. 0.18 eV blue-shifted, respectively, which is also indicative of aggregation.

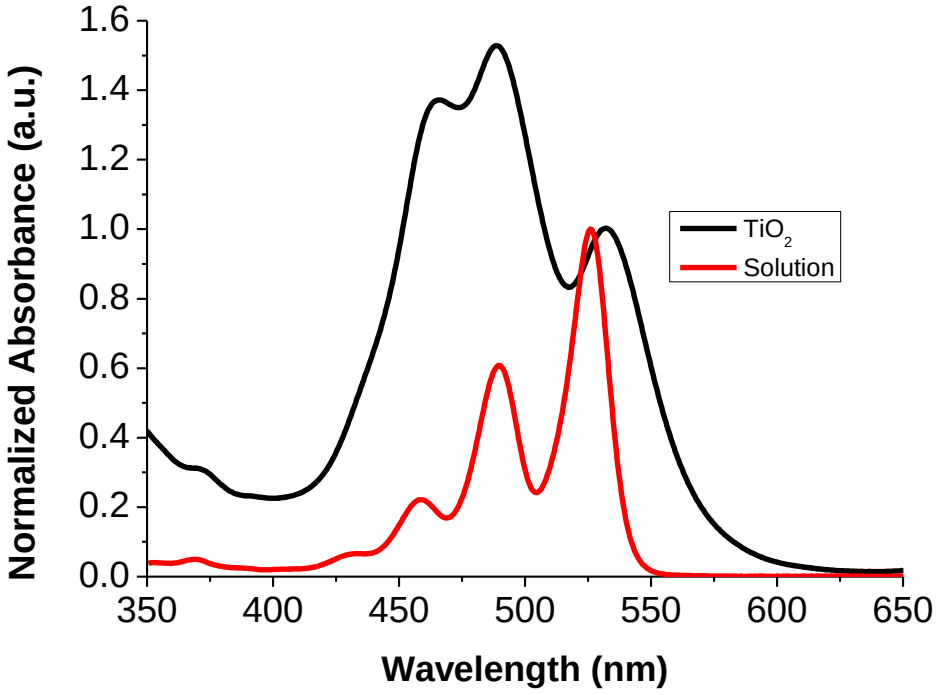

Figure 4.13 Absorption spectra of compound **4.3** in solution (Red) and on adsorbed on mesoporous TiO_2 (black). *Note:* Although the electron transfer measurements described later are conducted on ITO, the degree of aggregation is quantified first on TiO_2 as determining the absorption of monolayer requires a non-trivial setup unavailable in our lab. However, the information collected on TiO_2 can shed light on the dyes' behavior on ITO, as will be seen in the following section.

In order to determine the extent of aggregation of the PDI-PAs **4.5**-**4.7** on TiO_2's surface, their absorption spectra in solution and on TiO_2 were recorded and compared to that of **4.3**, Figure 4.14. It is evident that the new PDI-PAs, **4.5**-**4.7**, exhibit less aggregation on TiO_2's surface compared to **4.3**. The (0,0)/(0,1) ratio increased from 0.65 in the case of **4.3** to 1.03 for **4.5**, then to 1.22 in the case of **4.6** and finally to 1.40 for **4.7**. Although none of the dyes exhibit a ratio of 1.6, which indicates that they are not

monomeric on the surface, their ratios gradually increase to reach a value of 1.40 with **4.7** that is twice as high as **4.3**'s. Reduced aggregation on the surface is also expected to cause a narrowing of the absorption spectrum, which in our case is observed as a hypsochromic shift in the absorption onset by as much as 0.17 eV going from **4.3** to **4.7**. Along the same lines, the solid-state absorption maxima of the (0,0) peak were also blue shifted compared to **4.3** with that of **4.7** appearing at the same wavelength as that in solution.

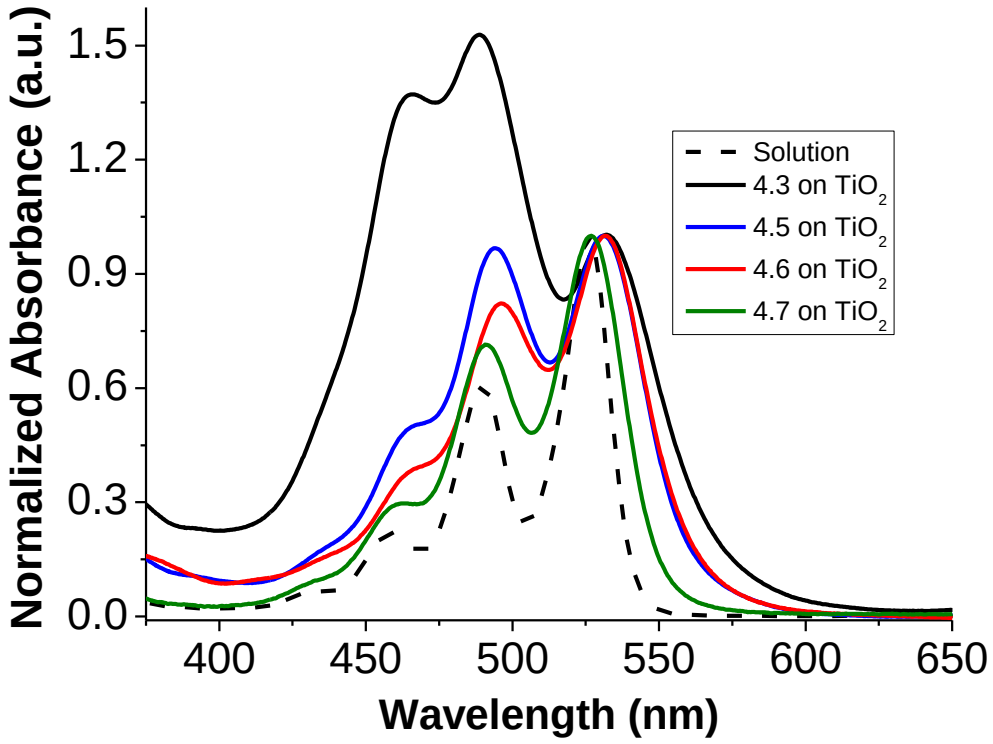

Figure 4.14 UV/Vis absorption spectra of **4.3** and the series **4.5-4.7** in THF and on mesoporous TiO_2; All of the dyes were dissolved in dry tetrahydrofuran solution at a concertation ca. 25 μM, and a TiO_2 coated glass was dipped in the solution for 75 minutes.

Overall, the observed trends in the solid-state optical properties of the new series of dyes are consistent with expectations based on their molecular structure. By substituting the alkyl chains with the out of plane phenyl substituents, the ratio of the (0,0)/(0,1) increased by 60%, displaying the effectiveness of the new design in reducing intermolecular interaction. Increasing the size of the substituent from phenyl (**4.5**) to

terphenyl (**4.6**) increased the ratio by an additional 18%, with negligible effect on the absorption onset and the absorption maximum. This suggested that intermolecular interaction at that particular imide position is essentially reduced, however since the absorption profile of **4.6** still did not resemble that in solution (dashed line in Figure 4.14), **4.7** was synthesized with isopropyl groups on the 2 and 6 carbon atoms of the phenyl phosphonic acid. The isopropyl groups were designed to twist the phenyl ring they are on, out of plane of the perylene in a similar manner to what the phenyl substituents did. This had a more pronounced effect on the solid-state absorption profile of **4.7**, compared to **4.6**, where the (0,0)/(0,1) ratio further increased by 15% to reach 1.40, its absorption onset blue-shifted by 0.08 eV, and its absorption maximum overlaying that of the solution absorption.

4.2.4 Determining the extent of aggregating on ITO

NOTE: The results discussed in the following sections are based on experiments that have been conducted by Mr. Yilong Zheng from Prof. Scott Saavedra's lab at University of Arizona. A detailed discussion about the techniques and procedures used to obtain the presented data will be incorporated in Mr. Zheng's thesis, and future collaborative publications. Permission has been obtained to use the data presented in this section.

The PDI-PAs were deposited on ITO (detergent followed by plasma cleaning) surfaces by dip coating in a 20 μM solution of the PDI-PA for 2 hours. Electrochemistry measurements were then used to characterize the electroactive surface coverage (Γ) and the redox properties, Table 4.2. All films showed two 1-electron reduction processes with similar midpoint potentials, Table 4.2, that are consistent with what is observed in literature for bay unsubstituted PDIs.[55] The electroactive surface coverages estimated from integrating under the voltammetric peaks and assuming two 1-electtron reductions shows that larger PDIs have a lower surface coverage, which is consistent with their larger footprint. These surface coverages give rise to monolayer percentages that are approaching 100% in all four PDI-PAs; the projected area of each PDI (180 $Å^2$molecule^{-1} for **4.3**, 315 $Å^2$molecule^{-1} for **4.5**, 418 $Å^2$molecule^{-1} for **4.6** and 420 $Å^2$molecule^{-1} for **4.7**)

was estimated from energy minimization of a single molecule on the surface, taking into account the tilt angle determined from polarized ATR measurement, Table 4.3.

Table 4.2. Reduction midpoint potentials and electroactive surface coverage (Γ) of the four PDI-PA calculated from cyclic voltammograms. The electrochemical values are referenced against silver/silver nitrate non-aqueous reference electrode ($Ag/AgNO_3$ 0.01M, with 0.1M tetrabtutylammonium perchlorate as supporting electrolyte in acetonitrile), scan speed is 500 mV/s.

	4.3	**4.5**	**4.6**	**4.7**
Γ [10^{-11} molcm^{-2}]	11 ± 2	4.2 ± 0.3	3.1 ± 0.4	3.2 ± 0.2
Monolayer Percentage [%]	120 ± 22	80 ± 6	78 ± 10	81 ± 5
$E_{1/2}^{0/-}$ **[V]**	–0.91 ± 0.04	–0.86 ± 0.02	–0.84 ± 0.03	–0.84 ± 0.01
$E_{1/2}^{-/2-}$ **[V]**	–1.15 ± 0.05	–1.14 ± 0.04	–1.12 ± 0.04	–1.13 ± 0.03

The degree of aggregation of a monolayer of PDI-PA, **4.3** and of the series **4.5**-**4.7** on ITO was probed by both solid-state absorption measurements, in a manner that is similar to what is presented in Figure 4.14. Similar to the case of TiO_2, none of the PDI-PAs were monomeric on ITO, in fact all of the PDI-PAs showed higher degrees of aggregation on ITO compared to TiO_2 (lower ratios of (0,0) to (0,1) vibronic band) which could be due to the rough and mesoporous nature of the TiO_2 compared to the smoother ITO surface, Figure 4.15. Even though more aggregation was observed, the trend holds where **4.3** showed the highest degree of aggregation with a (0,0)/(0,1) ratio = 0.33 and upon going to the bulkier PDIs this ratio gradually increased to reach 1.00 in the case of **4.7**.

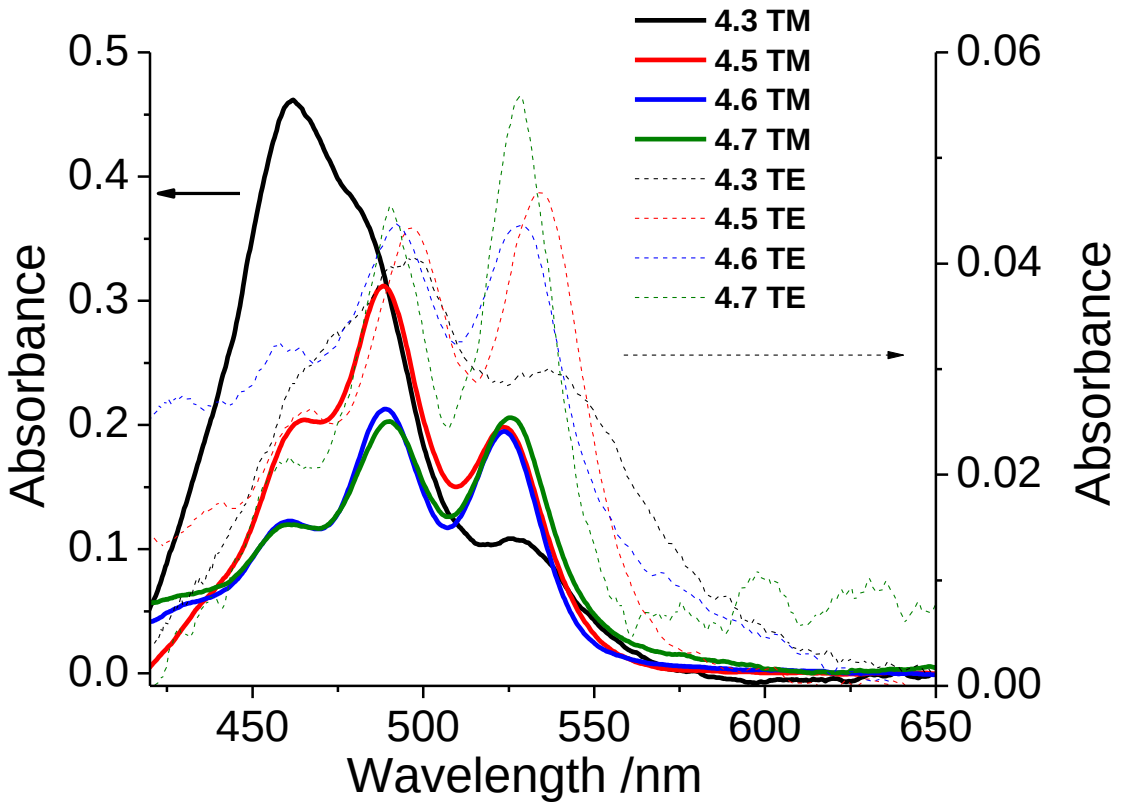

Figure 4.15 Attenuated total reflectance UV/Vis spectra of **4.3** and the series **4.5**-**4.7** on ITO, in both TM (transverse magnetic) and TE (transverse electric) polarizations; Figure A.34 shows the coordinate system defining two orthogonal polarizations, the TM and the TE, these polarizations are defined relative to the plane of incidence which is the x-z plane, while the ITO surface corresponds to the x-y plane. The TM polarized light oscillates in the plane of incidence along the x axis; while the TE polarized light oscillates along the y plane.

The same conclusion could be inferred from solid-state fluorescence spectra of the PDI-PAs on ITO, Figure 4.16. In solution, the fluorescence of PDI shows well-resolved vibronic structure and a minimal Stokes shift (ca. 0.03 eV).[41,53] However, on ITO's surface, none of the PDI's show monomeric-like emission, instead, a featureless broad band between 550-750 nm is seen in the case of **4.3** on ITO, with a Stokes' shift ca. 0.42 eV indicating the presence of PDI aggregates on ITO.[56,57] As the PDI-PAs get more bulky going to **4.5**, the emission maximum starts to hypsochromically shift closer to the monomeric emission until the Stokes' shift became around 0.26 eV in the case of **4.7**, green line vs. black lines in Figure 4.16, which indicates lower degree of aggregation on ITO surface in accordance with the previous conclusions.

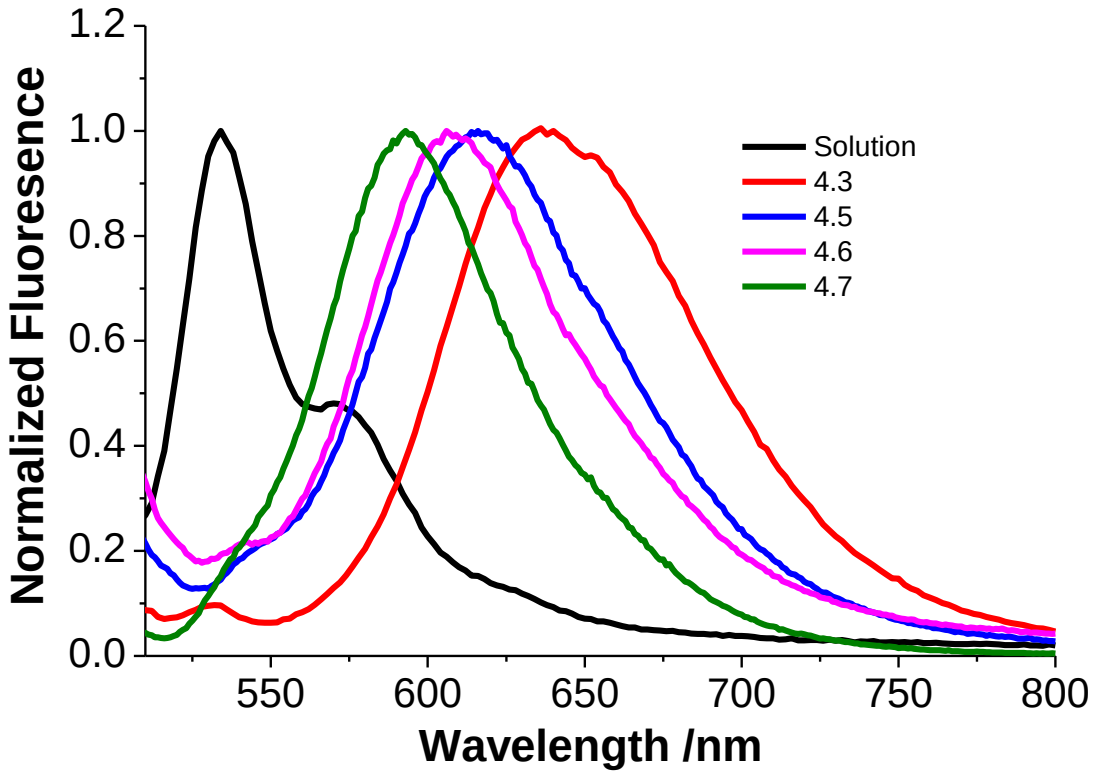

Figure 4.16 Fluorescence spectra of a monomeric PDI in solution (black line), and the solid-state spectra of **4.3** and the PDI-PA series **4.5-4.7** adsorbed on ITO surfaces.

4.2.5 Molecular orientation of the PDI-PA on ITO and electron transfer kinetics

Since orientation can have significant effects on the electron transfer across the interface, as was discussed in the introduction,[34,35] the orientation of the PDI-PA (**4.3** and **4.5-4.7**) was determined on ITO from the absorbance dichroic ratio determined from the TM and TE absorption spectra shown in Figure 4.15 (The mean tilt angles between the PDI's long molecular axis and the surface normal are summarized in Table 4.3. All four PDIs have relatively similar out-of-plane orientations, within 3°, with mean tilt angles that are smaller than 45°). This result is desired as it minimizes the effect of orientation on electron transfer and makes it more likely that any observed difference might be due to the extent of aggregation of the PDI on the surface of ITO.

Table 4.3 Mean tilt angles of the PDI-PA dyes on ITO surface and electron transfer rate constant ($k_{s,opt}$) determined.

	4.3	**4.5**	**4.6**	**4.7**
Tilt Angle	33° ± 4°	38° ± 2°	41° ± 3°	42° ± 2°
$k_{s,opt}$ **[10^3 s^{-1}]**	14 ± 0.3	1.9 ± 0.7	1.2 ± 0.1	1.0 ± 0.3

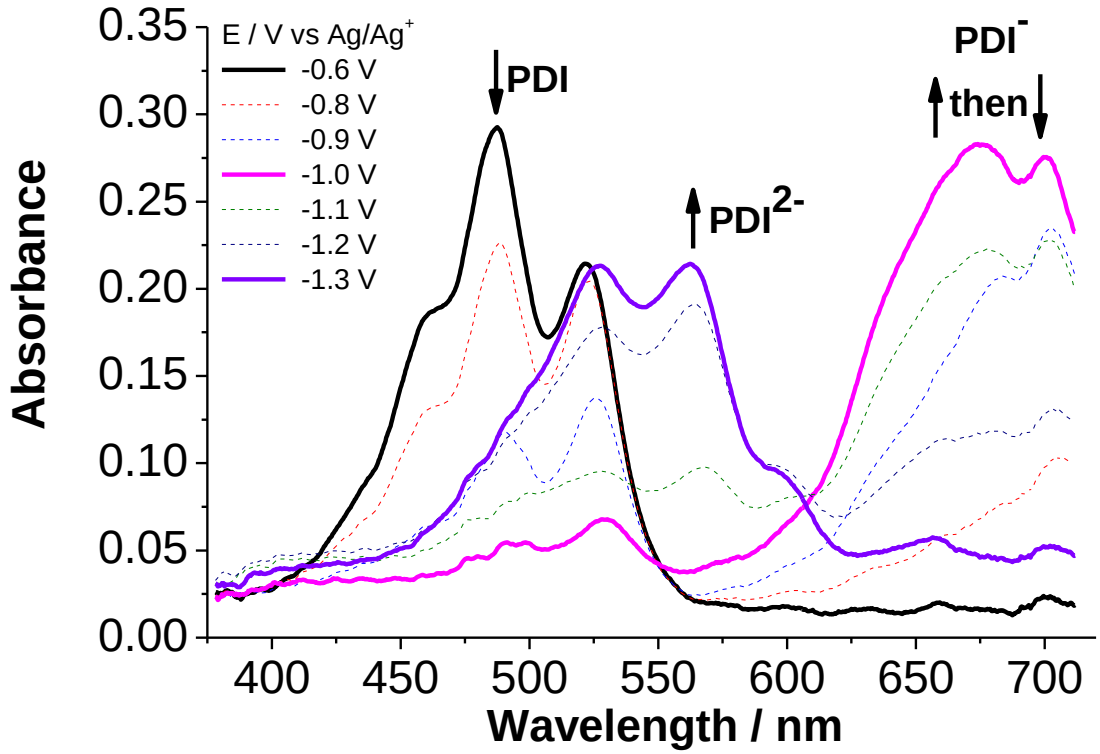

Figure 4.17 A representative PM-ATR spectra of **4.5** on ITO in TM polarization. A platinum wire was used as the counter electrode and a $Ag/AgNO_3$ (0.01 M in acetonitrile) was used as the nonaqueous reference electrode. The potential was stepped from –0.6 V to –1.3 V with a step size of 0.1 V.

The optically detected electron-transfer rate constant ($k_{s,opt}$) for the first and second reductions of the four PDIs were measured using potential modulated attenuated total reflectance (PM-ATR) in the TM polarization as shown in Figure 4.17. By changing the applied potential on the ITO from –0.6 V to –1.3 V the surface-bound PDIs can be reduced by either one or two electrons. By following the fall and rise in the absorbance of

the PDI (460 nm) and PDI^{2-} (569 nm) peaks, $k_{s,opt}$ can be determined. The measured rate constants, Table 4.3, state that a higher degree of aggregation results in a faster electron transfer processes between the PDI and ITO; order-of-magnitude higher rates were measured with **4.3** compared to the series **4.5**-**4.7**. As discussed previously, the conductivity of ITO is heterogeneous with the presence of hotspots, these measured rates suggest that the electron transfer at the PDI/ITO interface can be enhanced with PDI molecules that have higher intermolecular interactions, as these interactions will facilitate the electron transport between these aggregated PDIs until reaching one of these hotspots where fast electron transfer can take place.

4.2.6 Photo-electrochemical measurements of PDI-PA films on ITO

A faster electron transfer rate between the PDI and ITO does not necessarily equate to higher electron collection efficiency at the PDI/ITO electrode in an photoelectrochemical cell. In order to assess the electron collection efficiency at the electrode, a photoelectrochemical cell was assembled utilizing Aluminum phthalocyanine hydroxide (AlOHPc) as a solution electron donor and a PDI coated ITO acting as an electron acceptor. By using two different excitation wavelengths, selective excitation of the surface bound PDI molecules (488 nm) or the solution donor (632 nm) can be achieved. Exciting the donor will give an idea on the electron transfer efficiency across the PDI/ITO, Figure 4.18a while exciting the acceptor will test the PDI's ability to facilitate electron transfer from the donor to the ITO, Figure 4.18b.

Exciting the PDI (488 nm), it was found that the (absorbed photon-to-current efficiency) APCE values increase as aggregation is reduced even though the electron transfer rate determined earlier was higher with aggregates. One possible explanation can attribute this reduced electron collection efficiency to enhanced excited state quenching due to aggregation of PDIs on the surface. Exciting the donor (633 nm), on the other hand, showed that having a redox active modifier results in more efficient electron collection when compared to bare ITO, with higher IPCE values reported with the more aggregated perylenes **4.3** and **4.5**. Combining these two observations together, the following can be inferred; although the electron collection efficiency is higher with

deaggregated PDIs, the higher surface coverage provided by the aggregated perylenes, Table 4.2, allows for more electrons to be transferred, thus when looking at modifying ITO with PDIs a deaggregated perylene with a small footprint, similar to **4.5**, appears to be optimal.

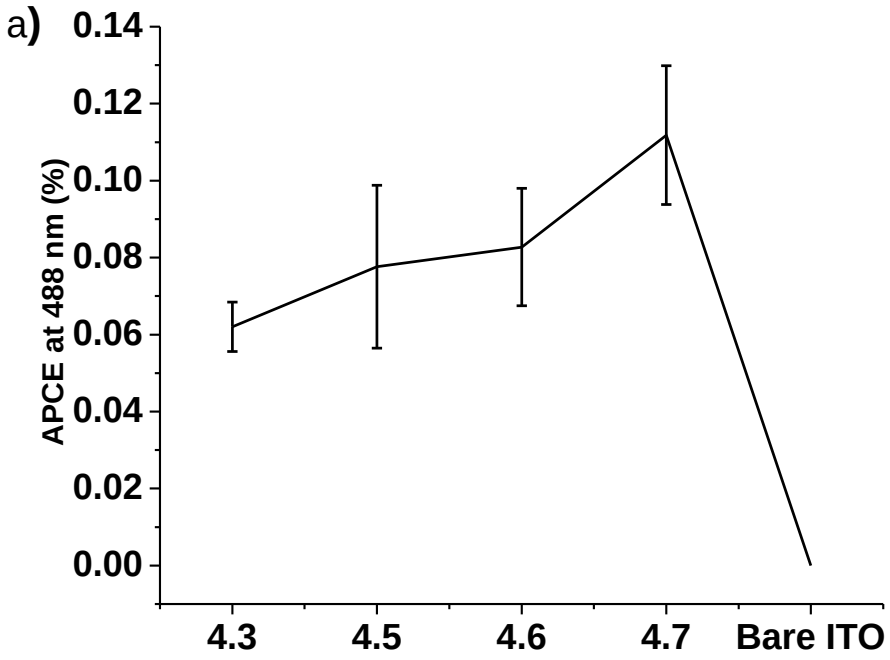

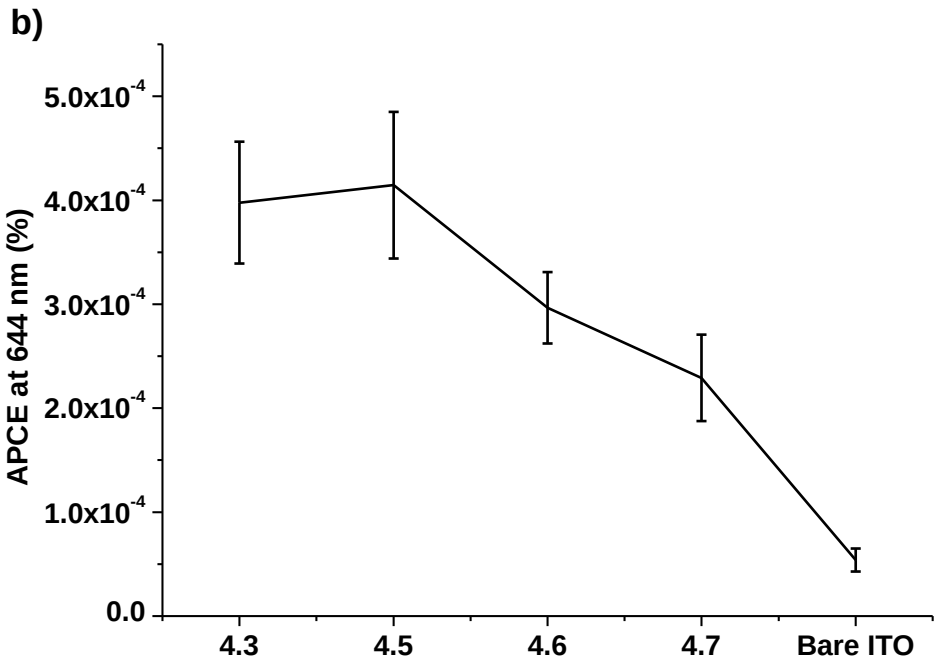

Figure 4.18 (a) Absorbed photon to current conversion efficiency (APCE) obtained from the electrochemical cell using by exciting the PDIs at 488 nm. (b) exciting the solution donor at 633 nm.

4.3 CONCLUSION

The effects of molecular aggregation in perylene diimide phosphonic acid (PDI-PA) deposited on ITO on the electron transfer process across the PDI/ITO interfaces was investigated. By introducing bulky aryl substituents, of different sizes, at the imide positions that point above and below the plane of the PDI, the aggregation of PDI-PAs on ITO surface is reduced without changing their electronic properties or significantly altering their orientations on the surface. The electron transfer rate constant across the PDI/ITO interface was found to decrease as the degree of PDI aggregation is reduced, which may be caused by the reduced electron self-exchange rates between aggregated PDI molecules, which might otherwise facilitate electron injection into ITO hotspots.

On the other hand, photo-electrochemical measurements suggest that the photo-induced electron transfer efficiency from PDI to ITO actually increases as the degree of PDI aggregation is reduced, which could be due to lower excited state quenching resultant from aggregation. In terms of the ability to facilitate the electron transfer and

then injection from a solution donor into ITO, the results suggest that modification of ITO electrodes with redox-active PDI modifiers does enhance the electron collection efficiency with respect to unmodified ITO.

4.4 EXPERIMENTAL

4.4.1 Synthetic procedures

Commercially available intermediates were purchased and used without further purification. ^{1}H, ^{13}C and ^{31}P NMR spectra were collected on a Bruker 400 MHz spectrometer. Deuterated solvents with tetramethylsilane as an internal standard were used; in the case of ^{31}P NMR, an external reference (tube filled with a solution of phosphoric acid) is utilized and referenced to 0 ppm. Mass spectra were measured on a VG Instruments 70-SE using the electron impact (EI) or fast-atom bombardment (FAB) mode and on an Applied Biosystems 4700 Proteomics Analyzer using MALDI mode. Elemental analyses were carried out by Atlantic Microlab using a LECO 932 CHNS elemental analyzer.

(4.10)

Compound **4.17** (8.80 g, 12.7 mmol), and imidazole (80 g) were heated to melt at 140 ^{o}C. 2,6-Dibromo-4-butylaniline **4.15** (5.08 g, 16.6 mmol), 4-dimethylaminopyridine (1.58 g, 12.7 mmol) and toluene (17 mL) were added and the mixture stirred at 140 ^{o}C overnight. The mixture was cooled to 70 ^{o}C, poured over chloroform and passed through a silica plug using dichloromethane as an eluent, then followed by silica gel column chromatography using ethyl acetate/hexane (20:80) as an eluent to yield **4.10** as a red solid (3.28 g, 26%). ^{1}H NMR (400 MHz, $CDCl_3$) δ 8.60 (d, J = 8.0 Hz, 2H); 8.25 (d, J = 8.2 Hz, 2H); 8.18 (d, J = 8.2 Hz, 2H); 7.95 (d, J = 7.9 Hz, 2H); 7.59 (s, 2H); 4.39 (t, J = 7.2 Hz, 4H); 2.69 (t, J = 7.8 Hz, 2H); 1.87 (quintet, J = 7.7 Hz, 4H); 1.70 (sextet, J = 7.6 Hz, 2H); 1.55-1.20 (m, 30H); 1.01 (t, J = 7.4 Hz, 3H); 0.91 (t, J = 7.00 Hz, 6H). $^{13}C\{^{1}H\}$ NMR (100 MHz, $CDCl_3$) δ 168.02, 161.95, 146.88, 135.69, 132.27, 131.85, 131.84, 131.80, 131.41, 129.95, 129.68, 128.72, 128.59, 125.91, 123.56, 122.49, 121.61, 121.45, 65.78, 34.78, 32.75, 31.75, 29.43, 29.42, 29.21, 29.17, 28.46, 25.88, 22.52, 22.19, 13.95,

13.71. HRMS (MALDI): m/z 978.2979 [M+H]+ (calcd. for $C_{54}H_{62}Br_2NO_6$: 978.2944). Anal. Calcd. for $C_{54}H_{61}Br_2NO_6$ (%): C, 66.19; H, 6.27; N, 1.43. Found: C, 66.42; H, 6.60; N, 1.44.

(4.23)

Compound **4.10** (0.38 g, 0.39 mmol), 2-(3,5-di-*tert*-butylphenyl)-4,4,5,5-tetramethyl-1,3,2-dioxaborolane – **4.11** (0.37 g, 1.16 mmol), $PdCl_2(dppf).CH_2Cl_2$ (0.03 g, 0.04 mmol) and K_2CO_3 (0.27 g, 1.94 mmol) were added into a 25 mL round bottomed flask, that was pump-filled with nitrogen three times. Toluene (5 mL) and methanol (5 mL) were added and the reaction was stirred at 75 ^oC overnight. The organic layer was extracted from DCM (2 × 100 mL) washed with brine solution (2 × 100 mL), dried over sodium sulfate, and solvent evaporated under reduced pressure to give a crude product that was purified by silica gel column chromatography in 6% ethyl acetate in hexane solvent mixture to yield **4.23** as a red solid (0.35 g, 76%). ^1H NMR (400 MHz, $CDCl_3$) δ 8.42 (d, J = 8.0 Hz, 2H); 8.39 (d, J = 8.2 Hz, 2H); 8.36 (d, J = 8.2 Hz, 2H); 8.10 (d, J = 8.0 Hz, 2H); 7.41 (s, 2H); 7.29 (d, J = 1.8 Hz, 4H); 7.13 (t, J = 1.8 Hz, 2H); 4.37 (t, J = 6.8 Hz, 4H); 2.84 (t, J = 7.9 Hz, 2H); 1.82 (sextet, J = 7.6 Hz, 4H); 1.60 - 1.24 (m, 32H); 1.13 (s, 36H); 1.03 (t, J = 7.3 Hz, 3H); 0.92 (t, J = 7.0 Hz, 6H). $^{13}C\{^1H\}$ NMR (100 MHz, $CDCl_3$) δ 168.23, 163.50, 149.84, 143.50, 142.17, 138.67, 135.20, 132.31, 131.80, 131.12, 130.33, 129.64, 129.50, 129.31, 129.27, 129.15, 125.83, 122.98, 122.45, 122.26, 121.61, 120.57, 65.82, 35.59, 34.68, 33.22, 31.93, 31.43, 31.25, 29.58, 29.56, 29.34, 29.33, 28.59, 26.03, 22.70, 14.13, 14.04. HRMS (MALDI): m/z 1198.7900 [M+H]+ (calcd. for $C_{82}H_{104}NO_6$: 1198.7864). Anal. Calcd. for $C_{82}H_{103}NO_6$ (%): C, 82.16; H, 8.66; N, 1.17. Found: C, 82.03; H, 8.78; N, 1.25.

(4.24)

Compound **4.10** (3.00 g, 3.06 mmol), 4,4,5,5-tetramethyl-2-(3,3",5,5"-tetra-*tert*-butyl-[1,1':3',1"-terphenyl]-5'-yl)-1,3,2-dioxaborolane – **4.19** (4.00 g, 6.74 mmol), $PdCl_2(dppf).CH_2Cl_2$ (0.25 g, 0.30 mmol) and K_2CO_3 (2.12 g, 15.3 mmol) were added into a 250 mL round bottomed flask, which was pump-filled with nitrogen three times. Toluene (60 mL) and methanol (60 mL) were added and the reaction was stirred at 75 ^oC overnight. The organic layer was extracted from dichloromethane (3 × 200 mL) washed

with brine solution (3 × 100 mL), dried over sodium sulfate and solvent removed under reduced vacuum to yield a crude product that was purified by silica gel column chromatography in dichloromethane/hexane (2:1) solvent mixture to yield **4.24** as a red solid (3.50 g, 66 %). ^{1}H NMR (400 MHz, $CDCl_3$) δ 8.45 (d, J = 8.0 Hz, 2H); 8.33 (d, J = 8.0 Hz, 2H); 8.23 (d, J = 8.2 Hz, 2H); 8.06 (d, J = 8.0 Hz, 2H); 8.45 (bs, 4H); 7.58 (m, 2H); 7.53 (s, 2H); 7.38 (m, 4H); 7.34 (m, 8H); 4.33 (t, J = 6.8 Hz, 4H); 2.86 (t, J = 8.0 Hz, 2H); 1.86 -1.75 (m, 6H); 1.55-1.20 (m, 108 H); 1.01 (t, J = 7.6 Hz, 3H); 0.90 (t, J = 7.4 Hz, 3H). ^{13}C{^{1}H} NMR (100 MHz, $CDCl_3$) δ 168.30, 163.95, 151.00, 143.82, 142.02, 141.49, 140.26, 140.08, 135.48, 132.18, 131.73, 131.56, 130.40, 130.34, 129.65, 129.27, 129.17, 129.02, 126.22, 125.93, 125.57, 122.42, 121.81, 121.60, 121.33, 65.83, 35.57, 34.93, 33.20, 32.84, 31.90, 31.50, 29.63, 29.56, 29.55, 29.45, 29.33, 29.32, 28.56, 26.01, 22.69, 141.12, 141.04. HRMS (MALDI): m/z 1727.1593 [M+H+] (calcd. For $C_{122}H_{152}NO_6$: 1727.1620). Anal. Calcd. for $C_{122}H_{151}NO_6$ (%): C, 84.82; H, 8.81; N, 0.81. Found: C, 84.54; H, 9.02; N, 0.86.

(4.25)

Compound **4.23** (0.50 g, 0.42 mmol), and toluene (50 mL) were added into a 100 mL round bottom flask and stirred at 95 ^{o}C until all the perylene dissolved. *p*-Toluenesulfonic acid (0.43 g, 2.50 mmol) was added and the reaction stirred at 95 ^{o}C overnight. The solvent was evaporated, and the crude product was purified via silica gel column chromatography using hexane/dichloromethane (30:70) as an eluent to yield **4.25** (0.26 g, 71 %). ^{1}H NMR (400 MHz, $CDCl_3$) δ 8.70 (d, J = 8.0 Hz, 2H); 8.62 (d, J = 8.2 Hz, 2H); 8.55 (d, J = 8.2 Hz, 2H); 8.49 (d, J = 8.0 Hz, 2H); 7.39 (s, 2H); 7.24 (d, J = 1.8 Hz, 4H); 7.09 (t, J = 1.8 Hz, 2H); 2.82 (t, J = 8.0 Hz, 2H); 1.79 (qunitet, J = 7.6 Hz, 2H); 1.51 (sextet, J = 7.4 Hz, 2H); 1.10 (s, 36H); 1.01 (t, J = 7.4 Hz, 3H). ^{13}C{^{1}H} NMR (100 MHz, $CDCl_3$) δ 163.03, 159.99, 149.88, 143.81, 142.04, 138.49, 136.46, 136.46, 133.54, 131.84, 131.13, 129.67, 129.22, 129.05, 126.83, 126.31, 123.99, 123.63, 123.14, 122.92, 120.58, 118.94, 35.57, 34.67, 33.19, 31.22, 22.69, 14.03. HRMS (MALDI): m/z 900.4651 [M+H]+ (calcd. For $C_{62}H_{62}NO_5$: 900.4628). Anal. Calcd. for $C_{62}H_{61}NO_5$ (%): C, 82.73; H, 6.83; N, 1.56. Found: C, 82.48; H, 6.81; N, 1.65.

(4.26)

Compound **4.24** (3.50 g, 2.03 mmol) and toluene (150 mL) were added into a 250 round bottomed flask and stirred at 95 ^{o}C until all the solid was dissolved. p-Toluenesulfonic acid (2.31 g, 12.2 mmol) was added and the reaction stirred at 95 ^{o}C overnight. The solvent was evaporated, and the crude product was purified via silica gel column chromatography using a mixture of dichloromethane/hexane (1:1) as an eluent to yield **4.26** (2.08 g, 72 %). ^{1}H NMR (400 MHz, $CDCl_3$) δ 8.66 (d, J = 8.00 Hz, 2H); 8.52 (d, J = 7.8 Hz, 2H); 8.51 (d, J = 7.6 Hz, 2H); 8.37 (d, J = 8.08 Hz, 2H); 7.67 (s, 4H); 7.58 (s, 2H); 7.53 (s, 2H); 7.39 (s, 4H); 7.34 (s, 8H); 2.87 (t, J = 7.8 Hz, 2H); 1.81 (quintet, 2H, J = 7.4 Hz); 1.53 (sextet, J = 7.3 Hz, 2H); 1.33 (s, 72 H); 1.01 (t, J = 7.3 Hz, 2H). ^{13}C{^{1}H} NMR (100 MHz, $CDCl_3$) δ 163.52, 159.95, 151.09, 144.14, 142.01, 141.44, 140.14, 139.95, 136.20, 133.73, 133.52, 131.77, 131.52, 130.40, 129.36, 129.23, 126.60, 126.37, 126.17, 125.54, 123.55, 123.47, 123.01, 121.53, 121.44, 119.03, 35.57, 34.94, 33.20, 31.50, 22.68, 14.03. HRMS (MALDI): m/z 1427.8325 [M+H]+ (calcd. For $C_{102}H_{109}NO_5$: 1427.8306). Anal. Calcd. for $C_{102}H_{111}NO_6 \cdot H_2O$ (%): C, 84.67; H, 7.73; N, 0.97. Found: C, 84.80; H, 7.85; N, 1.02.

(4.5)

Compound **4.25** (0.26 g, 0.29 mmol), diethyl (4-aminophenyl)phosphonate – **4.21** (0.20 g, 0.87 mmol), $ZnOAc_2 \bullet 2H_2O$ (0.06 g ,0.29 mmol), imidazole (6 g), and toluene (2 mL) were heated up to 150 ^{o}C and stirred for 3 h. The content was then poured into water (100 mL), extracted with dichloromethane (3 × 25 mL), dried over sodium sulfate, and solvent evaporated under reduced pressure to get the mono hydrolyzed species [PO(OEt)OH) instead of the $PO(OEt)_2$] as a red solid that was purified by column chromatography starting first with dichloromethane as an eluent to remove unreacted starting material, then 5% methanol in dichloromethane to isolate the desired species. This mono hydrolyzed species (0.23 g, 0.22 mmol) was then converted to the phosphonic acid by dissolving it in dry dichloromethane (200 mL) followed by the addition of bromotrimethyl silane (0.14 mL, 2.16 mmol) and stirring at room temperature for 3 d. Water/methanol 1:1 mixture (50 mL) was added and content stirred for 1 h at room temperature to quench the bromotrimethyl silane. The organic layer was isolated, dried

with anhydrous sodium sulfate, and solvent evaporated to yield **4.5** as a red solid that was washed several times with hexanes and acetonitrile (0.16 g, 55% combined yield over two steps). ^{1}H NMR (400 MHz, $CDCl_3$) δ 8.66 (d, J = 8.4 Hz, 2H); 8.59 (d, J = 7.5 Hz, 2H); 8.52 (d, J = 7.5 Hz, 2H); 8.43 (d, J = 8.4 Hz, 2H); 8.03 (bs, 2H); 7.39 (bs, 2H); 7.30 (s, 2H); 7.18 (d, J = 1.8 Hz, 4H); 7.05 (t, J = 1.8 Hz, 2H); 2.76 (t, J = 8.1 Hz, 2H); 1.73 (quintet, J = 7.8 Hz, 2H); 1.45 (sextet, J = 7.5 Hz, 2H); 1.05 (s, 36H); 0.96 (t, J = 7.4 Hz, 3H). ^{13}C{^{1}H} NMR (100 MHz, $CDCl_3$) δ 163.28, 149.87, 143.75, 142.02, 138.41, 135.49, 134.14, 131.99, 131.17, 129.77, 129.59, 129.20, 129.01, 126.66, 126.13, 123.38, 123.27, 123.14, 122.84, 122.73, 120.56, 35.49, 34.60, 33.19, 31.13, 29.64, 22.60, 13.93. HRMS (MALDI): m/z 1055.4780 [M+H]+ (calcd. For $C_{68}H_{68}N_2O_7P$: 1055.4764). ^{31}P{^{1}H} NMR (161.91 MHz, $CDCl_3$): δ 15.91 (s). Purity was also confirmed by HPLC, see HPLC in the appendix.

(4.6)

Compound **4.26** (0.50 g, 0.35 mmol), diethyl (4-aminophenyl)phosphonate – **4.21** (0.24 g, 1.05 mmol), $ZnOAc_2$•$2H_2O$ (0.02 g ,0.07 mmol), imidazole (20 g), and toluene (2 mL) were heated to 150 ^{o}C and stirred overnight. The reaction mixture was cooled, diluted in dichloromethane and then passed through a silica gel plug using first dichloromethane as an eluent to remove any unreacted starting material, then dichloromethane/acetone (85:15) to remove some unidentified impurities, then finally 10% acetic acid in dichloromethane to get the mono-hydrolyzed species [PO(OEt)OH) instead of the $PO(OEt)_2$] as a red solid which was further recrystallized from acetonitrile/dichloromethane mixture solid. The mono-hydrolyzed species (0.15 g, 0.09 mmol) was then converted to the phosphonic acid by dissolving it in dichloromethane (5 mL) then adding bromotriemthylsilane (0.12 mL, 0.93 mmol) and stirring overnight at room temperature. Water/methanol (1:1 mixture, 10 mL) was added and the content was stirred for 1 h at room temperature to quench the bromotrimethyl silane. The organic layer was isolated, dried with anhydrous sodium sulfate, and solvent evaporated under reduced pressure to yield a red solid that was then recrystallized from an acetonitrile/dichloromethane mixture to give **4.6** (0.09 g, 20% combined yield over two steps). ^{1}H NMR (400 MHz, $CDCl_3$) δ 8.58 (d, J = 8.1 Hz, 2H); 8.43 (t, J = 8.0 Hz, 4H); 8.28 (d, J = 7.8 Hz, 2H); 7.9 (m, 2H); 7.67 (d, J = 0.8 Hz, 4H); 7.49 (t, J = 1.5 Hz, 2H);

7.46 (s, 2H); 7. 35 (m, 2H); 7.31 (t, *J* = 1.5 Hz); 7.26 (t, *J* = 1.6 Hz, 8H); 2.79 (t, *J* = 7.2 Hz, 2H); 1.73 (qunitet, *J* = 7.5 Hz, 2H); 1.46 (sextet, *J* = 6.9 Hz, 2H); 1.25 (s, 72 H); 0.93 (t, *J* = 7.5 Hz, 3H). $^{13}C\{^{1}H\}$ NMR (100 MHz, $CDCl_3$) δ 163.54, 163.37, 150.88, 143.91, 141.87, 141.25, 139.96, 139.76, 137.78, 135.08, 134.10, 132.10, 132.02, 131.80, 131.29, 130.18, 129.57, 129.20, 129.03, 128.47, 128.33, 126.29, 125.98, 125.34, 122.90, 122.88, 122.83, 122.64, 121.32, 121.21, 35.33, 34.71, 32.99, 31.25, 22.43, 13.77. HRMS (MALDI): m/z 1583.8555 [M+H]+ (calcd. For $C_{108}H_{116}N_2O_7P$: 1583.8520). Anal. Calcd. for $C_{108}H_{115}N_2O_7P$. $2H_2O$ (%): C, 80.07; H, 7.40; N, 1.73. Found: C, 80.11; H, 7.32; N, 1.81.

(4.29)

Compound **4.26** (0.90 g, 0.63 mmol), diethyl (4-amino-3,5-diisopropylphenyl) phosphonate – **4.22** (0.98 g, 3.15 mmol), were dissolved in propanoic acid (7 mL) and the reaction was stirred at 160 ^{o}C overnight. The reaction mixture was poured over water and extracted from hexane, dried over anhydrous sodium sulfate, and solvent removed under reduced pressure to yield a red solid which was purified by silica gel column chromatography in 5 % ethyl acetate in dichloromethane to give compound **4.29** (0.30 g, 27%) as a red solid. ^{1}H NMR (400 MHz, $CDCl_3$) δ 8.70 (d, *J* = 8.0 Hz; 2H); 8.56 (d, *J* = 8.0 Hz; 2H); 8.55 (d, *J* = 8.2 Hz; 2H); 7.78 (d, *J* = 14 Hz; 2H); 7.70 (d, *J* = 1.7 Hz; 4H); 7.61 (t, *J* = 1.6 Hz; 2H); 7.54 (s, 2H); 7.41 (t, *J* = 1.7 Hz; 4H); 7.38 (d, *J* = 1.7 Hz; 8H); 4.19 (m, 4H); 2.88 (t, *J* = 7.7 Hz; 2H); 2.79 (quintet, *J* = 6.8 Hz; 2H); 1.82 (quintet, *J* = 7.6 Hz; 2H); 1.54 (sextet, *J* = 7.4 Hz; 2H); 1.41 (t, *J* = 7.0 Hz; 6H); 1.36 (s, 72H); 1.21 (d, *J* = 6.8 Hz; 12H); 1.02 (t, *J* = 7.40 Hz; 3H). $^{13}C\{^{1}H\}$ NMR (100 MHz, $CDCl_3$) δ 163.67, 163.29, 151.11, 146.57, 146.42, 144.04, 141.97, 141.51, 140.17, 140.05, 135.25, 134.38, 132.08, 131.59, 130.43, 130.08, 129.48, 129.34, 127.84, 127.73, 126.64, 126.31, 126.22, 125.53, 123.14, 123.04, 122.94, 122.82, 121.57, 121.46, 62.26, 35.58, 34.97, 33.22, 31.52, 29.35, 23.86, 22.7, 16.44, 14.04. HRMS (MALDI): m/z 1724.0227 [M+H]+ (calcd. For $C_{118}H_{135}N_2O_7P$: 1724.0085). Anal. Calcd. for $C_{118}H_{135}N_2O_7P$. H_2O (%): C, 81.34; H, 7.93; N, 1.61. Found: C, 81.43; H, 7.98; N, 1.61.

(4.7)

Bromotrimethyl silane (0.3 mL, 2.26 mmol) was added to **4.29** (0.13 g, 0.08 mmol) dissolved in anhydrous dichloromethane (5 mL). The reaction was stirred overnight at room temperature and under a nitrogen atmosphere. A tetrahydrofuran/methanol mixture (2:1, 9 mL) along with few drops of hydrochloric acid were added and the reaction was stirred overnight. The organic layer was separated, dried over anhydrous sodium sulfate, solvent evaporated under reduced pressure to yield a red solid, that was recrystallized from a dichloromethane/acetonitrile mixture to give **4.7** (70 mg, 60%). ^{1}H NMR (400 MHz, $CDCl_3$) δ 8.68 (d, J = 8.0 Hz, 2H); 8.54 (dd, J_1 = 8.2 Hz, J_2 = 2.0 Hz, 4H); 8.41 (d, J = 8.0 Hz, 2H); 7.83 (d, J = 14 Hz, 2H); 7.67 (d, J = 1.7 Hz, 4H); 7.58 (t, J = 1.6 Hz, 2H); 7.51 (s, 2H); 7.39 (t, J = 3.2 Hz, 4H); 7.35 (d, J = 1.7 Hz, 8H); 2.85 (t, J = 8.0 Hz, 2H); 2.73 (quintet, J = 6.6 Hz, 2H); 1.79 (m, 2H); 1.51 (sextet, J = 7.5 Hz, 2H); 1.33 (s, 72H); 1.18 (d, J = 6.8 Hz, 12H); 1.00 (t, J = 7.3 Hz, 3H). ^{13}C{^{1}H} NMR (100 MHz, $CDCl_3$) δ 163.51, 163.33, 150.91, 145.89, 145.78, 143.86, 141.79, 141.30, 139.95, 139.83, 135.16, 134.16, 131.97, 131.39, 130.22, 129.88, 129.22, 129.12, 126.98, 126.90, 126.43, 126.09, 126.00, 125.32, 122.94, 122.79, 122.48, 121.35, 121.25, 35.35, 34.75, 33.01, 31.29, 29.10, 23.58, 22.47, 13.81. HRMS (MALDI): m/z 1667.9421[M+H]+ (Calcd. For $C_{114}H_{127}N_2O_7P$: 1667.9459). Purity was confirmed by HPLC, see HPLC trace in the appendix

4.4.2 High performance liquid chromatography

High performance liquid chromatography (HPLC) traces of the dyes were collected on a Shimadzu Class-VP series HPLC system equipped with a SCL-10A system controller, a SPD-10AV UV-Vis detector, a SPD-M10A diode array detector, and a Chromegabond WR C18 5µ, 120Å, 150 × 4.6 mm column. The mobile phase adapted for the measurements of **4.5** was a 5mM phosphate buffer (Sodium Phosphate dibasic) in water solution (55%) with tetrahydrofuran (45%). The mobile phase adapted for the measurements of **4.7** was a 5mM phosphate buffer (sodium phosphate dibasic) in water solution (50%) with tetrahydrofuran (50 %). For the traces, the reader is referred to the Appendix.

4.5 REFERENCES

(1) Cui, J.; Wang, A.; Edleman, N. L.; Ni, J.; Lee, P.; Armstrong, N. R.; Marks, T. J. *Adv. Mater.* **2001**, *13*, 1476.

(2) Brabec, C. J. *Sol. Energy Mater. Sol. Cells* **2004**, *83*, 273.

(3) Brabec, C.; Scherf, U.; Dyakonov, V. *Organic photovoltaics: materials, device physics, and manufacturing technologies*; John Wiley & Sons, 2011.

(4) Hagfeldt, A.; Boschloo, G.; Sun, L.; Kloo, L.; Pettersson, H. *Chem. Rev.* **2010**, *110*, 6595.

(5) Lee, M. M.; Teuscher, J.; Miyasaka, T.; Murakami, T. N.; Snaith, H. J. *Science* **2012**, *338*, 643.

(6) Armstrong, N. R.; Veneman, P. A.; Ratcliff, E.; Placencia, D.; Brumbach, M. *Acc. Chem. Res.* **2009**, *42*, 1748.

(7) Paniagua, S. A.; Hotchkiss, P. J.; Jones, S. C.; Marder, S. R.; Mudalige, A.; Marrikar, F. S.; Pemberton, J. E.; Armstrong, N. R. *J. Phys. Chem. C* **2008**, *112*, 7809.

(8) Brumbach, M.; Veneman, P. A.; Marrikar, F. S.; Schulmeyer, T.; Simmonds, A.; Xia, W.; Lee, P.; Armstrong, N. R. *Langmuir* **2007**, *23*, 11089.

(9) Sharma, A.; Kippelen, B.; Hotchkiss, P. J.; Marder, S. R. *Appl. Phys. Lett.* **2008**, *93*, 163308.

(10) Li, F.; Tang, H.; Shinar, J.; Resto, O.; Weisz, S. Z. *Appl. Phys. Lett.* **1997**, *70*, 2741.

(11) Wu, C.; Wu, C.; Sturm, J.; Kahn, A. *Appl. Phys. Lett.* **1997**, *70*, 1348.

(12) Zhou, Y.; Fuentes-Hernandez, C.; Shim, J.; Meyer, J.; Giordano, A. J.; Li, H.; Winget, P.; Papadopoulos, T.; Cheun, H.; Kim, J.; Fenoll, M.; Dindar, A.; Haske, W.; Najafabadi, E.; Khan, T. M.; Sojoudi, H.; Barlow, S.; Graham, S.; Brédas, J.-L.; Marder, S. R.; Kahn, A.; Kippelen, B. *Science* **2012**, *336*, 327.

(13) Hotchkiss, P. J.; Jones, S. C.; Paniagua, S. A.; Sharma, A.; Kippelen, B.; Armstrong, N. R.; Marder, S. R. *Acc. Chem. Res.* **2012**, *45*, 337.

(14) Steim, R.; Kogler, F. R.; Brabec, C. J. *J. Mater. Chem.* **2010**, *20*, 2499.

(15) Hanson, E. L.; Guo, J.; Koch, N.; Schwartz, J.; Bernasek, S. L. *J. Am. Chem. Soc.* **2005**, *127*, 10058.

(16) Oura, K.; Zotov, A.; Lifshits, V.; Saranin, A.; Katayama, M. *Surface science*; Springer, 2003.

(17) Love, J. C.; Estroff, L. A.; Kriebel, J. K.; Nuzzo, R. G.; Whitesides, G. M. *Chem. Rev.* **2005**, *105*, 1103.

(18) Haensch, C.; Hoeppener, S.; Schubert, U. S. *Chem. Soc. Rev.* **2010**, *39*, 2323.

(19) Allara, D. L.; Nuzzo, R. G. *Langmuir* **1985**, *1*, 52.

(20) Allara, D. L.; Nuzzo, R. G. *Langmuir* **1985**, *1*, 45.

(21) Vercelli, B.; Zotti, G.; Schiavon, G.; Zecchin, S.; Berlin, A. *Langmuir* **2003**, *19*, 9351.

(22) Hotchkiss, P. J.; Li, H.; Paramonov, P. B.; Paniagua, S. A.; Jones, S. C.; Armstrong, N. R.; Brédas, J. L.; Marder, S. R. *Adv. Mater.* **2009**, *21*, 4496.

(23) Kim, J. S.; Park, J. H.; Lee, J. H.; Jo, J.; Kim, D.-Y.; Cho, K. *Appl. Phys. Lett.* **2007**, *91*, 112111.

(24) Goh, C.; Scully, S. R.; McGehee, M. D. *J. Appl. Phys.* **2007**, *101*, 114503.

(25) Weber, J.; Volke, J. *Electrochim. Acta* **1979**, *24*, 113.

(26) Clarke, E. D.; Wardman, P.; Goulding, K. H. *Biochem. Pharmacol.* **1980**, *29*, 2684.

(27) Laviron, E. *J. Electroanal. Chem. Interfacial. Electrochem.* **1979**, *100*, 263.

(28) Donley, C.; Dunphy, D.; Paine, D.; Carter, C.; Nebesny, K.; Lee, P.; Alloway, D.; Armstrong, N. R. *Langmuir* **2002**, *18*, 450.

(29) Marrikar, F. S.; Brumbach, M.; Evans, D. H.; Lebrón-Paler, A.; Pemberton, J. E.; Wysocki, R. J.; Armstrong, N. R. *Langmuir* **2007**, *23*, 1530.

(30) Carter, C.; Brumbach, M.; Donley, C.; Hreha, R. D.; Marder, S. R.; Domercq, B.; Yoo, S.; Kippelen, B.; Armstrong, N. R. *J. Phys. Chem. B* **2006**, *110*, 25191.

(31) Brown, D. G.; Schauer, P. A.; Borau-Garcia, J.; Fancy, B. R.; Berlinguette, C. P. *J. Am. Chem. Soc.* **2013**, *135*, 1692.

(32) Ernstorfer, R.; Gundlach, L.; Felber, S.; Storck, W.; Eichberger, R.; Willig, F. *J. Phys. Chem. B* **2006**, *110*, 25383.

(33) Hau, S. K.; Cheng, Y.-J.; Yip, H.-L.; Zhang, Y.; Ma, H.; Jen, A. K. Y. *ACS Appl. Mater. Interfaces* **2010**, *2*, 1892.

(34) Lin, H.-C.; MacDonald, G. A.; Shi, Y.; Polaske, N. W.; McGrath, D. V.; Marder, S. R.; Armstrong, N. R.; Ratcliff, E. L.; Saavedra, S. S. *J. Phys. Chem. C* **2015**, *119*, 10304.

(35) Lin, H.-C.; Polaske, N. W.; Oquendo, L. E.; Gliboff, M.; Knesting, K. M.; Nordlund, D.; Ginger, D. S.; Ratcliff, E. L.; Beam, B. M.; Armstrong, N. R. *J. Phys. Chem. Lett.* **2012**, *3*, 1154.

(36) Feng, Z. Q.; Sagara, T.; Niki, K. *Anal. Chem.* **1995**, *67*, 3564.

(37) Araci, Z. O.; Runge, A. F.; Doherty, W. J.; Saavedra, S. S. *J. Am. Chem. Soc.* **2008**, *130*, 1572.

(38) D'Souza, F.; Maligaspe, E.; Ohkubo, K.; Zandler, M. E.; Subbaiyan, N. K.; Fukuzumi, S. *J. Am. Chem. Soc.* **2009**, *131*, 8787.

(39) Zheng, Y.; Giordano, A.; Cowan, S. R.; Fleming, S. R.; Shallcross, R. C.; Gliboff, M.; Huang, Y.; Nordlund, D.; Ginger, D. S.; McGrath, D. V.; Armstrong, N. R.; Olson, D. C.; Marder, S. R.; Saavedra, S. S. manuscript in preparation, 2016.

(40) Nielsen, C. B.; Holliday, S.; Chen, H.-Y.; Cryer, S. J.; McCulloch, I. *Acc. Chem. Res.* **2015**, *48*, 2803.

(41) Huang, C.; Barlow, S.; Marder, S. R. *J. Org. Chem.* **2011**, *76*, 2386.

(42) Wurthner, F. *Chem. Commun.* **2004**, 1564.

(43) Lin, M.-J.; Jimenez, A. J.; Burschka, C.; Wurthner, F. *Chem. Commun.* **2012**, *48*, 12050.

(44) Xue, C.; Sun, R.; Annab, R.; Abadi, D.; Jin, S. *Tetrahedron Lett.* **2009**, *50*, 853.

(45) Ramanan, C.; Smeigh, A. L.; Anthony, J. E.; Marks, T. J.; Wasielewski, M. R. *J. Am. Chem. Soc.* **2012**, *134*, 386.

(46) Glockler, G. *J. Phys. Chem.* **1959**, *63*, 828.

(47) Ishiyama, T.; Murata, M.; Miyaura, N. *J. Org. Chem.* **1995**, *60*, 7508.

(48) Finke, A. D.; Moore, J. S. *Org. Lett.* **2008**, *10*, 4851.

(49) Chang, K.-J.; Moon, D.; Lah, M. S.; Jeong, K.-S. *Angew. Chem.* **2005**, *117*, 8140.

(50) Bedard, T. C.; Moore, J. S. *J. Am. Chem. Soc.* **1995**, *117*, 10662.

(51) Bessmertnykh, A.; Douaihy, C. M.; Guilard, R. *Chem. Lett.* **2009**, *38*, 738.

(52) Abdalla, M. A.; Bayer, J.; Rädler, J. O.; Müllen, K. *Angew. Chem. Int. Ed.* **2004**, *43*, 3967.

(53) Würthner, F.; Thalacker, C.; Diele, S.; Tschierske, C. *Chem.--Eur. J.* **2001**, *7*, 2245.

(54) Gómez, R.; Veldman, D.; Blanco, R.; Seoane, C.; Segura, J. L.; Janssen, R. A. J. *Macromolecules* **2007**, *40*, 2760.

(55) Lee, S. K.; Zu, Y.; Herrmann, A.; Geerts, Y.; Müllen, K.; Bard, A. J. *J. Am. Chem. Soc.* **1999**, *121*, 3513.

(56) Haines, C.; Chen, M.; Ghiggino, K. P. *Sol. Energy Mater. Sol. Cells* **2012**, *105*, 287.

(57) Chen, Z.; Stepanenko, V.; Dehm, V.; Prins, P.; Siebbeles, L. D. A.; Seibt, J.; Marquetand, P.; Engel, V.; Würthner, F. *Chem.--Eur. J.* **2007**, *13*, 436.

CHAPTER 5 SMALL MOLECULE DONORS FOR SOLUTION PROCESSED ORGANIC PHOTOVOLTAICS

5.1 INTRODUCTION

Functional oligothiophenes are among the most frequently used π-conjugated materials as active components in organic electronics.[1] This could be attributed to; the developed nature of the thiophene chemistry, especially in transition-metal catalyzed cross-coupling chemistry;[2] their structural versatility, which allows tuning of their electronic and optical properties, as well as their physical properties such as solubility and packing; and the high polarizability of the sulfur atoms in the thiophene rings, which can lead to good charge transport, necessary for organic electronic applications.[3]

In organic photovoltaics, when compared to their polymeric analogues, oligothiophenes have attracted attention as hole-transporting material due to their well-defined molecular structures, exact molecular weights, and the ability to reproduce their synthesis in high purity without batch to batch variations. In 2006, Roquet *et al.* reported three dimensional tetra(terthiophene) donors, connected by a tetrahedral silicon core, who when incorporated in OPV devices with $PC_{61}BM$, resulted in low PCE ca. 0.3% due to their low absorption in the visible and near infra-red region (absorption onset ca. 500 nm).[4] In an attempt to increase the oligothiophenes' light absorption, and adjust their optical gap, following reports either increased the conjugation lengths, by adding extra thiophene units, or changed the oligothiophene design to a "push-pull" design that incorporates alternating donor (D) and acceptor (A) groups in a D-A-D or A-D-A manner.[5-7] For example, Liu *et al.* reported three oligothiophenes with three, five, and seven thiophene units, and observed a decrease in the optical gap from 1.90 eV to 1.74 eV and 1.68 eV (**5.5**) respectively, due to extended conjugation.[7] Solution processed OPV devices fabricated from **5.1**, Figure 5.1, and $PC_{71}BM$ showed a PCE ca. 3.7%, however the devices suffered from low FF, which the authors attributed to low film quality caused by the high rigidity of the system and the material's low solubility.[8]

Substituting the electron withdrawing malononitrile with cyanoacetate electron acceptor in **5.2** and **5.3**, Figure 5.1, increased the material's solubility and enhanced the quality of the films spin-casted from it and solution processed OPV devices fabricated

with a **5.3**:$PC_{61}BM$ blend achieved PCE ca. 5.10%.[9] **5.3** had an optical gap ca. 1.84 eV (absorption onset ca. 674 nm) and in an attempt to achieve better overlap with the solar spectrum, the cyanoacetate electron acceptor groups were then substituted with stronger electron acceptors such as indanedione, 1,3-dimethylbarbituric acid, and *N*-ethyl rhodanine (**5.4** in Figure 5.1) which further reduced the optical gap to as low as 1.53 eV. Solution processed OPV devices fabricated with **5.4**:$PC_{61}BM$ blends where shown to result in PCE values ca. 6.1% which could be attributed to their higher J_{SC}.[10,11] More recently, Zhang *et al.* and Kan *et al.* synthesized quinque- and septethiophene with *N*- *N*-ethyl cyanorhodanine end groups, **5.5** and **5.6** respectively,[12,13] and achieved PCE ca. 10%. In the solid-state, these films had an absorption onset at ca. 800 nm, and upon thermal annealing exhibited a red absorption feature, bathochromically shifted from the main absorption band, which was attributed to increased intermolecular interaction. When blended with $PC_{71}BM$, these materials formed interpenetrating networks of crystalline fibrils (10-20 nm in diameter), and demonstrated hole-mobilities on the order of 10^{-4} $cm^2V^{-1}s^{-1}$, which is beneficial for exciton dissociation and transport.

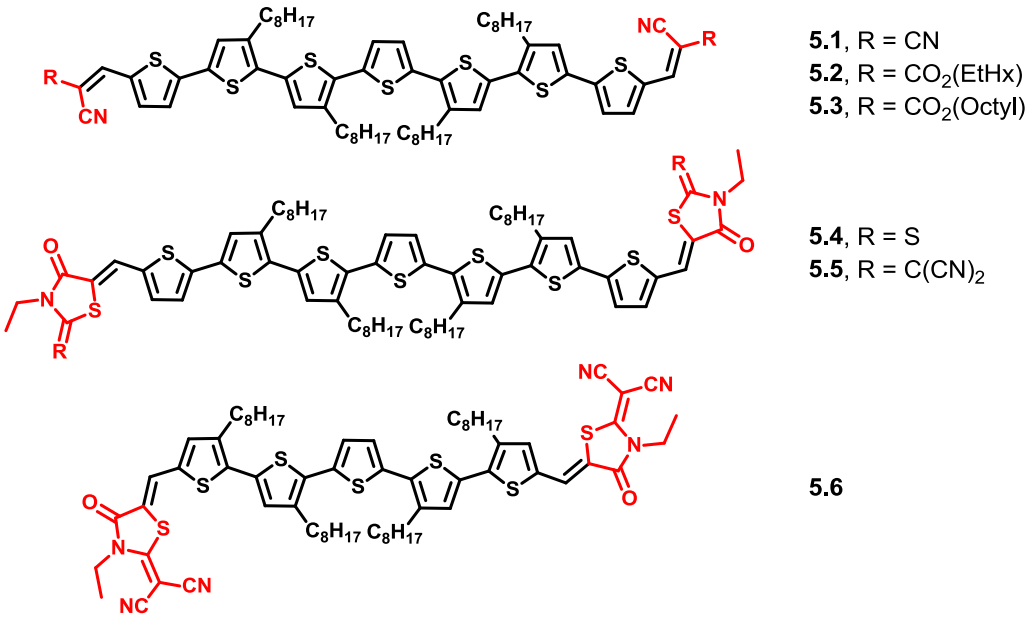

Figure 5.1 Molecular structure of oligothiophenes (A-D-A) donor described in literature.

Bauerle *et al.* compared the position of the alkyl solubilizing groups on the oligothiophene's packing and device performance in a vacuum deposited OPV, and reported that by changing the position of the methyl groups to point away from each

other, **5.8** vs. **5.7**, better molecular order could be achieved with **5.8**, as suggested by solid-state optical measurements (presence of a red-shifted shoulder) and crystal structure which showed molecules stacking with intermolecular distance ca. 3.28 Å. The PCE of vacuum deposited OPV devices formed from **5.8**:C_{60} blends reached ca. 6.9% which is higher than those fabricated from **5.7** ca. 4.8%. The enhanced performance was attributed to the higher J_{SC} in the devices fabricated from **5.8** due to better EQE at low energy.[14]

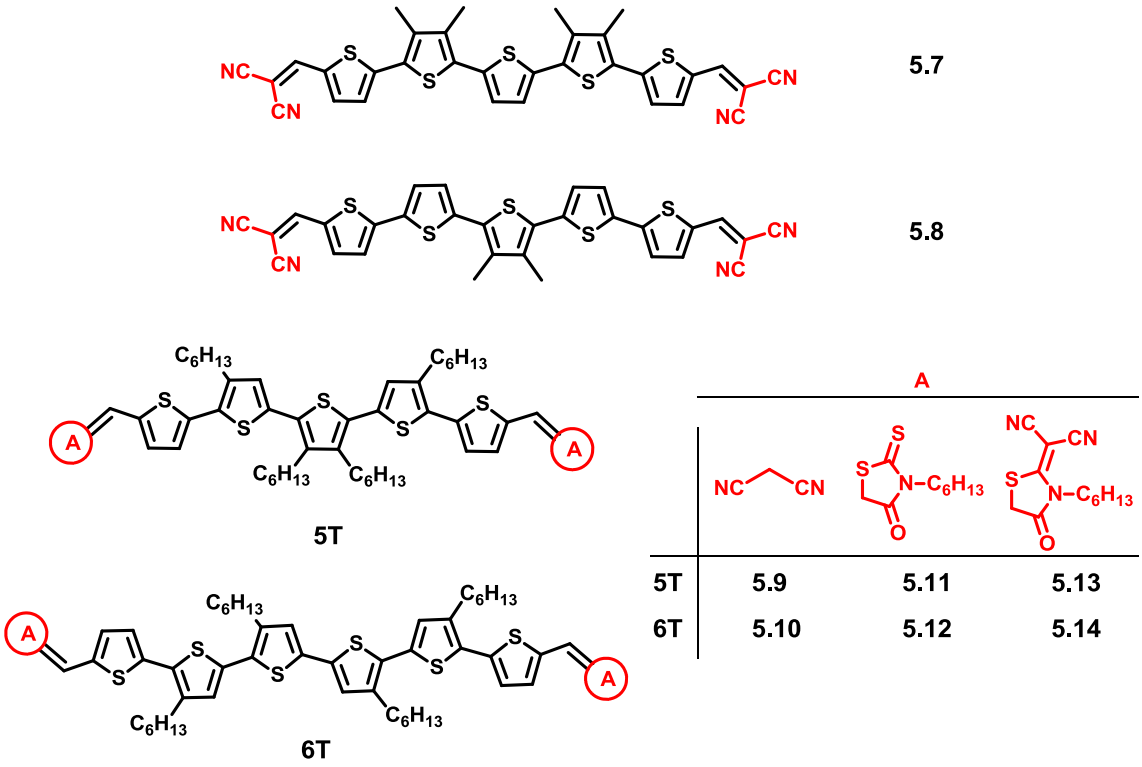

Figure 5.2 Structure of the synthesized quinquethiophene and sexithiophene hole transporting materials studied in this chapter, **5.9**-**5.14**, as well as the structures of quinquethiophenes reported by Bauerle *et al*,[14] **5.7** and **5.8**.

To further explore the potential of these oligothiophenes as hole-transport materials, namely the effect of their intermolecular interaction on solar cell performance, a series of quinquethiophene (five thiophene units) and sexithiophene (six thiophene units) hole transport materials were designed according to the ADA geometry, Figure 5.2. These oligothiophenes have four hexyl solubilizing groups on their central thiophenes, and either malononitrile, **5.9** and **5.10**, *N*-hexyl rhodanine, **5.11** and **5.12**, or *N*-hexyl cyanorhodanine, **5.13** and **5.14**, electron accepting end groups. Unlike **5.6** and its analogues reported by Kan *et al.*[12] the hexyl solubilizing group point away from each

other, which can be envisioned to enhance molecular order and stacking in a similar manner observed with Bauerle *et al.*[14]

Another promising small molecule hole transporting materials are those based on benzodithiophene core.[15,16] By changing the central thiophene unit in an analogue of **5.3** to a benzodithiophene unit, **5.15** in Figure 5.3, Liu *et al.* reported a solution processed OPV device fabricated using **5.15** and $PC_{61}BM$ with PCE ca. 5.4%.[17] Compound **5.15**, had a solid-state absorption onset around 700 nm, and in an attempt to increase its light absorbing ability, a more conjugated analogue (having four extra thiophene units),[15] was synthesized. However, the extended conjugation only decreased the optical gap by ca. 40 mV to 1.79 eV, while the V_{OC} dropped by ca.140 mV due to the higher lying HOMO energy level. A more successful attempt to increase the light absorption of small molecules based on benzodithiophene core, without affecting the other photovoltaic parameters, was reported by Zhou *et al.* who upon changing the electron acceptor on **5.15**, to *N*-ethyl rhodanine in **5.16**, were able to reduce the optical gap of the material to 1.72 eV, while maintaining the HOMO energy level unchanged. This resulted in PCEs ca. 8.1% in solution processed OPV devices based on **5.16** and $PC_{71}BM$ blends.[18]

More recently Sun *et al.* reported a benzodithiophene based hole-transport with ADA architecture having *N*-hexyl rhodanine as an electron acceptor, **5.17** in Figure 5.3.[19] A solution processed bulk heterojunction OPV device fabricated from **5.17** and $PC_{71}BM$ have yielded PCEs that exceeded 9.0%.[19] this performance was attributed to **5.17**'s liquid crystalline behavior and strong intermolecular interactions and hole-mobility ca. 1.6×10^{-3} $cm^2V^{-1}s^{-1}$. The absorption onset of **5.17** in film was ca. 681 nm which is equivalent to an optical gap of 1.82 eV and devices fabricated by **5.17** showed a J_{SC} ca. 13 $mAcm^{-2}$, which in part could be attributed to its relatively large optical gap.

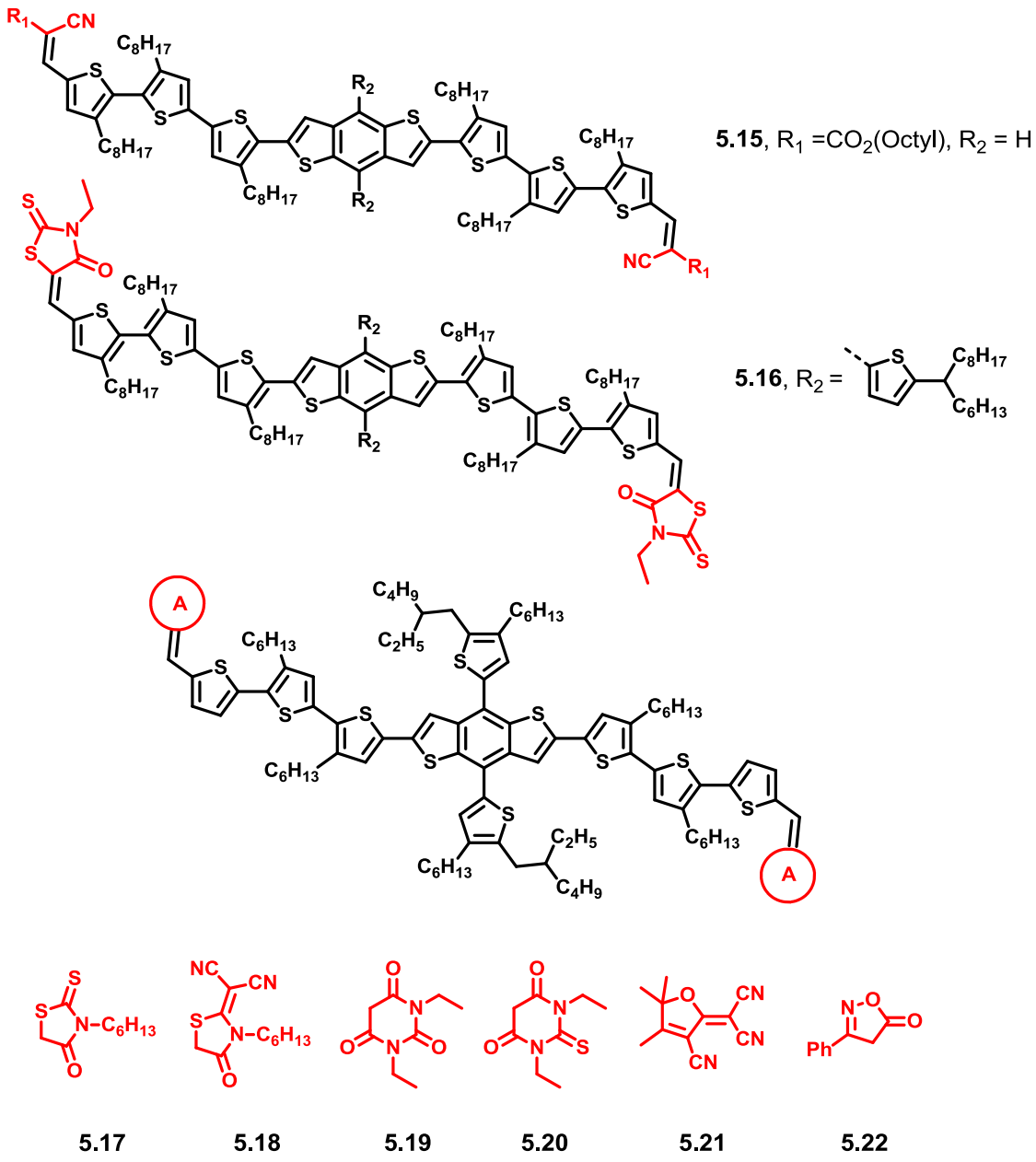

5.17 **5.18** **5.19** **5.20** **5.21** **5.22**

Figure 5.3 Molecular structure of the benzodithiophene hole transporting material reported in literature, **5.15**-**5.17**, as well as those reported in this chapter, **5.18** to **5.22**.

This chapter aims towards exploring the extent by which **5.7**'s EA, estimated at ca. 3.52 eV, can be changed without adversely altering the other desirable physical properties that the material possesses, such as packing, solubility and charge transport. This is going to be achieved through changing the electron end groups from *N*-hexyl rhodanine to those highlighted in Figure 5.3 (**5.18** to **5.22**), while keeping the benzodithiophene core unchanged.

5.2 RESULTS AND DISCUSSION

5.2.1 Material synthesis

Scheme 5.1 highlights the synthetic routes towards the oligothiophene cabroxaldehyde intermediates **5.27** and **5.32**. To synthesize **5.27**, 2,3,4,5-tetrabromothiophene **5.23** was debrominated using zinc to get 3,4-dibromothiophene, **5.24**,[20] which, upon Kumada coupling with hexyl magnesium bromide yielded 3,4-dihexylthiophene, **5.25**.[21] Iridium-catalyzed C–H Borylation of **5.25** with bis(pinacolato)diboron gave rise to **5.26**,[22] which, after a Suzuki-Miyaura coupling reaction with **5.29** yielded the desired carboxaldehyde intermediate **5.27**.[23] On the other hand, to get **5.22**, lithiation of commercially available 3-hexylthiophene followed by copper assisted oxidative homo coupling yielded 4,4'-dihexyl-2,2'-bithiophene, **5.30**, in high yields.[24] Similar to before, iridium-catalyzed C-H bond borylation yielded compound **5.31**, which, after Suzuki-Miyaura coupling with **5.29** afford **5.32**. The building block **5.29**, common to both synthesis, was prepared by **5.28** with iodine monochloride.[25] **5.28** was, in turn, prepared via the Suzuki-Miyaura coupling reaction of 5-bromothiophene-2-carbaldehyde, and **5.28A**, which was synthesized according to literature procedure.[26]

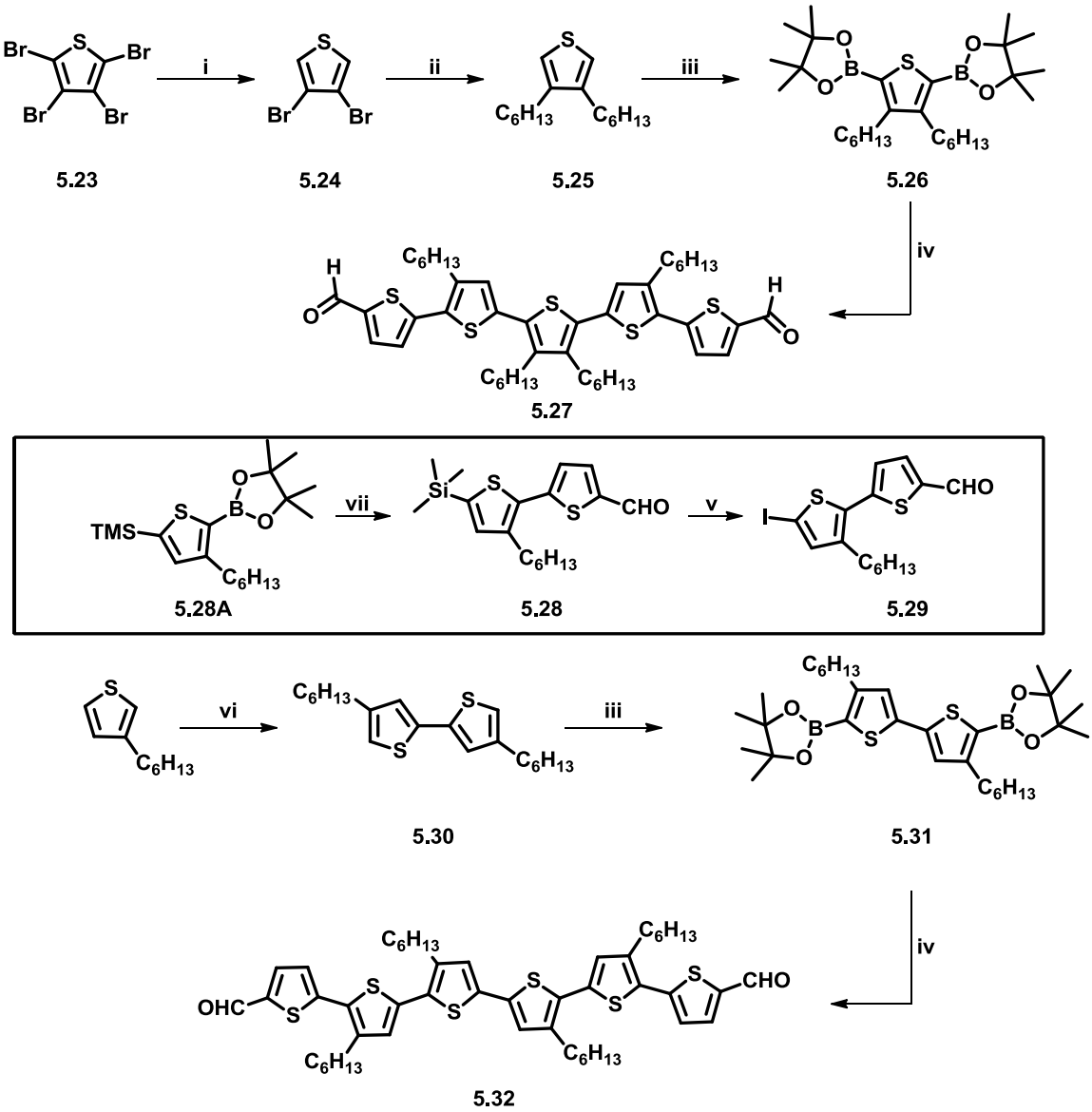

Scheme 5.1 Synthesis of the oligothiophene cabroxaldehyde intermediates (i) a) Acetic acid, water; b) Zinc dust, 2 days, RT; 99% (ii) a) 1-Bromohexane, Mg, THF, 0 ^{o}C, 30 min then reflux for 2 hours; b) **5.24**, THF, Ni(dppp)$_2$, $C_6H_{17}MgBr$, reflux overnight; 92% (iii) a) **5.25**, DME, b) In the following order: [Ir(COD)$_2$OMe]$_2$ then B_2Pin_2 then 4,4'-di-*tert*-butyl-2,2'-Bipyridine, 85 ^{o}C overnight; 42% (iv) **5.29**, Pd_2dba_3, P(o-tolyl)$_3$, K_3PO_4 (2M), THF, 60 ^{o}C; 61% v) a) DCM, -15 ^{o}C, N_2 atm; b) ICl in DCM added dropwise, stir for 1h; 64%. (vi) a) TMEDA, THF, 0 ^{o}C; b) ^{n}BuLi, 0 ^{o}C to 50 ^{o}C for 1h then to -78 ^{o}C; c) $CuCl_2$, -78 ^{o}C, 40 min; 90% (vii) 5-bromothiophene-2-carbaldehyde, Pd_2dba_3, P(o-tolyl)$_3$, K_3PO_4 (2M), THF, 60 ^{o}C; 70%

The oligothiophene carboxaldehydes **5.27** and **5.32** were then transformed into the desired hole-transporting materials, presented in Figure 5.2, by Knoevenagel condensation as shown in Scheme 5.2. The respective aldehydes were reacted with 10

molar equivalents of the appropriate acceptor (malononitrile, *N*-hexyl rhodanine, or *N*-hexyl cyanorhodanine) in the presence of 1.8-diazabicycloundec-7-ene (DBU) as a base for three hours at room temperature to yield the desired compounds on 100-200 mg scale, with low to moderate yields. It is worth mentioning some of the material was lost during the multiple purification steps.

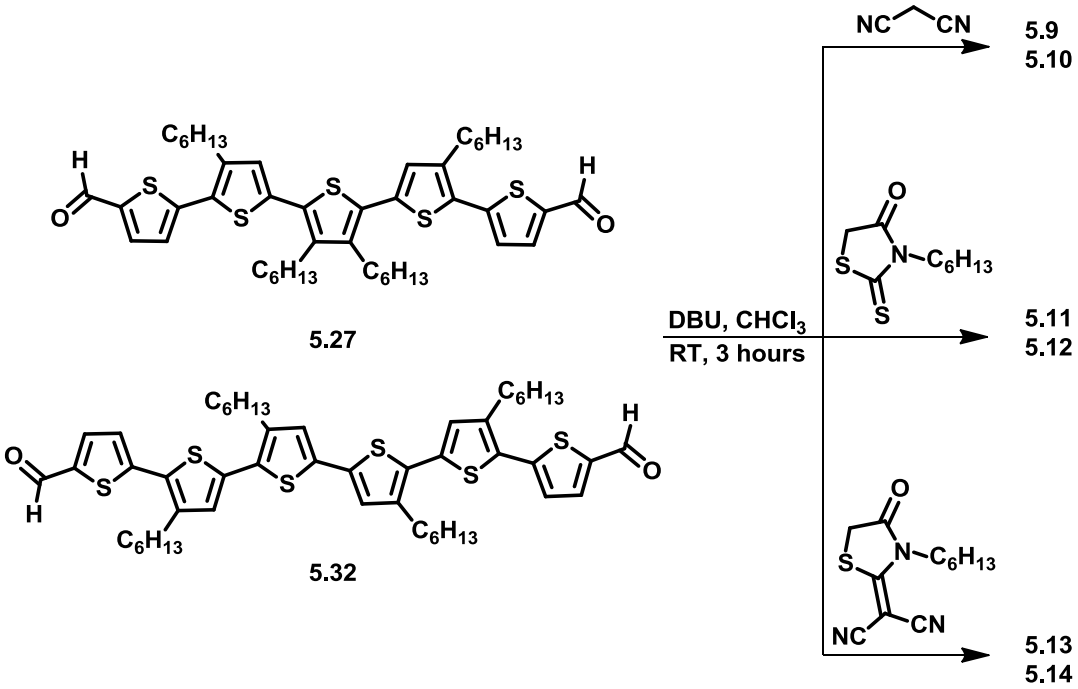

Scheme 5.2 Synthesis of the target oligothiophene hole transporting materials. Reaction yields varied from 20 to 70 %.

The benzodithiophene terthiophene carboxaldehyde core, **5.36**, was prepared via a Stille coupling reaction between a bis-stannylated benzodithiophene core,[27] **5.33**, and a brominated terthiophene π-bridge,[28] **5.34**, as highlighted in Scheme 5.3. Knoevenagel condensations with the appropriate acceptors highlighted in Figure 5.3 yielded the respective ADA materials in moderate yields.[19] In all of the condensations, DBU or tetramethyl piperidine (in the case of **5.21**) was used as a base and the starting material was consumed after 3 hours, with the exception of **5.21** where longer reaction times were required to drive the reaction forward.

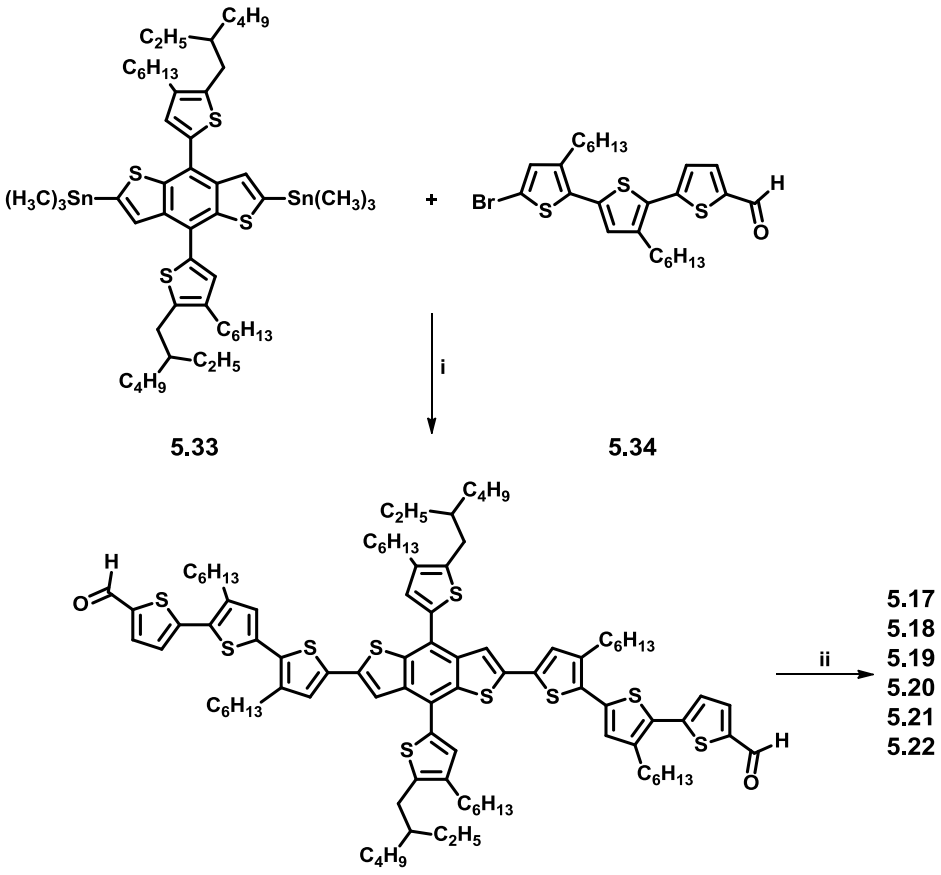

Scheme 5.3 Synthesis of the benzodithiophene derivatives. (i) Pd_2dba_3, P(o-tolyl)$_3$, toluene, 125 ^oC, 12h; 53% (ii) $CHCl_3$, Base (DBU or tetramethylpiperidine); RT or 70 ^oC, 3h or overnight; 50-70 %.

5.2.2 Optical and electrochemical properties

5.2.2.1 Oligothipohenes

The solution and solid-state normalized absorption spectra of the oligothiophene hole transport materials are presented in Figure 5.4 and Figure 5.5, with the relevant values listed in Table 5.1. Two prominent features were observed in the spectra of all A-D-A oligothiophenes; a low energy band in the 450-650 nm range, and a higher energy band between 350 and 450 nm, with the lower energy peaks exhibiting larger molar extinction coefficients that are on the order of 5×10^4 $M^{-1}cm^{-1}$, Table 5.1. The high energy bands are associated with π-π^* transitions of the oligothiophene core, while the lowest energy absorption can be assigned to the intermolecular charge transfer (ICT) between the thiophene donor part and the acceptor end groups.[29,30] Upon extending π-conjugation (increasing the number of thiophene units), the absorption maxima red-shifted to longer wavelengths by ca. 0.04 eV. On the other hand, relative to the absorption maxima of oligothiophenes having *N*-hexyl rhodanine acceptors (**5.11** and **5.12**), those having malononitrile and *N*-hexyl cyanorhodanine acceptors were red-shifted by up to 0.09 eV (between **5.11** and **5.13** as an example), which is consistent with what has been reported in literature.[7,10,13]

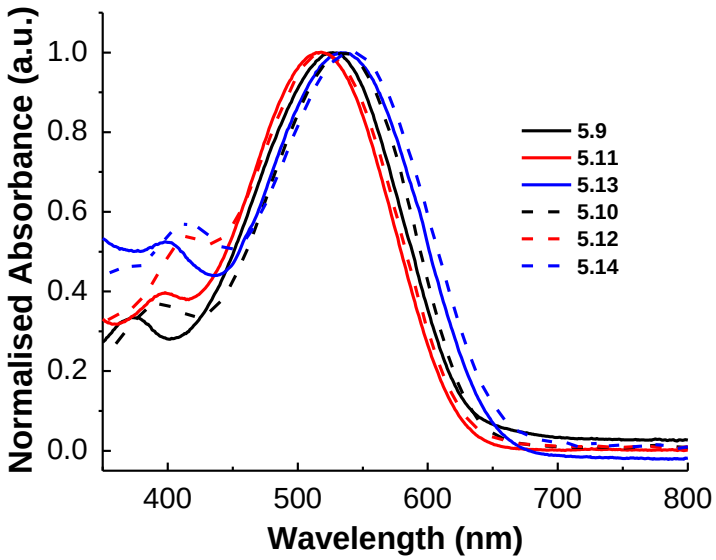

Figure 5.4 UV/Vis absorption measurements of the oligothiophenes in chloroform. Solid lines are quinquethiophenes while dashed lines are sexithiophenes

Table 5.1 Optical properties of the oligothiophenes

		Solution		Film		
		λ_{max} [nm]	ε [$M^{-1}cm^{-1}$]	λ_{max} [nm]	λ_{onset} [nm][a]	$E_{0\text{-}0}^{opt}$ [eV][b]
	5.9	527	4.2×10^4	594, 644	711	1.74
5T	**5.11**	514	4.9×10^4	586, 622	716	1.73
	5.13	533	5.7×10^4	598	733	1.69
	5.10	536	4.4×10^4	604, 656	718	1.73
6T	**5.12**	520	5.0×10^4	602, 656	752	1.65
	5.14	534	5.4×10^4	624	767	1.62

[a] Estimated from the intersection of a tangent drawn at the leading edge of the peak and the x-axis. [b]Estimated following the equation $E_{0\text{-}0}^{opt} = 1240/\lambda_{onset}$ [nm].

Upon transitioning from the liquid phase into the solid phase, supramolecular arrangements driven by intermolecular π-π and σ-π interactions come into play, and dictate the packing mode.[31,32] For example, these intermolecular interactions can lead to either edge-to-edge or face-to-face stacks that can be observed optically as a bathochromic or a hypsochromic shift in the main absorption band, respectively, compared to the monomer.[33,34] In polymers, and to an extent in the case of oligothiophenes discussed in this chapter, spectral red-shifts that retain high degrees of vibrational resolution may be assigned to structures going from mainly twisted conformations in solution to planar conformations in the solid state.[35-37] The solid-state absorption spectra of these oligothiophenes spun on glass were bathochromically shifted compared to solution, and experienced general broadening. In addition, the solid-state absorption spectra showed the presence of two bands: a low energy band between 622-660 nm and a high energy band between 580-625 nm. In the case of oligothiophenes with *N*-hexyl cyanorhodanine acceptors (**5.13** and **5.14**) the lowest energy peak is a barely resolvable shoulder.

This behavior in the solid state has been observed for oligothiophene A-D-A molecules,[27,38,39] and has been suggested to arise from a more ordered structure that experiences increased intermolecular π–π interactions. Moreover, the energy separation between the two sharp absorption maxima in the solid-state absorption spectra of **5.9**, and

of **5.10** as well, (black lines in Figure 5.5) were estimated to be ca. 1300 cm^{-1} (in conjugated molecules, such as oligothiophene, the vibrational mode is basically a symmetric stretching and ring-breathing with an energy ca. 1400 cm^{-1})[40] which might suggest a vibronic progression that could be intensified from planarization of the oligothiophene in the solid state due to the aforementioned intermolecular π–π interactions.

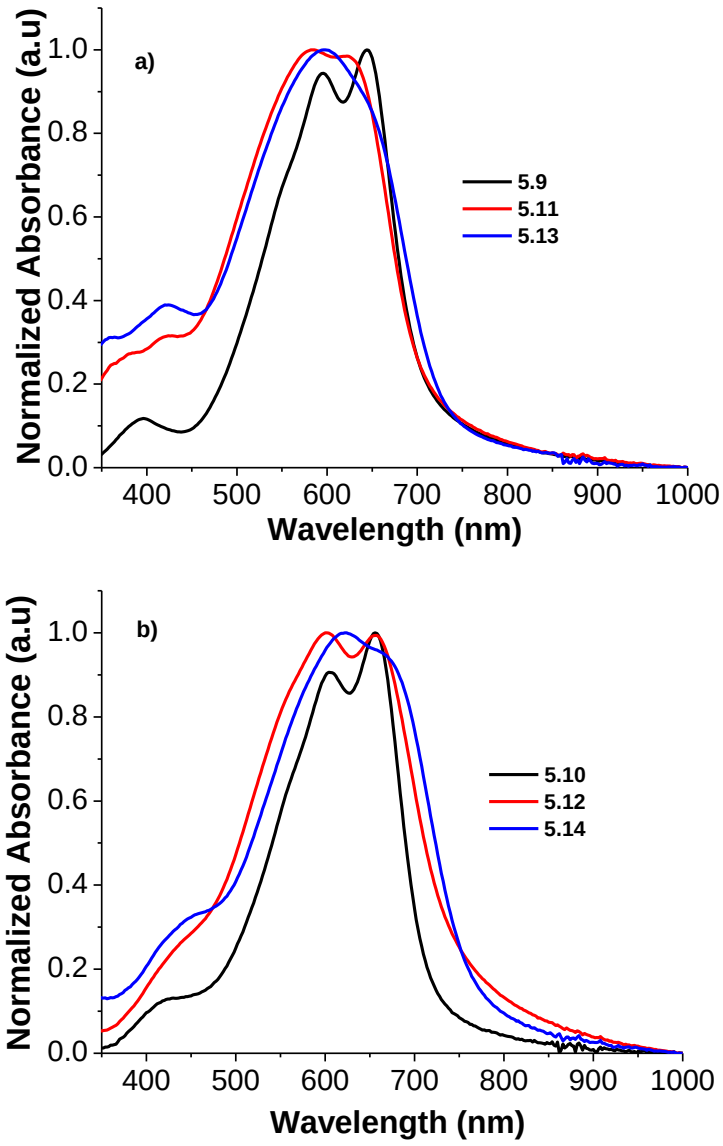

Figure 5.5 UV-Vis absorption measurement of the (a) quinquethiophenes and (b) sexithiophenes, spin-casted on a glass plate from a 2 mg/mL chloroform solution.

The optical gaps of the oligothiophenes were estimated from the solid-state absorption onsets and the values are reported in Table 5.1. In general, the sexithiophenes

had smaller optical gaps compared to quinquethiophenes, which is expected due to the extended conjugation in the sexithiophenes. On the other hand, upon changing the acceptor, the optical gaps in both series decreased going from **5.9** and **5.10** (malononitrile) to **5.11** and **5.12** (*N*-hexyl rhodanine) to **5.13** and **5.14** (*N*-hexyl cyanorhodanine), the extent of this decrease was higher in the sexithiophenes series. The electrochemical properties of **5.9**-**5.14** were investigated using cyclic voltammetry (CV); representative CV traces are shown in Figure 5.6, and the redox potentials and estimates of the solid-state ionization energies (IEs) and electron affinities (EAs) are summarized in Figure 5.2.

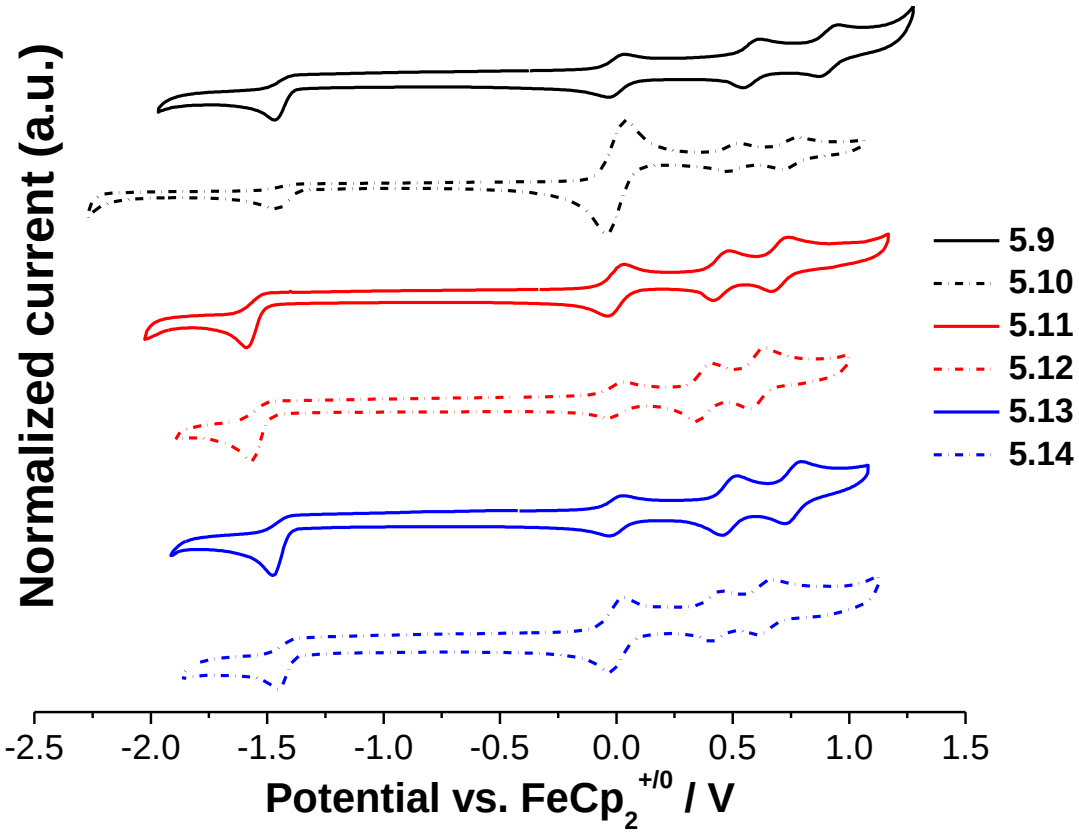

Figure 5.6 Cyclic voltammograms of the oligothiophenes determined in deoxygenated dichloromethane vs $FeCp_2^{+/0}$ in the presence of 0.1 M tetra-*n*-butylammonium hexafluorophosphate as an electrolyte. Solid lines represent quinquethiophene derivatives and dashed-doted lines represent sexithiophene derivatives. Scan rate was 50 mVs^{-1}.

All oligothiophenes displayed two reversible oxidation processes and one irreversible reduction process within the accessible solvent window. The electrochemical

gaps, obtained from the difference between oxidation and reduction potentials are larger than the optical gaps obtained from the onset of absorption, in Table 5.1, by around 200 meV, which can be attributable to exciton binding energy. However, the same trends observed in the optical measurements hold for the electrochemical measurements, where the electrical gaps in both series decreased going from **5.9** and **5.10** (malononitrile) to **5.11** and **5.12** (*N*-hexyl rhodanine) and finally to **5.13** and **5.14** (*N*-hexyl cyanorhodanine).

Table 5.2 Electrochemical potentials (V vs. $FeCp_2^{+/0}$) and electrochemically estimated solid-state ionization energies and electron affinities.

		$E_{1/2}^{+/0}$ [V]	$E_{1/2}^{0/-}$ [V]	EA(*s*) [eV][a]	IE(*s*) [eV][a]	$E_{0\text{-}0}^{elec}$ [eV][b]
	5.9	+ 0.58	– 1.39	+ 3.4	+ 5.3	1.97
5T	**5.11**	+ 0.45	– 1.51	+ 3.3	+ 5.2	1.96
	5.13	+ 0.48	– 1.40	+ 3.4	+ 5.2	1.88
	5.10	+ 0.55	– 1.35	+ 3.5	+ 5.2	1.90
6T	**5.12**	+ 0.38	– 1.48	+ 3.3	+ 5.1	1.86
	5.14	+ 0.43	– 1.37	+ 3.4	+ 5.2	1.80

[a]Estimated according to IE(s) = $eE_{1/2}^{+/0}$ [vs. $FeCp_2^{+/0}$] + 4.8 eV.[1] and EA(s) = $eE_{1/2}^{0/-}$ + 4.8 eV. [(b)] Electrochemical gap estimated according to $E_{0\text{-}0}^{elect.} = e(E_{1/2}^{+/0} - E_{1/2}^{+/-})$

Extending conjugation by one thiophene, from quinque- to sexithiophenes, caused the molecules to become slightly easier to oxidize (ca. 30-70 mV), and also slightly easier to reduce (ca. 30-40 mV). Also, within the same series, changing *N*-hexyl rhodanine acceptor end groups (**5.11** and **5.12**) to malononitrile (**5.9** and **5.10**) or *N*-hexyl cyanorhodanine (**5.13** and **5.14**) rendered the materials easier to reduce by up to 130 mV, however it had the opposite effect on the oxidation potential where changing *N*-hexyl rhodanine acceptor end groups (**5.11** and **5.12**) to malononitrile (**5.9** and **5.10**) or *N*-hexyl cyanorhodanine (**5.13** and **5.14**) rendered these materials harder to oxidize by up to 170 mV. This data suggests that the HOMOs and LUMOs in these oligothiophenes are delocalized on the entire structure and are not confined to any component in particular, which is somewhat consistent with the optical behavior of these materials in the solid state in terms of the presence of vibronic structures.[38,39]

The EAs and IEs (which were defined as the energy gained by dropping an electron from the vacuum level to the lowest unoccupied state, and the minimum energy necessary to remove an electron from the highest occupied state to vacuum, respectively) of the materials estimated from cyclic voltammetry are also presented in Figure 5.2. The IEs of all the materials were ca. +5.2 eV and the EAs were ca. +3.3 eV, consistent with what is reported with similar systems.[12,15] The driving force for exciton dissociation ($-\Delta G_{diss}$), necessary for OPV operation, can be estimated according to the following equation:[41]

$$-\Delta G_{diss} = \left((IE_D - EA_A) - E_{0-0}{}^{opt}{}_D \right)$$

Where IE_D is the ionization energy of the donor, EA_A the electron affinity of the acceptor, which in this case is $PC_{71}BM$ (ca. 3.91 eV), and $E_{0\text{-}0}{}^{opt}(D)$ is the optical gap of the donor.

A $-\Delta G_{diss}$ value greater than zero indicates enough driving force for exciton dissociation, which in the case of the oligothiophene ranges between 0.30 and 0.45 eV indicating sufficient driving force is present.[42] Also, the IEs of the donor materials were estimated to be ca. 5.2 eV which should not hinder the possibility of attaining photovoltages that are on par with what is previously reported with such systems.[15,39]

5.2.2.2 Benzodithiophene derivatives

The solution and solid-state normalized absorption spectra of the benzodithiophene hole transport materials are presented in Figure 5.7 and, Figure 5.8 with the relevant values listed in Table 5.3. As with the oligothiophenes, two prominent features were observed in the solution UV-Vis spectra; a low energy band in the 450-700 nm range, with the exception of **5.21** whose absorption onset is at around 800 nm, that can be assigned to the intermolecular charge transfer (ICT), and a higher energy band between 400 and 470 nm, that is associated with π-π^* transitions of the core, Figure 5.7.

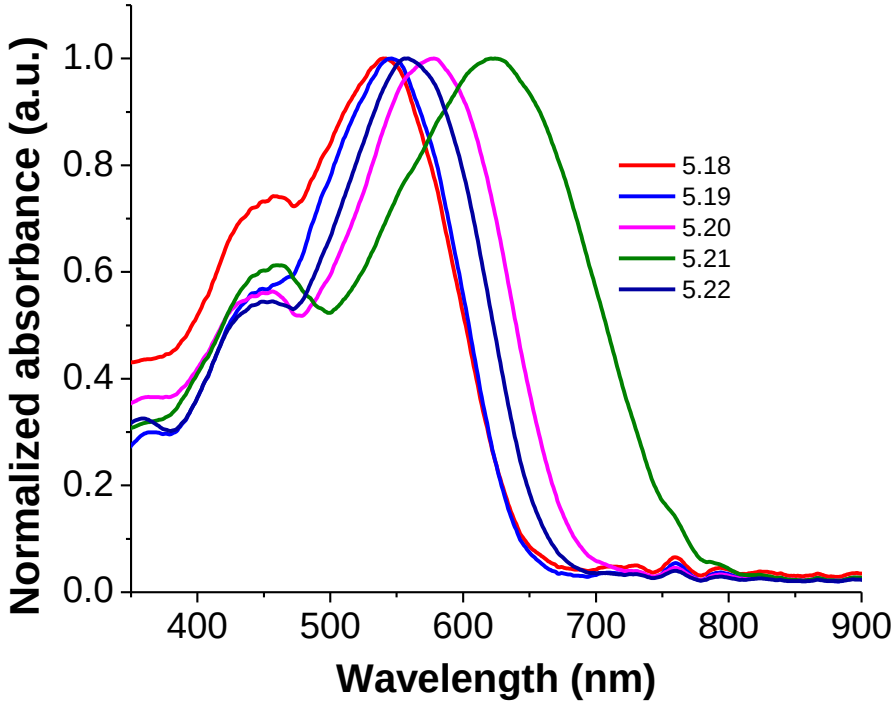

Figure 5.7 UV-Vis absorption measurement of the benzodithiophene derivatives in chloroform solution.

The solid-state absorption spectra of the benzodithiophene derivatives, Figure 5.8, were bathochromically shifted compared to solution, experienced general broadening and showed the presence of two features (peaks or a peak and a shoulder) which, as discussed earlier, could be indicative of planarized backbone and increased intermolecular π–π interactions. What is significantly different between the different materials in the series is the extent of the aforementioned bathochromic shift, particularly of the absorption onset. In an ADA-type semiconducting material, changing the acceptor can stabilize/destabilize the LUMO of the material, increases its EA, and consequentially, reduces the optical gap (given that the HOMO energy is static).

In this series, and compared to the published material, **5.17**, changing the electron acceptor from rhodanine to *N*-hexyl cyanorhodanine, **5.18**, and diethyl barbituric acid, **5.19**, shifted the absorption onset from 697 nm for **5.17**, to 709 nm and 708 nm, for **5.18** and **5.19** respectively. A larger bathochromic shift was observed by changing the acceptors to diethyl thiobarbituric acid, **5.20**, and phenyl-isoxazolone, **5.22**, where the

onset was shifted to 733 nm and 743 nm, respectively. This is equivalent to 87 meV and 110 meV change in the absorption onset in **5.20** and **5.22** respectively compared to ca. 30 meV in the case of **5.18** and **5.19**. However, the largest change in the absorption onset was experienced with benzodithiophene derivatives with tricyanofuran electron accepting groups, **5.21**, where the absorption onset red-shifted by 282 meV relative to **5.17** to 828 nm. These corresponding absorption onsets have given rise to optical gaps that range from 1.78 to 1.50 eV with the full list presented in Table 5.3

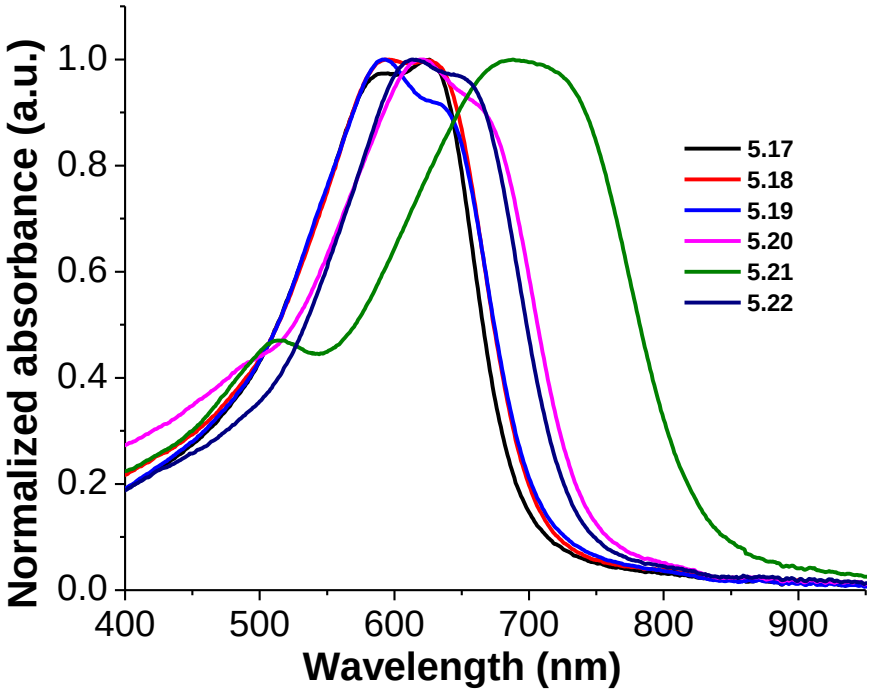

Figure 5.8 UV-Vis absorption measurement of the benzodithiophene derivatives spin-cast onto a glass film from a 2 mg/mL chloroform solution.

The electrochemical properties of **5.17**-**5.22** were investigated using cyclic voltammetry (CV) in DCM and representative CV traces are shown in Figure 5.9. The redox potentials and estimates of the solid-state ionization energies (IEs) and electron affinities (EAs) are summarized in Table 5.3. The benzodithiophene displayed what appears to be two oxidation processes and one irreversible reduction process within the accessible solvent window.

Table 5.3 Electrochemical Potentials (V vs. $FeCp_2^{+/0}$), [a]Electrochemically estimated solid-state ionization energies and electron affinities (eV), [b]Estimated electrochemical and [c]optical gaps (eV).

	λ_{onset} [nm]	$E_{0\text{-}0}^{opt}$ [eV][c]	$E_{1/2}^{+/0}$ [V]	$E_{1/2}^{0/-}$ [V]	EA(s) [eV][a]	IE(s) [eV][a]	$E_{0\text{-}0}^{elec}$ [eV][b]
5.17	697	1.78	+ 0.40	– 1.56	+ 3.2	+ 5.2	1.96
5.18	709	1.75	+ 0.43	– 1.43	+ 3.4	+ 5.2	1.86
5.19	708	1.75	+ 0.43	– 1.41	+ 3.4	+ 5.2	1.84
5.20	733	1.69	+ 0.43	– 1.28	+ 3.5	+ 5.2	1.71
5.21	828	1.50	+ 0.44	– 0.99	+ 3.8	+ 5.2	1.43
5.22	743	1.67	+ 0.47	– 1.29	+ 3.5	+ 5.3	1.76

[a]Estimated according to IE(s) = e$E_{1/2}^{+/0}$ [vs. $FeCp_2^{+/0}$] + 4.8 eV.[1] and EA(s) = e$E_{1/2}^{0/-}$ + 4.8 eV; [b] Electrochemical gap estimated according to $E_{0\text{-}0}^{elec}$ = e($E_{1/2}^{+/0} - E_{1/2}^{0/-}$); [c]Estimated according to 1240/λonset [nm]. Cyclic voltammetry was conducted in adeoxygenated dichloromethane vs $FeCp_2^{+/0}$ in the presence of 0.1 M tetra-*n*-butylammonium hexafluorophoephate, scan rate is 50 mVs^{-1}; For the irreversible reduction processes, $E_{1/2}^{0/-}$ was estimated from the $FeCp_2^{+/0}$ cathodic peak potential (E_{Pc}), and anodic peak potential (E_{Pa}) using the following equation: $E_{1/2}^{0/-} = E_{red}$ (of the specific material) + (E_{Pc} +E_{Pa})/2, under the assumption that the $FeCp_2^{+/0}$ peak to peak separation would have been similar to the reduced species, had it been reversible.

The electrochemical gaps, obtained from the difference between oxidation and reduction potentials are with the exception of **5.21**, larger than the optical gaps obtained from the onset of absorption, Table 5.3, which is attributable to exciton binding energy. As expected, changing the electron acceptor changed the materials' reduction potentials, and hence their EAs. Changing rhodanine, **5.17**, to cyanorhodanine, **5.18**, and diethyl-barbituric acid, **5.19**, rendered them easier to reduce by 130 and 150 mV, respectively. Changing rhodanine to diethyl-thiobarbituric acid, **5.20**, and phenyl-isoxazolone, **5.22**, resulted in reduction potentials that are around –1.28 V vs. $FeCp_2^{+/0}$, a 280 mV anodic shift compared to **5.17**. The highest anodic shift was observed with tricyanofuran acceptors, **5.21**, where an anodic shift of 570 mV was observed compared to **5.17**.

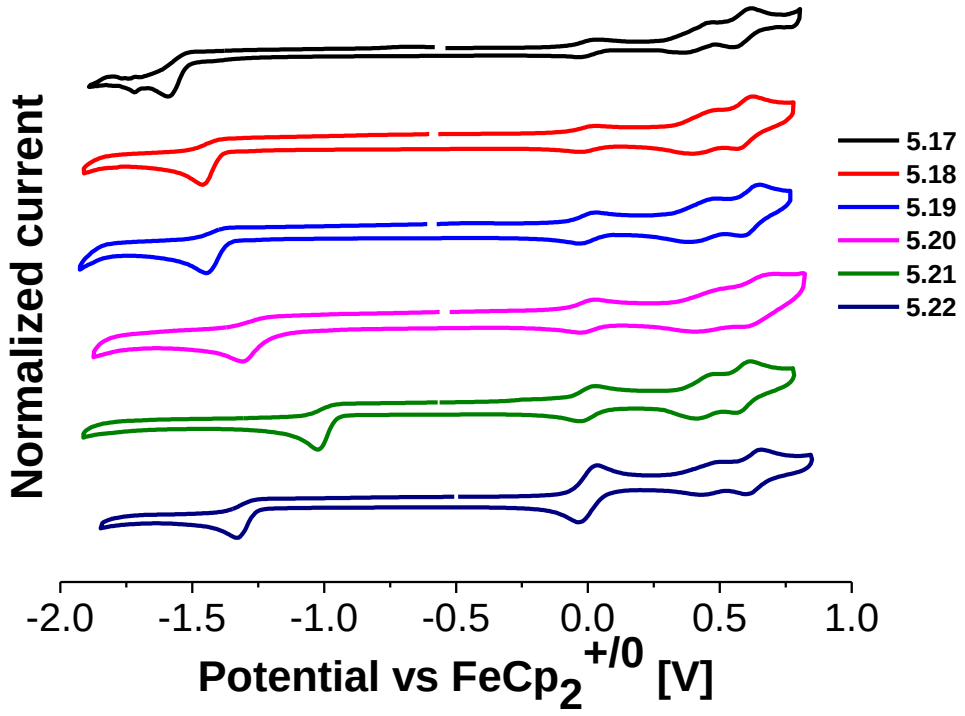

Figure 5.9 Cyclic voltammograms of the series of benzodithiophene derivatives, determined in dichloromethane vs $FeCp_2^{+/0}$.

The electron affinities estimated from cyclic voltammetry are listed in Table 5.3. The EAs ranged between +3.2 eV and +3.8 eV with estimated $-\Delta G_{diss}$ (0.49 for **5.17**, 0.46 for **5.18** and **5.19**, 0.40 eV for **5.20**, 0.21 eV for **5.21** and 0.38 eV for **5.22**) which indicate

sufficient driving force for exciton dissociation. On the other hand, changing the electron acceptor had little effect on the oxidation potential of the materials with a maximum change of +70 mV between **5.17** and **5.22**. This caused the IEs to remain essentially unchanged throughout the series at ca. 5.2 eV.

Overall, the structural modifications introduced to the reference compound **5.17** achieved the intended reduction in the optical gap, allowing for more panchromatic absorption without sacrificing the driving force for exciton dissociation and the ability of the system to maintain its photovoltages through proper frontier energy level matching with $PC_{71}BM$.

5.2.3 Thermal properties

Thermal annealing of the active layer can enhance light absorption and hole-mobility by inducing order with in the active material.[43-45] In oligothiophenes, thermal annealing of the active layer has been shown to enhance the photovoltaic properties by enhancing the J_{SC} as is going to be highlighted in the next section.[12,44] The thermal properties of the oligothiophenes were investigated by differential scanning calorimetry (DSC, under nitrogen atmosphere and with a heating/cooling rate of 10 ^{o}C min^{-1}, three heating-cooling cycles, Figure 5.10 and Table 5.4). Increasing the length of the oligothiophene caused an increase in the melting point of the materials which could be due to the increased molecular weight of the materials as seen in similar systems.[7] The quinquethiophene **5.9**, **5.11** and **5.13** exhibited two endothermic transitions at 111/198 ^{o}C, 143/151 ^{o}C and 198/214 ^{o}C for **5.9**, **5.11** and **5.13** respectively. While the second endothermic transitions in all three materials (at 198 ^{o}C, 151 ^{o}C, and 214 ^{o}C) can be attributed to melting, the first endothermic transition in **5.9** and **5.11** at 111 ^{o}C and 143 ^{o}C, have small enthalpies and could be assigned to solid-solid transitions involving rearrangements of the side chains. In **5.13**, the transition at 198 ^{o}C has higher enthalpy and could be due to a crystallization phase prior to melting at 214 ^{o}C. Sexithiophenes **5.10**, **5.12** and **5.14** showed primarily single endothermic processes presumably attributed to melting at 232 ^{o}C, 170 ^{o}C, and 243 ^{o}C.

Table 5.4 Melting (T_m) Temperatures for the oligothiophenes **5.9**-**5.14** obtained using DSC.

	5.9	**5.11**	**5.13**	**5.10**	**5.12**	**5.14**
T_m (ºC)	111/198	143/151	198/214	232	170	243

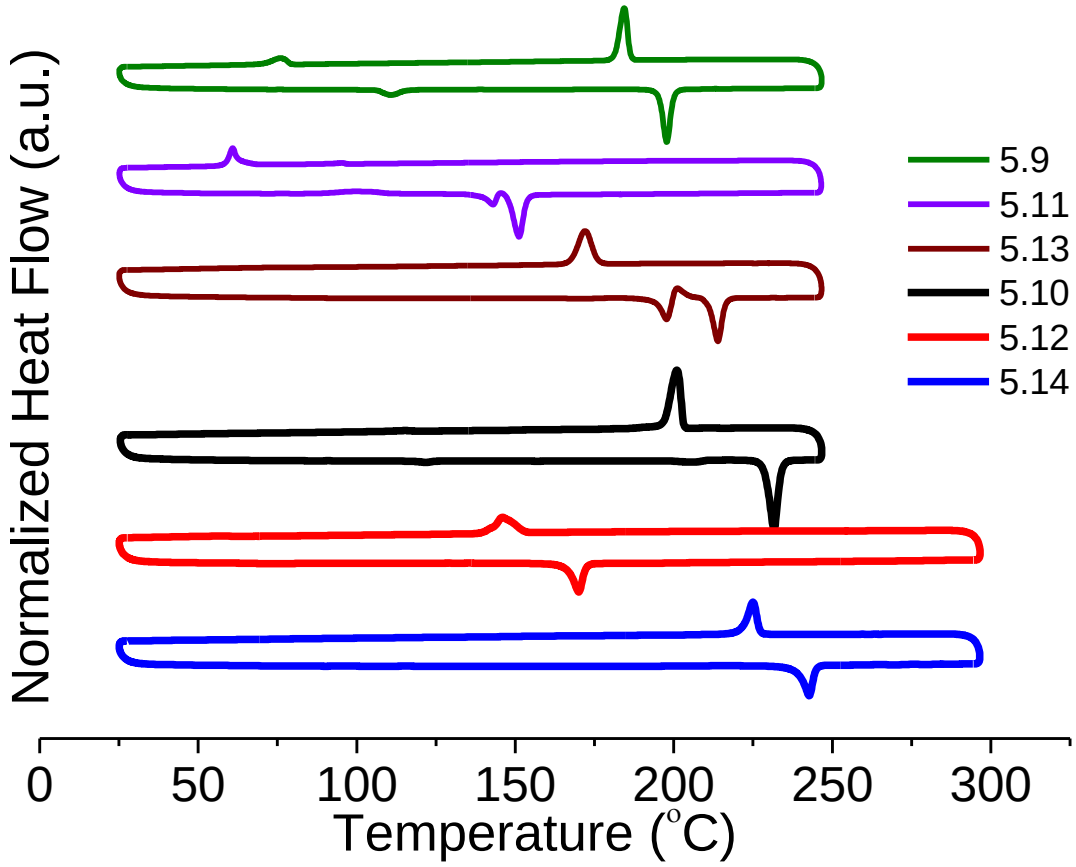

Figure 5.10 Differential scanning calorimetry (second heating and cooling scans) for **5.1**–**5.6** at 10 ºC min^{-1}. Negative heat flow corresponds to endothermic processes.

5.2.4 Initial photovoltaic characterization

Note: The results discussed in this section are based on experiments that have been conducted by Dr. Jegadesan Subbiah from Dr. David Jones' lab at the University of Melbourne. For details regarding device fabrication please refer to future collaborative publications.

Organic photovoltaic devices were fabricated with a 1:1 blend of **5.9**, **5.11**, **5.12** or **5.13** and $PC_{71}BM$ (as an electron transporting material) using the following device

configuration ITO/PEDOT:PSS/active material (1:1 blend)/PFN/Al.[46] The photovoltaic characteristics of the devices are summarized in Table 5.5, and the values reported are the average values of 10 devices with the error corresponding to the standard deviation. Devices fabricated with **5.9** and **5.13** showed enhanced PCEs after thermal annealing at 120 ºC for 10 minutes, while devices fabricated from **5.11** and **5.12** showed enhanced performances upon solvent vapor annealing in tetrahydrofuran for 20 seconds. **5.13** showed further improvement in performance upon both thermal annealing at 120 ºC followed by solvent vapor annealing in THF for 20 seconds.

Table 5.5 Photovoltaic characterization of the oligothiophenes

	5.X:$PC_{71}BM$ (1:1)	**J_{SC} [mAcm^{-2}]**	**V_{OC} [V]**	**FF [%]**	**PCE [%]**
5T	**5.9** (before annealing)	2.8 ± 0.2	0.92 ± 0.01	31 ± 3	0.8 ± 0.3
	5.9 (120 ºC – 10 min)	6.1 ± 0.2	0.90 ± 0.01	46 ± 2	2.5 ± 0.2
	5.11 (before annealing)	3.9 ± 0.3	0.98 ± 0.01	31 ± 3	1.4 ± 0.3
	5.11 (SVA– THF, 20s)	7.1 ± 0.2	0.98 ± 0.01	60 ± 2	4.2 ± 0.2
	5.13 (before annealing)	6.5 ± 0.4	0.98 ± 0.01	46 ± 2	2.6 ± 0.3
	5.13 (120 ºC 10 min)	11.9 ± 0.3	1.02 ± 0.01	59 ± 2	7.2 ± 0.2
	5.13 (120 ºC + SVA, 20s)	12.7 ± 0.2	1.02 ± 0.01	63 ± 2	8.0 ± 0.2
	5.10	Not soluble			
6T	**5.12** (before annealing)	3.8 ± 0.3	0.92 ± 0.01	46 ± 5	1.0 ± 0.3
	5.12 (SVA –THF, 20s)	11.4 ± 0.3	0.92 ± 0.01	63 ± 2	6.9 ± 0.2
	5.14	Not soluble			

Although further experiments are required to gather further understanding of the factors causing this enhancement in performance upon annealing, solid-state absorption measurements on a **5.13**:$PC_{71}BM$ film, Figure 5.11, as cast (black line) and after thermal annealing and solvent vapor annealing (red line) suggests that upon annealing, enhanced molecular ordering is observed inferred from the presence of a more structured spectra with absorption maxima at ca. 568 nm, 609 nm and 661 nm, as opposed to a single broad

absorption feature with maxima at ca. 556 nm. Compared to the state-of-the-art A-D-A oligothiophene hole-transport material reported in the literature, **5.6**,[12] the best performing OPV in this series, based on **5.13**, had a V_{OC} equal to 1.02 V which is slightly higher than the aforementioned oligothiophene, V_{OC} equal to 0.92 V. However, the overall PCE is lower due to the lower current (ca. 16 $mAcm^{-2}$ vs. 13 $mAcm^{-2}$ in **5.13**), the origin of which could be the bathochromically shifted onset of the former, evident in absorbance and IPCE spectra, which allows that dye to take greater advantage of the infrared region. This red absorbance feature is theorized to be related to effective molecular packing between molecular backbones[12]; structural studies are currently underway on the system described in this section to allow a better comparison.

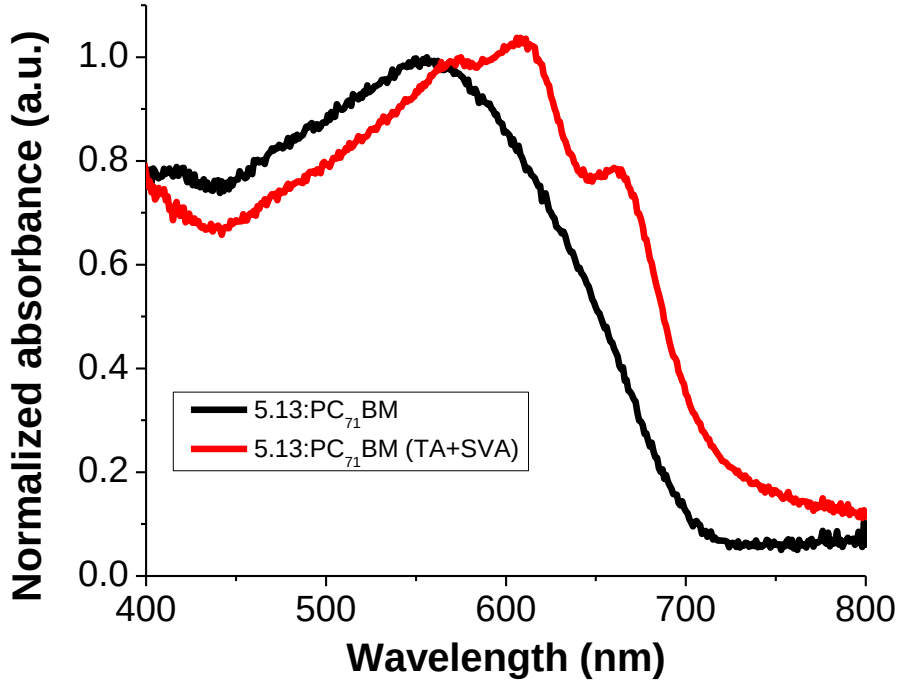

Figure 5.11 Solid-state absorption measurement on a **5.13**:PC71BM blend as cast, and after thermal annealing (TA) at 120 ºC for 10 minutes, followed by solvent vapor annealing (SVA) in THF for 20 seconds.

5.3 SUMARRY AND ONGOING WORK

In this chapter, two series of hole transport materials were synthesized based on two classes of materials; oligothiophenes and benzodithiophenes. The materials were characterized by UV-vis spectroscopy, electrochemistry, differential scanning calorimetry and OPV device performance. The oligothiophenes showed enhanced photovoltaic properties upon either thermal- or solvent vapor annealing, which could be ascribed to increased molecular order, a conclusion that can also be inferred from their solid-state optical properties in neat films and in 1:1 blends with $PC_{71}BM$. Some materials, **5.10** and **5.14**, suffered from low solubility which lowered the quality of films prepared from them; however, future directions could be focused toward synthesizing analogues with longer solubilizing alkyl chains to increase solubility. In the second part of this chapter, a series of benzodithiophene derivatives of **5.7** with different electron-accepting groups were designed in an attempt to increase the panchromaticity of these materials towards absorbing near infra-red light. The optical gaps of these derivatives were in fact reduced by up to 280 meV to 1.50 eV, allowing them to absorb light in the near infra-red. The performance of these materials in OPV devices remains to be seen.

5.4 EXPERIMENTAL SECTION

5.4.1 Optical and electrochemical measurements

Electronic spectroscopic data were collected in chloroform or on glass on UV-Vis-NIR spectra in 1 cm quartz cuvette using a Agilent Cary 5000 spectrophotometer. Electrochemical measurements were carried out under an inert atmosphere in dry deoxygenated dichloromethane solution containing 0.1 M tetrabutylammonium hexafluorophosphate as electrolyte. A Solartron 1287A potentiostat/galvanostat equipped with a conventional three-electrode cell utilizing a glassy carbon working electrode, platinum wire counter electrode, and a silver wire coated with silver chloride as the pseudo-reference electrode, was used for the measurements. Potentials were referenced to the ferrocenium/ferrocene ($FeCp_2^{+/0}$).[47] Cyclic voltamograms were recorded at a scan rate of 50 mV s^{-1}.

5.4.2 Differential scanning calorimetry

Differential scanning calorimetry was performed on a PerkinElmer Sapphire DSC under nitrogen atmosphere and with a heating/cooling rate of 10 $^{o}Cmin^{-1}$ under nitrogen.

5.4.3 Synthetic procedures

Commercially available intermediates were purchased and used without further purification. For water sensitive reactions, commercially acquired anhydrous *N*,*N*-dimethylformamide was used, tetrahydrofuran and toluene were dried by the distillation from sodium benzophenone ketyl or used directly from MBRAUN solvent purification system (MBRAUN-SPS). Bases, such as piperidine and diisopropylamine, were distilled over calcium hydride, and stored in Schlenk flasks under nitrogen in the presence of molecular sieves. ^{1}H and $^{13}C\{^{1}H\}$ spectra were collected on a Bruker 400 MHz spectrometer. Deuterated solvents with tetramethylsilane as an internal standard were used. Mass spectra were measured on a VG Instruments 70-SE using the electron impact (EI) or fast-atom bombardment (FAB) mode and on an Applied Biosystems 4700 Proteomics Analyzer using MALDI mode. Elemental analyses were carried out by Atlantic Microlab using a LECO 932 CHNS elemental analyzer.

(5.26)

5.25 (3.00 g, 11.9 mmol), which was synthesized according to literature procedure,[20-22] was added into a 100 mL Schlenk flask and dried under vacuum for 2 h. Dimethoxyethane–DME (20 mL), (1,5-cyclooctadiene)(methoxy)iridium(I) Dimer (0.39 g, 0.59 mmol), bis(pinacolato)diboron (4.62 g, 18.2 mmol) and 4,4'-di-*tert*-butyl-2,2'-bipyridine (0.96 g, 3.56 mmol) were added in this order and the reaction temperature then increased to 85 ^{o}C and stirred overnight. Isopropanol (100 mL) were added and the solvents removed under reduced pressure; the resultant dark brown liquid which was purified by column chromatography in DCM/hexane 1:1 mixture to get a colorless liquid **5.26** (2.52 g, 42%). ^{1}H NMR ($CDCl_3$, 400 MHz) δ 2.79 (t, J = 7.6 Hz, 4H); 1.48 (quintet, J = 8.0 Hz, 4H); 1.42-1.25 (m, 12H); 1.31 (2, 24H); 0.90 (t, J = 7.2 Hz, 6H). $^{13}C\{^{1}H\}$ NMR ($CDCl_3$, 100 MHz) δ 154.05, 83.40, 32.38, 31.66, 29.45, 28.48, 24.74, 22.61, 14.12. HRMS (ESI-LTQ-FTICP): m/z 505.3674 [(M+H)+] (Calcd. For $C_{28}H_{51}B_2O_4S$: 505.3699).

(5.27)

5.26 (0.24 g, 0.48 mmol), **5.29** (0.40 g, 0.99 mmol) and P(*o*-tolyl)$_3$ (0.03 g, 0.1 mmol) were dissolved in THF (4 mL), and tri-potassium phosphate (1 mL, 2 M aq. solution), and the solution was bubbled for 30 minutes. Tris(dibenzylideneacetone) dipalladium(0) (0.02 g, 0.02 mmol) was then added and reaction stirred at 60 ^{o}C overnight. The organic layer was separated, washed with water, dried and organic solvent evaporated to get a red liquid which was purified via column chromatography with hexane/DCM (1:1) as an eluent and then with a size-exclusion column, eluting in toluene to give **5.27** as an orange solid (230 mg, 61%).^{1}H NMR ($CDCl_3$, 600 MHz) δ 9.89 (s, 2H); 7.72 (d, J = 4.0 Hz, 2H); 7.23 (d, J = 4.0 Hz, 2H); 7.02 (s, 2H); 2.82 (t, J = 7.8 Hz, 4H); 2.72 (t, J = 8.4 Hz, 4H); 1.69 (quintet, J = 7.6 Hz, 4H); 1.61 – 1.51 (m, 4H), 1.48 – 1.39 (m, 8H), 1.37 – 1.29 (m, 16H), 0.92 – 0.87 (m, 12H). ^{13}C{^{1}H} NMR ($CDCl_3$, 151 MHz) δ 182.53, 146.10, 142.47, 142.17, 141.04, 136.83, 136.15, 129.70, 129.40, 129.09, 125.82, 31.63, 31.47, 30.57, 30.20, 29.76, 29.57, 29.21, 28.27, 22.61, 22.57, 14.06, 14.05. Anal. Calcd. For $C_{46}H_{60}O_2S_5$ (%).C, 68.61; H, 7.51; S, 19.91. Found, C, 68.82; H, 7.70; S, 19.72.

(5.32)

5.31 (0.50 g, 0.85 mmol), **5.29** (0.72 g, 1.79 mmol) and P(o-tolyl)$_3$ (0.05 g, 0.17 mmol) were dissolved in THF (8 mL), and tri-potassium phosphate (2 mL, 2 M aq. solution), and the solution was bubbled for 30 min. Tris(dibenzylideneacetone) dipalladium(0) (0.04 g, 0.04 mmol) was then added and reaction stirred at 60 ^{o}C overnight. The organic layer was separated, washed with brine, dried, and organic solvent removed to afford a red liquid that was purified multiple times by column chromatography in DCM:hexane (2:1) to get a **5.32** (0.65 g, 86%) as a red solid. ^{1}H NMR ($CDCl_3$, 400 MHz) δ 9.84 (s, 2H); 7.67 (d, J = 4.0 Hz, 2H); 7.20 (d, J = 5.0 Hz, 2H); 6.97 (d, J = 3.8 Hz, 2H); 2.77 (t, J = 7.8 Hz, 4H); 2.77 (t, J = 8.0 Hz, 4H); 1.64 (quintet, J = 7.2 Hz; 8H); 1.45-1.25 (m, 25H); 0.85 (t, J = 7.0 Hz, 12H). ^{13}C{^{1}H} NMR ($CDCl_3$, 100 MHz) δ 182.54, 146.09, 142.55, 142.16, 141.17, 136.84, 136.06, 135.13, 129.33, 129.13, 128.94, 126.84, 125.84, 31.64, 30.37, 30.21, 29.76, 29.59, 29.22, 22.59, 22.58, 14.08, 14.06 (peaks are missing due to overlap). Anal. Calcd. For $C_{50}H_{62}O_2S_6$ (%):

C, 67.67; H, 7.04. Found C, 67.66; H, 7.07. HRMS (ESI-LTQ-FTICP): m/z 886.3101 [M^+] (Calcd. $C_{50}H_{62}O_2S_6$: 886.3069).

(5.9)

5.27 (0.1 g, 0.12 mmol), and malononitrile (0.08 g, 1.24 mmol), were dissolved in chloroform (10 mL). DBU (2 drops) was added and the reaction mixture was stirred at room temperature for 3 h. Solvent was then removed under reduced pressure and the dark purple solid was purified by column chromatography using toluene as an eluent, followed by size-exclusion column eluting with toluene to afford **5.9** (40 mg, 37%) as a green solid. ^{1}H NMR ($CDCl_3$, 600 MHz) δ 7.75 (d, J = 0.4 Hz, 2H), 7.71 (d, J = 4.2 Hz, 2H), 7.26 (d, J = 4.2 Hz, 2H), 7.04 (s, 2H), 2.86 – 2.82 (t, J = 8.4 Hz, 4H), 2.76 – 2.71 (m, 4H), 1.70 (quintet, J = 7.5 Hz, 4H), 1.61 – 1.54 (m, 4H), 1.45 (m, 8H), 1.39 – 1.29 (m, 16H), 0.94 – 0.86 (m, 12H). ^{13}C{^{1}H} NMR ($CDCl_3$,151 MHz) δ 149.76, 148.25, 143.91, 141.58, 139.01, 137.38, 133.93, 129.87, 129.42, 128.96, 126.04, 114.35, 113.51, 75.86, 31.61, 31.45, 30.48, 30.14, 30.10, 29.55, 29.19, 28.32, 22.60, 22.55, 14.06, 14.05. HRMS (ESI-LTQ-FTICP): m/z 900.3447 [M^+] (calcd. For $C_{52}H_{60}N_4S_5$: 900.3416). Anal. Calcd. For $C_{52}H_{60}N_4S_5$ (%):C, 69.29; H, 6.71; N, 6.22; S, 17.78. Found, C, 69.49; H, 6.76; N, 6.13; S, 17.66.

(5.10)

5.22 (0.1 g, 0.11 mmol) and malononitrile (0.07 g, 1.13 mmol), were dissolved in chloroform (10 mL). DBU (2 drops) was added and the reaction stirred overnight. Solvent was removed under reduced pressure to yield a purple solid which was purified by silica gel column chromatography using chloroform as an eluent, then size-exclusion column eluting in toluene to yield a green solid which was recrystallized from 1,4-dioxane to get **5.10** as a green solid (80 mg, 73%).^{1}H NMR (1,2-dichlorobenzene, 600 MHz, 60 ^{o}C) δ 7.25 (d, J = 3.5 Hz, 2H), 7.20 (s, 2H), 6.99 (m, 4H), 6.96 (s, 2H), 2.68 (m, 8H), 1.65-1.50 (m, 8H), 1.38 – 1.25 (m, 8H), 1.22-1.10 (m, 17H), 0.75 (m, 12H). ^{13}C{^{1}H} NMR ($CDCl_3$,151 MHz) δ 148.69, 148.54, 147.64, 143.74, 141.65, 138.48, 138.35, 137.34, 135.54, 133.72, 125.81, 125.56, 114.02, 113.34, 75.89, 31.56, 31.54, 30.24, 30.09, 30.04, 29.74, 29.32, 29.18, 22.52, 22.50, 13.89, 13.74. HRMS (ESI-LTQ-FTICP):

m/z 982.3603 [M^+] (Calcd. For $C_{56}H_{62}N_4S_6$: 982.3293). Anal. Calcd. For $C_{56}H_{62}N_4S_6$ (%). C, 68.39; H, 6.35; N, 5.70. Found, C, 68.27; H, 6.32; N, 5.50.

(5.11)

5.27 (0.08 g, 0.10 mmol), and N-hexyl rhodanine (0.22 g, 1.00 mmol), were dissolved in chloroform (10 mL). DBU (2 drops) was added and the reaction stirred overnight. Solvent was removed under reduced pressure to yield a purple solid which was first purified by silica gel column chromatography using a hexane/DCM mixture (2:1) as an eluent, followed by a size exclusion column (SX1 beads) eluting in toluene to get a green solid which was precipitated from DCM/isopropanol, filtered, washed with isopropanol to get **5.11** (75 mg, 67%).^{1}H NMR ($CDCl_3$, 400 MHz) δ 7.85 (s, 2H); 7.36 (d, J = 4.0 Hz, 2H); 7.22 (d J = 4.0 Hz, 2H); 7.02 (s, 2H); 4.11 (t, J = 7.6 Hz, 4H); 2.83 (t, J = 8.0 Hz, 4H); 2.74 (t, J = 8.2 Hz, 4H); 1.71 (quintet; J = 6.8 Hz, 8H); 1.65-1.55 (m, 4H); 1.52-1.42 (m, 8H); 1.42-1.26 (m, 28H); 0.99-0.80 (m, 18H). $^{13}C\{^1H\}$ NMR ($CDCl_3$, 100 MHz) δ 192.16, 167.51, 144.32, 141.89, 140.98, 137.08, 135.84, 134.67, 129.77, 129.57, 129.08, 126.54, 124.99, 120.25, 44.88, 31.69, 31.48, 31.33, 30.55, 30.29, 29.83, 29.59, 29.28, 28.30, 26.93, 26.44, 22.64, 22.49, 14.11, 12.99. (2 aliphatic signals are missing probably due to overlaps). HRMS (ESI-LTQ-FTICP): m/z 1202.4161 [M^+] (Calcd for. $C_{64}H_{86}N_2O_2S_9$: 1202.4170). Anal. Calcd. For $C_{64}H_{86}N_2O_2S_9$ (%): C, 63.85; H, 7.20; N, 2.33; S, 23.97. found C, 63.68; H, 7.20; N, 2.11; S, 24.11.

(5.12)

5.32 (0.2 g, 0.23 mmol) and *N*-hexyl rhodanine (0.49 g, 2.25 mmol), were dissolved in chloroform (20 mL). DBU (2 drops) was added and the reaction stirred overnight. Solvent was removed under reduced pressure to yield a purple solid which was first passed through a silica plug eluting with chloroform, then purified multiple times by a size-exclusion column (SX1) in toluene to afford a green solid which was recrystallized from 1,4-dioxane to obtain **5.12** as a green solid (100 mg, 35%). ^{1}H NMR ($CDCl_3$, 600 MHz) δ 7.84 (s, 2H); 7.37 (d, J = 4.1 Hz, 2H); 7.22 (d, J = 4.0 Hz, 2H); 7.01 (d, J = 6.9 Hz, 4H); 4.11 (t, J = 7.8 Hz, 4H); 2.82 (t, J = 8.1 Hz, 4H); 2.77 (t, J = 8.1 Hz, 4H); 1.75-1.66 (m, 12H); 1.50-1.40 (m, 8H); 1.40-1.30 (m, 30H); 0.95-0.85 (m, 18H). $^{13}C\{^1H\}$ NMR ($CDCl_3$,126 MHz) δ 192.18, 167.51, 144.33, 141.96, 141.08, 137.08, 135.76,

135.08, 134.68, 129.52, 129.25, 128.93, 126.83, 126.54, 124.99, 120.24, 44.88, 31.70, 31.67, 31.34, 30.35, 30.30, 29.84, 29.70, 29.65, 29.31, 29.26, 26.95, 26.45, 22.66, 22.62, 22.51, 14.13, 14.00. HRMS (ESI-LTQ-FTICP): m/z 1284.4031 [M^+] (Calcd. For $C_{68}H_{88}N_2O_2S_{10}$: 1284.4048). Anal. Calcd. For $C_{68}H_{88}N_2O_2S_{10}$ (%). C, 63.51; H, 6.90; N, 2.18; S, 24.93. Found, C, 63.70; H, 6.97; N, 2.12; S, 25.02.

(5.13)

5.27 (0.1 g, 0.12 mmol) and 2-(3-hexyl-4-oxothiazolidin-2-ylidene) malononitrile (0.31 g, 1.24 mmol) were dissolved in chloroform (10 mL). DBU (2 drops) was added and the reaction stirred at room temperature for 3h. The solvent was then removed and the dark purple solid was purified by column chromatography eluting with toluene followed by size-exclusion column using toluene as an eluent to get **5.13** (100 mg, 64%) as a green solid. ^{1}H NMR ($CDCl_3$, 600 MHz) δ 8.00 (s, 2H), 7.41 (d, J = 4.1 Hz, 2H), 7.22 (d, J = 4.0 Hz, 2H), 7.01 (s, 2H), 4.18 (t, J = 7.8 Hz, 4H), 2.80 (t, J = 8.2 Hz, 4H), 2.72 (t, J = 8.2 Hz, 4H), 1.78 – 1.67 (m, 8H), 1.58 (m, 4H), 1.52 – 1.29 (m, 36H), 0.96 – 0.86 (m, 18H). ^{13}C{^{1}H} NMR ($CDCl_3$,151 MHz) δ 165.92, 165.28, 145.27, 142.61, 141.19, 136.42, 135.68, 135.62, 129.81, 129.09, 129.00, 128.34, 126.65, 113.33, 113.11, 112.27, 55.83, 45.31, 31.63, 31.45, 31.22, 30.42, 30.19, 30.00, 29.57, 29.24, 28.73, 28.36, 25.60, 22.62, 22.55, 22.41, 14.10, 13.92. HRMS (ESI-LTQ-FTICP): m/z 1266.4853 [M^+] (calcd. For $C_{70}H_{86}N_6O_2S_7$: 1266.4852). Anal. Calcd. For $C_{70}H_{86}N_6O_2S_7$ (%): C, 66.31; H, 6.84; N, 6.63; S, 17.70. Found, C, 66.53; H, 6.84; N, 6.66; S, 17.51.

(5.14)

5.32 (0.22 g, 0.25 mmol) and 2-(3-hexyl-4-oxothiazolidin-2-ylidene) malononitrile (0.62 g, 0.47 mmol) were dissolved in chloroform (20 mL) and deoxygenated for 20 min with nitrogen. DBU (4 drops) was added and the reaction stirred at room temperature for 3 h. The solvent was then removed and the crude purple product was purified with silica gel chromatography eluting with toluene to afford **5.14** (60 mg, 20%) as a green solid. ^{1}H NMR ($CDCl_3$, 600 MHz) δ 8.02 (s, 2H), 7.42 (d, J = 4.0 Hz, 2H), 7.24 (s, 2H), 7.01 (d, J = 3.0 Hz, 2H), 4.22 (t, J = 7.8 Hz, 4H), 2.83 (t, J = 7.8 Hz, 4H), 2.76 (t, J = 4.0 Hz, 2H), 1.78 – 1.66 (m, 12H), 1.48 – 1.39 (m, 12H), 1.40 – 1.30(m, 24H); 0.90 (m, 18H). ^{13}C{^{1}H} NMR ($CDCl_3$, 151 MHz) δ 165.96, 165.26,

145.26, 142.64, 141.35, 136.48, 135.86, 135.42, 135.33, 129.22, 129.04, 128.99, 128.29, 126.88, 126.83, 113.58, 113.02, 112.18, 56.02, 45.37, 31.59, 31.57, 31.18, 30.26, 30.20, 29.89, 29.64, 29.15, 28.71, 25.59, 22.52, 22.48, 22.33, 13.96, 13.94, 13.78. HRMS (ESI-LTQ-FTICP) m/z: $[M]^+$, Calcd. For $C_{74}H_{88}N_6O_2S_8$: 1349.4758; Found: 1349.4694.

5.5 REFERENCES

(1) Müllen, K.; Wegner, G. *Synthesis* **1998**, *2*, 1.

(2) Suzuki, A.; Diederich, F.; Stang, P. *by F. Diederich and PJ Stang, Wiley-VCH, Weinheim* **1998**, 49.

(3) Mishra, A.; Ma, C.-Q.; Bauerle, P. *Chem. Rev.* **2009**, *109*, 1141.

(4) Roquet, S.; de Bettignies, R.; Leriche, P.; Cravino, A.; Roncali, J. *J. Mater. Chem.* **2006**, *16*, 3040.

(5) Tamayo, A. B.; Dang, X.-D.; Walker, B.; Seo, J.; Kent, T.; Nguyen, T.-Q. *Appl. Phys. Lett.* **2009**, *94*, 103301.

(6) Schulze, K.; Uhrich, C.; Schüppel, R.; Leo, K.; Pfeiffer, M.; Brier, E.; Reinold, E.; Bäuerle, P. *Adv. Mater.* **2006**, *18*, 2872.

(7) Liu, Y.; Zhou, J.; Wan, X.; Chen, Y. *Tetrahedron* **2009**, *65*, 5209.

(8) Yin, B.; Yang, L.; Liu, Y.; Chen, Y.; Qi, Q.; Zhang, F.; Yin, S. *Appl. Phys. Lett.* **2010**, *97*, 023303.

(9) Liu, Y.; Wan, X.; Wang, F.; Zhou, J.; Long, G.; Tian, J.; You, J.; Yang, Y.; Chen, Y. *Advanced Energy Materials* **2011**, *1*, 771.

(10) Li, Z.; He, G.; Wan, X.; Liu, Y.; Zhou, J.; Long, G.; Zuo, Y.; Zhang, M.; Chen, Y. *Advanced Energy Materials* **2012**, *2*, 74.

(11) He, G.; Li, Z.; Wan, X.; Zhou, J.; Long, G.; Zhang, S.; Zhang, M.; Chen, Y. *Journal of Materials Chemistry A* **2013**, *1*, 1801.

(12) Kan, B.; Li, M.; Zhang, Q.; Liu, F.; Wan, X.; Wang, Y.; Ni, W.; Long, G.; Yang, X.; Feng, H. *J. Am. Chem. Soc.* **2015**, *137*, 3886.

(13) Zhang, Q.; Kan, B.; Liu, F.; Long, G.; Wan, X.; Chen, X.; Zuo, Y.; Ni, W.; Zhang, H.; Li, M. *Nat. Photonics* **2015**, *9*, 35.

(14) Fitzner, R.; Mena-Osteritz, E.; Mishra, A.; Schulz, G.; Reinold, E.; Weil, M.; Körner, C.; Ziehlke, H.; Elschner, C.; Leo, K. *J. Am. Chem. Soc.* **2012**, *134*, 11064.

(15) Chen, Y.; Wan, X.; Long, G. *Acc. Chem. Res.* **2013**, *46*, 2645.

(16) Liang, Y.; Yu, L. *Acc. Chem. Res.* **2010**, *43*, 1227.

(17) Liu, Y.; Wan, X.; Wang, F.; Zhou, J.; Long, G.; Tian, J.; Chen, Y. *Adv. Mater.* **2011**, *23*, 5387.

(18) Zhou, J.; Zuo, Y.; Wan, X.; Long, G.; Zhang, Q.; Ni, W.; Liu, Y.; Li, Z.; He, G.; Li, C.; Kan, B.; Li, M.; Chen, Y. *J. Am. Chem. Soc.* **2013**, *135*, 8484.

(19) Sun, K.; Xiao, Z.; Lu, S.; Zajaczkowski, W.; Pisula, W.; Hanssen, E.; White, J. M.; Williamson, R. M.; Subbiah, J.; Ouyang, J.; Holmes, A. B.; Wong, W. W. H.; Jones, D. J. *Nat. Commun.* **2015**, *6*.

(20) Punidha, S.; Sinha, J.; Kumar, A.; Ravikanth, M. *J. Org. Chem.* **2008**, *73*, 323.

(21) Barik, S.; Navarathne, D.; LeBorgne, M.; Skene, W. *Journal of Materials Chemistry C* **2013**, *1*, 5508.

(22) Ishiyama, T.; Takagi, J.; Hartwig, J. F.; Miyaura, N. *Angew. Chem. Int. Ed.* **2002**, *41*, 3056.

(23) Littke, A. F.; Dai, C.; Fu, G. C. *J. Am. Chem. Soc.* **2000**, *122*, 4020.

(24) Zhang, M.; Fan, H.; Guo, X.; Yang, Y.; Wang, S.; Zhang, Z. G.; Zhang, J.; Zhan, X.; Li, Y. *Journal of Polymer Science Part A: Polymer Chemistry* **2011**, *49*, 2746.

(25) Miyata, Y.; Nishinaga, T.; Komatsu, K. *J. Org. Chem.* **2005**, *70*, 1147.

(26) Turner, D. J.; Anemian, R.; Mackie, P. R.; Cupertino, D. C.; Yeates, S. G.; Turner, M. L.; Spivey, A. C. *Org. Biomol. Chem.* **2007**, *5*, 1752.

(27) Qin, T.; Zajaczkowski, W.; Pisula, W.; Baumgarten, M.; Chen, M.; Gao, M.; Wilson, G.; Easton, C. D.; Müllen, K.; Watkins, S. E. *J. Am. Chem. Soc.* **2014**, *136*, 6049.

(28) Kumar, R. J.; MacDonald, J. M.; Singh, T. B.; Waddington, L. J.; Holmes, A. B. *J. Am. Chem. Soc.* **2011**, *133*, 8564.

(29) Roquet, S.; Cravino, A.; Leriche, P.; Alévêque, O.; Frère, P.; Roncali, J. *J. Am. Chem. Soc.* **2006**, *128*, 3459.

(30) Roncali, J. *Chem. Rev.* **1997**, *97*, 173.

(31) Hunter, C. A.; Sanders, J. K. *J. Am. Chem. Soc.* **1990**, *112*, 5525.

(32) Martinez, C. R.; Iverson, B. L. *Chemical Science* **2012**, *3*, 2191.

(33) Kim, J.; Swager, T. M. *Nature* **2001**, *411*, 1030.

(34) Halkyard, C. E.; Rampey, M. E.; Kloppenburg, L.; Studer-Martinez, S. L.; Bunz, U. H. *Macromolecules* **1998**, *31*, 8655.

(35) Miteva, T.; Palmer, L.; Kloppenburg, L.; Neher, D.; Bunz, U. H. *Macromolecules* **2000**, *33*, 652.

(36) Levitus, M.; Schmieder, K.; Ricks, H.; Shimizu, K. D.; Bunz, U. H. F.; Garcia-Garibay, M. A. *J. Am. Chem. Soc.* **2001**, *123*, 4259.

(37) Rughooputh, S.; Hotta, S.; Heeger, A.; Wudl, F. *Journal of Polymer Science Part B: Polymer Physics* **1987**, *25*, 1071.

(38) Fitzner, R.; Reinold, E.; Mishra, A.; Mena-Osteritz, E.; Ziehlke, H.; Körner, C.; Leo, K.; Riede, M.; Weil, M.; Tsaryova, O.; Weiß, A.; Uhrich, C.; Pfeiffer, M.; Bäuerle, P. *Adv. Funct. Mater.* **2011**, *21*, 897.

(39) Sun, Y.; Welch, G. C.; Leong, W. L.; Takacs, C. J.; Bazan, G. C.; Heeger, A. J. *Nat. Mater.* **2012**, *11*, 44.

(40) Spano, F. C. *The Journal of chemical physics* **2005**, *122*, 234701.

(41) Bredas, J.-L. *Materials Horizons* **2014**, *1*, 17.

(42) He, Y.; Li, Y. *Phys. Chem. Chem. Phys.* **2011**, *13*, 1970.

(43) Wan, X.; Liu, Y.; Wang, F.; Zhou, J.; Long, G.; Chen, Y. *Organic Electronics* **2013**, *14*, 1562.

(44) Long, G.; Wan, X.; Kan, B.; Liu, Y.; He, G.; Li, Z.; Zhang, Y.; Zhang, Y.; Zhang, Q.; Zhang, M.; Chen, Y. *Advanced Energy Materials* **2013**, *3*, 639.

(45) Sakai, J.; Taima, T.; Yamanari, T.; Saito, K. *Sol. Energy Mater. Sol. Cells* **2009**, *93*, 1149.

(46) He, Z.; Zhong, C.; Huang, X.; Wong, W. Y.; Wu, H.; Chen, L.; Su, S.; Cao, Y. *Adv. Mater.* **2011**, *23*, 4636.

(47) Connelly, N. G.; Geiger, W. E. *Chem. Rev. (Washington, DC, U. S.)* **1996**, *96*, 877.

CHAPTER 6 CONCLUSION AND OUTLOOK

This thesis described the design, synthesis and optoelectronic properties of organic dyes and semiconducting materials of interest in emerging photovoltaics such as dye-sensitized solar cells (DSSCs) and organic photovoltaics (OPVs). The materials were subject to investigation either due to their possible role as primary light harvesters in their respective devices, or due to their ability to modify ITO and potentially promote electron transfer through the organic/ITO interface. Also, discussed throughout this thesis are the photovoltaic properties of devices fabricated using these organic dyes and semiconducting materials (although the discussion is preliminary in the case of the latter), or in the case of chapter 4 the electron transfer rates at the modified ITO surface.

Specifically, chapters 2 and 3 focused on addressing two issues often encountered with DSSCs fabricated with squaraine dyes (a class of near infra-red absorbers); aggregation on the surface of TiO_2 and lack of panchromatic absorption. In chapter 2, four different high energy absorbing groups (thiophene, dithienothiophene, dithienopyrrole, and dithienosilole) where introduced as π-bridges in asymmetric donor-π-acceptor squaraines and were demonstrated to (1) introduce high energy absorption to squaraine dyes, and (2) in the case of dithienosilole bridge, reduce surface aggregation between adsorbed squaraine dyes via the out-of-plane 2-ethylhexyl groups present in this dithienosilole bridge. DSSCs fabricated with squaraines dyes having the aforementioned dithienosilole bridge achieved the highest PCEs, ca. 8.9%, which is attributed to lower dye aggregation, high energy absorption and slower electron recombination rates. In addition, electron acceptors with different types of anchoring groups, phosphonic acids and carboxylic acids, were tested and it was found, through femtosecond transient absorption spectroscopy, that squaraines with phosphonic acid anchoring groups experienced lower charge injection efficiency into TiO_2 upon photo-excitation compared to squaraines with carboxylic acid anchoring groups. When coupled with phosphonic acid's higher affinity towards forming aggregates, due to the higher tendency of phosphonic acids to form H-bonds compared to carboxylic acids, squaraine with phosphonic acid anchoring groups yielded a lower and narrower IPCE and hence decreased PCEs.

In chapter 3, in an attempt to achieve panchromatic absorption, four porphyrin-squaraine (Por)–(Sq) dual-chromophoric dyes were synthesized by a convergent synthetic approach. Their optoelectronic properties, as well as their photovoltaic performance in a DSSC, were compared with those of their squaraine–only analogues, reported in the previous chapter. On TiO_2, these dual-chromophoric dyes were capable of absorbing light throughout the visible region of the solar spectrum, and in devices they demonstrated IPCE onsets in the near infra-red at around 850 nm. Although, some (Por)-(Sq) dyes demonstrated slightly better photovoltaic characteristics (up to 1.0% higher PCEs) compared to their squaraine-only analogues, mainly due to higher IPCE values at wavelengths above ca.750 nm, this was not observed universally. As an example, none of these (Por)-(Sq) dyes (highest PCE of 7.6%) were capable of surpassing the performance achieved by the dithienosilole squaraine dye reported in chapter 2 (PCE of 8.9%).

Although these (Por)-(Sq) dyes had higher optical densities at high energy, their IPCE values at those energies did not surpass that of the squaraines. One contributor to the lower IPCE identified in this work is the lower charge injection efficiency of the (Por)-(Sq) dyes into TiO_2 compared to squaraine-only dyes; as measured by femtosecond transient absorption spectroscopy. However, other reasonable contributors may play a role, such as lower dye regeneration by the electrolyte. Moving forward, investigating dye regeneration is necessary to gather a full understating of the factors causing the discrepancy between the absorption profiles of these (Por)-(Sq) dyes and the IPCE of DSSCs fabricated with them. If found problematic, one way to improve dye regeneration would be by adding an electron donating group, such as a diaryl amine,[1] to the *meso*-position of the porphyrin,[2] that would localize the hole to the diaryl amine as opposed to the bulky porphyrin, and hence facilitate the regeneration by the electrolyte.

Throughout chapters 2 and 3, DSSCs fabricated with squaraine-based dyes have achieved J_{SC} values up to 19 $mAcm^{-2}$, which is on par with some of the best performing DSSCs in the literature.[3] Surely, there is still room for improvement in this regard as the maximum IPCE values attained where 80% over some parts of visible solar spectrum, with an IPCE onset around 850 nm. An optimal IPCE would have values approaching 90% over the visible and near infra-red portion of the solar spectrum up to ca. 950 nm.

Rebecca Hill, a colleague in our lab, is currently exploring ways to increase the photocurrent obtained from DSSCs employing squaraine dyes. However, attention should be given to increase the V_{OC} of DSSCs fabricated using squaraine dyes.

As discussed in the introduction, DSSCs utilizing the triiodide/iodide redox shuttle suffer from lower V_{OC} values due in part to the shuttle's low redox potential (+0.35 V vs. NHE). Cobalt-based shuttles, on the other hand, have higher redox potential (+0.62 V for $[Co(phen)_3]^{3+/2+}$), and DSSCs utilizing this redox shuttle have been shown to achieve higher V_{OC} ca. 0.90 V vs. ca. 0.65 V in the case of squaraine-based DSSCs.[3-5] Also, the ground state oxidation potential for the squaraine dyes in chapters 2 and 3 were determined to be at least ca. +0.82 V vs. NHE which indicates that there should be enough driving force for dye regeneration.

However, cobalt-based redox shuttles have been also shown to increase electron recombination from TiO_2, which lowers the V_{OC};[6] so, when designing squaraine dyes it might prove beneficial to introduce alkyl chains at the donor end of the molecule to separate the cobalt and the TiO_2's surface which potentially will lower the ability of the cobalt to capture the injected electron from TiO_2. In fact, preliminary photovoltaic measurements done by Dr. El-Sayed's lab on DSSCs fabricated with the (Por)-(Sq) dye, **3.5**, utilizing a trihexylsilyl groups at its porphyrin and a $Co(phen)_3$ electrolyte, showed V_{OC} values that are ca. 0.1 V higher than those in a triiodide/iodide cell. One suggested squaraine for use in a DSSC with cobalt-based electrolyte is demonstrated in Figure 6.1. The molecular structure of **6.1** is very similar to the squaraine dye that achieved PCE ca. 8.9% but with one exception; the presence of 1-octylnonyl alkyl chain at the donor end, which shows promising results with cobalt-based electrolytes and is employed in some of the best performing dyes, such as perylene based dye, compound **1.4**, in the introductory chapter.[7,8]

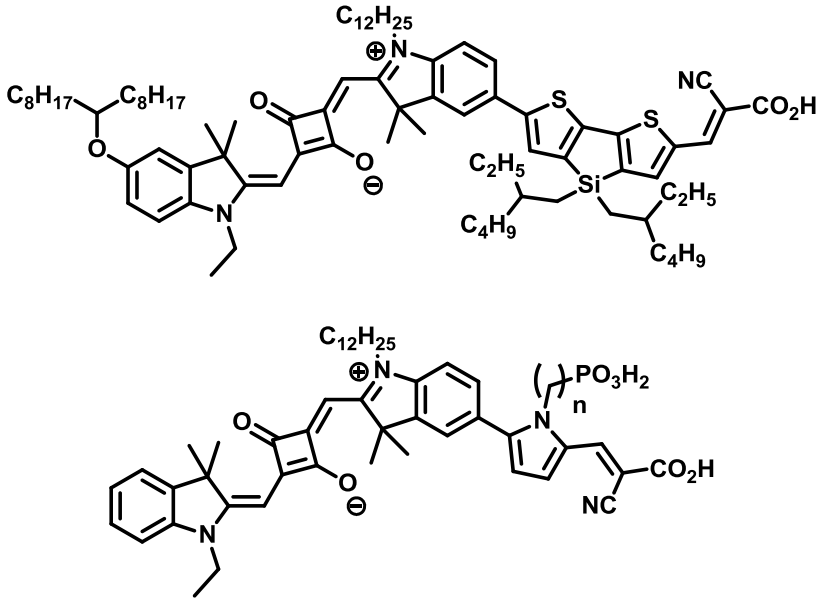

Figure 6.1 Suggested squaraine structures for future directions.

Another important future direction in terms of squaraine-based DSSCs is their long term stability. One reason dyes utilizing phosphonic acid anchoring groups are still of interest to researchers, despite the many reports (including our own in chapter 2) that demonstrate their inferior performance compared to carboxylic acid anchoring groups, is the enhanced stability observed with DSSCs employing them. The extra stability is a result of stronger binding to TiO_2, which can minimize desorption due to the presence of water contaminants, especially in DSSC employing a liquid electrolyte. A squaraine sensitizer with two anchoring groups; a carboxylic acid, and a phosphonic acid, such as **6.2**, Figure 6.1, has the potential of combining the best of both worlds; stronger binding to TiO_2 via the phosphonic acid, while allowing for efficient electron injection to TiO_2 through the carboxylic acid anchoring group.

Chapter 4 introduces a new approach to reduce aggregation in perylene diimides. Although reduced aggregation in perylene diimides and solid-state fluorescence quantum yields as high as 37% have been reported in literature via bay substitutions,[9] the aforementioned substitutions altered the optical and electronic properties (energy levels) of the perylene diimide. On the contrary, by introducing bulky aryl substituents, of different sizes, at the imide positions that point above and below the plane of the PDI, the aggregation of PDI-PAs on ITO surface was also reduced, but this time without changing

their the energy levels of the PDI as the substitutions lie on a nodal plane.[10] When tested in a photo-electrochemical cell, ITO modified with perylene diimides showed enhanced electron transfer efficiency across the interface from a solution donor compared to bare ITO, possibly due to reduced excited-state quenching resulting from aggregation.

Potential future directions could involve testing these perylene modified ITO as electron collecting electrodes in an OPV device to investigate if the enhanced electron-transfer efficiency across the modified ITO can translate to better device performance, especially since unpublished work have shown that depositing **4.3** on ITO caused a decrease in the work function to ca. 4.2 eV.[11] Performing similar studies, as reported in chapter 4, on PDI-PA modified ZnO surfaces could be also another future direction, as ZnO is often used as electron collecting electrode in OPV. Similarly, reducing aggregation in perylene diimides could prove useful in a DSSC setting where excited state quenching due to aggregation has been demonstrated to limit PCE. This, of course, needs to be performed in conjunction with structural modifications on the PDI core as an unmodified PDI's excited state oxidation potential might is too low for electron injection into TiO_2, bay unsubstituted PDI has an $E_{(S^+/S^*)}$ ca. -0.30 V.[10] In addition, we have recently demonstrated that a symmetric perylene diimide with bulky aryl substituents on both of its imide positions, synthesized using the same approach described in chapter 4, shows promise in an organic solar concentrator, due to enhanced solid-state fluorescence.[12]

Finally in chapter five, two series of hole-transport materials that are based on oligothiophene and benzodithiophene cores have been synthesized, with their optoelectronic properties as well as preliminary photovoltaic performance of OPV devices fabricated with them as hole-transport material, is reported. The A-D-A oligothiophenes, which were based on a recent work,[13] were designed in an attempt to enhance the intermolecular interaction in the solid-state via (1) orienting the side chain solubilizing groups away from each other, and (2) utilizing a variety of electron-acceptor group of similar electron affinity but bearing different size and solubilizing chains. Preliminary photovoltaic characterization showed enhanced performance upon annealing, which could be ascribed to increased molecular order, as inferred from their solid-state

optical properties in neat films and in 1:1 blends with $PC_{71}BM$. However, some of the materials synthesized suffered from low solubility, which lowered the quality of films spin-casted from them, and hence limited their performance. Future directions could be focused toward synthesizing analogues with longer or branched solubilizing chains to increase the material's solubility.

The second part of this chapter described attempts to increase the panchromaticity of an A-D-A benzodithiophene material,[14] through changing the nature of the electron-accepting groups. This modification did reduce the optical gaps, through stabilizing the LUMO of the benzodithiophene derivatives, by up to 280 mV to reach 1.50 eV, which give them the ability to absorb light in the infra-red. Measurement of the photovoltaic performance of OPV devices utilizing these materials is currently ongoing; however, an interesting future direction for these types of materials would be to explore their potential as non-fullerene electron acceptors, namely the A-D-A materials with tricyanofuran, and Sandoz acceptor. In fact the tricyanofuran substituted benzodithiophene material had an EA (estimated at ca. +3.8 eV) which is comparable to that of $PC_{71}BM$.

6.1 REFERENCES

(1) Ishida, M.; Park, S. W.; Hwang, D.; Koo, Y. B.; Sessler, J. L.; Kim, D. Y.; Kim, D. *J. Phys. Chem. C* **2011**, *115*, 19343.

(2) Li, L.-L.; Diau, E. W.-G. *Chem. Soc. Rev.* **2013**, *42*, 291.

(3) Mathew, S.; Yella, A.; Gao, P.; Humphry-Baker, R.; CurchodBasile, F. E.; Ashari-Astani, N.; Tavernelli, I.; Rothlisberger, U.; Nazeeruddin, M. K.; Grätzel, M. *Nat Chem* **2014**, *6*, 242.

(4) Yella, A.; Lee, H.-W.; Tsao, H. N.; Yi, C.; Chandiran, A. K.; Nazeeruddin, M. K.; Diau, E. W.-G.; Yeh, C.-Y.; Zakeeruddin, S. M.; Grätzel, M. *Science* **2011**, *334*, 629.

(5) Feldt, S. M.; Gibson, E. A.; Gabrielsson, E.; Sun, L.; Boschloo, G.; Hagfeldt, A. *J. Am. Chem. Soc.* **2010**, *132*, 16714.

(6) Hamann, T. W.; Ondersma, J. W. *Energy Environ. Sci.* **2011**, *4*, 370.

(7) Yao, Z.; Zhang, M.; Li, R.; Yang, L.; Qiao, Y.; Wang, P. *Angew. Chem. Int. Ed.* **2015**, *54*, 5994.

(8) Luo, J.; Xu, M.; Li, R.; Huang, K.-W.; Jiang, C.; Qi, Q.; Zeng, W.; Zhang, J.; Chi, C.; Wang, P.; Wu, J. *J. Am. Chem. Soc.* **2014**, *136*, 265.

(9) Lin, M.-J.; Jimenez, A. J.; Burschka, C.; Wurthner, F. *Chem. Commun.* **2012**, *48*, 12050.

(10) Huang, C.; Barlow, S.; Marder, S. R. *J. Org. Chem.* **2011**, *76*, 2386.

(11) Zheng, Y.; Giordano, A.; Cowan, S. R.; Fleming, S. R.; Shallcross, R. C.; Gliboff, M.; Huang, Y.; Nordlund, D.; Ginger, D. S.; McGrath, D. V.; Armstrong, N. R.; Olson, D. C.; Marder, S. R.; Saavedra, S. S. manuscript in preparation, 2016.

(12) Banal, J. L.; Soleimaninejad, H.; Jradi, F. M.; Liu, M.; White, J. M.; Blakers, A. W.; Cooper, M. W.; Jones, D. J.; Ghiggino, K. P.; Marder, S. R.; Smith, T. A.; Wong, W. W. H. **2016**, *submitted*.

(13) Kan, B.; Li, M.; Zhang, Q.; Liu, F.; Wan, X.; Wang, Y.; Ni, W.; Long, G.; Yang, X.; Feng, H. *J. Am. Chem. Soc.* **2015**, *137*, 3886.

(14) Sun, K.; Xiao, Z.; Lu, S.; Zajaczkowski, W.; Pisula, W.; Hanssen, E.; White, J. M.; Williamson, R. M.; Subbiah, J.; Ouyang, J.; Holmes, A. B.; Wong, W. W. H.; Jones, D. J. *Nat. Commun.* **2015**, *6*.

APPENDIX

A.1. HIGH PERFORMANCE LIQUID CHROMATOGRAPHY

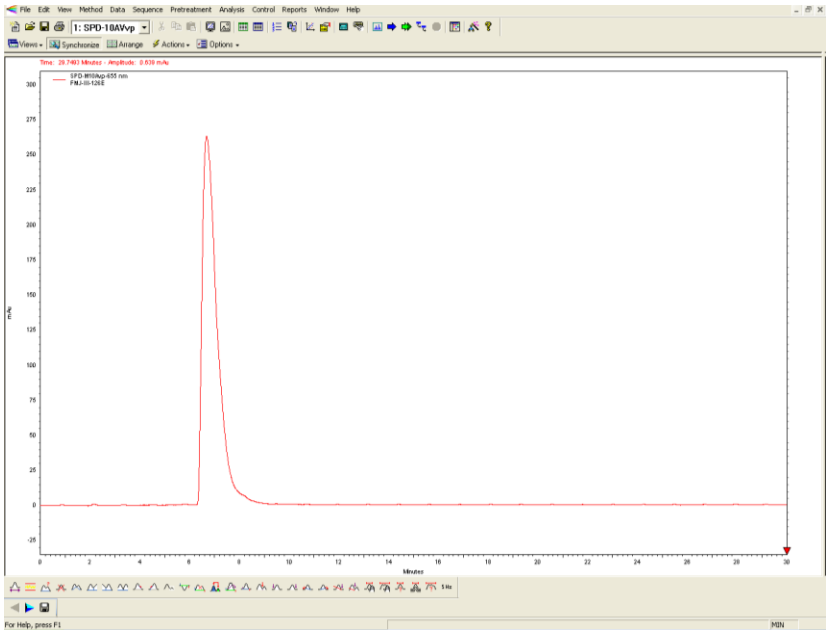

Figure A.1 Analytical HPLC trace for compound **2.3**

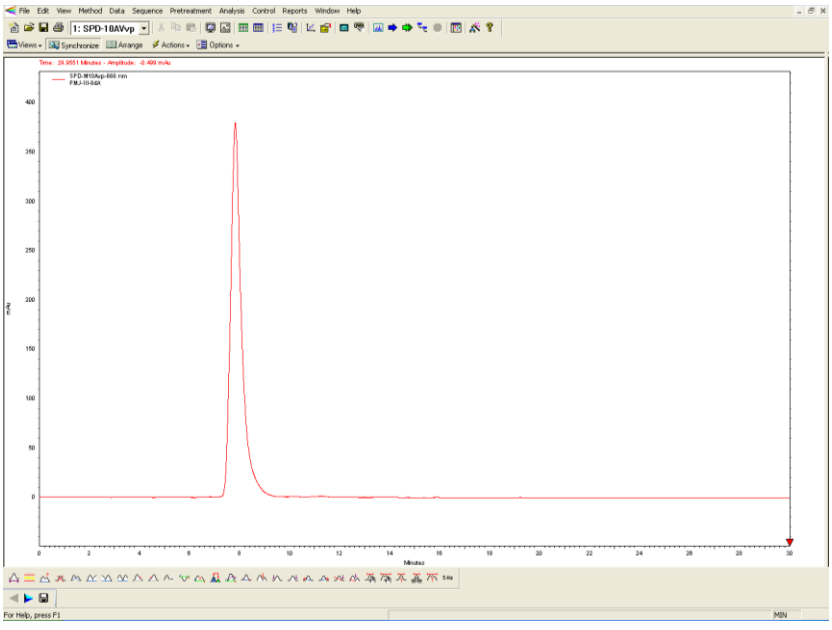

Figure A.2 Analytical HPLC trace for compound **2.5**

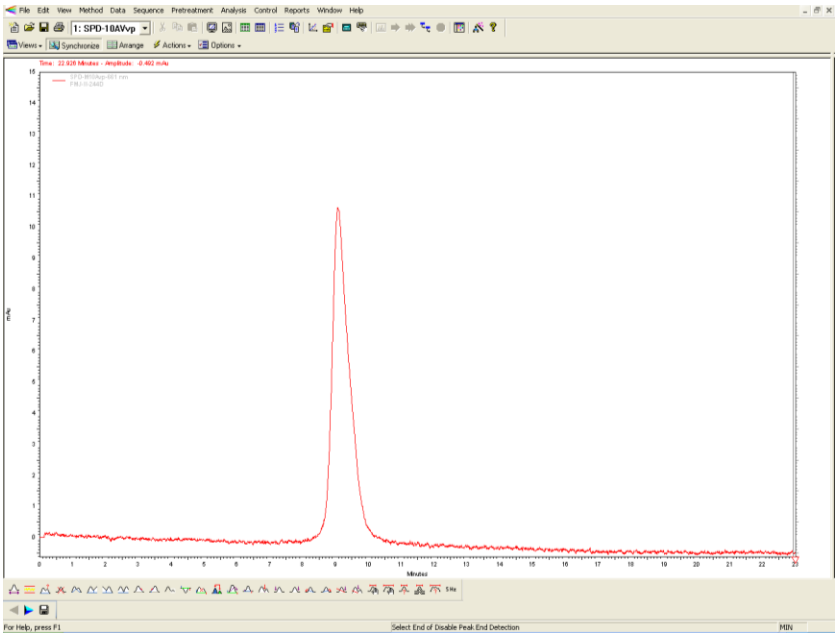

Figure A.3 Analytical HPLC trace for compound **2.6**

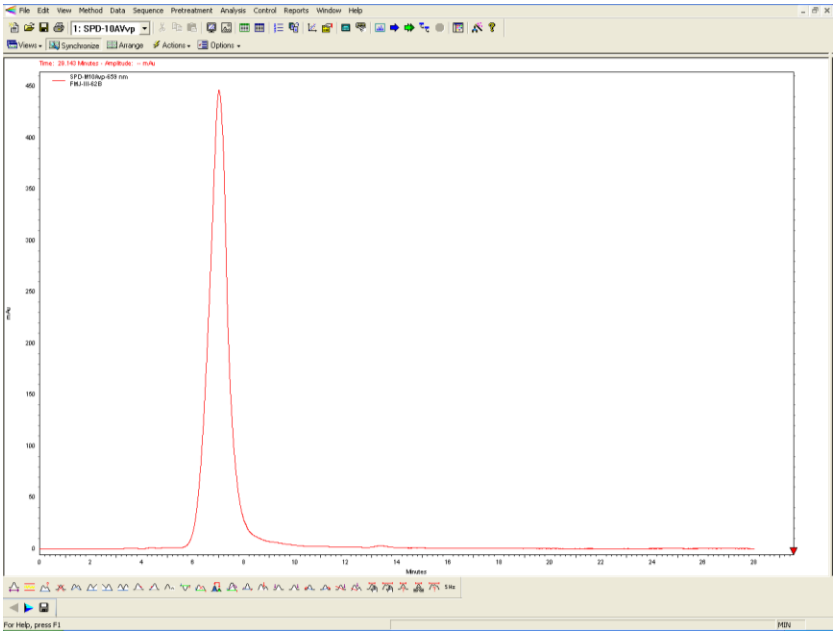

Figure A.4 Analytical HPLC trace for compound **2.7**

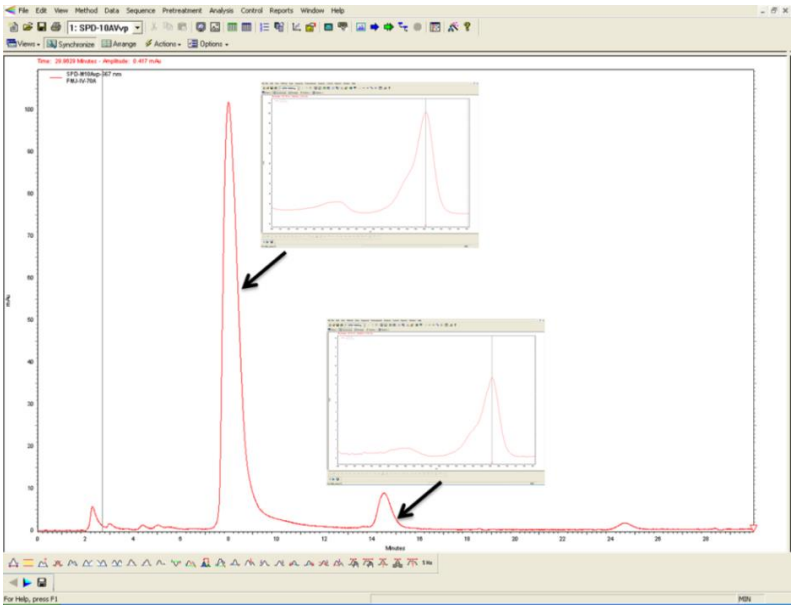

Figure A.5 Analytical HPLC trace of **2.9**, the peak at 8.3 minutes is 83% while the peak at 14.3 is 10% and they have nearly identical absorption spectra. The MALDI spectrum, Figure 1.14, shows that in addition to the product peak with an m/z equals to 1140. There exists a peak with an m/z equal to 1168, which corresponds to the DTS-PA mono ethyl ester, which would be the product of incomplete hydrolysis. This suggests that the HPLC peak at 14.3 min retention time is the PA mono ester, which should have a similar UV-Vis spectrum as the desired product

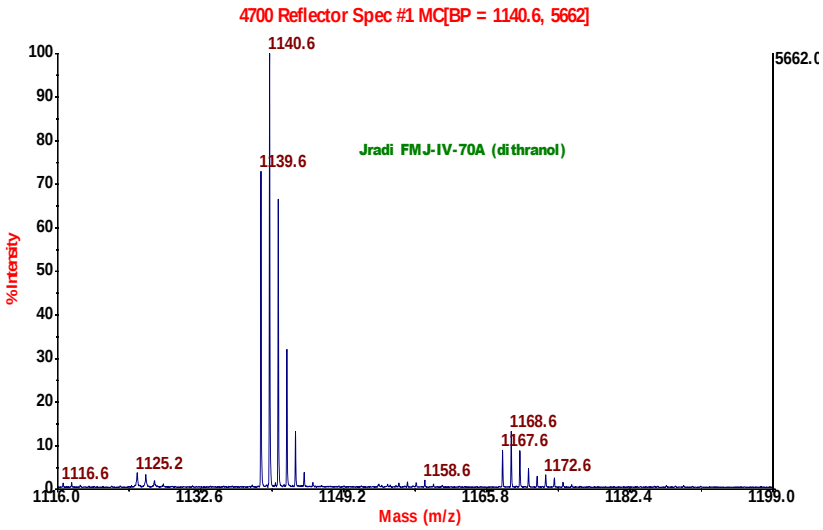

Figure A.6 MALDI spectrum of **2.9** showing the incomplete hydrolysis product at *m/z* 1168

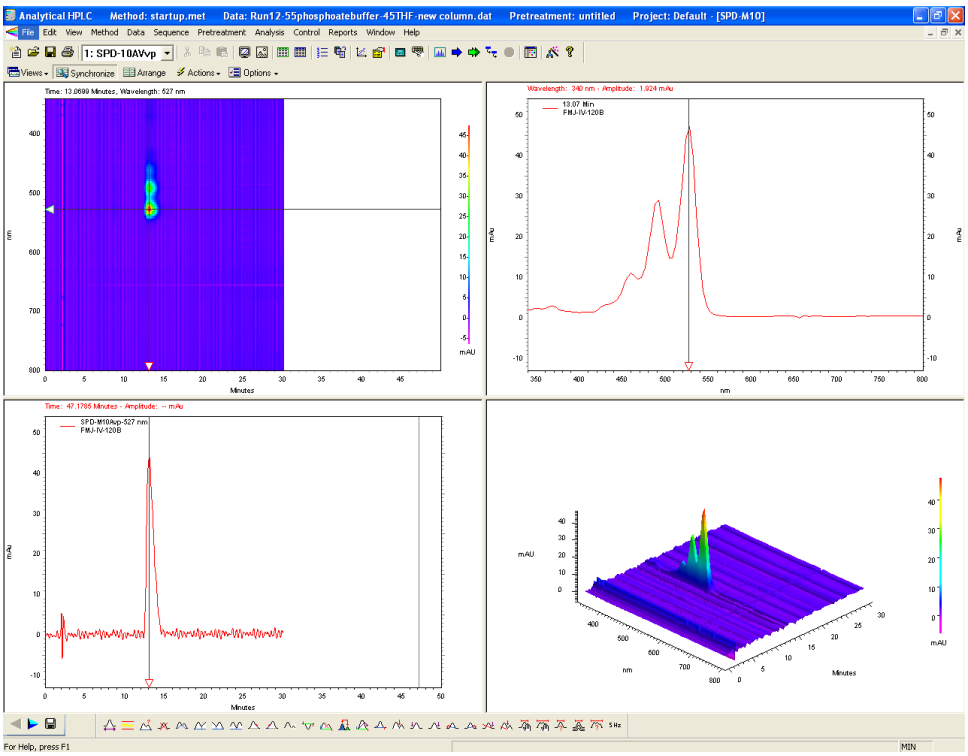

Figure A.7 Analytical HPLC trace of **4.5**

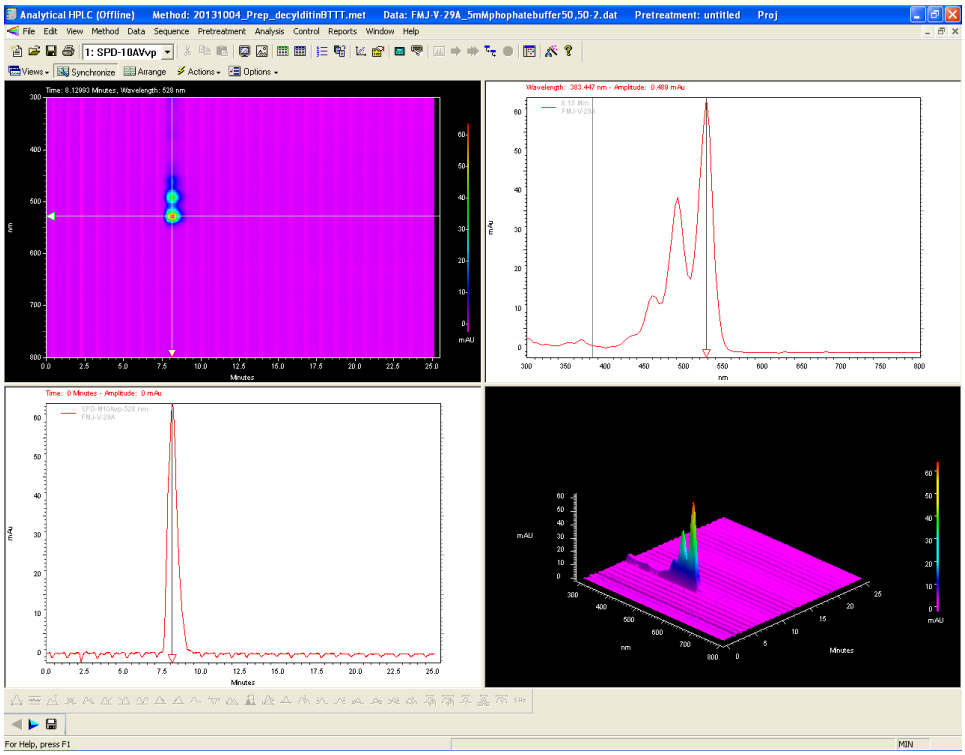

Figure A.8 Analytical HPLC trace of **4.7**

A.2. ABSORPTION AND ABSORPTION-EMISSION SPECTRA

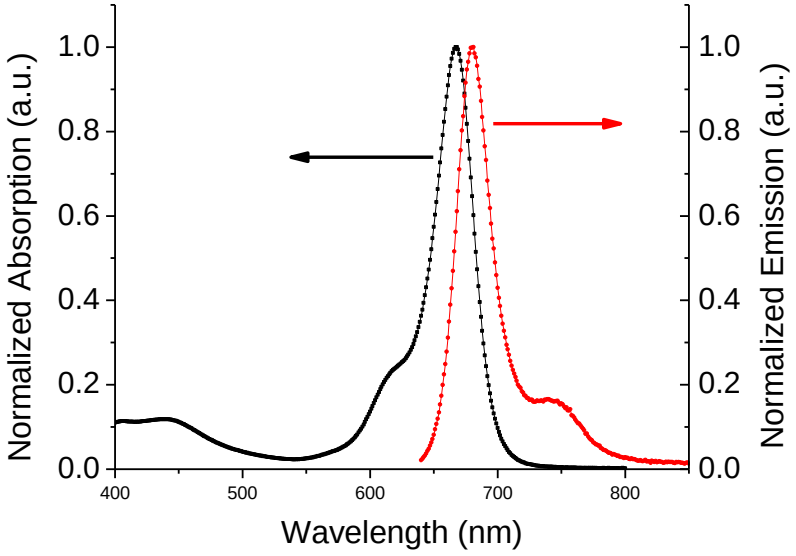

Figure A.9 Normalized absorption and emission spectra for compound **2.6**

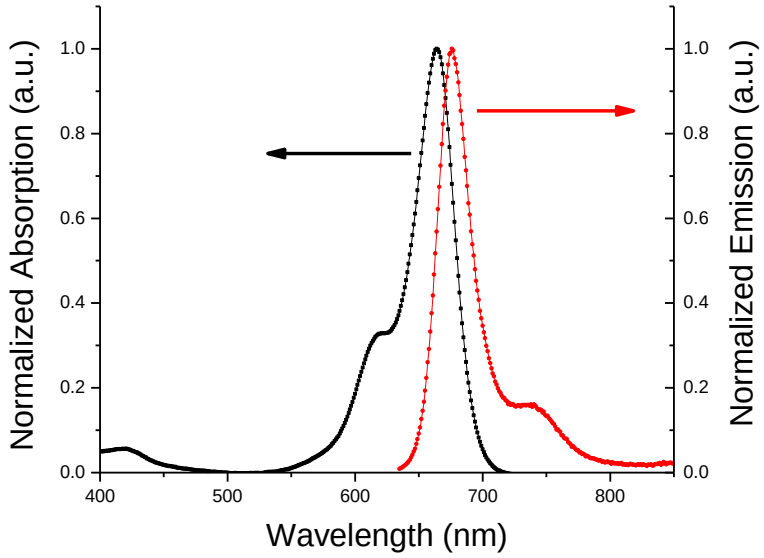

Figure A.10 Normalized absorption and emission spectra for compound **2.3**

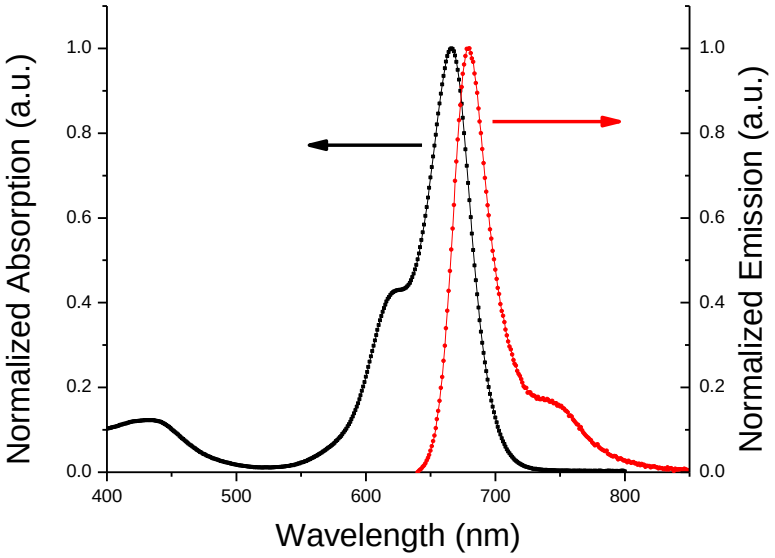

Figure A.11 Normalized absorption and emission spectra for compound **2.7**

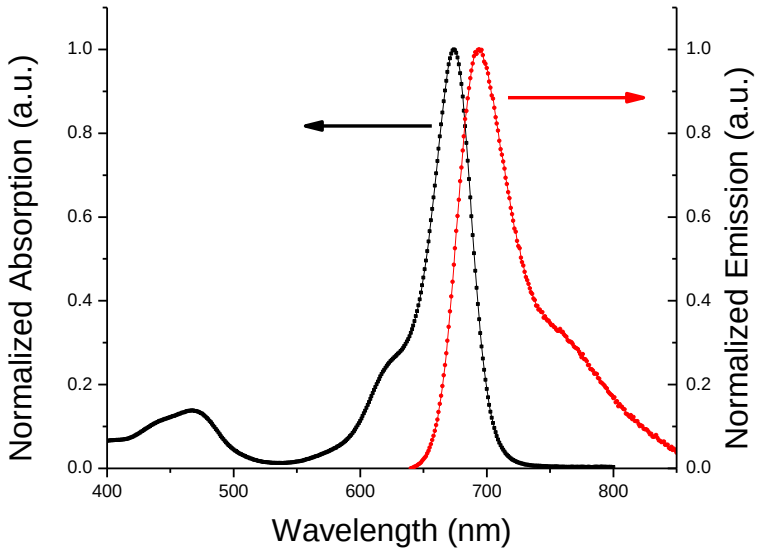

Figure A.12 Normalized absorption and emission spectra for compound **2.5**

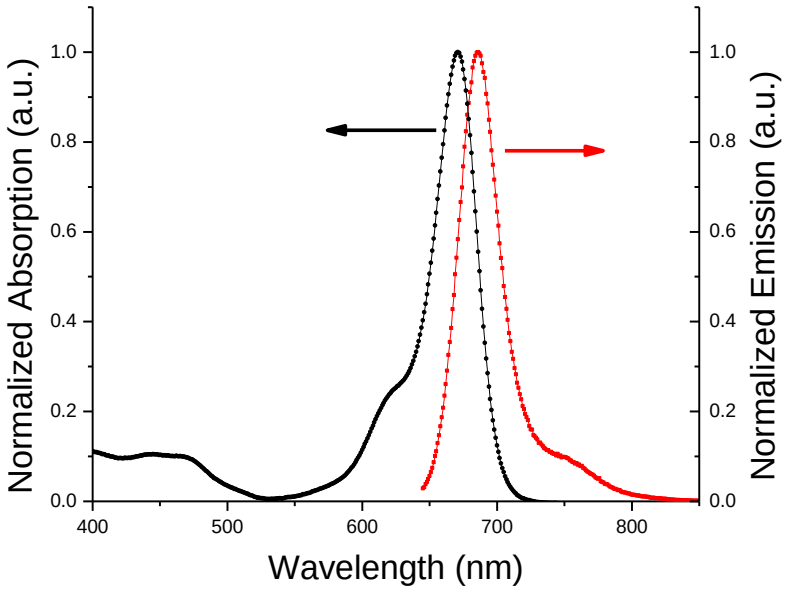

Figure A.13 Normalized absorption and emission spectra for compound **2.9**

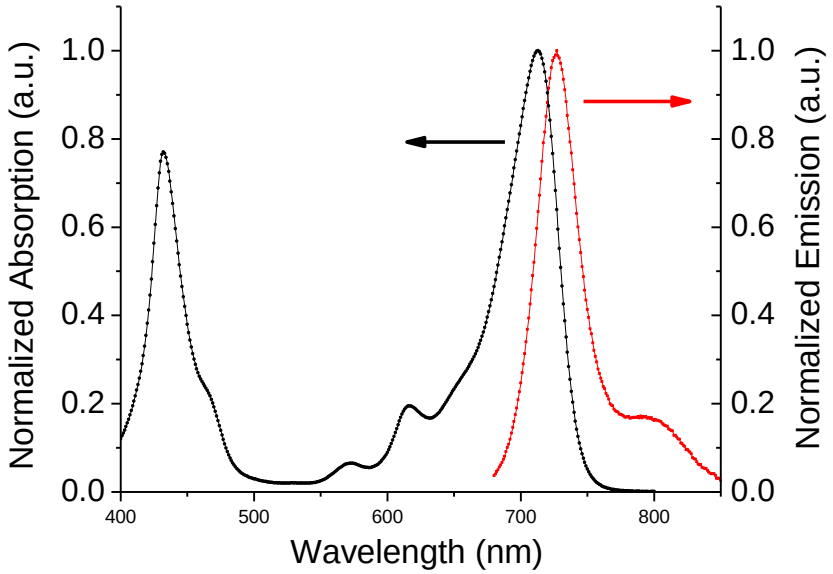

Figure A.14 Normalized absorption-emission spectra for **3.3**

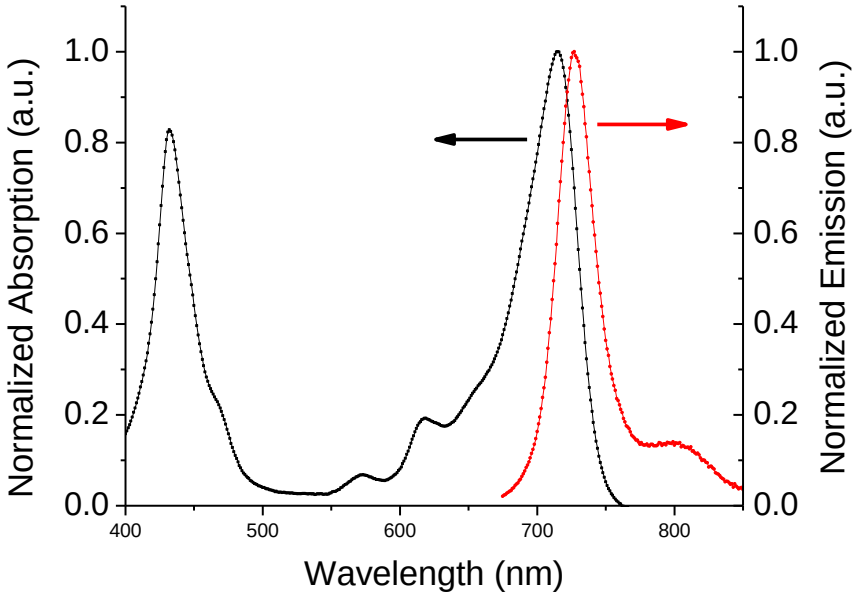

Figure A.15 Normalized absorption-emission spectra for **3.4**

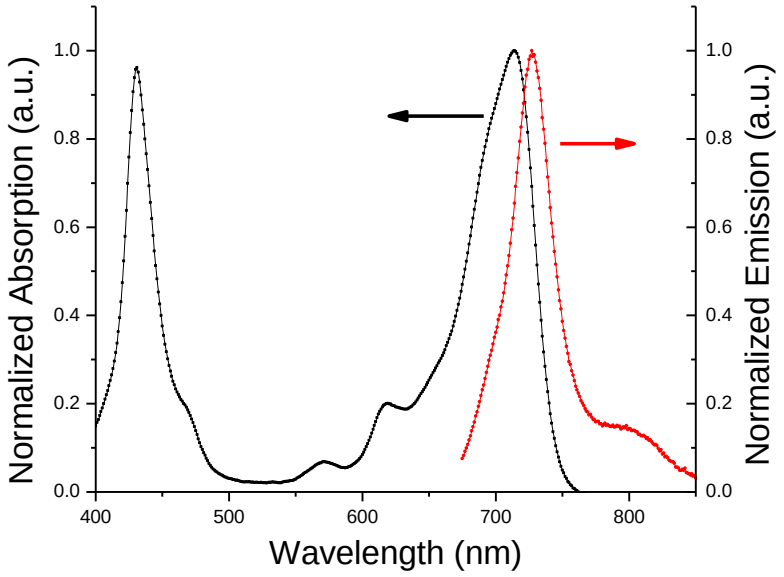

Figure A.16 Normalized absorption-emission spectra for **3.5**

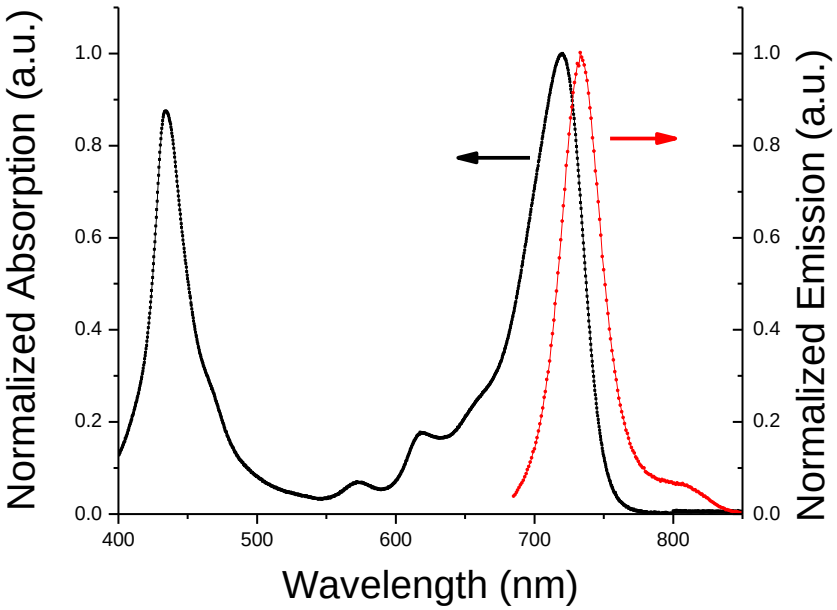

Figure A.17 Normalized absorption-emission spectra for **3.6**

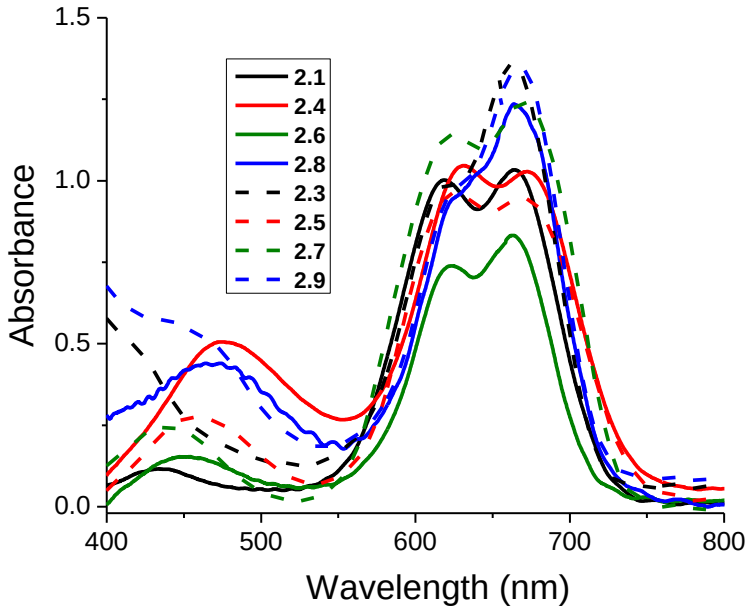

Figure A.18 UV-vis absorption spectra of the dyes presented in Figure 2.1 on TiO_2 films. TiO_2 films were dipped in a solution containing 0.05 mM dye and 10 mM CDCA for 1 hour. The solid lines correspond to the dyes with carboxylic acid anchoring groups, while the dashed lines correspond to dyes with phosphonic acid anchoring groups

A.3. CYCLIC VOLTAMMETRY

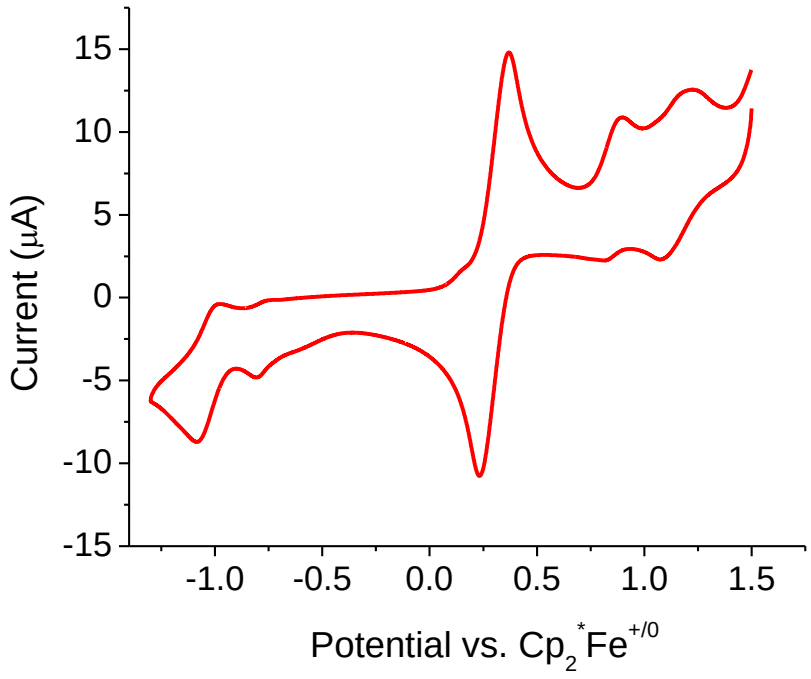

Figure A.19 Cyclic voltammogram of compound **3.3**

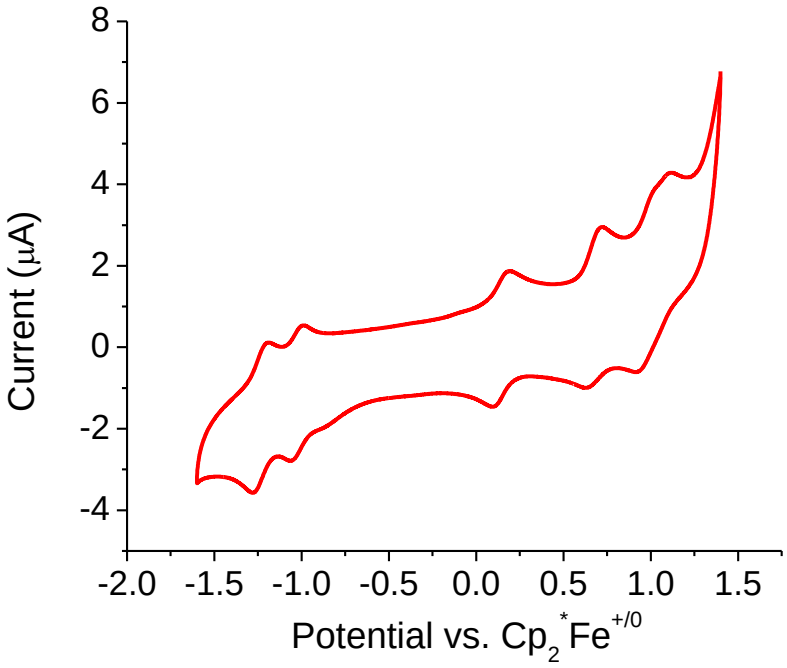

Figure A.20 Cyclic voltammogram of compound **3.4**

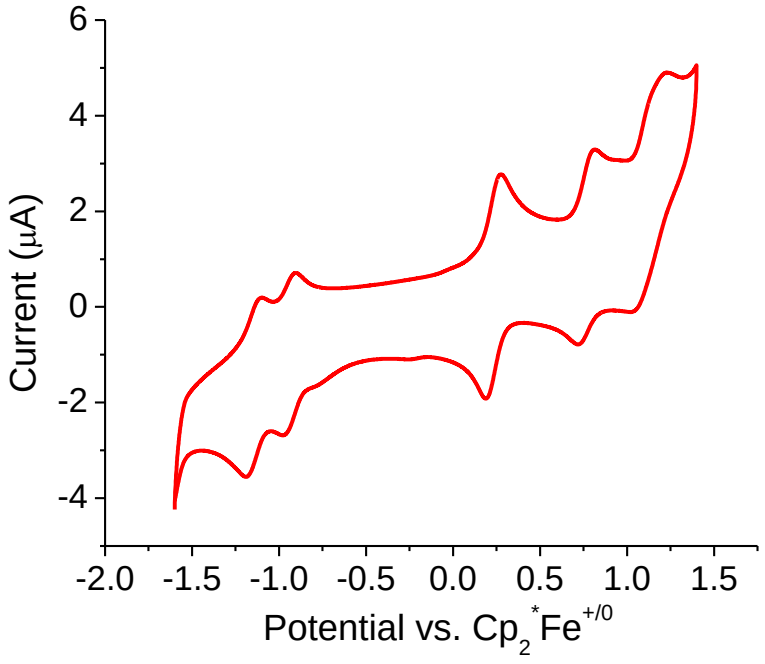

Figure A.21 Cyclic voltammogram of **3.5**

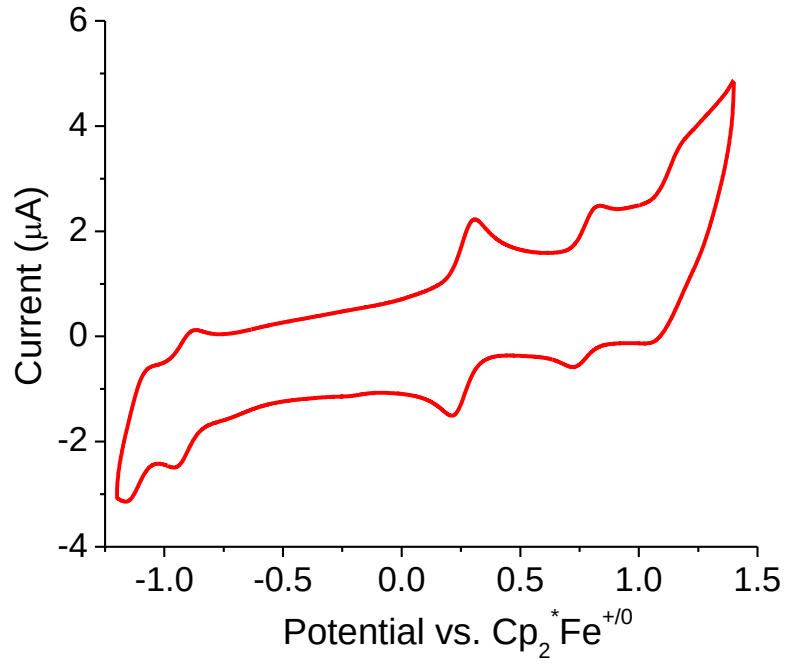

Figure A.22 Cyclic voltammogram of **3.6**

A.4. MOLECULAR MODELING

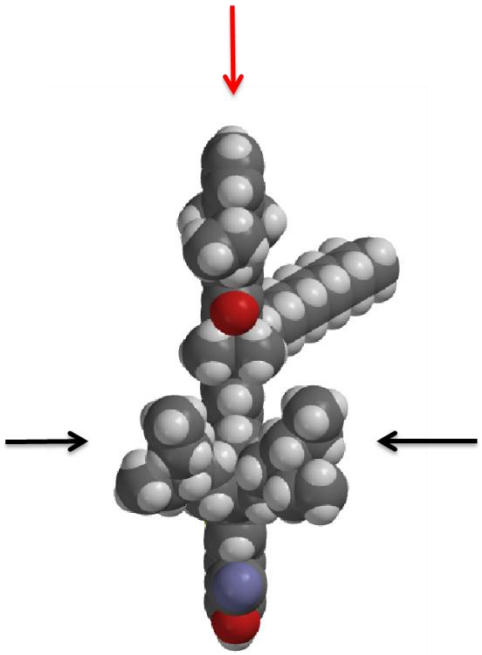

Figure A.23 A molecular model of compound **2.8**; Black arrows point at the 2-ethylhexyl groups pointing above and below the plane of the squaraine, red arrow

A.5. ^{1}H NMR SPECTRA

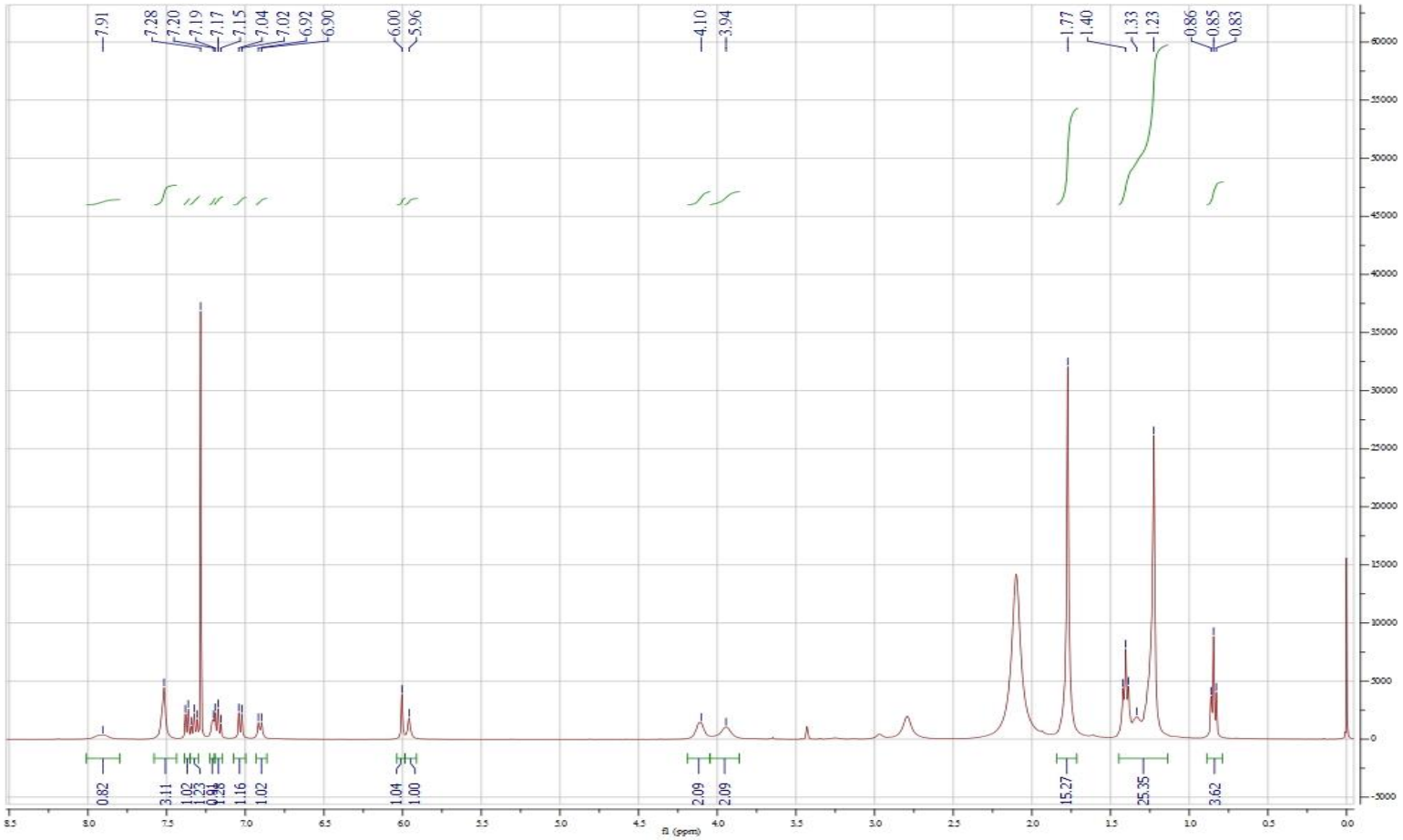

Figure A.24 ^{1}H NMR of compound **2.3**

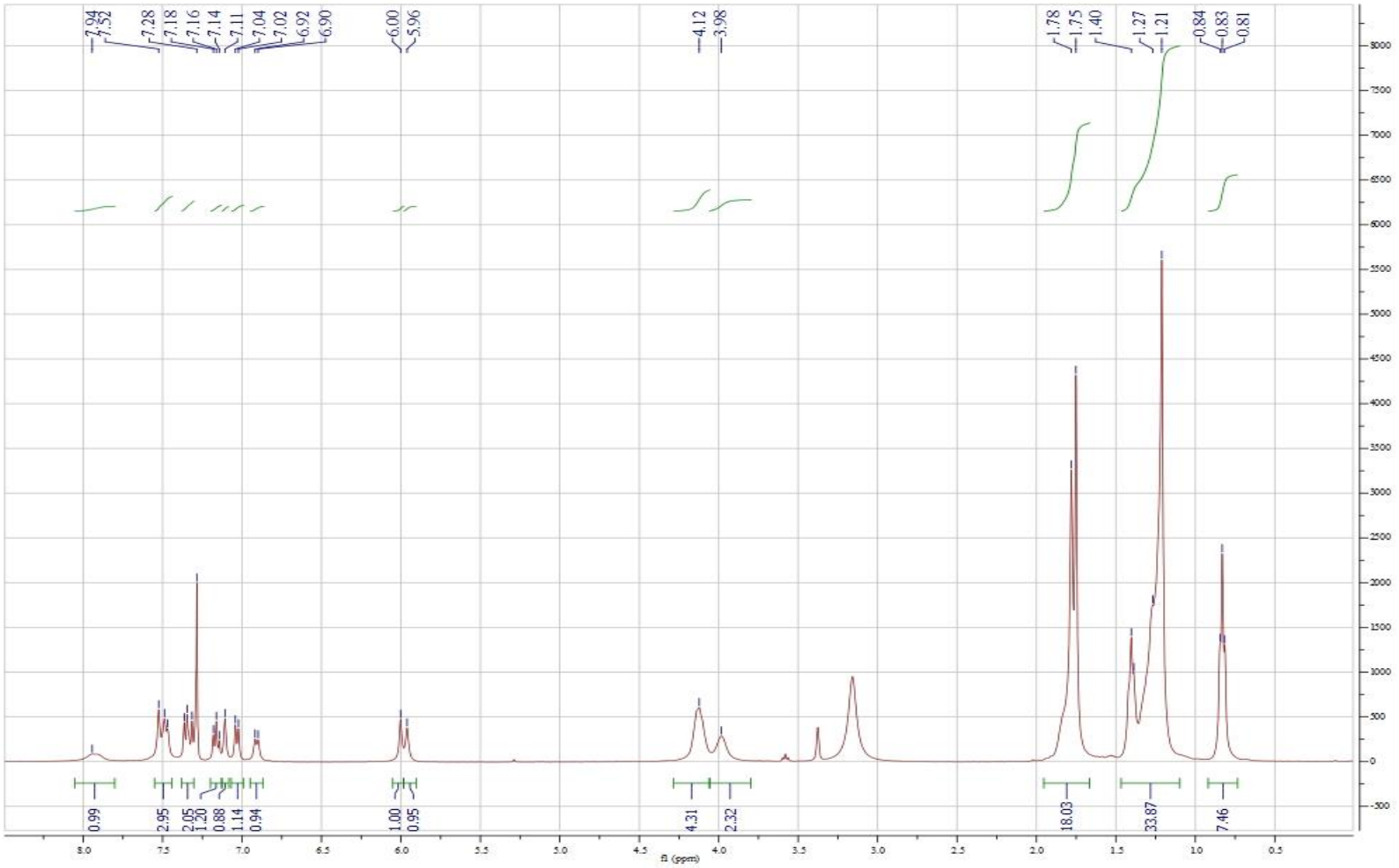

Figure A.25 ^{1}H NMR of compound **2.5**

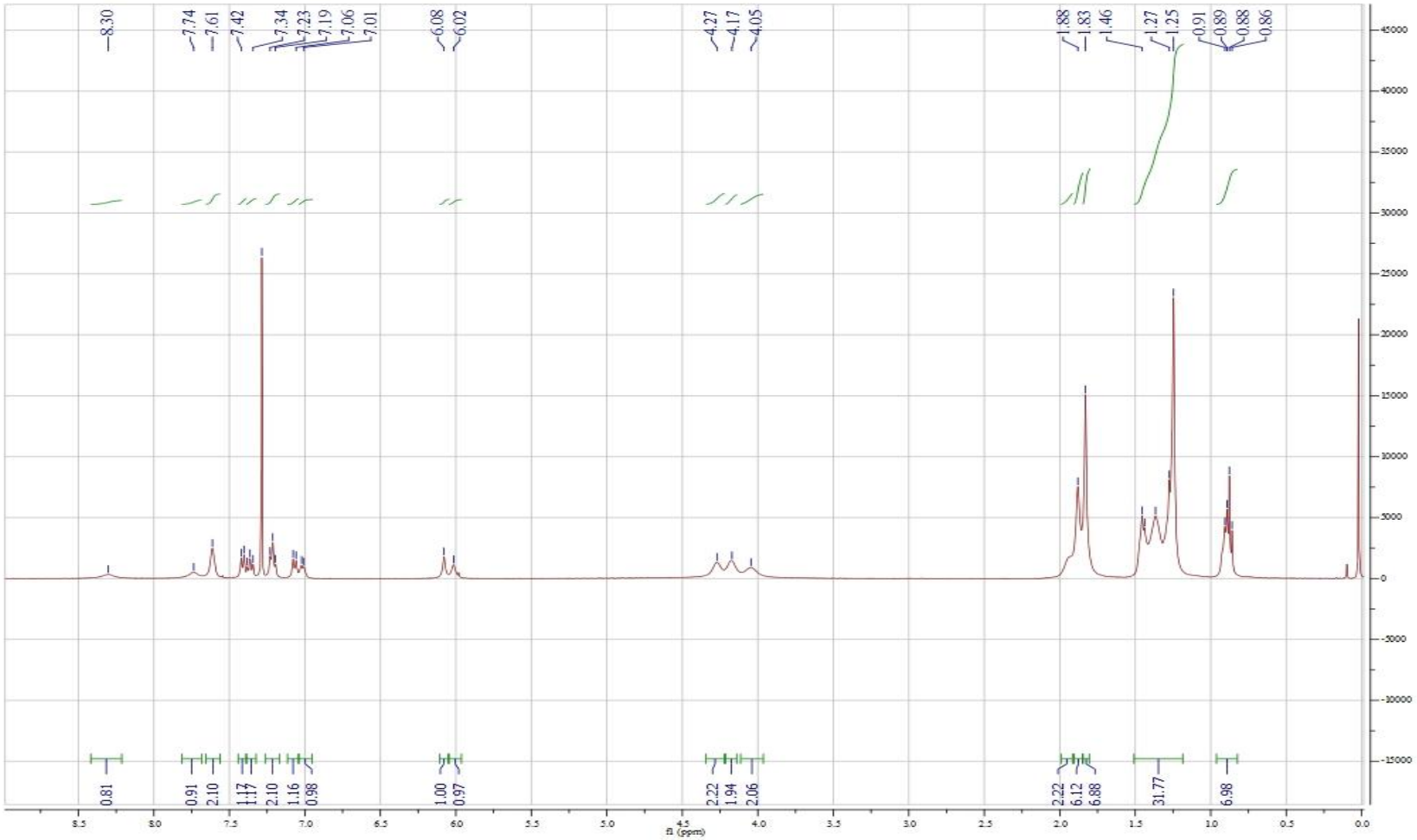

Figure A.26 ^{1}H NMR of compound **2.6**

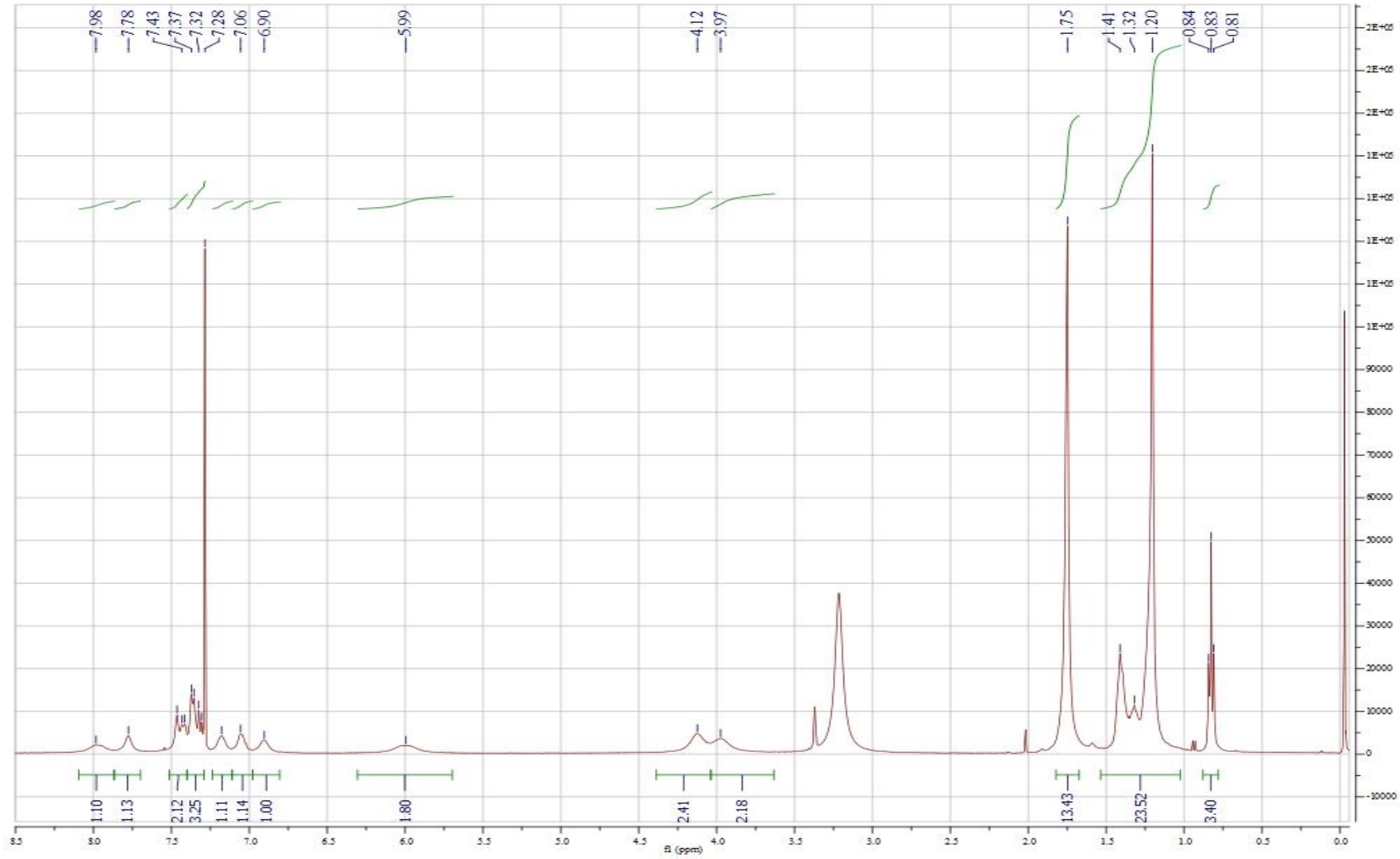

Figure A.27 ^{1}H NMR of compound **2.7**

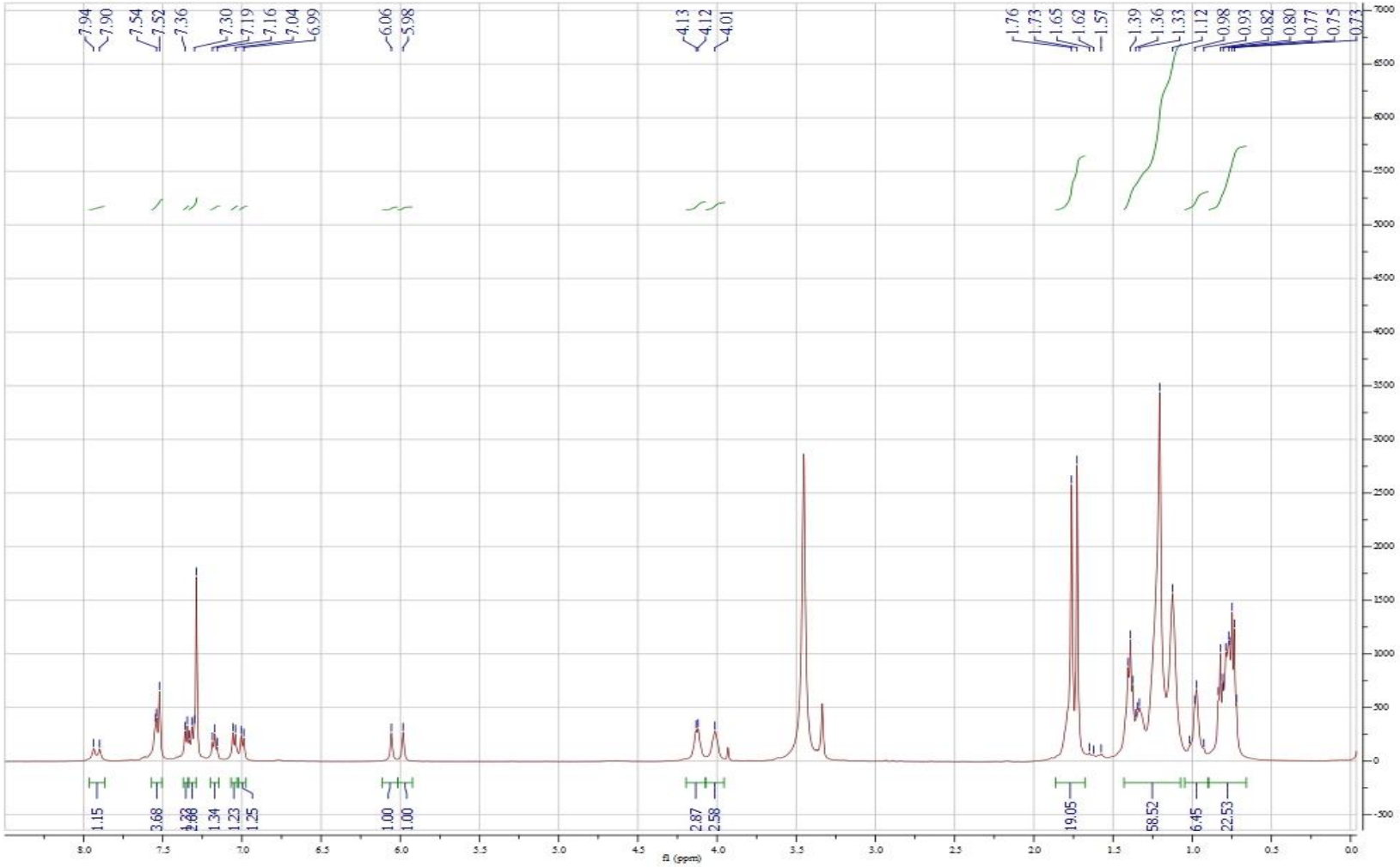

Figure A.28 ^{1}H NMR of compound **2.9**

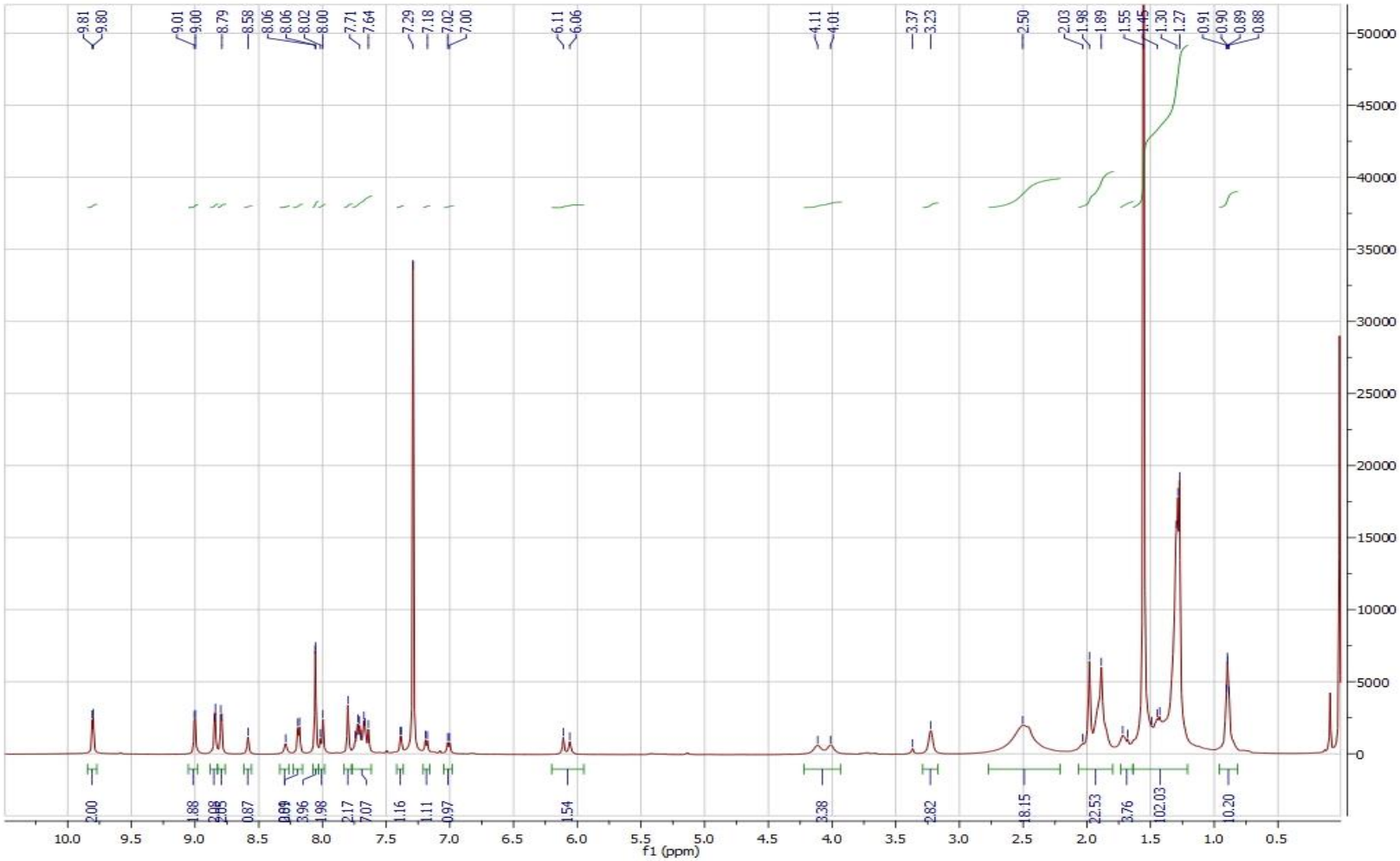

Figure A.29 ^{1}H NMR of compound **3.4**

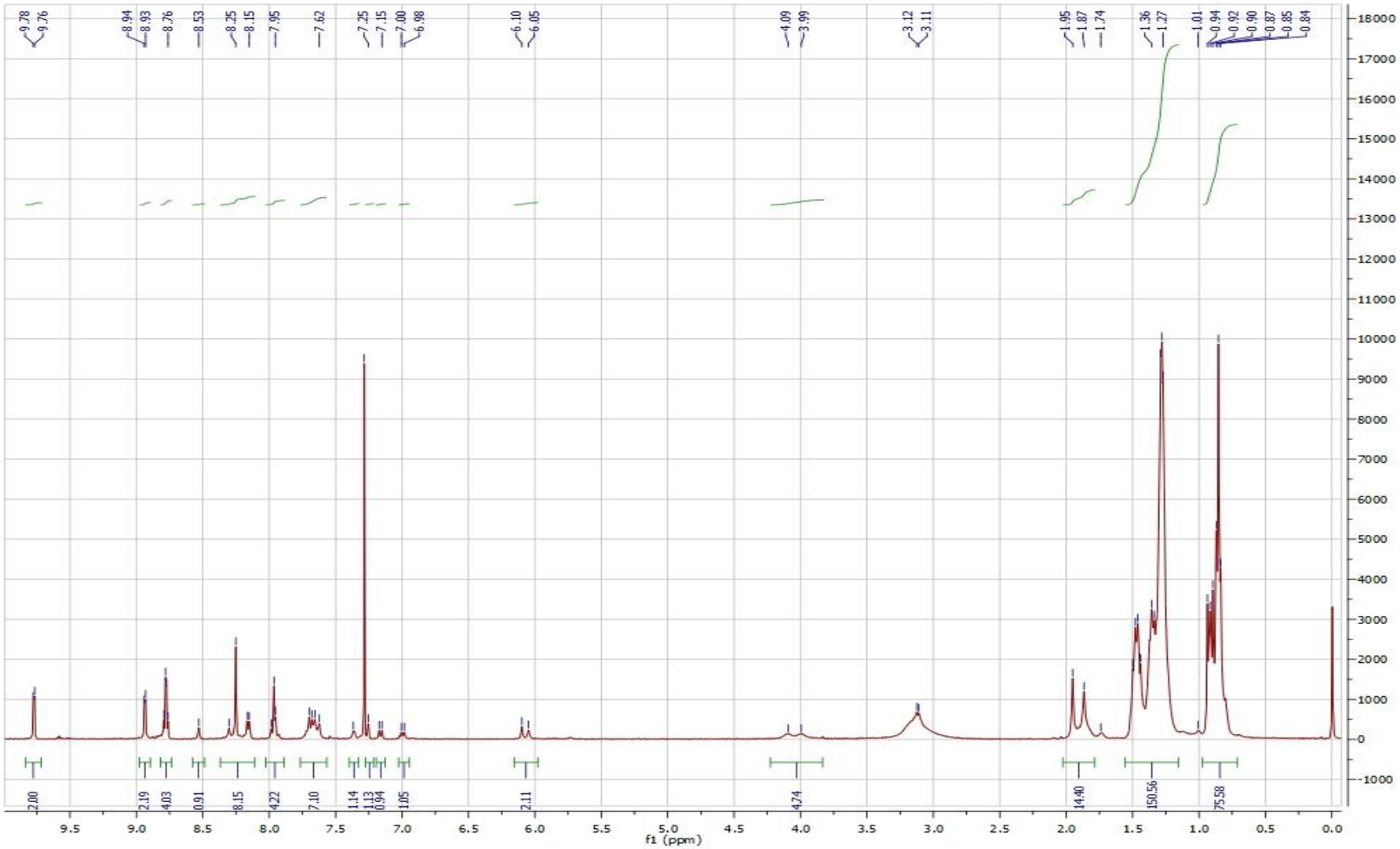

Figure A.30 ^{1}H NMR of compound **3.5**

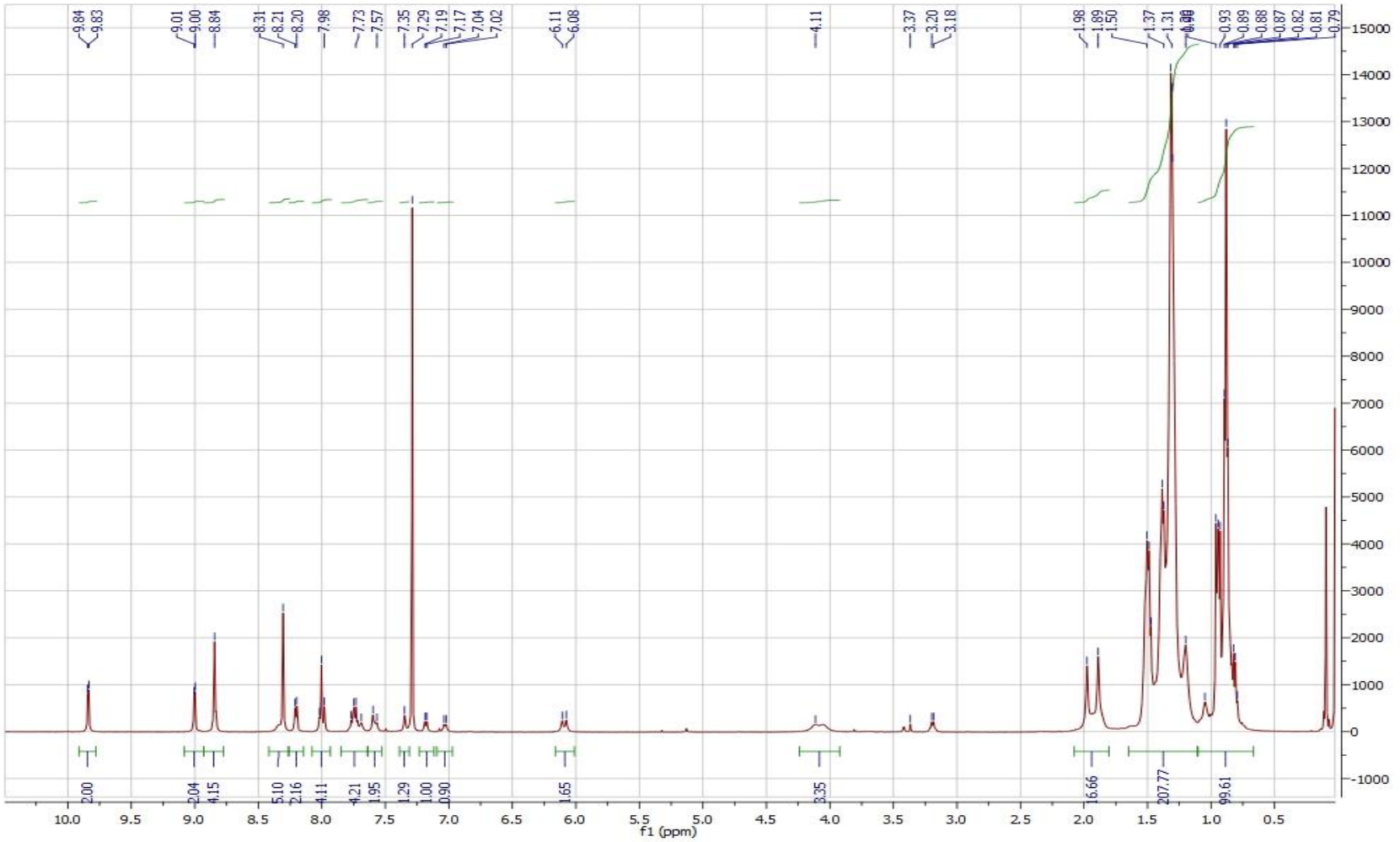

Figure A.31 ^{1}H NMR of compound **3.6**

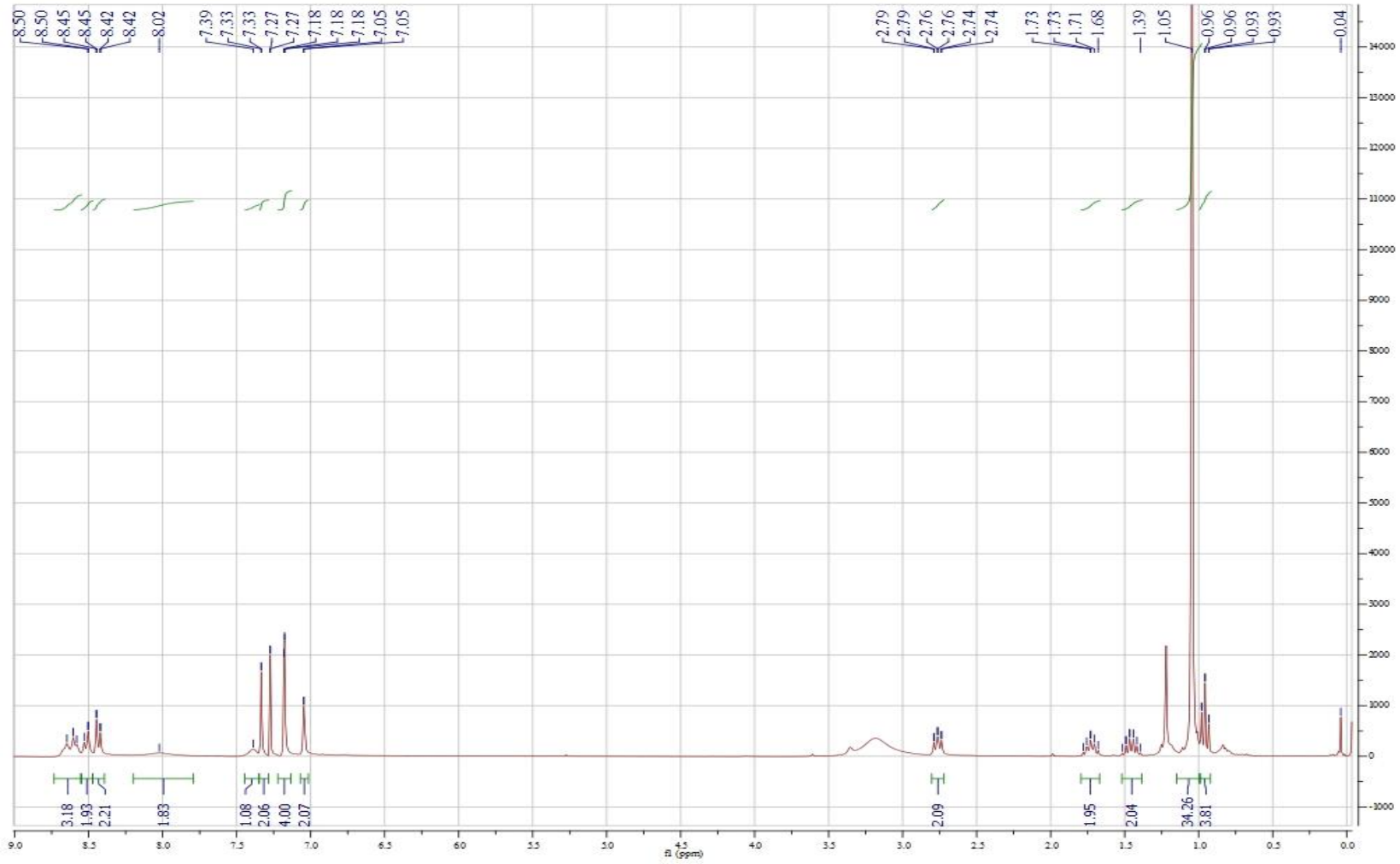

Figure A.32 ^{1}H NMR of compound **4.5**

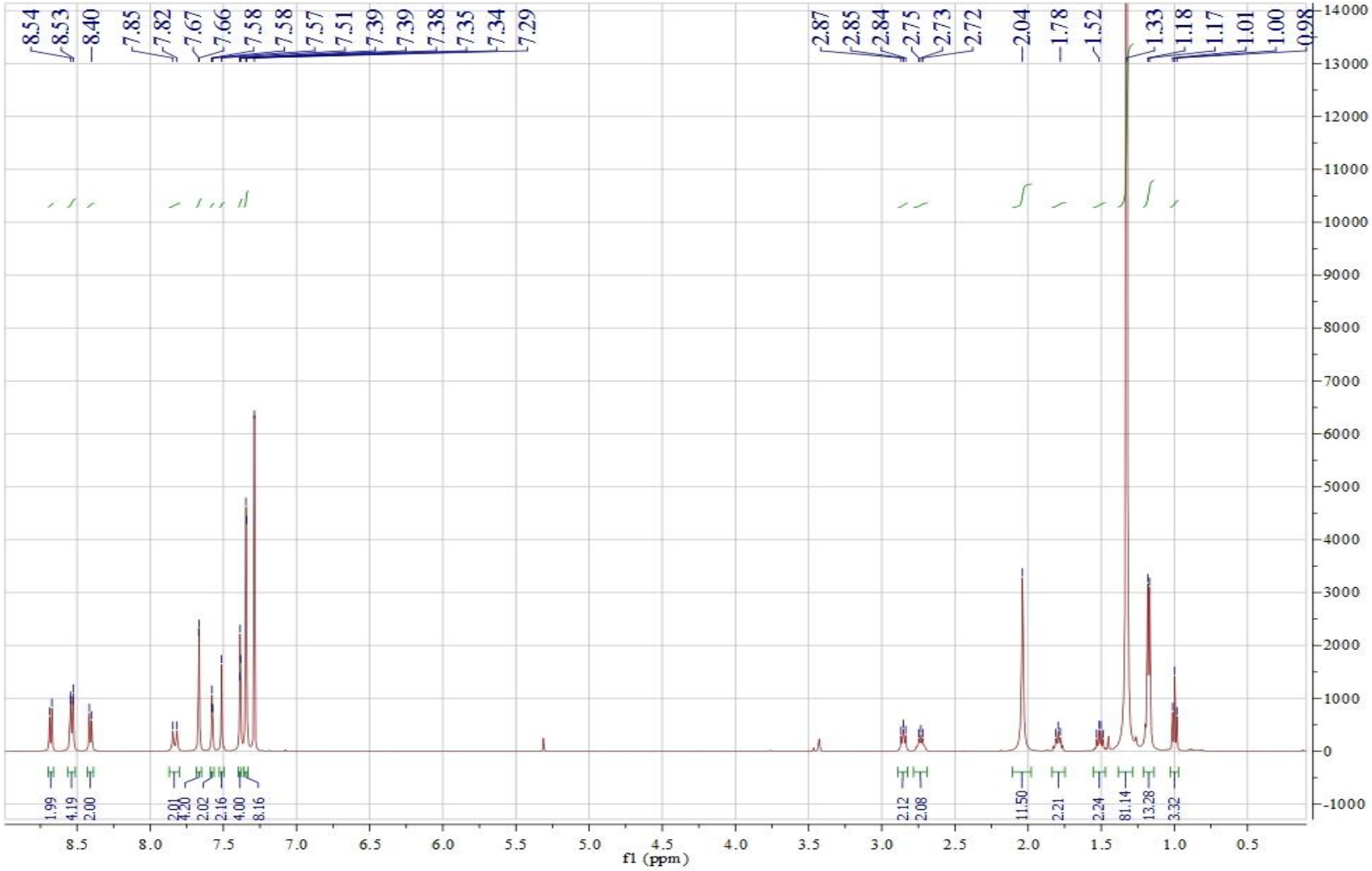

Figure A.33[1]H NMR of compound **4.7**

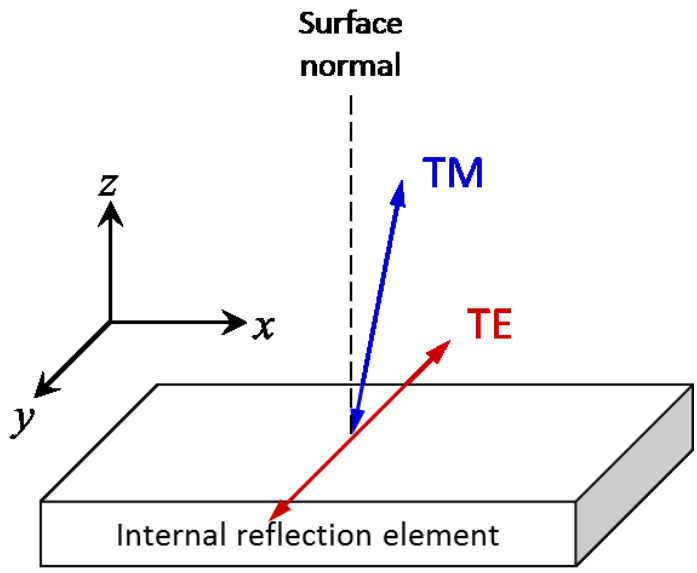

Figure A.34 The coordinate system defining transverse electric (TE) and transverse magnetic (TM) polarizations.